Fluctuations in Cold and Dense QCD Matter with Functional Methods

Dissertation

zur Erlangung des akademischen Grades
Doktor der Naturwissenschaften
(Dr. rer. nat.)

Konstantin Otto

November 2022

Institut für Theoretische Physik
Justus-Liebig-Universität Gießen

JUSTUS-LIEBIG-
UNIVERSITÄT
GIESSEN

Fluctuations in Cold and Dense QCD Matter with Functional Methods
Fluktuationen in kalter und dichter QCD-Materie mit funktionalen Methoden

Genehmigte Dissertation von Konstantin Otto, M.Sc.
Fachbereich 07: Mathematik und Informatik, Physik, Geographie

Justus-Liebig-Universität Gießen
Institut für Theoretische Physik
Heinrich-Buff-Ring 16
35392 Gießen

Eingereicht am 24.05.2022
Disputation am 26.10.2022

Erstgutachter: Priv.-Doz. Dr. Bernd-Jochen Schaefer
Zweitgutachter: Prof. Dr. Lorenz von Smekal

Zusammenfassung

Diese Arbeit befasst sich mit der Untersuchung von Fluktuationseffekten in kalter und dichter Materie, welche der starken Wechselwirkung unterliegt. In der Natur existiert solche Materie im Inneren von Neutronensternen und ihre Eigenschaften sind bisher größtenteils unbekannt. Unter Verwendung einer effektiven Quark-Meson-Trunkierung der Quantenchromodynamik mit zwei oder drei Quark-Flavors integrieren wir Quantenfluktuationen mit der funktionalen Renormierungsgruppe (FRG) aus und untersuchen ihren Einfluss auf die Eigenschaften von Neutronensternen.

Die erforderliche thermodynamische Zustandsgleichung wird hier für neutrale Materie im Beta-Gleichgewicht berechnet. Die Unterschiede zu konventionellen Zustandsgleichungen, welche in einfachen Mittelfeldnäherungen erzeugt werden, sind signifikant. Reine Quarkmateriesterne basierend auf dieser Zustandsgleichung haben größere Radien und Massen als ihre Pendants aus der Mittelfeldnäherung. Des Weiteren ist mit der FRG-Zustandsgleichung die Konstruktion von Hybridsternen, also Neutronensternen mit einem Quarkmateriekern, möglich, solange die nukeonische Zustandsgleichung nicht zu steif ist. Die zugrundeliegende Maxwell-Konstruktion nimmt eine scharfe Grenzfläche zwischen Kern- und Quarkmaterie an und führt zu einem einzelnen, durchgehenden Zweig im Masse-Radius-Diagram. Allerdings kann mit dem Hinzufügen von Strangeness die experimentell beobachtete Zwei-Sonnenmassen-Grenze nicht mehr erreicht werden.

Mit dem zusätzlichen Hinzufügen von repulsiven Vektormesonen-Wechselwirkungen in Mittelfeldnäherung beobachten wir einen ausreichenden Anstieg in der Steifigkeit der Zustandsgleichung, um Hybridsterne mit Massen über $2M_\odot$ zuzulassen. Allerdings ist eine Maxwell-Konstruktion mit nukleonischen Zustandsgleichungen, die zu insgesamt kleineren Radien und Deformabilitäten führen und in besserer Übereinstimmung mit dem Experment liegen, weiterhin nicht möglich.

Darüber hinaus untersuchen wir den Ursprung des seltsamen Zurückbiegens der chiralen Phasenübergangslinie im Quark-Meson-Modell in lokaler Potentialnäherung. Wir stellen fest, dass das Zurückbiegen von der Regulatorfunktion, welche in der FRG verwendet wird, abhängt. Für Callan-Symanzik-artige Regulatoren verschwindet es zusammen mit der damit assoziierten negativen Entropiedichte. Das ist ein Hinweis auf die Existenz starker regulatorabhängiger Trunkierungsartefakte in lokaler Potentialnäherung bei endlicher Dichte und kleinen Temperaturen.

Abstract

This work is aimed at the study of fluctuation effects in cold and dense strong-interaction matter. In Nature, such matter exists in the cores of neutron stars and its properties are largely unknown. Utilizing an effective quark-meson truncation to quantum chromodynamics with two and three quark flavors, we integrate out quantum fluctuations by means of the functional renormalization group (FRG) method and study their impact on the properties of compact stars.

The required thermodynamic equation of state (EoS) is hereby calculated for beta-equilibrated and neutral quark matter. We find significant differences to conventional EoS obtained from simple mean-field approximations. Pure quark-matter stars based on the nonperturbative EoS have larger radii and masses than their mean-field counterparts. Furthermore, the EoS obtained with the FRG allows for the construction of hybrid stars, i.e., neutron stars with a quark-matter core, as long as the utilized nucleonic equation of state is not too stiff. The underlying Maxwell construction assumes a sharp interface between nucleonic and quark matter and leads to a single continuous branch in the mass-radius diagram. However, with the inclusion of strangeness the popular two-solar-mass limit for the experimentally observed maximum mass cannot be reached anymore.

With the additional inclusion of repulsive vector-meson interactions on a mean-field level, we find a sufficient increase in the EoS's stiffness to permit hybrid stars with masses over $2M_\odot$. However, a Maxwell construction with nucleonic equations of state that lead to smaller overall radii and tidal deformabilities in better agreement with experiment is still not possible.

Moreover, we investigate the origin of the strange back-bending of the chiral phase transition line at low temperatures in the quark-meson model in local potential approximation. We observe that the back-bending depends on the regulator function used by the FRG. For Callan-Symanzik-type regulators, it vanishes along with the associated negative entropy densities. This hints at the existence of strong cutoff-scheme-dependent truncation artifacts in local potential approximation at finite density and low temperatures.

Contents

1 Introduction **1**

2 Quantum Chromodynamics and Neutron Stars: A Brief Overview **5**
2.1 Quantum Chromodynamics 5
2.2 Neutron Stars 10

3 Functional Methods **13**
3.1 Dyson-Schwinger Equations and nPI Approaches 14
3.2 Functional Renormalization Group 16
3.3 Flow Equations 18
3.4 Truncation Schemes 21
3.5 Regulator Optimization 22
3.6 Flows at Nonzero Chemical Potential 26

4 Functional Renormalization Group Approach to Low-Energy QCD **33**
4.1 Constructing a Low-Energy Effective Theory 33
4.2 Quark-Meson Model 35
4.3 Fluctuations and the Phase Structure 37
4.4 Beyond Local Potential Approximation 44
4.5 Dynamical Hadronization 50

5 Nonperturbative Quark-Matter Equation of State **55**
5.1 Beta Equilibrium and Charge Neutrality 55
5.2 EoS for Quark and Hybrid Stars 57
5.3 Speed of Sound 60
5.4 Quark- and Hybrid-Star Solutions 62
5.5 Conclusions 64

6 Vector-Meson Effects in Hybrid Stars **67**
6.1 Vector Mesons in Mean-Field Approximation 67
6.2 Quark Matter with Repulsive Vector Interactions 70
6.3 Quark- and Hybrid-Star Solutions 72
6.4 Tidal Deformability 74
6.5 Conclusions 76

7 Regulator Effects at Nonzero Chemical Potential **77**
7.1 Fermion Decoupling 77
7.2 Setup and Regulator Choices 78
7.3 Thermodynamics at Low Temperatures 82
7.4 Conclusions 88

8 Summary and Outlook **91**

A Basics, Notation, and Conventions **95**

B Compact Stars from General Relativity **101**

C Derivation of the Polchinski Equation **109**

D Matsubara Sums **111**

E Notes on the Derivation of Flow Equations **115**

F Approximate Flows in the Chirally Symmetric Regime **119**

G Pole Proximity of Vacuum Flows **123**

H Numerical Solution Techniques **127**

I Parameter Fixing **131**

Acknowledgments **151**

Chapter 1

Introduction

Two main pillars modern theoretical physics rests on are the concepts of quantum physics and relativity. Both developed at the beginning of last century, they have opened the doors to the description of Nature at length scales much smaller and much larger than those us humans are accustomed to. With the discovery that light exhibits not only wave-like, but also particle[1] properties, quantum mechanics was born and led to successes at the level of atomic and sub-atomic physics such as the determination of the spectrum of hydrogen [4]. The incorporation of Einstein's special relativity [5] eventually culminated in the reformulation of electromagnetism as *quantum electrodynamics* (QED)—a quantum field theory based on the local gauge symmetry group $U(1)$ [6–8]. The advance of quantum field theory continued: Nuclear decay processes like β decay are now understood as transmitted by the heavy W and Z exchange bosons via the weak interaction. Moreover, the large "zoo" of new unstable particles with different quantum numbers found at particle colliders could be ordered, e.g., via the "eightfold way" [9]. Group-theoretic considerations implied that the underlying gauge group for the strong interaction must be $SU(3)$. Implicitly, nucleons and all other such *hadrons* are made up of combinations of more fundamental particles, so-called *quarks* [10], each of them carrying one of three *color* charges giving the theory its name: *quantum chromodynamics* (QCD). The electromagnetic, weak, and strong nuclear forces and all associated fields plus the Higgs boson are nowadays collected in the *Standard Model* of particle physics.[2]

Despite the triumph of quantum field theory in the last century, there are still many open questions and unsolved problems even within the boundaries of the Standard Model. The computation of physical observables is particularly challenging in QCD because perturbative methods fail in the low- to intermediate-energy regime due to the theory's large coupling strength [16]. Much progress has been achieved with the formulation of QCD on a discretized lattice of spacetime points, but unfortunately lattice QCD suffers from a sign problem which strongly inhibits calculations at nonzero density [17]. Other nonperturbative methods like Dyson-Schwinger equations (DSE) and the functional renormalization group (FRG) have had more success with the search for a possible critical endpoint in the phase structure of QCD [18–20]. However, especially the description of cold and dense matter still presents many conceptual and technical difficulties. For example, the

[1] A corpuscular theory of light was already put forward in the 17th century by Descartes and Newton, but all known effects at the time were later better described by the physics of electromagnetic waves [3].

[2] The Higgs field is responsible for the generation of the masses of the elementary quarks, charged leptons, and the W and Z gauge bosons [11–13] and was experimentally discovered in 2012 [14, 15].

dynamical formation of baryonic degrees of freedom is not well-understood and reliable first-principle results in this regime do not exist so far; for a discussion of possible future avenues see, e.g., Ref. [21].

Intriguingly, some of the properties of cold and dense matter can be assessed from astrophysical observations: macroscopic properties like masses, radii, and tidal deformabilities of neutron stars correlate with the pressure–density relation determined by the underlying microscopic interactions. To a certain extent, quantum effects like the Pauli exclusion principle [22] help prevent the collapse of compact stars to black holes by accumulating enough outward pressure counteracting the force of gravity. Being the only fundamental force that is perturbatively nonrenormalizable, gravity is described as a classical (i.e., non-quantized) theory by Einstein's general relativity [23]. Theories of quantum gravity are are still of speculative nature as quantum effects are expected to start playing a role at distances close to the Planck length $l_\mathrm{P} \approx 10^{-35}$ m and can be ignored in our context.

At densities close to nuclear-matter density, interaction strengths can be determined from nuclear theory and calibrated with nuclear experiments. However, the core of neutron stars can reach up to several times nuclear matter density [24]. Here, the state of matter is unknown and the occurrence of hybrid stars with quark matter cores is one of the theorized possibilities. The description of quark matter oftentimes relies on effective models solved in simple approximations, with only few nonperturbative ansatzes [25–30] so far. Thus, it is the aim of this thesis to provide some of the first exploratory studies of fluctuation effects on neutron star properties with the functional renormalization group method.

In recent years, the utilized effective quark-meson truncation of QCD has seen some interest also in the application towards the low-temperature region for several reasons such as the study of inhomogeneous phases [31] or as a testbed for improved numerical methods [32]. A strange back-bending of the FRG-calculated chiral phase transition line in the model [33] was associated with the occurence of negative entropy densities at low temperatures [34]. The elucidation of the origin of this unphysical effect is a vital technical aspect for future studies in this direction and shall also be attempted in this work.

Outline

The thesis is organized as follows:

In Ch. 2 we give a very brief overview of Quantum Chromodynamics and the relevant aspects of neutron star physics. In Ch. 3 we introduce functional methods and particularly detail the functional renormalization group with technical aspects that will play a role in the following parts. The application of the functional renormalization group to the quark-meson model as a low-energy effective model is motivated and exemplified in Ch. 4. Afterwards, in Ch. 5 a nonperturbative quark-matter EoS is constructed and fluctuation effects on quark and hybrid stars are investigated. This is extended in Ch. 6 where additional repulsive vector-meson interactions are added in a phenomenological way. Finally, in Ch. 7 regulator effects on the thermodynamics of the quark-meson model at low temperatures are studied. A summary and outlook is given in Ch. 8.

For details and general conventions, especially on functional notation, we refer the reader to App. A. The Tolman-Oppenheimer-Volkoff equations as well as the tidal deformability of neutron stars are derived in App. B. For completeness, a derivation of the

Polchinski equation in a modern framework is given in App. C. Technical details on Matsubara sums and the derivation of flow equations can be found in Apps. D and E. The attainment of fixed points utilized in the parameter fixing procedure in Ch. 7 is described in App. F and an analysis of the associated regulator-dependent challenges in vacuum flows is given in App. G. The last to appendices H and I contain information about the numerical solution techniques used in this work and the general parameter fixing procedure for Chs. 4–6.

Publications

Parts of this work are already published:

[1] Konstantin Otto, Micaela Oertel, and Bernd-Jochen Schaefer,
Hybrid and quark star matter based on a nonperturbative equation of state,
Phys. Rev. D **101**, 103021 (2020).

[2] Konstantin Otto, Micaela Oertel, and Bernd-Jochen Schaefer,
Nonperturbative quark matter equations of state with vector interactions,
Eur. Phys. J. ST **229**, 3629 (2020).

While the results have been obtained in collaboration with my colleagues, I have solely compiled this dissertation. Texts and figures taken from these references are not cited explicitly. Large parts of the first two articles are contained in Chs. 5 and 6, as well as some portions in Ch. 4 and Apps. H and I. A third article that contains portions of Chs. 3 and 7 and Apps. F, G, and H is in preparation.

Chapter 2

Quantum Chromodynamics and Neutron Stars: A Brief Overview

This chapter is a short introduction into some basic aspects of QCD and current challenges of neutron star physics as a motivation and for later reference. It is in no way exhaustive and we refer to basic textbooks [35–37] and reviews on the topics [24, 38–40] for more information.

2.1 Quantum Chromodynamics

As hinted at in the introduction, quantum chromodynamics describes the strong interaction between elementary particles called quarks. It is a gauge theory of the local $SU(3)$ group, i.e., there are three color charges and the quarks live in its fundamental representation. Quarks come in six different *flavors* of which only the lightest three, *up*, *down* and *strange*, are relevant to us.[1] They interact via a flavor-space diagonal exchange boson, the *gluon*. The QCD Lagrangian in Euclidean spacetime reads

$$\mathcal{L}_{\mathrm{QCD}} = \bar{q}\left(\not{D} + m\right) q + \frac{1}{4} F^a_{\mu\nu} F^a_{\mu\nu} \tag{2.1}$$

with the covariant derivative

$$D_\mu := \partial_\mu - \mathrm{i} g A^a_\mu T_a \tag{2.2}$$

and the field strength tensor

$$F^a_{\mu\nu} = \partial_\mu A^a_\nu - \partial_\nu A^a_\mu + g f^{abc} A^b_\mu A^c_\nu \ . \tag{2.3}$$

The T_a are the generators of local $SU(3)$ color transformations and the f^{abc} are the structure constants, i.e., the components of the adjoint representation of $SU(3)$. They follow from the commutation relations of the generators. Hence, the nonabelian nature of the gauge group leads to gluon self-interactions. The Lagrangian is invariant under local gauge transformations which transform the quarks as

$$q(x) \to U(x) q(x) \ , \quad \bar{q}(x) \to \bar{q}(x) U^\dagger(x) \tag{2.4}$$

[1] The heavier quarks decay rapidly via weak interaction channels and cannot participate in, e.g., stable quark matter at the energy scales we are interested in.

and the gluons as

$$A_\mu(x) \to U(x)A_\mu(x)U^\dagger(x) - \frac{\mathrm{i}}{g}\left(\partial_\mu U(x)\right)U^\dagger(x) \tag{2.5}$$

where $A_\mu(x) := T_a A^a_\mu(x)$ and the transformation matrices U are generated by exponentiating a spacetime-dependent linear combination of the generators, i.e., an element of the associated Lie algebra:

$$U(x) = \mathrm{e}^{-\mathrm{i}\alpha^a(x)T_a} \ . \tag{2.6}$$

Gauge Fixing

In a simple scalar-field theory, we could now write down the path integral over all field configurations. In a gauge theory, quantization requires a few more considerations to obtain the generating functional. Although we will later resign ourselves to calculations in an effective low-energy theory, these shall be shortly outlined here. Mainly, functional continuum approaches necessitate the selection of a specific gauge. Otherwise, the path integral for the gauge field would include infinitely many physically equivalent paths that can be transformed into each other by gauge transformations that leave the action invariant. In practice, this is done via the Fadeev-Popov trick [41] by inserting the identity [35]

$$1 = \int \mathcal{D}\alpha\ \delta[G(A^\alpha)]\ \det\left(\frac{\delta G(A^\alpha)}{\delta\alpha}\right) \tag{2.7}$$

into the path integral. A^α denotes the transformed field according to Eq. (2.5) with the local set of parameters $\alpha^a(x)$ and the gauge-fixing condition $G(A) = \partial_\mu A_\mu - \omega$ where the components $\omega^a(x)$ specify an arbitrary set of functions. Shifting the field variable in the path integral from A to A^α (which leaves the action invariant), we further perform a Gaussian path integral over all ω in order to eliminate the functional delta distribution. Suppressing the index α, this yields the gauge-fixed Lagrangian

$$\mathcal{L}_{\mathrm{gauge-fixed}} = \bar{q}(\not{D} + m)q + \frac{1}{4}F^a_{\mu\nu}F^a_{\mu\nu} + \frac{1}{2\xi}(\partial_\mu A^a_\mu)^2 \tag{2.8}$$

with the width of the Gaussian distribution specified by ξ. The value $\xi = 1$ is commonly referred to as Feynman gauge while the limit $\xi \to 0$ is Landau gauge. The limit can be taken in expressions for correlation functions; for example, the free gluon propagator reads

$$\left\langle A^a_\mu(p)A^b_\nu(-p)\right\rangle = \delta^{ab}\,\frac{p^2\delta_{\mu\nu} - (1-\xi)p_\mu p_\nu}{p^4} \ . \tag{2.9}$$

In contrast to Abelian gauge theories such as QED, the determinant in Eq. (2.7) is field dependent. From an infinitesimal version of the gauge-field transformation (2.5) we follow [35]

$$\frac{\delta G(A^\alpha)}{\delta\alpha} = \frac{1}{g}\partial_\mu D_\mu \tag{2.10}$$

with the covariant derivative in the adjoint representation

$$D^{ab}_\mu = \delta^{ab}\partial_\mu + g f^{abc}A^c_\mu \ . \tag{2.11}$$

The result only depends on α via the field in the covariant derivative and since we shifted the path integration variable to A^α, we can now rename $A^\alpha \to A$ again. The infinite factor due to the physically equivalent gauge orbits is now expressed by the path integral over α which can just be discarded since none of the quantities depend on it. Furthermore, the determinant can be expressed as a Grassmann-valued path integral,

$$\det\left(\frac{1}{g}\partial_\mu D_\mu\right) = \int \mathcal{D}\bar{c}\mathcal{D}c\, \mathrm{e}^{-\int \bar{c}\,(\partial_\mu D_\mu)\,c} \,. \tag{2.12}$$

Conventionally, the factor $1/g$ is absorbed into the definition of the ghost fields $c^a(x)$, $\bar{c}^a(x)$ [35]. They couple to the gluon have spin zero and thereby violate the spin-statistics theorem. However, using a residual global symmetry of the gauge-fixed theory called BRST symmetry [42, 43] one can prove that a projection on asymptotic states that contain only physical particles, i.e., no (anti)ghosts and only transversally polarized gauge bosons, retains unitarity of the S matrix [35]. The total partition function reads

$$Z_{\mathrm{QCD}} = \int \mathcal{D}\bar{q}\mathcal{D}q\mathcal{D}\bar{c}\mathcal{D}c\mathcal{D}A\, \mathrm{e}^{-\int \mathcal{L}_{\mathrm{gauge-fixed}} - \int \bar{c}\,(\partial_\mu D_\mu)\,c} \,. \tag{2.13}$$

Unfortunately, there are further complications in such calculations. Firstly, the gauge-fixing condition $G(A)$ does not uniquely specify a gauge. While it is clear that any infinitesimal gauge transformation would break the condition, there are generally multiple physically equivalent configurations fulfilling the condition which are distinguished by finite gauge transformations. These are referred to as Gribov copies [44]. While there are methods of circumventing a certain number of these copies, e.g., with the ideas proposed by Gribov and Zwanziger [44, 45], there is no complete solution so far. Determining the number of Gribov copies and thus their overall impact is also a nontrivial problem [46].

Secondly, functional renormalization group approaches additionally need to take care of symmetry relations that need to be fulfilled in the infrared regime. These are generalized Ward-Takahashi identities [47, 48] called Slavnov-Taylor identities (STIs) [49, 50] in the context of nonabelian gauge symmetries. A derivation of such relations in the functional context can again be achieved using BRST invariance [51]. Similarly to the preservation of the Silver-Blaze property discussed in the previous chapter, modified scale dependent versions of these identities (mSTIs) need to be imposed throughout a truncated flow to guarantee the fulfillment of the STIs in the infrared [51]. To this point, functional renormalization group results in such setups—with quarks, gluons, and ghosts as the only degrees of freedom—have been achieved for two-flavor vacuum QCD [52] and Yang-Mills theory (pure gauge sector) in vacuum [53] and at finite temperature [54].

Asymptotic Freedom and Confinement

In contrast to QED which has a Landau pole at large energies, the effective gauge coupling g of QCD becomes weaker with increasing energy scale. This has the peculiar feature that QCD eventually becomes perturbative in the high-energy regime. For example, hard initial scattering processes in the hadron jet production in collider experiments can be described perturbatively. Denoting the renormalization scale as μ, the perturbative β function of QCD reads to one-loop order [35]

$$\beta(g) := \mu\frac{\partial g}{\partial \mu} = -\frac{g^3}{(4\pi)^2}\left(11 - \frac{2}{3}N_f\right) \tag{2.14}$$

where N_f is the number of quark flavors. For not too many quark flavors, it is negative as expected. Note that unlike the Landau pole where the coupling diverges at a finite scale, the QCD coupling does not completely vanish at finite energies, thus giving the feature the name *asymptotic freedom*.

Going to small momentum transfers, g becomes large in QCD and perturbative expansions fail. Together with its gauge group structure, this leads to a feature called *confinement*: There are no open color charges. In QED, single electrons are measurable and contained in approximate asymptotic noninteracting states as dictated by the cluster-decomposition property, but in QCD color-charged states are not present in this set. Only color-neutral composite objects like *mesons* (one quark and one anti-quark of the same color), *baryons* (one quark of each color), or more exotic states like *glueballs* with pure gluon content, *tetraquarks* etc. are observable. For a heavy quark–antiquark pair, confinement can be seen in terms of an effective flux-tube potential that can be simulated on the lattice [55]. For increasing distance the potential increases linearly, giving rise to a constant string tension. With sufficient separation of the quarks the confining potential becomes large enough to create a new quark–antiquark pair from the vacuum, resulting in two color-neutral mesons [56]. Taking pure Yang-Mills theory [57], deconfinement can be measured by means of the Polyakov loop

$$L(\boldsymbol{x}) = \operatorname{Tr} \mathcal{P} \exp\left(\mathrm{i}g \int_0^\beta \mathrm{d}\tau \, A_0(\tau, \boldsymbol{x})\right) \ . \tag{2.15}$$

$L(x)$ is not invariant under transformations of the center symmetry $Z(3)$ of $SU(3)$. While $Z(3)$ is explicitly broken by dynamical quarks, in pure Yang-Mills theory or for infinitely heavy quarks it is broken at most spontaneously. The expectation value of the Polyakov loop can be related to the free energy F of a static test quark via [38]

$$\langle L \rangle = \mathrm{e}^{-\beta F} \ . \tag{2.16}$$

Hence, for an intact center symmetry $\langle L \rangle = 0$, placing a single open-color quark in the system costs an infinite amount of energy, hinting at color confinement, whereas a spontaneously broken center symmetry $\langle L \rangle \neq 0$ signals deconfinement.

So far, there is no concise proof of confinement in pure Yang-Mills theory. Multiple technical confinement scenarios for full QCD are proposed [58, 59] but their discussion is beyond the scope of this work. At large momentum transfers (i.e., short-distance physics) confinement is not an issue and individual particles can be probed. Thus, it is expected that matter at large densities and/or temperatures is essentially deconfined.

Global Symmetries

Next to the gauge symmetry or the residual BRST symmetry, QCD possessed multiple additional global symmetries. Most prominently, for massless quarks left- and right-handed quark fields can be rotated independently in flavor space, giving rise to the vector and axial symmetries

$$U(N_f)_L \times U(N_f)_R \simeq U(N_f)_V \times U(N_f)_A \ . \tag{2.17}$$

Roughly speaking, the vector transformation rotates left- and right-handed particle species equally, the axial one oppositely. Up to irrelevant $Z(N_f)$ factor groups (see App. A), we can rewrite the symmetry as

$$U(1)_V \times SU(N_f)_V \times U(1)_A \times SU(N_f)_A \ . \tag{2.18}$$

The splitting is helpful for the following reason: $U(1)_V$ just corresponds to a global phase factor whose conserved charge can be associated with the baryon number. Outside color-superconducting phases, this symmetry is always intact. Conversely, $U(1)_A$ is always anomalously broken by quantization [60, 61]. While its classical Noether current is conserved in the Lagrangian, the quantum version is not. $SU(N_f)_V$ is only broken for inequivalent quark masses. As the up and down quarks possess approximately the same (small) current quark masses, isospin symmetry $SU(2)_V$ can be assumed (at least for flavor-blind chemical potentials) to good precision. $SU(N_f)_A$ is referred to as chiral symmetry. It is explicitly broken by any quark-mass terms present in the Lagrangian as they connect left- and right-handed spinors. Moreover, chiral symmetry is spontaneously broken in the vacuum and becomes restored at large temperatures, giving rise to a chiral phase transition.

As any causal quantum field theory, QCD is invariant under the combined discrete transformations of charge conjugation, parity, and time reversal, in short CPT. The individual conservation of CP and T, however, is not guaranteed as the Lagrangian would allow a term of the form

$$\sim F^a_{\mu\nu}\tilde{F}^a_{\mu\nu} \tag{2.19}$$

with $\tilde{F}^a_{\mu\nu} := \epsilon^{\mu\nu\alpha\beta}F^a_{\alpha\beta}$. Experimentally, such a CP violation by the strong interaction has not been observed and the resulting unnaturally small coupling parameter still presents an unsolved issue [62].

The QCD Phase Diagram

Based on the previous considerations, it is clear that QCD matter must undergo a phase transition from hadronic matter with spontaneously broken chiral symmetry at low temperatures and densities to deconfined matter where the fundamental degrees of freedom, quarks and gluons, play a role at large temperatures and/or densities. The nature of the phase diagram of QCD has been the subject of intensive study both from first-principle methods as well as effective theories. An exemplary sketch of a conjectured phase diagram is given in Fig. 2.1.

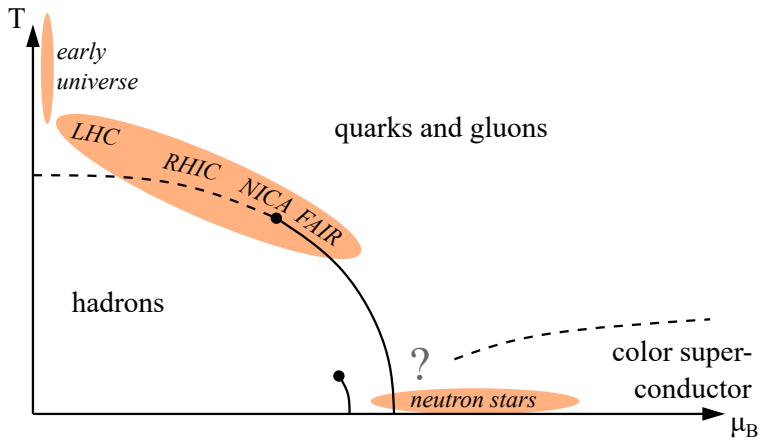

Figure 2.1: Sketch of the conjectured QCD phase diagram. Critical endpoints are labeled as black dots. At small temperatures, nucleonic matter undergoes a liquid–gas phase transition. The entire region around the questionmark at larger densities is essentially unknown.

According to lattice QCD calculations [39] and experimental observations [63], it is undoubtedly clear that at vanishing density, hadronic matter exhibits a crossover transition to a quark-gluon plasma. At increasing density, the situation is not yet settled, but effective theories have always predicted the existence of a critical endpoint somewhere along the transition line, see e.g. Refs. [33, 64, 65]. This hypothesis is backed by increasingly sophisticated studies with functional methods [18–20]. Future experiments like *NICA* [66] and *FAIR* [38] are specifically aimed at finding possible signatures of a critical endpoint.

At low temperatures, the situation becomes vastly more complex. Provided the critical endpoint exists and there is not a second critical endpoint, there must be a first-order phase transition to a quark-matter phase somewhere beyond the liquid–gas transition of nuclear matter. However, the phase structure at large baryon chemical potential μ_B can become quite involved, with many possible color-superconducting, superfluid, and spatially inhomogeneous phases [67, 68]. At vanishing temperature and asymptotically large densities, it is known that the color-flavor locked (CFL) [69] phase is the ground state [70]. Hence, chiral symmetry might not become fully restored along the μ_B axis.

2.2 Neutron Stars

Neutron stars are the most compact non-black-hole stars. They have masses ranging from about $1M_\odot$ [71] to at least $2M_\odot$ [72–74] at a radius of only approximately 10 km and are the remnants of core-collapse supernovae of very massive stars with masses above $8M_\odot$ [71]. Being electrically neutral objects with densities of nuclear-matter density and above, they feature a large neutron fraction which gives neutron stars their name.

The mathematical description of compacts stars under the assumption of a static, nonrotating ideal fluid in hydrostatic equilibrium was achieved by Tolman, Oppenheimer, and Volkoff (TOV) [75, 76], see App. B for their equation and a derivation. With the equation of state (EoS) $p(\varepsilon)$ determined by the microscopic properties of matter, the TOV equation yields a one-parameter curve of mass-radius relationships and a maximal attainable stable mass. Solutions for spinning stars are also available and generally lead to about 20% larger maximum masses [77]. These properties can be compared to experiment, e.g., to precise mass determinations of heavy pulsars (i.e., neutron stars spinning with a very high frequency) [72–74], but also other observables like pulsar glitches hinting at possible superfluid phases in the center of the star [78] are possible. The complex cooling process of neutron stars can also be used for predictions for the state of matter at high densities [79].

At low baryon density a neutron star can be characterized by nonrelativistic nucleons via nuclear forces. In the denser regimes, there are many possible scenarios that, next to superfluid phases, feature the possibility of pion and kaon condensation [80] or the occurrence of quark matter, leading to so-called hybrid stars [81]. The interface between hadronic and quark matter could be continuous or—as previously speculated—a first-order transition. Generally, the different phases of matter allow for the existence of a second or even third branch of stable stars in the mass-radius diagram, implying the existence of massive neutron and hybrid stars of equal masses, but different radii [82]. Hence, the observation of two compact stars with almost equal masses, but different radii could be proof for such a scenario. Precise radius determinations are oftentimes much harder than that of the star's mass but there is first data from the NICER experiment at the

International Space Station [83, 84] and future experiments could lead to even more precise insights.

Another avenue for experimental observation was opened not too long ago with the GW170817 gravitational-wave measurement of a neutron-star merger [85]. Besides the classical mass determinations, e.g., a range of possible tidal deformabilities (see App. B for a discussion) for the stars can be extracted from such observations and compared to theoretical predictions.

Without precise experimental input on the state of matter at large densities, for now there are basically two roads: First, the description of quark matter by means of effective theories based on some assumptions about the underlying physics or second, the general parameterization of the EoS, finding trends and probability regions by comparing the results to experimental and observation data; see Ref. [86] for a prominent example.

Chapter 3

Functional Methods

In the modern path integral formalism, the physics content of a quantum field theory is encoded in its generating functional $\mathcal{Z}$. All correlation functions can be expressed as derivatives operating on $\mathcal{Z}$ or functions thereof. For example, in d Euclidean dimensions the full two-point correlator of a real scalar fields $\varphi(x)$ reads

$$\langle\varphi(x)\varphi(y)\rangle = \frac{1}{\mathcal{Z}[0]}\,\frac{\delta}{\delta J(x)}\frac{\delta}{\delta J(y)}\mathcal{Z}[J]\bigg|_{J=0}\,, \tag{3.1}$$

where J is a source term and $\mathcal{Z}$ is defined via the path integral

$$\mathcal{Z}[J] := \int \mathcal{D}\varphi\, \mathrm{e}^{-S[\varphi]+\int J\varphi}\,. \tag{3.2}$$

The measure $\mathcal{D}\varphi$ stands for a variation of all possible field configurations and S is the classical action of the theory.[1] Although this formalism is very general, there exist several known ways to formulate self-consistency or differential equations for functional quantities derived from $\mathcal{Z}$. They are commonly referred to as functional methods and provide exact functional equations which are inherently nonperturbative. Thus, such methods are well-suited to study field theories in a strong-coupling regime. Furthermore, they do not generally suffer from problems involving rapidly oscillating complex phases like the fermion sign problems in Lattice QCD [17], which facilitates an extension to nonvanishing chemical potentials.

However, any one of these functionals contains an infinite amount of information and can in practice never be known exactly. As Eq. (3.1) illustrates, the generating functional encodes the information of all n-point correlators $\langle\varphi(x_1)\dots\varphi(x_n)\rangle$, which for an interacting theory are generally nonvanishing at any order of n. It is therefore necessary to expand a given functional in some physically reasonable scheme and truncate the expansion at some order. As we will see in the course of this chapter, functional methods usually lead to a tower of coupled equations, which implies that any truncation comes with a loss of information and hence with a truncation error. Since functional approximation schemes can not be seen as strictly convergent expansions, there is no fixed notion of how to gauge the size of such errors. Functional methods should therefore be understood as important tools that can lead to powerful predictions, but not as the single method of choice for quantitative precision.

[1] For short-hand notation concerning contractions of fields like $\int J\varphi$, we refer to App. A.

In the realm of quantum field theories, they typically encompass *Dyson-Schwinger equations*, *nPI* methods, and the *functional renormalization group*. In the course of this chapter, we will briefly introduce the former two and discuss the functional renormalization group in some detail, with a special emphasis placed on regulator functions in the last two sections.

3.1 Dyson-Schwinger Equations and nPI Approaches

Before turning to the functional renormalization group, let us get a brief overview of Dyson-Schwinger equations and nPI methods. The former are founded on Freeman Dyson's observation that—based on a diagrammatic expansion—Green's functions are subject to an implicit relation. For the propagator $G(p)$ of a particle, this is the Dyson equation [87]

$$G(p) = G_0(p) + G_0(p)\Sigma(p)G(p) \ , \tag{3.3}$$

where $G_0(p)$ is the free propagator and all amputated 1PI (one-particle irreducible)[2] diagrams are collected in the self-energy Σ. With the subsequent works of Julian Schwinger [88], it was possible to express such relations solely in terms of (bare and fully dressed) n-point functions. Picking up the example of a real scalar field $\varphi(x)$, we can derive the Dyson-Schwinger master equation and introduce some helpful quantities for later use on the way. In the path integral language, Dyson-Schwinger equations follow from the shift invariance of the integration measure.[3] The shift $\varphi(x) \to \varphi'(x) := \varphi(x) + \alpha\chi(x)$ leaves $\mathcal{D}\varphi = \mathcal{D}\varphi'$ invariant, so we can write:

$$\begin{aligned} 0 &= \frac{\partial}{\partial\alpha} \int \mathcal{D}\varphi \, \mathrm{e}^{-S[\varphi+\alpha\chi]+\int J(\varphi+\alpha\chi)} \Big|_{\alpha=0} \\ &= \int_x \chi(x) \int \mathcal{D}\varphi \left(-\frac{\delta S[\varphi]}{\delta\varphi(x)} + J(x) \right) \mathrm{e}^{-S[\varphi]+\int J\varphi} \ . \end{aligned} \tag{3.4}$$

As $\chi(x)$ is an arbitrary real scalar field, we must have

$$\int \mathcal{D}\varphi \left(-\frac{\delta S[\varphi]}{\delta\varphi(x)} + J(x) \right) \mathrm{e}^{-S[\varphi]+\int J\varphi} = 0 \ . \tag{3.5}$$

The term in parenthesis can be pulled out of the path integral by replacing all fields $\varphi(x')$ with derivatives $\delta/\delta J(x')$[4] acting on $Z[J]$:

$$\left(-\frac{\delta S[\varphi]}{\delta\varphi(x)}\bigg|_{\varphi\to\frac{\delta}{\delta J}} + J(x) \right) Z[J] = 0 \ . \tag{3.6}$$

With the following trick, we can pull Z all the way to the left and remove it from the equation: first, we define the Schwinger functional

$$W[J] := \ln Z[J] \ , \tag{3.7}$$

[2] Diagrams are called n-particle irreducible if they cannot be separated into two (nontrivial) parts by cutting n or less lines.

[3] Applying the following procedure to other symmetry transformations that leave the integration measure unchanged leads to quantum versions of Noether current conservation. For gauge symmetries, these are the Ward-Takahashi [47, 48] or—in the nonabelian case—Slavnov-Taylor [49, 50, 89] identities.

[4] In momentum space, $\varphi(p) \to \delta/\delta J(-p)$, see App. A for details.

which is the generating functional for the connected correlators $\langle\varphi(x_1)\dots\varphi(x_n)\rangle_c$. Second, we make use of the relation

$$\frac{\delta}{\delta J(x)}\left(\mathrm{e}^{W[J]}A[J]\right) = \mathrm{e}^{W[J]}\left(\frac{\delta W[J]}{\delta J(x)} + \frac{\delta}{\delta J(x)}\right)A[J] \tag{3.8}$$

where $A[J]$ stands for any functional J-dependencies to the right of the derivative operator, to arrive at

$$-\left.\frac{\delta S[\varphi]}{\delta\varphi(x)}\right|_{\varphi\to\frac{\delta W}{\delta J}+\frac{\delta}{\delta J}} + J(x) = 0\ . \tag{3.9}$$

To get an expression in terms of 1PI correlators, we define their generator, the effective action, as the functional Legendre transform of $W[J]$:

$$\Gamma[\phi] := \sup_J\left(-W[J] + \int J\phi\right)\ . \tag{3.10}$$

It immediately follows that

$$J(x) = \frac{\delta\Gamma[\phi]}{\delta\phi(x)} \tag{3.11}$$

for a given field ϕ and

$$\phi(x) = \frac{\delta W[J]}{\delta J(x)} = \langle\varphi(x)\rangle^J\ , \tag{3.12}$$

that is, ϕ is the macroscopic field expectation value in the presence of the source J. Using the previous definitions and writing

$$\frac{\delta}{\delta J(x)} = \int_y \frac{\delta\phi(y)}{\delta J(x)}\frac{\delta}{\delta\phi(y)} = \int_y \frac{\delta^2 W[J]}{\delta J(x)\delta J(y)}\frac{\delta}{\delta\phi(y)} \tag{3.13}$$

as well as introducing

$$G(x,y) := \frac{\delta^2 W[J]}{\delta J(x)\delta J(y)} \tag{3.14}$$

for the propagator, the master equation becomes

$$\frac{\delta\Gamma[\phi]}{\delta\phi(x)} = \left.\frac{\delta S[\varphi]}{\delta\varphi(x)}\right|_{\varphi\to\phi+\int G\frac{\delta}{\delta\phi}}\ . \tag{3.15}$$

Dyson-Schwinger equations for 1PI n-point functions $\Gamma^{(n)}$ are obtained by acting on both sides with the appropriate number of functional derivatives. From the additional functional derivatives in the replacement terms on the right-hand side, we can follow that in any nontrivial case, the DSE for a given n-point function will always include higher-order correlation functions which leads to the previously mentioned infinite tower of coupled equations.

Example: Quark propagator. One of the central objects in DSE calculations for QCD is the quark propagator. Let us assume the flavor-degenerate case for simplicity. Then, the DSE for the full (inverse) quark propagator $S(p)$ is diagonal in flavor space and reads

$$S^{-1}(p) = S_0^{-1}(p) + \mathrm{i}g\gamma^\mu T_a\int_q S(q)D^{ab}_{\mu\nu}(p-q)(\Gamma^{\bar{q}qA})^\nu_b(q,-p) \tag{3.16}$$

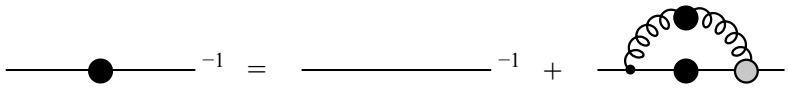

Figure 3.1: Dyson-Schwinger equation for the quark two-point function (inverse propagator). Propagators with a large black blob in the middle are dressed, those without are bare. The small black dot represents the bare quark-gluon vertex, the large gray one the dressed vertex.

with the dressed quark-gluon vertex $\Gamma^{\bar{q}qA}$, the dressed gluon propagator D and the bare (inverse) quark propagator

$$S_0^{-1}(p) = \mathrm{i}p_\mu\gamma^\mu + m_q \ . \tag{3.17}$$

A diagrammatic version of the equation is shown in Fig. 3.1. Note that for a formulation in terms of renormalized fields and vertices, multiplicative renormalization constants must be added; see e.g. Ref. [90] for details. For thermodynamic applications, the dressed vertex and gluon propagator are oftentimes approximated by means of phenomenologically motivated models and Lattice data [19, 91, 92], but input from functional renormalization group calculations has also been used recently [18, 93].

Bethe-Salpeter equations and nPI method. Further applications include the calculation of QCD n-particle bound states [94–97] with the help of Bethe-Salpeter equations [98] which can be inferred from the Dyson equation for $2n$-point Green's functions. This has also been achieved for glueball states in pure Yang-Mills theory [99] based on a self-consistent framework that takes into account nPI equations of motion [100]. In the nPI framework, source terms are added to the generating functional for vertices up to order n: $\mathcal{Z} = \mathcal{Z}[J^{(1)}, J^{(2)}, J^{(3)}, \dots]$. The nPI effective action follows as the Legendre transform with respect to all sources, schematically (omitting the supremum for clarity) [100]

$$\Gamma[\phi, G, V_3, \dots] = -W[J^{(1)}, J^{(2)}, \dots] + \int J^{(1)}\phi + \iint J^{(2)}G + \iiint J^{(3)}V_3 + \dots \tag{3.18}$$

The dressed field, propagator, three-point function, etc. are determined by the equation of motion for vanishing source

$$\frac{\delta\Gamma}{\delta\phi} = 0 \ , \quad \frac{\delta\Gamma}{\delta G} = 0 \ , \quad \frac{\delta\Gamma}{\delta V_3} = 0 \ , \quad \dots \ , \tag{3.19}$$

and all vertices of order $k > n$ remain bare. Completely self-contained setups can be attained by expanding Γ up to loop order $l = n$. For $n > l$ no new information is gained, i.e., $\Gamma^{(l-\text{loop})}_{n\text{PI}} = \Gamma^{(l-\text{loop})}_{(n+1)\text{PI}}$ for $n \geq l$ [101].

3.2 Functional Renormalization Group

For the remainder of this thesis we shall focus on the basic principles of the functional renormalization group (FRG) as well as results obtained within the FRG framework. The fundamental idea of the renormalization group (RG) is the study of physical quantities under a change of scale in, e.g., length or momentum. Already in perturbative calculations, the first groundworks for the renormalization group were laid. The divergence of loop integrals requires a regularization and a subsequent renormalization procedure, which makes

the running of coupling constants under a change of renormalization scale μ apparent. An example is the perturbative beta function of QCD, Eq. (2.14). The independence of physical observables under a change of renormalization scale was later expressed in general and concise form by Callan and Symanzik [102, 103]. Powerful predictions can be made especially in the case of scale invariance, as shown by Kadanoff in the picture of block-spin transformations in a spin model [104]. Kenneth Wilson picked up this idea in his Nobel prize winning work [105, 106] to relate the renormalization group to critical phenomena where scale invariance close to a fixed point leads to universal behavior.

The change of RG scale can be implemented in a field theory by so-called *momentum-shell transformations*. Given a theory with an initial action $S_\Lambda[\varphi]$ where the field is cut off at momenta larger than the UV scale Λ,

$$\varphi(x) = \int_{|p|\leq\Lambda} \frac{\mathrm{d}^d p}{(2\pi)^d}\, \varphi(p)\, \mathrm{e}^{ip\cdot x} \ , \tag{3.20}$$

Wilson's approach was to integrate out quantum fluctuations only in the interval $\Lambda' < |p| \leq \Lambda$. This leads to a new effective action $S^{\mathrm{eff}}_{\Lambda'}$ defined at the scale Λ':

$$\mathcal{Z} := \int_\Lambda \mathcal{D}\varphi\, \mathrm{e}^{-S_\Lambda[\varphi]} = \int_{\Lambda'} \mathcal{D}\varphi \left(\int_{(\Lambda',\Lambda]} \mathcal{D}\chi\, \mathrm{e}^{-S_\Lambda[\varphi+\chi]} \right) = \int_{\Lambda'} \mathcal{D}\varphi\, \mathrm{e}^{-S^{\mathrm{eff}}_{\Lambda'}[\varphi]} \tag{3.21}$$

with $(\Lambda', \Lambda]$ indicating that the fourier modes of χ are only nonvanishing in this interval, similar to Eq. (3.20). Note that the path integral and hence the theory does not change. Some of the fluctuations have just been absorbed into the redefinition of the action and do not need to be integrated out anymore. In this picture, even the initial action can be seen as an effective action at scale Λ generated by, perhaps, a yet unknown theory valid at much larger energy scales. This allows for the extension of the notion of renormalizability to a nonperturbative context, for example, the study of an asymptotic safety scenario in quantum gravity [107].

The term functional renormalization group refers to a functional implementation of Wilson's nonperturbative renormalization group, expressing Eq. (3.21) in a mathematically applicable framework. This is done by adding an RG-scale dependent modification $\Delta S_k[\varphi]$ to the classical action, yielding a scale-dependent generating functional:

$$\mathcal{Z}_k[J] := \int \mathcal{D}\varphi\, \mathrm{e}^{-S[\varphi]-\Delta S_k[\varphi]+\int J\varphi} \ . \tag{3.22}$$

Conventionally, the RG scale is here denoted as $k \in [0, \Lambda]$. The additional term serves as a dynamical mass that suppresses the fluctuation of field modes with momenta smaller than k. Note that this construction is given in a Euclidean formulation, making use of the Gaussian suppression of the path integral by the regulator and hence providing a well-suited method for the study of equilibrium systems. However, spectral functions have also been retrieved from analytically continued flow equations and a formulation on the real-time Keldysh contour is also possible [108] and sees some recent progress [109, 110]. As only the high momenta are integrated out, $\mathcal{Z}_k$ can be roughly identified with the term in parenthesis in Eq. (3.21) with the renaming $\Lambda' = k$. This identification, however, is not exact as we keep the definition of ΔS_k as general as possible, only insisting that the term should be quadratic in the field:

$$\Delta S_k[\varphi] := \int \frac{\mathrm{d}^d p}{(2\pi)^d}\, \frac{1}{2} \varphi(-p) R_k(p^2) \varphi(p) \ . \tag{3.23}$$

Even more general setups are discussed in Ref. [51]. The regulator function $R_k(p^2)$ determines how momenta are cut off in relation to the scale k. If we choose the so-called sharp regulator,

$$R_k^{\text{sharp}}(p^2) = \begin{cases} \infty & p^2 \leq k^2 \ , \\ 0 & \text{else} \ , \end{cases} \tag{3.24}$$

we exactly recover the inner path integral in Eq. (3.21) for $\Lambda \to \infty$ since fluctuations at momenta smaller than k are infinitely suppressed while there is no modification of the theory at higher scales. Eq. (3.23) also allows for other choices for R_k which includes smooth cutoffs, as long as the following conditions are fulfilled:

(I) The regulator needs to vanish for momenta $p^2 \gg k$ such that UV modes in the path integral are not regularized anymore. A special case is $k \to 0$ where the absence of the regulator at all momenta recovers the original theory, $\mathcal{Z}_0[J] = \mathcal{Z}[J]$. In compact notation,

$$\lim_{p^2/k^2 \to \infty} (p^2)^{\frac{d-1}{2}} R_k(p^2) = 0 \ , \tag{3.25}$$

where the additional momentum factor ensures that R_k vanishes sufficiently fast such that the loop integral in the Wetterich equation introduced later is properly regularized [51].

(II) R_k is always positive in the infrared, i.e., for momenta smaller than k:

$$\lim_{p^2/k^2 \to 0} R_k(p^2) > 0 \tag{3.26}$$

which ensures the regularization of massless modes.

(III) For infinitely large RG scale the regulator diverges,

$$\lim_{k \to \infty} R_k(p^2) \to \infty \ , \tag{3.27}$$

suppressing all quantum fluctuations and yielding a classical theory with action $S[\varphi]$. For all practical purposes, this is already achieved at a sufficiently large UV scale Λ, which is where we define our theory.

The very general definition of ΔS_k has an important implication: for given k, each regulator function defines a different theory with different couplings. They only coincide for $k = 0$ and $k \to \infty$ due to above regulator conditions. If theory space is imagined as an infinite-dimensional space of all couplings $\{g_i\}$, the one-parameter flow $\{g_i(k)\}$ through this space differs for each choice of regulator, with the boundary condition of coinciding starting and end points. This notion is depicted by the black lines in Fig. 3.2.

3.3 Flow Equations

The abstract thought of a flow through theory space can be made precise in terms of flow equations which are differential equations including the scale derivative $\partial_t = k\partial_k$ of the couplings where

$$t := \ln \frac{k}{\Lambda} \tag{3.28}$$

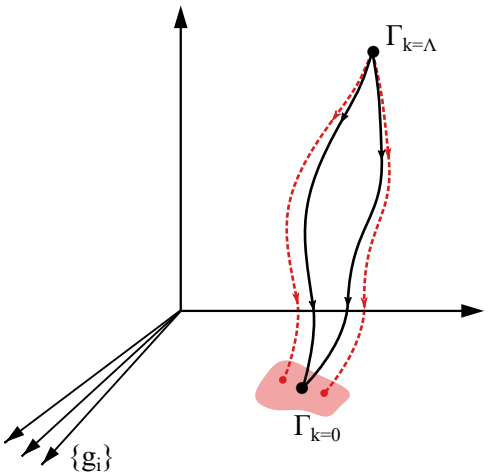

Figure 3.2: Sketch of the effective action's flow in theory space for two different regulators. The dashed red lines symbolize deviations due to truncation errors which leads to different infrared results (red region).

is the dimensionless RG time. Applying this operator on a generating functional, one ends up with a functional partial differential equation. We first consider the flow of the modified Schwinger functional

$$W_k[J] := \ln \mathcal{Z}_k[J] \ . \tag{3.29}$$

The partial scale derivative (keeping the source independent of k) follows from Eq. (3.22):

$$\begin{aligned} \partial_t W_k[J] &= -\frac{1}{2}\int_p \left(\partial_t R_k(p^2)\right) \frac{1}{\mathcal{Z}_k[J]} \int \mathcal{D}\varphi\, \varphi(-p)\varphi(p)\, \mathrm{e}^{-S[\varphi]-\Delta S_k[\varphi]+\int J\varphi} \\ &= -\frac{1}{2}\int_p \left(\partial_t R_k(p^2)\right) \left(\frac{\delta^2 W_k[J]}{\delta J(-p)\delta J(p)} + \frac{\delta W_k[J]}{\delta J(-p)}\frac{\delta W_k[J]}{\delta J(p)}\right) \ . \end{aligned} \tag{3.30}$$

The connected part is just the propagator

$$G_k(p) = \frac{\delta^2 W_k[J]}{\delta J(-p)\delta J(p)} \ , \tag{3.31}$$

while the disconnected part is given by the field expectation values in presence of a source,

$$\langle\varphi(p)\rangle_k^J = \frac{\delta W_k[J]}{\delta J(-p)} \ . \tag{3.32}$$

As expected, we obtain a functional partial differential equation and functional derivatives appear up to second order. Similar to the derivation of Dyson-Schwinger equations, we strive for a reformulation in terms of macroscopic fields. Therefore, we consider the flow of the effective average action

$$\Gamma_k[\phi] := \sup_J \left(-W_k[J] + \int J\phi\right) - \Delta S_k[\phi] \ . \tag{3.33}$$

In contrast to a common Legendre transformation, the RG modification inherited by Z_k is additionally removed. In the limit $k \to 0$, the original definition of the 1PI generating

functional $\Gamma[\phi]$ is recovered. Γ_k is a functional of the macroscopic fields $\phi = \langle\varphi\rangle_k^{J_{\text{sup}}}$ where J_{sup} is the source that gives the supremum in Eq. (3.33). Taking the scale derivative and keeping ϕ fixed, the only term that does not cancel out is

$$\partial_t \Gamma_k[\phi] = \frac{1}{2} \int_p \left(\partial_t R_k(p^2)\right) G_k(p) \ . \tag{3.34}$$

G_k is the second functional derivative of $W_k[J]$ at $J = J_{\text{sup}}$, but we can write it as the functional inverse of $\Gamma_k^{(2)}[\phi] + R_k$ since

$$\int_q W_k^{(2)}(p,-q) \left(\Gamma_k^{(2)} + R_k\right)(q,r) = \int_q \frac{\delta\phi(p)}{\delta J(q)} \frac{\delta J(q)}{\delta\phi(-r)} = (2\pi)^4 \delta(p+r) \ . \tag{3.35}$$

In abstract notation and repeating the procedure for fermions, we obtain the Wetterich equation [111, 112]

$$\partial_t \Gamma_k = \frac{1}{2} \mathrm{STr} \left(\frac{\partial_t R_k}{\Gamma_k^{(2)} + R_k} \right) \tag{3.36}$$

where the supertrace gives an additional minus sign for fermions. A generalization to composite field notation and more information concerning momentum space conventions are given in App. A. The equation has a one-loop structure with the insertion of the regulator derivative providing UV regularization. The regulator term in the denominator ensures positivity and provides IR regularization even for massless fields. Flow equations for higher-order n-point functions $\Gamma_k^{(n)}$ can be obtained by taking functional derivatives of Eq. (3.36). In contrast to Dyson-Schwinger equations, all propagators and vertices are always fully dressed (at scale k) since there are no bare quantities in the Wetterich equation.

It should be noted that historically, the Wetterich equation was not the first functional renormalization group equation to be formulated. Already in 1984, Polchinski [113] considered a path integral

$$\mathcal{Z} = \int \mathcal{D}\varphi \, \mathrm{e}^{-S_k^{\text{eff}}[\varphi]} \tag{3.37}$$

based on Wilson's effective action (3.21) with high momenta cut off by a smooth regulator function applied to the bare propagator

$$G_{0,k}(p) = \frac{K(p^2/k^2)}{p^2 + m^2} \ , \tag{3.38}$$

where m is the bare mass and the kernel K goes to zero for $p^2 \gg k^2$. The effective action thus reads

$$S_k^{\text{eff}}[\varphi] = \frac{1}{2} \int_p \varphi(-p) \frac{p^2 + m^2}{K(p^2/k^2)} \varphi(p) + S_k^{\text{int}}[\varphi] \ . \tag{3.39}$$

All interactions and modifications to the bare propagator are stored in S_k^{int}. The condition that the full partition function $\mathcal{Z}$ may not change under a variation of the renormalization scale,

$$\partial_t \mathcal{Z} = \int \mathcal{D}\varphi \left[-\frac{1}{2} \int_p \varphi(-p) \left(\partial_t G_{0,k}^{-1}(p)\right) \varphi(p) - \left(\partial_t S_k^{\text{int}}[\varphi]\right) \right] \mathrm{e}^{-S_k^{\text{eff}}[\varphi]} \stackrel{!}{=} 0 \ , \tag{3.40}$$

is nontrivially fulfilled only if S_k^{int} satisfies (up to field-independent terms) the flow equation [113]

$$\partial_t S_k^{\text{int}}[\varphi] = -\frac{1}{2}\int_p (\partial_t G_{0,k}(p)) \left(\frac{\delta^2 S_k^{\text{int}}[\varphi]}{\delta\varphi(-p)\delta\varphi(p)} - \frac{\delta S_k^{\text{int}}[\varphi]}{\delta\varphi(-p)} \frac{\delta S_k^{\text{int}}[\varphi]}{\delta\varphi(p)} \right) . \tag{3.41}$$

Intriguingly, Polchinski's equation looks very similar to the flow of the Schwinger functional (3.30). A connection is not immediately obvious since $S_k^{\text{int}}[\varphi]$ is defined on the microscopic fields φ and based on the full partition function $\mathcal{Z}$, whereas $W_k[J]$ is directly connected to the modified partition function $\mathcal{Z}_k[J]$ and depends on an external source field. However, since both $S_k^{\text{int}}[\varphi]$ and $W_k[J]$ contain the high-momentum fluctuations, they can be related to each other if both cutoff functions $R_k(p^2)$ and $K(p^2/k^2)$ are chosen in a compatible fashion. For the interested reader, this rather technical derivation is given in App. C.

3.4 Truncation Schemes

In the previous section it was shown that exact functional renormalization group flows incorporate field derivatives up to second order. Hence, to calculate the flow of an n-point function $\Gamma_k^{(n)}$ one requires the full knowledge of the flow of $\Gamma_k^{(n+1)}$ and $\Gamma_k^{(n+2)}$. Formally, the effective average action can be expanded in those n-point vertices:

$$\Gamma_k[\phi] = \sum_{n=0}^{\infty} \int_{x_1,\ldots,x_n} \Gamma_k^{(n)}(x_1,\ldots,x_n)\, \phi(x_1)\ldots\phi(x_n) . \tag{3.42}$$

For simplicity, the expansion schemes are here given in position space. The vertex expansion can be truncated at some order m, setting all $\Gamma_k^{(n)} \equiv 0$ for $n > m$. Of course, due to the missing derivatives the flow of $\Gamma_k^{(m)}$ and $\Gamma_k^{(m-1)}$ will be erroneous, which will in turn lead to errors in the flows of all lower-order couplings. Unfortunately, no convergence criteria are known that would allow one to gauge the size of such errors. Instead, heuristic criteria like apparent convergence—which is reached when the result only changes marginally upon increasing the truncation order—or complementary methods must be relied upon.

That also holds for other truncation schemes such as the derivative expansion where Γ_k is expanded in powers of local derivative operators acting on the fields,

$$\Gamma_k[\phi] = \int_x \left[U_k(\phi^2) + \frac{1}{2} Z_k(\phi^2)(\partial_\mu\phi)^2 + \mathcal{O}(\partial^4) \right] . \tag{3.43}$$

Here, we have assumed the Z_2 symmetry $\phi \to -\phi$. The effective potential $U_k(\phi^2)$ incorporates the momentum-independent part of all n-point functions to infinite order. For a spatially invariant infrared vacuum expectation value $\phi_0 = \langle\varphi(x)\rangle$ the effective potential—evaluated at its minimum ϕ_0—becomes proportional to a thermodynamic potential:

$$\Gamma[\phi_0] = \frac{V}{T} U_0(\phi_0^2) = -\ln \mathcal{Z} = -\frac{Vp}{T} \tag{3.44}$$

with the three-dimensional spatial volume V, temperature T, and pressure p. The derivative expansion is therefore well-suited for thermodynamic applications. To lowest nontrivial order—the so-called *local potential approximation* (LPA)—only U_k is kept scale dependent and Z_k is set to unity such that the second term becomes the standard kinetic

term. Since all higher order couplings are fixed to zero, the two-point function in LPA will always have canonical momentum behavior

$$\Gamma_k^{(2)}(p) = p^2 + 2\,U_k'(\phi^2) + 4\,\phi^2\,U_k''(\phi^2) \tag{3.45}$$

where the primes refer to derivatives with respect to ϕ^2. The first step beyond LPA, commonly referred to as LPA', includes a scale- but usually not field-dependent wavefunction renormalization Z_k, allowing for a nonvanishing anomalous dimension $\eta = -\partial_t \ln Z_k$.

3.5 Regulator Optimization

For truncated flows, the notion that each choice of regulator, although it defines a different trajectory in theory space, will lead to the same endpoint characterized by the fully interacting theory at vanishing regulator is clearly not true anymore. Since the flows are not exact, they will drive each trajectory to a different endpoint, introducing a truncation error as well as a spurious regulator dependence on physical observables. This notion is pictorially represented by the dashed red lines and the red region in Fig. 3.2. Furthermore, it is clear that by truncating, one will never be able to take into account all infinitely many couplings. Hence, the task is to find an optimum regulator function in the sense that for a given finite set of observables $\{\mathcal{O}_l\}$ the flow drives all couplings $\{g_m\}$ associated with those observables as closely as possible to their exact values.

PMS criterion. One possible criterion of choice is the *principle of minimum sensitivity* (PMS) [114, 115]. Originally developed in the context of perturbation theory, in the spirit of a saddle point approximation it seeks those solutions that are least sensitive to variations in the regularization scheme. If we abstractly parameterize a regularization scheme (RS) with the set of parameters $\{a_n\}$, the condition reads [116]

$$\frac{\mathrm{d}\mathcal{O}_l}{\mathrm{d}(RS)} = \sum_{g_m,a_n} \frac{\mathrm{d}\mathcal{O}_l}{\mathrm{d}g_m}\,\frac{\mathrm{d}g_m}{\mathrm{d}a_n}\,\frac{\mathrm{d}a_n}{\mathrm{d}(RS)} \stackrel{!}{=} 0\ . \tag{3.46}$$

Correct solutions are those where the regularization scheme delivers a coinciding extremum for all observables $\mathcal{O}_l$. Such studies, however, are usually tedious as for each tested regulator function the FRG flow needs to be solved down to $k = 0$ to obtain the corresponding observables [51]. Furthermore, such coinciding extrema do not necessarily exist or they might not be unique [116].

There are two more optimization criteria proposed in the literature which are not tied to specific observables. In order to discuss those, we first express the regulator function R_k in terms of a dimensionless shape function:

$$R_k(p^2) := p^2\,r(y)\ , \quad y = p^2/k^2\ . \tag{3.47}$$

For the dimensionless inverse propagator of a massless field we use the short-hand notation $P^2(y)$ which in LPA—the truncation we mainly employ in this work—reads

$$P^2(y) = \frac{p^2[1 + r(y)]}{k^2} = y[1 + r(y)]\ . \tag{3.48}$$

Note that even in LPA' (i.e., for a field-independent wavefunction renormalization), with the redefinition

$$R_k(p^2) := Z_k\, p^2 r(y) \tag{3.49}$$

the only change to P^2 is the well-known global scaling factor Z_k which can be absorbed into the renormalized two-point function. Hence, the following arguments still apply.

Litim criterion. The criterion developed by Litim states that, for a given normalization, any regulator that maximizes the gap in the inverse propagator is optimal [117]:

$$C_{\text{opt}} := \max_R \left(\min_{y\geq 0} P^2(y) \right) . \tag{3.50}$$

It is reasoned that such optimal regulators lead to the greatest stability of the flow [117] and that an expansion of the flow in inverse powers of P^2, which is always possible due to its gap, leads to quickest convergence of the series if the gap is maximal [116]. Indeed, in Ref. [118] it was shown that flows optimized according to this criterion lead to critical exponents closest to the real physical values in $O(N)$ scalar theories. The need for a normalization is also clear: without it, the gap could be made arbitrarily large just by means of multiplying a given shape function with a large factor. In the following, we will show that the act of normalizing a regulator is closely tied to choosing an *effective* RG scale k_{eff}. To simplify the discussion, we restrict ourselves to continuous, strictly monotonously decreasing shape functions $r(y)$. In a Euclidean setup, this is not a hard restriction as we generally aim at a smooth transfer from regulated IR modes to unregulated UV modes. Any shape function will diverge for vanishing momenta $y \to 0$ at least like $1/y$ to render $R_k(p^2)/k^2 = y\, r(y)$ positive, and vanish for $y \to \infty$ in compliance with the general regulator conditions. Hence, it takes on each positive value exactly once.

A normalization is understood as the requirement that all shape functions considered in Eq. (3.50) intersect at one common point [51],

$$r(y_0) = c \tag{3.51}$$

with $c > 0$ and finite. Both y_0 and c are free of choice but we can associate some physical intuition with it. The typical choice is $c = 1$ [117] such that

$$R_k(y_0 k^2) = y_0 k^2 . \tag{3.52}$$

At $p^2 = y_0 k^2$ the standard kinetic term and the regulator term are equal in size. For larger momenta, the kinetic term dominates, and for smaller momenta the regulator dominates (as long as it is a monotonously decreasing function). Hence, $y_0 k^2$ might be interpreted as the effective RG scale $k^2_{\text{eff}}(k)$ if we define k_{eff} as "the momentum scale below which modes are suppressed to a sufficient degree". What sufficient means (i.e., the ratio between the regulator and kinetic terms) is essentially defined by the parameter c.

The connection between the normalization and k_{eff} becomes even more tangible if, for a given shape function r and $c = 1$, we consider the following family of shape functions:

$$r^\lambda(y) := r(y/\lambda^2) . \tag{3.53}$$

r^λ can be obtained from r by the simple multiplicative rescaling $k \to \lambda k$ with $\lambda > 0$. Such a rescaling just corresponds to a reparameterization of the trajectory in theory space—it leads to the exact same flow even in the presence of truncations. Formally, this can

be expressed by the relation $\Gamma_k^\lambda = \Gamma_{\lambda k}$ where Γ_k^λ is the effective action in the presence of the regulator defined by r^λ. The modified shape function obeys the normalization $r^\lambda(\lambda^2 y_0) = 1$, which implies $k_{\text{eff}}^\lambda(k) = \lambda k_{\text{eff}}(k)$. In contrast to the RG scale k which is just a parameter subject to arbitrary rescalings, k_{eff} can thus be associated with a fixed physical scale. Furthermore, the previously demanded continuity and strict monotonicity imply uniqueness, i.e., there is always exactly one shape function r^{λ_0} from each family that satisfies a given normalization condition. Hence, the normalization exactly cancels out redundant shape functions that are related to each other by simple scale transformations. Eq. (3.50) only compares regulators yielding the same effective scale $k_{\text{eff}}(k)$ which implies that the gap can not be made arbitrarily large.

Indeed, there is a fixed value C_{opt} for each normalization. For $c = 1$, we have $C_{\text{opt}} = P^2(y_0) = 2y_0$ which directly follows from Eq. (3.50) [119]. It should be stressed that the Litim criterion does not uniquely determine an optimal shape function. Rather, there are many shape functions that fulfill it. Typically used regulators can be obtained as limits of generalized compactly supported smooth (CSS) regulators [120], some of which become optimal for the correct choice of parameters. However, already in Ref. [119] it was pointed out that the flat (or Litim) regulator defined by the shape function

$$r_{\text{flat}}(y) = \left(\frac{1}{y} - 1\right) \Theta\,(1 - y) \tag{3.54}$$

is special due to its analytic properties. The inverse propagator becomes $P^2(y) = 1$ for $0 \leq y \leq 1$ and $P^2(y) = y$ for $y > 1$ which means the minimum is attained not at a single point, but over the entire interval $[0, 1]$. Indeed, it can be easily shown by insertion into Eq. (3.50) that the flat regulator is optimal not only for $c = 1$, but for any arbitrary choice of $c > 0$ with the corresponding effective scale given by $y_0 = 1/(c + 1)$ and a constant $C_{\text{opt}} \equiv 1$.

Other optimal regulators generally exhibit an isolated minimum of P^2 at y_0 and are only optimal for one specific choice of c. Hence, the requirement that the regulator shape function r be optimal for any choice of c might be seen as an extension of the Litim criterion. In this more restrictive formulation, the unsatisfying freedom of choice in the normalization condition is eliminated and the flat regulator emerges as the single optimal regulator choice in LPA.

Pawlowski criterion. Another stability-related criterion was formulated by Pawlowski [51, 121]. In contrast to the Litim criterion, the effective scale is understood to be the physical cutoff scale k^2_{phys} which is defined as the propagator gap. This turns the previous optimization criterion into a normalization condition: all regulators under consideration have the same $k_{\text{phys}}(k)$. Optimal regulator functions are those that render any correlation function insensitive to local variations of the regulator at scale k_{phys}. This condition can be shown to be satisfied if the kernel of the flow operator

$$\partial_t = -\frac{1}{2}\text{Tr}\, G_k[\phi](\partial_t R_k) G_k[\phi] \frac{\delta^2}{\delta\phi^2}\ . \tag{3.55}$$

is minimized [121]. Eq. (3.55) can be understood as a generalized operator that yields flow equations for all composite operators such as full n-point correlation functions (not connected ones) $\langle\varphi(x_1)\dots\varphi(x_n)\rangle$; see Ref. [121] for details. As an interpretation, this

means that the length of the flow trajectory is minimized and physics is approached as quickly as possible.

This condition can be further recast into multiple applicable functional forms. For a general truncation, the setup requires the choice of an appropriate operator norm which allows for a defined notion of length of a trajectory in theory space; again, see Ref. [121] for examples. In LPA for a single scalar field, the Pawlowski criterion can be shown to reduce to the condition [51]

$$r_{\mathrm{opt}}(y) \leq r(y) \quad \forall\, r, y \ . \tag{3.56}$$

Since only regulators at the same physical cutoff scale are compared,

$$\min_{y\geq 0} P^2(y) = k_{\mathrm{phys}}^2/k^2 \ , \tag{3.57}$$

and $P^2(y) = y + y\, r(y)$, for the choice $k_{\mathrm{phys}}(k) := k$ it follows that $r(y) \geq 1/y - 1$ for $0 \leq y \leq 1$ and $r(y) \geq 0$ for $y > 1$. The optimum is, again, given by the flat regulator. Hence, at least at the level of the local potential approximation, both the Litim criterion in its extended formulation and the Pawlowski criterion become equivalent.

So far, we have only considered bosonic fields and corresponding regulators. The discussion can be extended to fermionic regulators with the choice

$$R_k^F(p) = \mathrm{i}\not{p}\, r^F(y) \ . \tag{3.58}$$

The formulation proportional to the standard kinetic term in Dirac space preserves possible symmetries of massless fields. The propagator in LPA and for vanishing mass reads

$$G_k^F(p) = \frac{1}{\mathrm{i}\not{p}[1 + r^F(y)]} = \frac{-\mathrm{i}\not{p}[1 + r^F(y)]}{p^2[1 + r^F(y)]^2} \ . \tag{3.59}$$

The numerator is contracted with the regulator insertion $\partial_t R_k$ in the trace of the Wetterich equation and we are free to define the fermionic analogon of the inverse propagator via the denominator [119],

$$P_F^2(y) = y[1 + r^F(y)]^2 \ . \tag{3.60}$$

For given $r(y)$, the choice

$$r^F(y) = \sqrt{1 + r(y)} - 1 \tag{3.61}$$

yields the same inverse propagator as the bosonic analogon. For example, the fermionic version of the flat regulator has the shape function

$$r_{\mathrm{flat}}^F(y) = \left(\sqrt{\frac{1}{y}} - 1\right) \Theta(1 - y) \ . \tag{3.62}$$

With this choice, up to a sign in the Wetterich equation (see App. A) and multiplicity factors, the massless bosonic and fermionic flows are equal and all previous discussions apply.

3.6 Flows at Nonzero Chemical Potential

Thermodynamic ensembles with a given average particle number are characterized by a chemical potential μ which can be defined as the derivative of the free energy with respect to the particle number.[5] At vanishing temperature, no particle states of a quantum mechanical many-body system can be excited as long as μ is smaller than the threshold given by the energy of the lowest lying state. In thermal field theories, this analogously leads to the so-called *Silver-Blaze* property of n-point functions [122]. As we shall see in this section, for any practical application the preservation of this feature requires a generally μ-dependent regulator function. This dependency can be removed by the usage of dimensionally reduced regulators that only depend on the spatial momentum components.

In order to exemplify all points made in this section, it is sufficient to consider a free, massive Dirac fermion field coupled to a chemical potential:

$$Z = \int \mathcal{D}\bar{\psi}\mathcal{D}\psi \, \mathrm{e}^{-\int_p \bar{\psi}(p)\left(\mathrm{i}\not{p}-\mu\gamma_0+m\right)\psi(p)} \sim \det G_\psi^{-1} \tag{3.63}$$

with the propagator

$$G_\psi(p_1, p_2; \mu) = \frac{\delta(p_1 - p_2)}{\mathrm{i}\not{p} - \mu\gamma_0 + m} \ . \tag{3.64}$$

Note that we used the formal version with two external momenta and deviated from the definition of momentum routing in App. A such that the delta function has the argument $p_1 - p_2$ instead of $p_1 + p_2$. For this choice, the Silver-Blaze property for the propagator reads

$$G_\psi(p_1, p_2; \mu) = G_\psi(\tilde{p}_1, \tilde{p}_2; 0) \tag{3.65}$$

with

$$\tilde{p}_i := (p_i^0 + \mathrm{i}\mu, \boldsymbol{p}_i) \ . \tag{3.66}$$

Up to a shift in external momenta, the propagator at $\mu > 0$ is equal to the one at $\mu = 0$. While this case is trivial, the relation generalizes to n-point functions in an interacting theory:

$$\Gamma^{(n)}(p_1, \ldots, p_n; \mu) = \Gamma^{(n)}(\tilde{p}_1, \ldots, \tilde{p}_n; 0) \ . \tag{3.67}$$

One could, for example, take an additional real scalar field φ and allow for a Yukawa interaction term $\sim \bar{\psi}\varphi\psi$. Then, only the external momenta that belong to a fermion are shifted as only those couple to the chemical potential.

A proof of the Silver-Blaze property in the 2PI framework can be found in Ref. [123]. Generally, it only holds for $\mu < \mu_c$, where μ_c is the lowest lying state of particles coupling to μ.[6] In an interacting theory, μ_c is equal the pole mass of the corresponding propagator. Here, it is simply the bare mass $\mu_c = m$. Although this restriction is not necessary for the free propagator, it appears whenever loop diagrams contribute. In our simple example, this can be seen at hand of the fermion pressure which is related to the partition function via Eq. (3.44). Solving the fermion determinant in Eq. (3.63) in the usual way [125]

[5] Analogously, there are also associated chemical potentials for other conserved charges.

[6] This depends on the way the chemical potential couples to the particles. For diquarks, the critical quark chemical potential is actually half their mass gap, as diquarks are composite particles made up out of two quarks [124].

and keeping only the nondivergent thermodynamic parts, we recover the result for a free relativistic fermi gas

$$p^{\mathrm{fermi-gas}} = \frac{1}{24\pi^2}\left[-5\mu p_F^3 + 3\mu^3 p_F - 3m^4 \ln\left(\frac{p_F+\mu}{m}\right)\right]\Theta(\mu - m) \tag{3.68}$$

with the fermi momentum $p_F := \sqrt{\mu^2 - m^2}$. Only beyond the threshold $\mu > \mu_c = m$ the first particle states are populated and the pressure deviates from zero.

Clearly, it is desirable to retain this property in a functional renormalization group approach. This can be ensured by lifting the Silver-Blaze property to hold not only in the infrared, but at all scales k:

$$\Gamma_k^{(n)}(p_1, \ldots, p_n; \mu) = \Gamma_k^{(n)}(\tilde{p}_1, \ldots, \tilde{p}_n; 0)\ . \tag{3.69}$$

The threshold $\mu_{c,k}$ is now generally scale dependent and given by the running pole mass. Eq. (3.69) can be achieved by imposing a similar property on the (fermionic) regulator function:

$$R_k^F(p;\mu) = R_k^F(\tilde{p};0)\ . \tag{3.70}$$

A simple general outline of a proof can be found in Ref. [124]. The idea is that in any loop diagram, the frequency component of the loop momentum can be shifted by $-\mathrm{i}\mu$ and the contour in the complex plane closed at (positive and negative) infinite real frequency. As long as there are no poles inside the contour and all external momenta are shifted as well, the vacuum result is recovered.

In our example, writing down the FRG flow of the fermion potential U_k^F, i.e., the (negative) contributions to the pressure in our free theory, and using Eq. (3.70) we find for $T = 0$

$$\begin{aligned}\partial_t U_k^F &= -\mathrm{tr}\int_p \frac{\partial_t R_k^F(p;\mu)}{\mathrm{i}\not{p} + m + R_k^F(p;\mu)} \\ &= -\mathrm{tr}\int_p \frac{\partial_t R_k^F(\tilde{p};0)}{\mathrm{i}\not{p} + m + R_k^F(\tilde{p};0)}\end{aligned} \tag{3.71}$$

where the trace lives in Dirac space. Note that for the Cauchy theorem to work and the vacuum flow to be recovered, the regulator needs to fulfill certain analyticity requirements that ensure the expression is complex differentiable in the domain enclosed by the real axis and the shifted contour $p_0 \to p_0 - \mathrm{i}\mu$. Especially, if the Silver-Blaze property ought to hold for $\mu < \mu_c$, we need to demand $\mu_{c,k} > \mu_c$ for all $k > 0$, i.e., the pole mass needs to approach the physical infrared value from above and the regulator can not introduce any additional, lower lying poles. This is actually a challenging restriction as the following example shows.

Example: Exponential regulator. If we explicitly choose the fermionic version (see Eq. (3.61)) of the well-established exponential regulator defined as

$$r^{\exp}(y) := \frac{1}{\mathrm{e}^y - 1} \tag{3.72}$$

and impose the Silver-Blaze condition, we obtain

$$R_k^{F,\exp}(p;\mu) = R_k^{F,\exp}(\tilde{p};0) = \mathrm{i}\not{p}\left(\sqrt{1 + \frac{1}{\mathrm{e}^{\tilde{p}^2/k^2} - 1}} - 1\right) \tag{3.73}$$

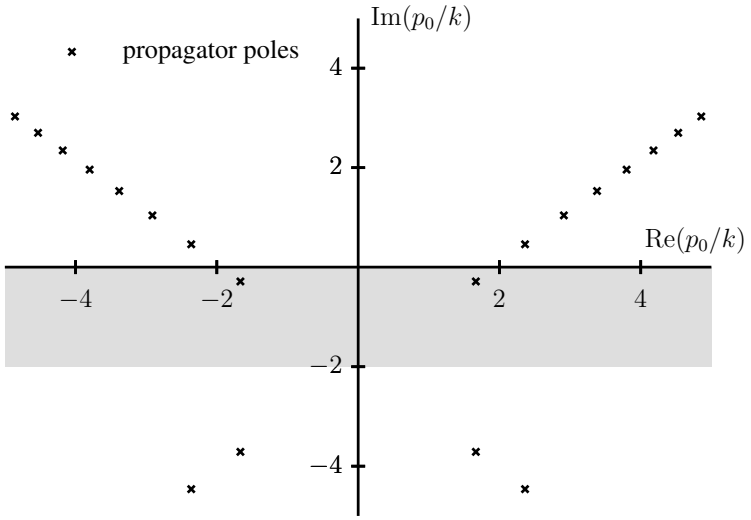

Figure 3.3: Propagator poles for the μ-dependent exponential regulator $R_k^{F,\exp}(p;\mu)$ in the dimensionless complex frequency plane for vanishing three-momentum $\boldsymbol{p} = 0$. The dimensionless parameters are chosen as $\mu/k = 2$, $m/k = 3$ and the shaded area is the one enclosed by the contour belonging to the shift $p_0 \to p_0 - \mathrm{i}\mu$ outlined in the text.

which yields the flow equation

$$\partial_t U_k^{F,\exp} = -4 \int_p \frac{\tilde{p}^4}{k^2} \frac{\mathrm{e}^{\tilde{p}^2/k^2}}{(\mathrm{e}^{\tilde{p}^2/k^2}-1)^2} \frac{1}{\tilde{p}^2\left[1+\left(\mathrm{e}^{\tilde{p}^2/k^2}-1\right)^{-1}\right]+m^2} \,. \tag{3.74}$$

The propagator poles are depicted in Fig. 3.3. Instead of two physical poles at imaginary frequency like the free bare, unregularized propagator which has (for vanishing spatial momenta) poles at $p_0 = \mathrm{i}(\pm m - \mu)$, there are infinitely many complex poles. Note that with the doubly exponential regulator defined as

$$r^{\mathrm{doubly-exp}}(y) = \frac{y}{\mathrm{e}^{y^2}-1} \tag{3.75}$$

one again recovers two physical poles at imaginary frequency on top of the infinitely many poles that radiate outwards in similar fashion [126].

Importantly, even for $\mu < m$ poles can perturb the area relevant for the shift in Eq. (3.71) (the shaded area in Fig. 3.3). As $k \to 0$, the dimensionless parameter μ/k increases and pushes even more poles from the upper dimensionless frequency half plane into the contoured area, further breaking the Silver-Blaze condition. In the context of real time correlation functions, a procedure to shift these poles by introducing an additional artificial mass term to the regulator function has been outlined in Ref. [126]. Further discussion can also be found in Ref. [127]. A possible adaption to thermodynamics at finite chemical potential is beyond the scope of this example; it should be sufficiently clear that the recovery of correct physics even for a simple problem like a free fermi gas becomes nontrivial.

At this point, it might be questionable why it is even necessary to ensure that the Silver-Blaze property holds at $k > 0$ when it is recovered for vanishing regulator in the limit

$k \to 0$—where the physics takes place—anyway. First, this is only the case in exact flows, not in truncated ones. For a truncated effective action, the integrity of this property can only be ensured if it is imposed along the full flow. Our free fermion loop, however, is exact. Second, by not keeping the Silver-Blaze property intact, one introduces unphysical μ-dependencies to the flow. These do not fully decouple at large momenta and thus the UV potential becomes μ-dependent, leading to issues with RG consistency as outlined in Ref. [128]. This is illustrated in the following example.

Example: Conventional flat regulator. Let us now choose the (fermionic) flat regulator defined by the shape function in Eq. (3.62) and refrain from introducing a μ dependency. Keeping only the real part as the imaginary part is odd in p_0 and vanishes in the integration, the flow becomes

$$\begin{aligned}\partial_t U_k^{F,\text{flat}} &= -4k^2 \int_p \Theta\left(1-\frac{p^2}{k^2}\right) \frac{p^2(k^2+m^2-\mu^2)+p_0^2\mu^2}{p^2(k^2+m^2-\mu^2)^2+p_0^2k^2\mu^2} \\ &= -\frac{k^4}{8\pi^2}\left[1+2\left(1-\sqrt{1+\frac{k^2\mu^2}{(k^2+m^2-\mu^2)^2}}\right)\frac{(m^2-\mu^2)(k^2+m^2-\mu^2)}{k^2\mu^2}\right] .\end{aligned} \tag{3.76}$$

For $k \gg \mu, m$ an expansion of the flow in μ^2/k^2 and m^2/k^2 to first order yields

$$\partial_t U_k^{F,\text{flat}} \approx -\frac{k^4}{8\pi^2}\left(1-\frac{m^2-\mu^2}{k^2}\right) . \tag{3.77}$$

Clearly, the regulator induces terms that scale as $k^2\mu^2$ similarly to a mass term and do not vanish towards the ultraviolet. By dimensional analysis, the μ-dependency at the UV scale Λ can be schematically expressed as (omitting the upper index referring to the regulator in the following)

$$\begin{aligned}U_\Lambda(\mu^2) &= \alpha_0\,\Lambda^4 + \alpha_1\,\Lambda^2\mu^2 + \tilde{\alpha}\,\mu^4\ln(\Lambda) + \alpha_2\,\mu^4 + \alpha_3\,\frac{\mu^6}{\Lambda^2} + \dots \\ &= \Lambda^4\sum_{i=0}^{\infty}\alpha_i\left(\frac{\mu^2}{\Lambda^2}\right)^i + \tilde{\alpha}\mu^4\ln(\Lambda)\end{aligned} \tag{3.78}$$

The α_i are generic coefficients that can also depend on ratios of μ and m. All thermodynamic contributions to observables must depend only on the inherent scales of the theory, i.e., mass and chemical potential. They should therefore be of the same order in size as the term with the coefficient α_2 in the UV potential. Possible UV cutoff effects due to the tail of thermodynamic distributions being cut off are part of α_3 and higher and vanish for $\Lambda \to \infty$. Hence, nonzero coefficients α_1, α_2 and $\tilde{\alpha}$ lead to strong μ dependencies of the UV potential and can be interpreted as regulator artifacts.

In order to extract any physics (and retain the Silver-Blaze property), one would have to know this spurious μ dependency of the UV potential. The gravity of this issue becomes clear if one tries to calculate the pressure at nonvanishing μ. Normalizing the vacuum pressure to zero, the UV potential can be extracted by integrating the vacuum flow from $k = 0$ to $k = \Lambda$,

$$U_\Lambda(0) = \int_0^\Lambda \mathrm{d}k\,\partial_k U_k(0) . \tag{3.79}$$

Then, starting at the UV scale we integrate the flow down to $k = 0$ in the presence of the chemical potential:

$$-p = U_0(\mu^2) = U_\Lambda(0) - \int_0^\Lambda \mathrm{d}k\, \partial_k U_k(\mu^2) \ . \tag{3.80}$$

However, since the UV potentials at different chemical potentials do not agree, $U_\Lambda(\mu^2) \neq U_\Lambda(0)$, we have actually made an error of size $\Delta U_\Lambda := U_\Lambda(\mu^2) - U_\Lambda(0)$ which carries over to the final result. For a nonvanishing coefficient α_1 this error is of order $\mu^2\Lambda^2$. It dominates all physical contributions and even increases with the cutoff scale.

A possible remedy for the problem could be to consider a sufficient number of derivatives of $U_k(\mu^2)$ with respect to μ^2 such that all parts diverging with Λ vanish [129]. This works as long as α_1 and $\tilde{\alpha}$ do not possess any additional μ dependency through dimensionless terms such as μ^2/m^2. Coming back to our example, Eq. (3.76), this condition is fulfilled. Taking three derivatives with respect to μ^2 removes even the logarithmic divergence and allows us to take the limit $\Lambda \to \infty$. In the UV, this corresponds to a mapping onto $\mathrm{d}\alpha_2/\mathrm{d}\mu^2$. Since the flow can be integrated analytically, the result in this limit takes—up to constant shifts—the explicit form

$$U_0'''(\mu^2) = -\frac{27}{64\pi^2}\frac{2\mu^2 - 3m^2}{(4m^2 - 3\mu^2)^2} \tag{3.81}$$

where the primes resemble derivatives with respect to μ^2. The correct result, which can be obtained by taking derivatives of our exact result for the pressure, Eq. (3.68), reads

$$U_0'''(\mu^2) = -\frac{1}{8\pi^2}\Theta(\mu^2 - m^2)\frac{m^4}{\mu^5\sqrt{\mu^2 - m^2}} \ . \tag{3.82}$$

Even in the limit $\Lambda \to \infty$ and for exact flows, the results do not agree. The error made at the UV scale is of the same order as the physical result because of a nonvanishing α_2 coefficient. Naively, this looks like a contradiction to the renormalization group idea. After all, we should recover the same microscopic action independent of the regulator in the limit $k \to \infty$, especially for an exact flow. The fault in the argument lies in the fact that we first mapped onto a subleading contribution to the potential by differentiating and then took the limit of infinite cutoff. If we instead regarded the dimensionless version of the full UV potential, $U_\Lambda(\mu^2)/\Lambda^4$, and then took the limit $\Lambda \to \infty$, all terms but the constant α_0 would vanish. Asymptotically, the potentials are equal, but the subleading terms are not. Similarly to the counterterms to the squared mass and coupling constant in φ^4 perturbation theory, there are quadratically and logarithmically divergent contributions to the chemical potential term in the UV action and $U_\Lambda(\mu^2)$ essentially has to be fine-tuned for each μ to produce the desired result, taking away all predictive power.

Dimensionally reduced regulators. So far, none of the outlined methods have delivered satisfying results. In the literature, these problems are commonly circumvented by the use of dimensionally reduced cutoff functions regularizing only the spatial momentum modes:

$$R_k^{\mathrm{3d}}(\boldsymbol{p}^2) = \boldsymbol{p}^2\, r(x) \ , \quad R_k^{F,\mathrm{3d}}(\boldsymbol{p}) = \mathrm{i}\not{\boldsymbol{p}}\, r^F(x) \tag{3.83}$$

with $x := \boldsymbol{p}^2/k^2$. Since those *3d regulators* do not depend on the frequency argument, they also remain μ-independent and always fulfill the Silver-Blaze condition, Eq. (3.70).

For such a regulator, the flow equation for the fermion potential becomes

$$\begin{aligned}\partial_t U_k^F &= -4\int_{-\infty}^{\infty}\frac{\mathrm{d}p_0}{2\pi}\int_{\boldsymbol{p}}\frac{\boldsymbol{p}^2\left[1+r^F(x)\right]\partial_t r^F(x)}{(p^0+\mathrm{i}\mu)^2+\boldsymbol{p}^2[1+r^F(x)]^2+m^2}\\ &= -4\int_{\boldsymbol{p}}\frac{\boldsymbol{p}^2\left[1+r^F(x)\right]\partial_t r^F(x)}{2E_k(\boldsymbol{p})}\,\Theta(E_k(\boldsymbol{p})-\mu)\end{aligned} \tag{3.84}$$

with

$$E_k(\boldsymbol{p}) = \sqrt{\boldsymbol{p}^2[1+r^F(x)]^2+m^2}\,. \tag{3.85}$$

The μ-dependence is solely given by the Heaviside step function and since regulator shape functions may not become negative, $E_k(\boldsymbol{p}) > m$ for all momenta and the Silver-Blaze property fulfilled as long as $\mu < m$. Note that with 3d regulators, $O(4)$ Euclidean space-time symmetry is broken, but this is expected to have only small quantitative impact in a thermodynamic context. In interacting fermionic theories at very large densities, it might be advantageous to neglect the Silver Blaze property in favor of other regulator characteristics. In Ref. [130] a regulator which does not keep Silver Blaze intact but sums up fluctuations symmetrically around the Fermi surface is introduced and shown to lead to better results for BCS-type theories.

Chemical potential and truncations. The implementation of a chemical potential is not only relevant in the context of the regulator function, but also for the truncation scheme. In the Lagrangian the chemical potential effectively induces a shift in the zero component of the derivative operator $\partial_0 \to \partial_0 - \mu$ when it acts on a fermion field. Perturbatively speaking, all of the infinite number of operators arising from the exponentiated action in the generating functional must therefore be shifted in this way. Thus, it seems reasonable to perform this shift in the derivative expansion as well. For a schematic example, let us assume an interacting theory and let the unspecified effective potential U_k^{eff} include all momentum-independent interacting and noninteracting parts as well as any bosonic contributions. Then, the derivative expansion in terms of the fermion field reads

$$\Gamma_k = \int_x \left[U_k^{\mathrm{eff}} + Z_{\psi,k}\bar{\psi}\not{D}\psi + \mathcal{O}\left(D^2\right)\right] \tag{3.86}$$

with the shifted derivative $D_\nu := \partial_\nu - \delta_{\nu 0}\mu$. In momentum space, this implies a shift in the frequency component of the expansion point from zero to $-\mathrm{i}\mu$. This conclusion has also been reached in Ref. [130]. Of course, an expansion in orders of the conventional derivative ∂_ν is also possible, in which case the chemical potential terms would be absorbed by lower order terms in the expansion. However, as we will see in the next chapter, this would again lead to RG consistency issues and the violation of the Silver-Blaze property.

Chapter 4

Functional Renormalization Group Approach to Low-Energy QCD

After introducing the fundamentals for functional methods and particularly the functional renormalization group, we consider an application towards QCD in the low-energy regime. First, we lay out some of the arguments and procedures leading towards low-energy effective theories for QCD. Next, we put particular emphasis on the quark-meson model which will be the basis for all the works presented in the coming chapters of this thesis. We detail the phase structure obtained with the functional renormalization group in local potential approximation and discuss some results and associated challenges that one has to face when going beyond LPA. At the end of this chapter, we give a general outlook on the so-called *dynamical hadronization* procedure which allows the incorporation of a smooth transition from QCD degrees of freedom to effective low-energy degrees of freedom.

4.1 Constructing a Low-Energy Effective Theory

Suitable descriptions of physical observables at a given length scale oftentimes rely on employing effective degrees of freedom which do not necessarily carry information about the underlying microscopic physics anymore. A typical example is classical mechanics which works at scales where the quantum (statistical) nature of elementary particles becomes irrelevant and objects can be assumed to be localized at a fixed point in space at any given time. The emergence of new effective degrees of freedom in a coarse-graining process, i.e., going from small length (large momentum) to large length (small momentum) scales, is closely related to the renormalization group picture. In a quantum field theory, this procedure is described by the running of couplings, leading to new effective infrared actions in Wilson's RG formulation as outlined in the previous chapter. In this process, new (composite) operators might emerge that take the role of effective degrees of freedom at lower energies. Due to the semi-group structure of the renormalization group, information about the microscopic theory at small scales is not necessarily retained, i.e., in case of an infrared fixed point of the RG flow there are infinitely many microscopic theories that all lead to the same macroscopic action.

The emergence of effective degrees of freedom becomes especially relevant in the context of QCD where confinement limits the maximum length scale at which quarks and gluons can be directly measured and asymptotic particle states are color-neutral com-

posite objects. Appropriately, effective low-energy theories work with hadronic degrees of freedom and construct the most general Lagrangians that are compatible with the symmetries of QCD. In chiral perturbation theory, one usually takes the dynamics of the lightest mesons, the pions (but also the addition of heavier ones and light nuclei is possible [131]) and includes all possible terms up to a certain order in momenta and pion mass [132]. Both parameters are small compared to the chiral symmetry breaking scale due to the low-energy dynamics and the approximate Goldstone nature of the pions.

Another ansatz is motivated by starting from the QCD action and considering only one-gluon exchange between quarks. From the color-neutral interaction spectrum at low energies, we expect that the gluon will not play a role as an effective degree of freedom in this regime. Indeed, gluon dynamics are observed to decouple at scales around 500-700 MeV [133]. Hence, we can neglect the gluon exchange in favor of a point-like current-current interaction [134]

$$\frac{g^2\kappa}{2} j_a^\mu j_a^\mu = \frac{g^2\kappa}{2} \left(\bar{q}\gamma^\mu T_a^c \mathbb{1}_f q\right)\left(\bar{q}\gamma^\mu T_a^c \mathbb{1}_f q\right) \ , \tag{4.1}$$

where the color and flavor structure is written out explicitly and κ is a parameter with dimension of inverse mass squared representing a heavy gapped gluon. The quarks are now to be understood as effective constituent quarks.

Using Fierz transformations, this interaction can be recast into a sum of various forms of mesonic $(\bar{q}\,\Gamma^{\boldsymbol{a}}\,q)(\bar{q}\,\Gamma^{\boldsymbol{a}}\,q)$ and diquark $(\bar{q}\,\tilde{\Gamma}^{\boldsymbol{a}}\,q^c)(\bar{q}^c\,\tilde{\Gamma}^{\boldsymbol{a}}\,q)$ channels where $\boldsymbol{a}$ is a multi-index for Dirac, flavor, and color space, Γ and $\tilde{\Gamma}$ represent all of the occurring matrix structures, and q^c is the charge conjugate field. For example, in Dirac space all possible matrix structures are given by the basis elements of a Clifford algebra,

$$\{\mathbb{1}, \gamma_\mu, \mathrm{i}\gamma_5, \gamma_\mu\gamma_5, \sigma_{\mu\nu}\} \ , \tag{4.2}$$

with the antisymmetric tensor

$$\sigma_{\mu\nu} = \frac{\mathrm{i}}{2}[\gamma_\mu, \gamma_\nu] \tag{4.3}$$

encoding 6 of the total 16 independent degrees of freedom. For further details and flavor and Dirac, flavor, and color channel Fierz identities see, e.g., Ref. [134].

Keeping only the mesonic (pseudo)scalar interactions, we arrive at the Nambu–Jona-Lasinio (NJL) model [135, 136]

$$\mathcal{L}_{\mathrm{NJL}} = \bar{q}\,\partial\!\!\!/\,q - \frac{\lambda}{2}\left[\left(\bar{q}T_f^a q\right)^2 + \left(\bar{q}T_f^a \mathrm{i}\gamma_5 q\right)^2\right] \tag{4.4}$$

where the T_f^a are generators of $U(N_f)$ flavor space transformations, see Sec. 2.1. The NJL model and variants of it with additional vector or diquark interactions have been extensively studied both in the context of the chiral phase transition and color superconducting phases; see, e.g., Refs. [67, 137] for reviews of the topic.

In the low-density regime, the scalar-pseudoscalar channel is the most relevant one [52, 133, 138–140]. Solving the functional renormalization group flow for the momentum-independent coupling λ, it grows larger and eventually diverges. The divergence at scale k_χ is to be understood as the onset of spontaneous chiral symmetry breaking where the emergence of massless Goldstone bosons leads to long-range correlations and the truncation in terms of a local interaction breaks down [141]. This can be resolved by means of a

Hubbard-Stratonovich transformation [142, 143] which allows for the bosonization of the interaction. The trick is to insert a Gaussian path integral over scalar fields into the partition function:

$$1 = \mathcal{N} \int \mathcal{D}\sigma_a \mathcal{D}\pi_a \, \mathrm{e}^{-\frac{1}{2}m^2 \int (\sigma_a^2 + \pi_a^2)} \tag{4.5}$$

where the (divergent) path integral is normalized by a factor $\mathcal{N}$. With the shifts

$$\sigma_a \to \sigma_a + \frac{h}{m^2} \left(\bar{q} T_f^a q\right) \ , \quad \pi_a \to \pi_a + \frac{h}{m^2} \left(\bar{q}\, \mathrm{i}\gamma_5 T_f^a q\right) \tag{4.6}$$

and the parameter choice $h^2/m^2 := \lambda$ the four-fermion vertex is cancelled in favor of Yukawa-type interactions

$$\mathcal{L}_{\text{bosonized}} = \bar{q} \left(\partial\!\!\!/ + h\, T_f^a (\sigma_a + \mathrm{i}\gamma_5 \pi_a)\right) q + \frac{1}{2} m^2 (\sigma_a^2 + \pi_a^2) \ . \tag{4.7}$$

The current interactions are now carried by the auxiliary fields which do not yet have any dynamics themselves. By additionally introducing standard kinetic terms $(\partial_\mu \sigma_a)^2/2 + (\partial_\mu \pi_a)^2/2$ for the bosonic fields, we can now allow for nonlocal interactions between the quarks. Phenomenologically, the σ_a and π_a can be associated with the scalar and pseudoscalar mesons of the theory as evident by the shifts in Eq. (4.6).

4.2 Quark-Meson Model

The Lagrangian (4.7) with additional kinetic and potential terms is commonly referred to as a quark-meson model. To phenomenologically add additional potential terms beyond the mass (i.e., direct meson-meson interactions generated by the flow), we need to respect the global chiral symmetry of QCD. From Eq. (4.6) we see that under $U(2)_L \times U(2)_R$ flavor transformations as introduced in Sec. 2.1, the shifted parts of the scalar fields transform as

$$\bar{q} T_f^a q \to \bar{q}_L \left(U_L^\dagger T_f^a U_R\right) q_R + \bar{q}_R \left(U_R^\dagger T_f^a U_L\right) q_L \ . \tag{4.8}$$

The pseudoscalars are transformed into each other in the same manner. Introducing the matrices

$$\Sigma := T_f^a (\sigma_a + \mathrm{i}\pi_a) \ , \quad \Sigma_5 := T_f^a (\sigma_a + \mathrm{i}\gamma_5 \pi_a) \tag{4.9}$$

we further see that, to keep the Yukawa interaction term

$$h\, \bar{q} \Sigma_5 q \to h\, \bar{q}_L \left(U_L^\dagger \Sigma_5 U_R\right) q_R + h\, \bar{q}_R \left(U_R^\dagger \Sigma_5 U_L\right) q_L \tag{4.10}$$

chirally invariant, Σ (and thus also Σ_5) has to transform like $\Sigma \to U_L \Sigma U_R^\dagger$ or $\Sigma \to U_R \Sigma U_L^\dagger$, depending on the respective Dirac subspace. Without loss of generality, we can just choose either transformation behavior within our applications.

Furthermore, we can construct the chiral invariants

$$\rho_n := \mathrm{Tr}\left[\left(\Sigma^\dagger \Sigma\right)^n\right] \ , \quad n = 1, \ldots, N_f \ . \tag{4.11}$$

It is easy to see that with the cyclic property of the trace, those expressions must be invariant under general $U(2)_L \times U(2)_R$ transformations and since any power of $\Sigma^\dagger \Sigma$ is

hermitian, there are N_f independent degrees of freedom signified by the number of real-valued diagonal entries. We explicitly consider the cases $N_f = 2+1$ with two degenerate light quark flavors and a strange quark as well as $N_f = 2$ where only the light spectrum is retained. In the former case, the Lagrangian reads

$$\mathcal{L}_{\mathrm{qm}}^{2+1} = \bar{q}\left(\partial\!\!\!/ + g\Sigma_5\right) q + \mathrm{Tr}\left(\partial_\mu \Sigma^\dagger \partial_\mu \Sigma\right) + U_\Lambda(\rho_1, \rho_2) - c_A\xi - c_l\sigma_l - c_s\sigma_s \ . \tag{4.12}$$

The generators for flavor space rotations in three dimensions are the Gell-Mann matrices $\hat{\lambda}_a$, i.e. $T_f^a = \hat{\lambda}_a/2$. Conventionally, the Yukawa coupling has been renamed $h \to g$. Because the third chiral invariant ρ_3 is of sixth power in the fields and thus its coupling has negative mass dimension and is perturbatively irrelevant, we do not include it in the quartic UV potential. As an approximation, the effective potential is assumed to depend only on ρ_1 and ρ_2 throughout the functional renormalization group flow.

The last three terms break chiral symmetry explicitly. Firstly, the anomalous breaking of axial $U(1)_A$ symmetry due to quantization is modeled by the lowest order instanton-induced term in the form of a 't Hooft determinant [144]

$$\xi := \det\Sigma + \det\Sigma^\dagger \ . \tag{4.13}$$

It gives rise to the splitting of the η and η' meson mass [65]. Secondly, the explicit breaking of chiral symmetry due to finite current quark masses is modeled by the linear terms $-c_l\sigma_l - c_s\sigma_s$ where the fields have been expressed in the nonstrange-strange basis (σ_l, σ_s) which is obtained from the singlet-octet basis (σ_0, σ_8) via the rotation

$$\begin{pmatrix}\sigma_l\\ \sigma_s\end{pmatrix} = \frac{1}{\sqrt{3}}\begin{pmatrix}\sqrt{2} & 1\\ 1 & -\sqrt{2}\end{pmatrix}\begin{pmatrix}\sigma_0\\ \sigma_8\end{pmatrix} \ . \tag{4.14}$$

Only the scalar fields σ_l and σ_s are included in the explicit breaking because all other fields are taken to have vanishing expectation value[1]

$$\langle\Sigma\rangle = T_f^0\,\sigma_0 + T_f^8\,\sigma_8 = \mathrm{diag}\left(\frac{\sigma_l}{2}, \frac{\sigma_l}{2}, \frac{\sigma_s}{\sqrt{2}}\right) \ . \tag{4.15}$$

The only additional condensate in agreement with the vacuum quantum numbers could be a finite σ_3 field whose generator is also diagonal in field space but it leads to a mass splitting between up and down quarks, i.e., the breaking of isospin symmetry which we assume to be intact. Note that in above equation, we omitted the brackets when writing down the nonvanishing meson field expectation values.

To prevent cluttering the expressions, the same symbol will be used for microscopic and macroscopic fields and brackets will only be used when it is necessary to make a distinction. In this manner, the expectation values of the chiral invariants and the axial breaking term can be written

$$\langle\rho_1\rangle = \frac{1}{2}\left(\sigma_l^2 + \sigma_s^2\right) \ , \quad \langle\rho_2\rangle = \frac{1}{8}\left(\sigma_l^4 + 2\sigma_s^4\right) \ , \quad \langle\xi\rangle = \frac{1}{2\sqrt{2}}\sigma_l^2\sigma_s \ . \tag{4.16}$$

For $N_f = 2$, the generators are $T_f^a = \tau_a/2$, with $\tau_0 = \mathbb{1}$ and τ_i, $i \in \{1,2,3\}$, denoting the three Pauli matrices which are also conveniently summed up in the vector $\boldsymbol{\tau}$. Then, the $U(1)_A$ breaking term becomes

$$-c_A\xi = -\frac{c_A}{2}(\sigma_0^2 + \boldsymbol{\pi}^2 - \pi_0^2 - \boldsymbol{\sigma}^2) \tag{4.17}$$

[1] This also holds for the fermion fields: $\langle\bar{q}\rangle = \langle q\rangle = 0$.

where again the three "spatial" indices are collected in a vector. It leads to a mass splitting between the two meson multiplets $\{\sigma_0, \pi_1, \pi_2, \pi_3\} \leftrightarrow \{\pi_0, \sigma_1, \sigma_2, \sigma_3\}$. We will only keep the light multiplet collected in the four-vector (dropping the superfluous index of the σ_0 field)

$$\phi := \begin{pmatrix} \sigma \\ \boldsymbol{\pi} \end{pmatrix} \tag{4.18}$$

and identify the light modes with the pions and the sigma resonance. This procedure is referred to as maximal axial symmetry breaking because the other set of mesons is made infinitely heavy and thus vanishes from the physical spectrum. The Lagrangian simplifies to

$$\mathcal{L}^{(2)}_{\mathrm{qm}} = \bar{q}\left(\partial\!\!\!/ + \frac{g}{2}(\sigma + \mathrm{i}\gamma_5 \boldsymbol{\tau}\cdot\boldsymbol{\pi})\right) q + \frac{1}{2}(\partial_\mu \phi)^2 + U_\Lambda(\phi^2) - c\sigma \ . \tag{4.19}$$

The potential is written as a function of ϕ^2 which is trivially related to the only remaining independent chiral invariant:

$$\rho = \frac{1}{2}(\sigma^2 + \boldsymbol{\pi}^2) = \frac{\phi^2}{2} \ . \tag{4.20}$$

As we can see, chiral and isospin symmetry look like $SO(4)$ when acting on the vector ϕ. This should not come as a surprise since $SU(2) \times SU(2)$ is the double cover of $SO(4)$. Since finite meson condensates break chiral symmetry of the vacuum, they are an order parameter for the chiral phase transition. Hence, this low-energy effective theory allows the qualitative study of the chiral phase transition.

In the chiral limit, i.e. for $N_f = 2$ and vanishing current quark masses $c = 0$, the quark-meson model is expected to lie in the same universality class as QCD as long as $U(1)_A$ stays broken at all temperatures [145]. An extended version of the model is the Polyakov-quark-meson (PQM) model [146]. In such PQM models the deconfinement phase transition is captured statistically by including an effective potential for the gluon background field in terms of the order parameter for deconfinement, the Polyakov loop. Next to one of the many variants of the effective Polyakov loop potential [147–150], the Polyakov-loop variables implictly depend on the quark loop dynamics. At vanishing temperature, these degenerate to the standard Fermi-Dirac distributions and the quark-meson model becomes equivalent to its Polyakov-loop extended version. As we are aiming predominantly at the low-temperature region of the phase diagram, we do not further consider including a Polyakov loop potential. However, a phenomenological finite density generalization of the Polyakov loop potential at zero temperature can stiffen the EoS [151]. For a review see e.g. [152] and for (P)QM phase structure investigations with the FRG see e.g. [153, 154].

4.3 Fluctuations and the Phase Structure

As a first application, we discuss the phase diagram of the quark-meson model in local potential approximation and compare the results to two different implementations of mean-field approximation (MFA). The aim is to judge the effect of additional fluctuations on the phase structure of the chiral transition. Note that similar studies of the phase diagram—both with the FRG [33, 155] and in MFA [65]—were been conducted in the past. The specific results of this section have already been attained in a previous work [156], but they are compiled here nonetheless as they provide a basis for the subsequent chapters.

Functional Renormalization Group Flows

Starting with the FRG approach, in the notation previously introduced the LPA truncation reads

$$\Gamma_k = \int_x \bar{q}\left(\partial\!\!\!/ + gT_f^a(\sigma_a + \mathrm{i}\gamma_5\pi_a)\right) q + \mathrm{Tr}\left(\partial_\mu\Sigma^\dagger\partial_\mu\Sigma\right) + \tilde{U}_k^{(N_f)} \ . \tag{4.21}$$

Neither the scale and field dependence of the wavefunction renormalization nor that of the Yukawa coupling are taken into account at the level of the LPA, but the important back-coupling in the meson sector in included by means of an effective potential that fully includes all momentum-independent parts of meson interactions. The full potential includes explicit symmetry breaking terms and is always denoted with a tilde. For $N_f = 2+1$, it reads

$$\tilde{U}_k^{(2+1)} = U_k^{(2+1)}(\rho_1, \tilde{\rho}_2) - c_A\xi - c_l\sigma_l - c_s\sigma_s \tag{4.22}$$

with the scale-dependent chirally symmetric potential $U_k^{(2+1)}$ whose arguments include the shifted second chiral invariant $\tilde{\rho}_2 := \rho_2 - \rho_1^2/3$ which simplifies the analytical determination of meson masses [155]. Note that in our approximation, the $U(1)_A$ breaking term c_A stays scale independent, albeit feeding into the flow of the chiral potential. Due to their linear order, the constant chiral breaking terms c_l and c_s do not contribute to any flow; this is why the assumption that all quantum fluctuations stored in $U_k^{(2+1)}$ preserve chiral symmetry remains valid.

The meson masses required for the Wetterich equation (3.36) are curvature masses given by the second derivative of the effective potential with respect to the fields. They follow from a generally nondiagonal matrix in field space,

$$M_{k,ab}^2 := \left.\frac{\partial^2\tilde{U}_k}{\partial\Phi_a\partial\Phi_b}\right|_{\langle\Phi\rangle} \ , \tag{4.23}$$

where Φ is a vector collecting all meson fields (i.e., a generalization of ϕ in Eq. (4.18) to N_f flavors) and the expression has to be evaluated at the expectation value only after taking the derivatives.[2] The derivatives incorporate contributions both from the axial breaking term and the chiral potential where they follow from derivatives with respect to the invariants via the chain rule. Details and the explicit expressions can be found in Refs. [155, 156].

In order to invert the two-point function for the flow equation, the mass matrix has to be diagonalized at each step in k. In this specific setup, the only nondiagonal entries are in the mixed singlet-octet $(0-8)$ channel of the scalar and pseudoscalar mesons, leading to a nontrivial mixing between strange and nonstrange mass eigenstates; see Ref. [65] for details and calculations of mixing angles in MFA. Choosing the 3d flat regulator defined by the shape functions given in Eqs. (3.54) and (3.62) together with Eq. (3.83), the flow

[2] The symbol Φ is used in the next section and the appendices for an even more general composite field that also includes the fermionic fields.

equation for the chiral potential reads

$$\partial_t U_k^{(2+1)} = \frac{k^5}{12\pi^2}\Bigg\{ \sum_b \frac{1}{E_b} \coth\left(\frac{E_b}{2T}\right) - 2N_c \sum_f \frac{1}{E_f}\left[\tanh\left(\frac{E_f-\mu_f}{2T}\right) + \tanh\left(\frac{E_f+\mu_f}{2T}\right)\right]\Bigg\} . \tag{4.24}$$

The energies are $E_i^2 := k^2 + m_i^2$ with the bosonic masses m_b^2 given by the eigenvalues of the mass matrix (4.23) and the fermion masses following from the Yukawa term as $m_u = m_d = g\sigma_l/2$ and $m_s = g\sigma_s/\sqrt{2}$. The bosonic sum covers all $2N_f^2 = 18$ mesons and the fermion sum is over the u, d, and s flavors. Additionally, we include chemical potentials in the typical manner (see Chapter 3) and allow a different chemical potential for each quark flavor for later convenience. For now, $\mu_f \equiv \mu$ is set equal for all quarks.

In the two-flavor case, the effective potential has the form

$$\tilde{U}_k^{(2)} = U_k^{(2)}(\phi^2) - c\sigma \ . \tag{4.25}$$

The flow reduces to

$$\partial_t U_k^{(2)} = \frac{k^5}{12\pi^2}\Bigg\{ \frac{1}{E_\sigma}\coth\left(\frac{E_\sigma}{2T}\right) + \frac{3}{E_\pi}\coth\left(\frac{E_\pi}{2T}\right) - \frac{2N_c}{E_q}\sum_f \left[\tanh\left(\frac{E_q-\mu_f}{2T}\right) + \tanh\left(\frac{E_q+\mu_f}{2T}\right)\right]\Bigg\} \tag{4.26}$$

with the flavor sum iterating over u and d quarks, the flavor blind quark mass $m_q = g\sigma/2$, and the explicit sigma and pion masses $m_\sigma^2 = 2U_k' + 4\sigma^2 U_k''$ and $m_\pi^2 = 2U_k'$. The primes denote derivatives with respect to ϕ^2, evaluated at the expectation value $\langle\phi^2\rangle = \sigma^2$. All parameter choices concerning the explicit breaking terms and the starting potentials for two and three quark flavors can be found in App. I.

For $T = 0$ and N_f generic quark flavors the flow reduces to

$$\partial_t U_k|_{T=0} = \frac{k^5}{12\pi^2}\Big[\sum_b \frac{1}{E_b} - 4N_c \sum_f \frac{1}{E_f}\Theta(E_f-\mu_f)\Big] . \tag{4.27}$$

In this limit the Fermi-Dirac distributions of the fermionic threshold functions become a sharp Heaviside function. This is a special case of the 3d regulator flow introduced in Eq. (3.84) for the flat regulator where the Θ-function survives the trivial momentum integral. For $\mu_f^2 > m_f^2$, only scales above the Fermi sea $k^2 > k_{f,\text{sea}}^2$ with $k_{f,\text{sea}}^2 \equiv \mu_f^2 - m_f^2$ contribute to the corresponding quark loop and are integrated out, yielding a finite quark density. Hence, an increase in the chemical potential suppresses more and more the quark dynamics of the model. As discussed in the previous chapter, the μ_f independence of the flow below the onset chemical potential implies that the Silver-Blaze property is satisfied.

Mean-Field Approximation

In mean-field approximation all meson fluctuations are neglected. Hence, the mesonic part of the effective potential becomes scale independent, i.e., with the definition

$$\tilde{U}^{(N_f)}_{\text{mean-field}} := \tilde{U}^{(N_f)}_{\text{mes}} + U^{(N_f)}_{q} \tag{4.28}$$

the meson potential for $N_f = 2 + 1$ is given by

$$\tilde{U}^{(2+1)}_{\text{mes}} = U^{(2+1)}_{\text{mes}}(\rho_1, \rho_2) - c_A\xi - c_l\sigma_l - c_s\sigma_s \tag{4.29}$$

whereas for $N_f = 2$ it reads

$$\tilde{U}^{(2)}_{\text{mes}} = U^{(2)}_{\text{mes}}(\phi^2) - c\sigma \tag{4.30}$$

in complete analogy to the FRG setup, with the exception of choosing ρ_2 instead of $\tilde{\rho}_2$ as the second argument of the chiral potential. The chiral potentials are just parameterized functions with up to quartic terms in the fields and are defined in App. I. Similarly to the exemplary pressure calculation in Sec. 3.6, an explicit calculation neglecting all divergent vacuum loops yields the thermodynamic contribution

$$U^{(N_f)}_{q,\text{sMFA}} = \frac{N_c}{\pi^2} T \sum_f \int_0^\infty \mathrm{d}p\, p^2 \left[\ln(1 - n_f(E_f, \mu_f, T)) + \ln(1 - n_f(E_f, -\mu_f, T))\right] \tag{4.31}$$

with the Fermi-Dirac distribution

$$n_f(E_f, \mu_f, T) = \frac{1}{\mathrm{e}^{(E_f - \mu_f)/T} + 1} \tag{4.32}$$

and the quark energies $E_f^2 = p^2 + m_f^2$. The quark masses are the same as in the previous FRG approach whereas the meson masses, which are again determined via the mass matrix (4.23), obtain contributions from both the static meson potential and the quark loop. The latter comes from a hidden field dependency of the quark masses m_f prior to taking the expectation values. Details on the calculation of the masses can be found in Refs. [65, 156]. This calculation neglects all vacuum fluctuations and we label it *standard mean-field approximation* (sMFA). Intuitively, this is no problem since we are not interested in constant shifts of the potential and any additional field-dependent contributions can be compensated by appropriate modifications of the meson potential.

However, as the vacuum expectation value σ changes with temperature and chemical potential, this also dynamically modifies the field dependent fermionic vacuum loops. It is therefore necessary to include these divergent expressions by regularizing them first and then renormalizing the potential, e.g. for a large momentum cutoff Λ. Other schemes like Pauli-Villars or dimensional regularization might be more appropriate and have been applied in the literature [157]. Another possibility which we here pursue is to let the functional renormalization group regulator take care of regularization, i.e., to take the flow equation and drop all back-coupled mesonic terms. After integration of the flow,

$$U^{(N_f)}_{q,\text{rMFA}} = \frac{N_c}{6\pi^2} \sum_f \int_0^\Lambda \mathrm{d}k\, \frac{k^4}{E_f} \left[\tanh\left(\frac{E_f - \mu_f}{2T}\right) + \tanh\left(\frac{E_f + \mu_f}{2T}\right)\right] , \tag{4.33}$$

the renormalization procedure simply consists of, for a given UV scale Λ, finding the appropriate modified coefficients for the meson potential. They are also given in App. I. We call this approach *renormalized mean-field approximation* (rMFA).

Phase Structure

The thermodynamics of a system is extracted by relating the infrared effective potential—evaluated at its global minimum—to the thermodynamic grand potential. As the effective potential has to be bounded from below, the global minimum must also be a local minimum, i.e., for a differentiable potential the gap equation

$$\left.\frac{\partial \tilde{U}}{\partial \Phi}\right|_{\langle\Phi\rangle} = 0 \tag{4.34}$$

is fulfilled. $\tilde{U}$ refers to any of the previous full potentials including all explicit symmetry breaking terms and in the FRG case is evaluated at the infrared scale $k = k_{\mathrm{IR}}$. The small infrared cutoff $k_{\mathrm{IR}} > 0$ is introduced for technical reasons since the effective potential becomes nonanalytic and flat for field values smaller than the infrared minimum when convexity is recovered in the limit $k \to 0$ [33]. This impedes a numerical solution, but stopping the flow at a finite scale well below the pion mass (which is the lightest particle in the spontaneously broken vacuum) usually yields sufficient accuracy since the position of the minimum freezes out at these scales [158]. Even though this argument refers to the vacuum flow, we will use the same infrared cutoff also at finite temperature and chemical potential. Chiral symmetry restoration generally leads to larger meson masses and although the quarks become light, they decouple at increasing temperature due to dimensional reduction and at finite chemical potential due to the fermi sea discussed earlier; hence, the error of this approximation is expected to be small. Some quantities like the position of the critical endpoint, however, will depend on the infrared cutoff. This is further discussed in Ch. 7. The infrared cutoff choices are given in App. I. Using Eq. (3.44), we find for the grand potential density

$$\Omega(T,\mu) = -\frac{T}{V}\ln \mathcal{Z} = \tilde{U}|_{\langle\Phi\rangle,T,\mu} \ . \tag{4.35}$$

As the effective potential is determined only up to constant shifts, the pressure is further normalized in the vacuum:

$$p = -[\Omega(T,\mu) - \Omega(0,0)] \ . \tag{4.36}$$

Since the grand potential is related to the internal energy by a Legendre transform, which in terms of densities (intrinsic quantities) reads

$$\Omega(T,\mu) = \varepsilon - Ts - \mu n \tag{4.37}$$

with the (internal) energy density ε and the entropy and particle densities

$$s = -\frac{\partial\Omega(T,\mu)}{\partial T} \ , \quad n = -\frac{\partial\Omega(T,\mu)}{\partial \mu} \ , \tag{4.38}$$

the inverted equation of state (EoS) $\varepsilon(p)$ can be computed from

$$\varepsilon(p) = -p + Ts + \mu n \ . \tag{4.39}$$

We will come back to the EoS in Ch. 5. For now, we are mainly interested in the effective potentials and the resulting vacuum expectation values for the fields. By varying the

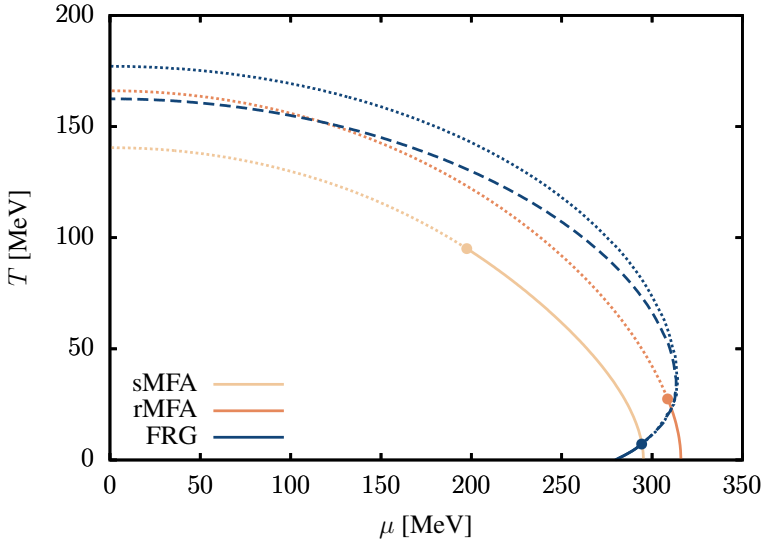

Figure 4.1: Phase diagrams of the $N_f = 2$ quark-meson model in three different approximations (sMFA, rMFA, and FRG). The dots are critical endpoints. Dotted lines are smooth crossovers and solid lines first-order phase transitions. In addition, the corresponding $N_f = 2+1$ phase structure obtained with the FRG is also shown (dashed line).

external parameters and determining the chiral condensate, the phase structure of the chiral transition can be analyzed.

Our numerical findings are collected in Fig. 4.1 where the phase diagrams for two quark flavors (dotted/solid lines) and for three flavors (dashed line) are shown. Details on the numerical implementation can be found in App. H. Typical for the phase structure obtained with the FRG is the back-bending behavior of the chiral phase transition line (blue lines) for small temperatures characterized by a positive slope of the critical chemical potential as a function of temperature. The critical endpoints (CEPs) are denoted as dots in the figure and the crossover regions/first-order transitions as dotted and solid lines, respectively. The origin of this back-bending phenomenon has so far been unclear but several possible scenarios are discussed in the literature [34]. We further investigate the issue in Ch. 7 where we associate it with regulator dependent truncation artifacts.

For the chosen vacuum input parameters and in the LPA truncation of the FRG equation, the CEP is located at very small temperatures, around $T \sim 10$ MeV for two and three quark flavors. In mean-field approximation the thermodynamical behavior at small temperatures is different and the first-order transition line hits the chemical potential axis perpendicularly [34]. Furthermore, since the inclusion of fluctuations generically smoothens the chiral phase transition, the crossover transition line is shifted to higher temperatures if more fluctuations in the thermodynamic potential are taken into account [154], except at very low temperatures where the back-bending phenomenon takes over. This is nicely demonstrated in Fig. 4.2a where both the light (solid lines) and the strange (dashed lines) chiral condensates are shown as a function of temperature for vanishing quark chemical potential.

In sMFA where only the thermal quark loop contribution is considered, the pseudo-critical crossover temperature $T_c \approx 140$ MeV at $\mu = 0$ is smallest. Already the inclusion of the vacuum quantum fluctuations of the quarks, labeled as rMFA in the figures, lifts the

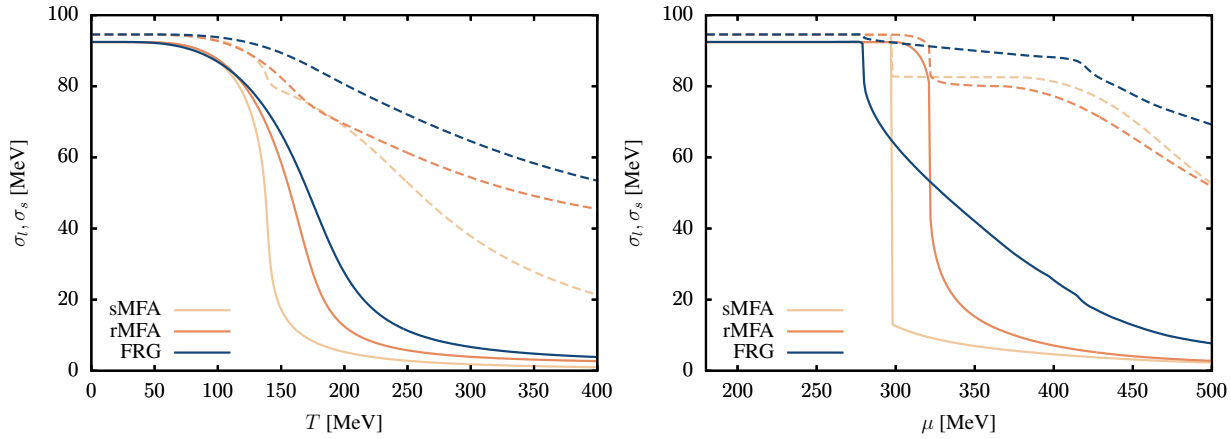

(a) $\mu = 0$. **(b)** $T = 0$.

Figure 4.2: Chiral condensates in the $N_f = 2 + 1$ flavor quark-meson model in three different approximations (FRG, rMFA and sMFA). The light condensates σ_l (solid) are the lower lines and the strange condensates σ_s (dashed) the upper lines.

pseudocritical temperature by about 30 MeV. Interestingly, the whole chiral phase transition is shifted constantly towards higher temperatures by roughly this amount for all chemical potentials, cf. Fig. 4.1. As a consequence, the first-order transition at $T = 0$ is also pushed to higher chemical potentials as visible in Fig. 4.2b. This trend is continued at least for moderate chemical potentials when additionally meson fluctuations with the FRG are taken into account. However, for smaller temperatures and due to the back-bending of the transition line, see. Fig. 4.1, the critical chemical potential is pushed to smaller values in contrast to the previous argument. This will be of relevance for the equation of state discussed in Ch. 5.

All condensates exhibit for $T = 0$ a first-order phase transition close to $\mu \approx 300$ MeV corresponding to the light quark mass in the vacuum. In sMFA, the first-order transition is strongest, in FRG weakest. Hence, the gap in the FRG light condensate is quite small and melts only moderately after the transition, still signaling a chirally broken phase in this density regime of the phase diagram [33]. In rMFA the light condensate is constant until $\mu = 300$ MeV and melts down before the first-order jump which is consistent with the Silver-Blaze property. It is likely that for a sigma mass below 560 MeV the rMFA condensates immediately jump when μ hits the light quark masses as well. Just below a quark chemical potential of about 430 MeV, the value that coincides with the strange quark mass in the vacuum, a further decrease is seen in all three strange condensates and a smooth chiral phase transition takes place. When strange quarks are added to the system, for vanishing and moderate chemical potentials three-flavor crossover line is pushed down again, see the dashed line in Fig. 4.1. The difference to the two-flavor phase structure shrinks for decreasing temperatures. Below $T < 50$ MeV almost no influence of the strange quark on the transition line is observed where the dashed line merges with the solid two-quark flavor line.

4.4 Beyond Local Potential Approximation

In this section, we incorporate some effects beyond local potential approximation to see the impact of a further improvement of the truncation. Even though we will focus on the cold and dense region of the phase diagram in the later course of this work, we limit ourselves here to the crossover region at low densities. This has the advantage of numerically more well-behaved flow equations and serves to outline some of the challenges posed by such improvements of the framework.

Going beyond local potential approximation essentially means extending the derivative expansion to include fluctuations beyond lowest order. As already stated in Ch. 3, the first step, oftentimes denoted as LPA', is to allow for running wavefunction renormalizations and a running Yukawa coupling but keeping both couplings field independent. The momentum structure stays essentially the same as in LPA, i.e., on a canonical level. Restricting ourselves to the two-flavor quark-meson model, the ansatz for the modified effective action is[3]

$$\Gamma_k[\Phi] = \int_x \left[U_k(\phi^2) + \frac{Z_{\phi,k}}{2}(\partial_\mu \phi)^2 + \bar{q}\left(Z_{q,k}\partial\!\!\!/ + \frac{g_k}{2}(\sigma + \mathrm{i}\gamma_5 \boldsymbol{\tau}\cdot\boldsymbol{\pi}) \right) q - c\sigma \right] . \tag{4.40}$$

We collect all bosonic and fermionic fields in the composite vector Φ. A schematic definition of how the fermions are added is given in App. A, Eq. (A.26). Its expectation value, subject to a possible chiral condensate in the σ direction, is

$$\langle \Phi \rangle = \begin{pmatrix} \sigma \\ \mathbf{0} \\ 0 \\ 0 \end{pmatrix} . \tag{4.41}$$

Note that this truncation does not include all terms of order $\mathcal{O}(\partial^2)$. A complete set that still respects chiral symmetry must also incorporate the additional term [159]

$$\int_x \frac{Y_k}{8}(\partial_\mu \phi^2)^2 . \tag{4.42}$$

Effectively, this term would lead to a splitting of the wavefunction renormalizations of the σ and π fields in the propagator already for field-independent Z_k and Y_k, an effect that has been mostly neglected also in the literature [20, 154]. Moreover, at finite temperature broken $O(4)$ symmetry generally leads to a splitting of each wavefunction renormalization Z into two couplings $Z_\parallel$ and $Z_\perp$, the former including fluctuations parallel and the latter the ones perpendicular to the heat bath; see Ref. [160] for an investigation of this matter. For simplicity, one usually projects out the spatial couplings $Z_\perp$ and applies them even to the temporal direction. As a last remark, neglecting the field dependence of the wavefunction renormalizations as well as the Yukawa coupling necessarily leads to inconsistencies especially for global, i.e. grid type, numerical solutions as the respective flows resulting from the evaluation at a single field value σ_{eval} feed into the partial differential equation for the effective potential which is a fully field dependent function.

[3] Henceforth, we omit the upper index indicating the number of flavors.

Flow Equations

In the following, we discuss the projections and resulting flow equations for the different couplings for the previously made assumptions and the flat regulator choice. General expressions for 3d regulators and details on the derivation of the flows can be found in App. E.

Effective potential. The flow of the effective potential is found with the standard projection already employed in LPA, i.e. the Wetterich equation evaluated at the expectation value and normalized with the spacetime volume:

$$\partial_t U_k|_{\langle\Phi\rangle} = \frac{1}{\beta V}\,\partial_t \Gamma_k|_{\langle\Phi\rangle} = \frac{1}{\beta V}\,\frac{1}{2}\mathrm{STr}\left[\left.\frac{\partial_t R_k}{(\Gamma_k^{(1,1)}+R_k)}\right|_{\langle\Phi\rangle}\right] . \tag{4.43}$$

To absorb the wavefunction renormalization, we further define the renormalized fields

$$\bar{\phi} := Z_{\phi,k}^{1/2}\phi \ , \tag{4.44}$$

and similarly for the fermions. The chiral potential must stay invariant under a change of variable:

$$\bar{U}_k(\bar{\phi}^2) = U_k(\phi^2) \ . \tag{4.45}$$

However, since the renormalized fields are scale dependent, the flow of the effective potential at fixed $\bar{\sigma}^2$ is amended by an additional term due to the chain rule:

$$\partial_t \bar{U}_k(\bar{\sigma}^2) = \partial_t U_k(\sigma^2) + \eta_{\phi,k}\,\bar{\sigma}^2\,\bar{U}_k'(\bar{\sigma}^2) \tag{4.46}$$

where a constant field expectation value $\langle\bar{\phi}^2\rangle = \bar{\sigma}^2$ has been inserted and the flow is determined as

$$\begin{aligned}\partial_t U_k(\sigma^2) = \frac{k^5}{12\pi^2}\Bigg\{ &\frac{1-\eta_{\phi,k}/5}{E_\sigma}\coth\left(\frac{E_\sigma}{2T}\right) + 3\frac{1-\eta_{\phi,k}/5}{E_\pi}\coth\left(\frac{E_\pi}{2T}\right) \\ &- 2N_cN_f\frac{1-\eta_{q,k}/4}{E_q}\left[\tanh\left(\frac{E_q-\mu}{2T}\right)+\tanh\left(\frac{E_q+\mu}{2T}\right)\right]\Bigg\} .\end{aligned} \tag{4.47}$$

Note the employed 3d flat regulator also incorporates the wavefunction renormalization factor, see Eq. (3.49). The energies are now defined as $E_i^2 := k^2+\bar{m}_i^2$ with the renormalized masses

$$\bar{m}_\sigma^2 := 2\bar{U}_k'(\bar{\sigma}^2) + 4\bar{\sigma}^2\bar{U}_k''(\bar{\sigma}^2) \ , \quad \bar{m}_\pi^2 := 2\bar{U}_k'(\bar{\sigma}^2) \ , \quad \bar{m}_q^2 := \frac{\bar{g}_k^2}{4}\bar{\sigma}^2 \ . \tag{4.48}$$

The renormalized Yukawa coupling reads

$$\bar{g}_k = \frac{g_k}{Z_{q,k}Z_{\phi,k}^{1/2}} \tag{4.49}$$

and the anomalous dimensions are given by the logarithmic derivative

$$\eta_{\phi,k} := -\partial_t \ln Z_{\phi,k} \ , \quad \eta_{q,k} := -\partial_t \ln Z_{q,k} \ . \tag{4.50}$$

Importantly, the chemical potential term in the truncation to the effective action also receives a modification by means of the wavefunction renormalization,

$$\Gamma_k^\mu := -Z_{q,k}\mu \int_x \bar{q}\gamma_0 q \ , \tag{4.51}$$

which retains the symmetry $\partial_0 \to \partial_0 - \mu$ from the Lagrangian as discussed in Sec. 3.6 and naturally preserves a scale-independent chemical potential in the particle distribution functions.

Anomalous dimensions. In order to determine the anomalous dimensions, we next consider the flow of the bosonic wavefunction renormalization. We project out the spatial coupling by taking two functional derivatives with respect to an arbitrary pion field and then taking the derivative with respect to the spatial momentum squared. Afterwards, the expression is evaluated at vanishing external momentum and $\langle\Phi\rangle$,

$$\partial_t Z_{\phi,k} = \frac{1}{\beta V}\lim_{p\to 0}\frac{\partial}{\partial \boldsymbol{p}^2}\frac{\delta^2}{\delta\pi_3(p)\delta\pi_3(-p)}\partial_t\Gamma_k\bigg|_{\langle\Phi\rangle} \ . \tag{4.52}$$

Taking derivatives with respect to the σ field would result in a different flow equation, even though in our simplified truncation it also projects out $Z_{\phi,k}$ in the same manner. The reason for this apparent contradiction is that, including field dependencies (which is inherently assumed by the exact Wetterich equation) and taking the σ derivatives instead of the pion ones, one additionally projects out a term proportional to the derivative $Z'_{\phi,k}(\sigma^2)$ that survives at the expectation value. Hence, in order to avoid such projection errors, the correct projection should always be determined formally in the presence of higher order corrections. With above projection, the anomalous dimension reads

$$\eta_{\phi,k} = \frac{k^5}{12\pi^2}\left\{4\bar{V}^2_{\pi\sigma\pi}\mathcal{M}^{(2,2)}_{\sigma\pi} + 4N_cN_f\frac{\bar{g}_k^2}{4}\left[\mathcal{M}^{(3)}_q 4(2-\eta_{q,k}) - \frac{1}{k^2}\mathcal{M}^{(2)}_q(3-2\eta_{q,k})\right]\right\} \tag{4.53}$$

with $\bar{V}_{\pi\sigma\pi} := 4\bar{\sigma}\bar{U}''_k$. The Matsubara sums $\mathcal{M}$ are given in App. D and more detailed information on the derivation of the flows can be found in App. E.

In similar fashion, the flow for the fermionic wavefunction renormalization is obtained via

$$\partial_t Z_{q,k} = \frac{1}{\beta V}\frac{1}{4N_cN_f}\lim_{p\to p_{\text{ext}}}\frac{\partial}{\partial \boldsymbol{p}^2}\mathrm{tr}\left[-\mathrm{i}\not{p}\frac{\overrightarrow{\delta}}{\delta\bar{q}(p)}\partial_t\Gamma_k\frac{\overleftarrow{\delta}}{\delta q(p)}\bigg|_{\langle\Phi\rangle}\right] \tag{4.54}$$

where the trace includes Dirac, color, and flavor space. At finite temperature, the frequency component of the external fermionic momentum ν_{ext} has to be nonvanishing as it is a Matsubara frequency. The typical choice is the lowest (positive) frequency, i.e., $p_{\text{ext}} = (\pi T, \mathbf{0})$. Note that this also leads to a projection error because contributions from higher-order momentum corrections in the local potential approximation do not vanish for nonzero external momentum. As evident from the mixed Matsubara sums including both bosonic and fermionic propagators (D.13), for nonvanishing external frequencies and in the presence of a chemical potential the flows for $Z_{q,k}$ and g_k become complex. This could very well be a consequence of the projection error. We adapt the current resolution in the literature [20, 161] by taking the real part of the expression which equals averaging

the flows for $\nu_{\text{ext}} = \pi T$ and $\nu_{\text{ext}} = -\pi T$. Note that an extension to frequency dependent wavefunction renormalizations where the imaginary parts of the anomalous dimensions cancel naturally in the flow of the effective potential has also been explored [162].

Further, for a nonzero chemical potential the external frequency needs to be shifted by $-\mathrm{i}\mu$, i.e. $\nu_{\text{ext}} = \pm\pi T - \mathrm{i}\mu$. Without this shift, there would be μ dependencies in the threshold functions outside of the particle number distributions, spoiling the Silver-Blaze property. Similar to Eq. (4.51), this is in agreement with our assertion made in Sec. 3.6 that a shifted derivative expansion in terms of the operator $D_\nu := \partial_\nu - \delta_{\nu 0}\mu$ yields the correct physics. The shifted expansion point exactly requires the insertion of the shifted external fermionic momentum p_{ext} in the projection (4.54) to make all higher order terms vanish. Evaluating the flow leads to

$$\eta_{q,k} = \frac{k^5}{12\pi^2}\frac{\bar{g}_k^2}{4}(4-\eta_{\phi,k})\left(\mathcal{M}_{q\sigma}^{(1,2)} + 3\mathcal{M}_{q\pi}^{(1,2)}\right) \ . \tag{4.55}$$

Note that the anomalous dimensions depend on each other. Eqs. (4.53) and (4.55) form a simple linear system of equations that can be resolved for $\eta_{\phi,k}$ and $\eta_{q,k}$.

Yukawa coupling. Last, for the flow of the Yukawa coupling we use the projection

$$\partial_t g_k = \frac{1}{\beta V}\frac{1}{4N_c N_f}\frac{2}{\sigma}\lim_{p\to p_{\text{ext}}}\operatorname{tr}\left[\frac{\overrightarrow{\delta}}{\delta\bar{q}(p)}\partial_t\Gamma_k\frac{\overleftarrow{\delta}}{\delta q(p)}\bigg|_{\langle\Phi\rangle}\right] \ . \tag{4.56}$$

The fermionic external momentum p_{ext} chosen as before and the same discussion applies. Note that there are two more possibilities for a projection, one featuring a functional derivative with respect to the sigma field instead of a division, and the other one a derivative with respect to a pion field and an appropriate Pauli matrix in flavor space. Clearly, only the last two options could resolve the full momentum dependence of the Yukawa coupling, as the insertion of a constant expectation value σ kills one of the two independent momenta. Hence, Eq. (4.56) only works in the point-like limit, i.e. when projecting onto the lowest order of the derivative expansion. Furthermore, including field dependencies the version with the sigma derivative again leads to an additional term proportional to $g_k'(\sigma^2)$, and should therefore be excluded.

Using above projection and taking into account the anomalous dimensions, we find for the renormalized Yukawa coupling

$$\begin{aligned}\partial_t\bar{g}_k = \bar{g}_k\Bigg\{\eta_{q,k} + \frac{1}{2}\eta_{\phi,k} + \frac{k^5}{12\pi^2}\bar{g}_k^2\Big[&\left(\mathcal{M}_{q\sigma}^{(1,2)} - 3\mathcal{M}_{q\pi}^{(1,2)}\right)\left(1-\frac{\eta_{\phi,k}}{5}\right)\\ &+\left(\mathcal{M}_{q\sigma}^{(2,1)} - 3\mathcal{M}_{q\pi}^{(2,1)}\right)\left(1-\frac{\eta_{q,k}}{4}\right)\Big]\Bigg\} \ .\end{aligned} \tag{4.57}$$

As already mentioned, the approximation of field-independent Yukawa coupling and wavefunction renormalizations necessitates the choice of a specific evaluation point σ_{eval} in field space. The flow will differ based on that choice. Here, we consider two different methods to deal with the issue:

Static: The vacuum infrared minimum $\sigma_{\text{eval}} = \sigma_{\text{min}} = 92.4\,\text{MeV}$ is chosen as the static evaluation point for the Yukawa coupling and wavefunction renormalizations throughout the flow. This is expected to become increasingly unprecise upon chiral symmetry restoration when the vacuum condensate melts down. A possible remedy is to approximate the new static infrared minimum $\sigma_{\text{min}}(T, \mu)$ for each individual T and μ (e.g., by a recursive procedure).

Co-moving: At each point in k, the local minimum of the potential $\tilde{U}_k$ (including the explicit symmetry breaking term) is determined numerically and used as the evaluation point $\sigma_{\text{eval},k} = \sigma_{\text{min},k}$. Advantageously, the minimum always dynamically adapts to changes in the flow due to changes in temperature or chemical potential. However, the running evaluation point introduces a modification to the flow much like the additional term in the flow equation for the renormalized potential (4.46). This modification term does not enter in our approximation as it is proportional to the first field derivative of the coupling, which could lead to inconsistencies and strong artifacts.

Masses and Phase Structure

To compare the static and co-moving approximations, the meson masses and phase structure are examined. As previously stated, we limit the investigation to the crossover regime for now. Some exploratory tests in the high-density region of the phase diagram have led to numerical issues especially in the co-moving approximation. Inconsistencies induced by the discontinuity of the minimum at the first-order phase transition may be responsible for or contribute to this problem. Other novel works in this direction suggest that—at least in simple approximations such as the static one—no significant qualitative changes occur at high densities and the observed peculiarities like the back-bending of the transition line persist [163]. As already hinted, we will elucidate the origin of this phenomenon in Ch. 7 and conclude that it must still be present at the level of LPA'.

First, we consider the renormalized meson masses on the temperature axis of the phase diagram (i.e., for $\mu = 0$). They are depicted in Fig. 4.3. For $T = 0$, the pion and sigma masses are fixed to their physical vacuum masses, cf. App. I for the parameters. With the smooth restoration of chiral symmetry at increasing temperature, the mesons degenerate. While both the static and co-moving approximations agree up to a temperature of about 150 MeV, a large discrepancy can be observed for higher temperatures, with the co-moving approximation leading to much larger renormalized masses. A noticeable decoupling effect of the renormalized masses due to the wavefunction renormalization is expected. According to observations made in Ref. [133], for RG scales $k \gtrsim 800\,\text{MeV}$ the bare meson masses freeze out and the decoupling of the mesons from the physical spectrum happens mainly due to the running of the wavefunction renormalization.

Conceptually, this behavior should be transferable to the decoupling at large temperatures. Indeed, even in the static approximation the renormalized masses are found to be larger than their bare counterparts in LPA. One might argue that, since for large temperatures the evaluation point in the static approach is much larger than the physical minimum of the potential, the running of the wavefunction renormalization is underestimated and therefore meson masses are still too small at large temperatures. A modified ansatz in which the constant evaluation point is chosen close to the actual infrared minimum $\sigma_{\text{min}}(T, \mu)$, however, yields only minor modifications to the static result depicted

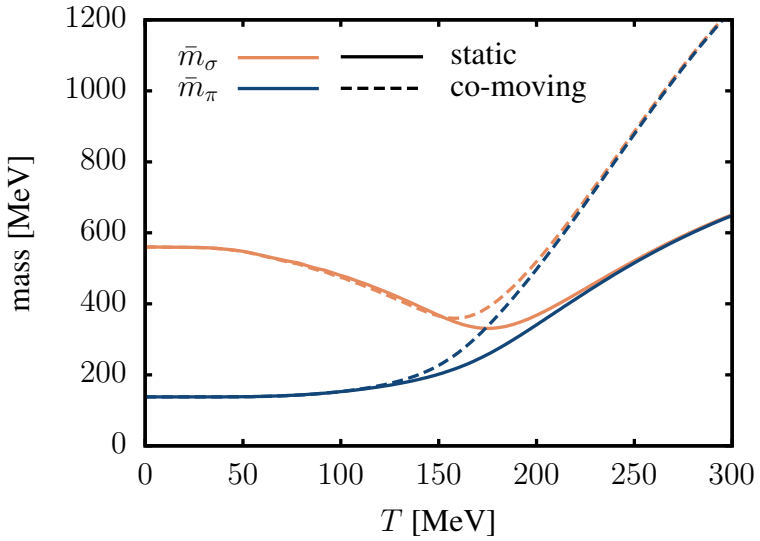

Figure 4.3: Renormalized meson masses as a function of temperature at vanishing chemical potential in the static and co-moving approximations.

in Fig. 4.3 and the same asymptotics.[4] In other words, the result is not as sensitive to the choice of evaluation point as the difference between the static and co-moving versions suggests. The extreme decoupling behavior in the co-moving approximation might therefore be an approximation error. It is possibly explained by the fact that the flow of the wavefunction approximations is always evaluated at the k-dependent minimum where the pion mass is smallest, leading to its overestimation.

The phase diagram for $\mu_B/T < 3$ with the baryonic chemical potential $\mu_B = 3\mu$ (as there are three constituent quarks to a baryon) is shown in Fig. 4.4. While the critical temperature of the crossover transition successively increases going from sMFA to rMFA to LPA (cf. Fig. 4.1), we now observe a decrease in LPA' compared to LPA. As with the masses, the co-moving approximation exhibits this tendency in a more extreme fashion, with the pseudocritical temperatures $T_c^{\mathrm{co-mov}} \approx 151\,\mathrm{MeV}$ and $T_c^{\mathrm{stat}} \approx 161\,\mathrm{MeV}$ for $\mu = 0$, respectively. These effects do not only constitute a shift of the crossover line. Fitting the lines to the polynomial

$$\frac{T_c(\mu_B)}{T_c} = 1 - \kappa \left(\frac{\mu_B}{T_c}\right)^2 + \lambda \left(\frac{\mu_B}{T_c}\right)^4 \tag{4.58}$$

where $T_c \equiv T_c(\mu_B = 0)$, we obtain the curvatures of the crossover line

$$\kappa^{\mathrm{stat}} = 0.01499(1)\ , \quad \kappa^{\mathrm{co-mov}} = 0.01675(2)\ . \tag{4.59}$$

These curvatures are of particular relevance for comparisons to results obtained from Taylor expansions about vanishing or at imaginary chemical potential in Lattice QCD calculations [164, 165]. Of course, a quantitative comparison to lattice results would require a matching definition of the pseudocritical temperature, expansion method, and expansion region. Details can be found, e.g., in Ref. [20] which includes a similar, more

[4] We will only state this result here and delay more detailed investigations to future works.

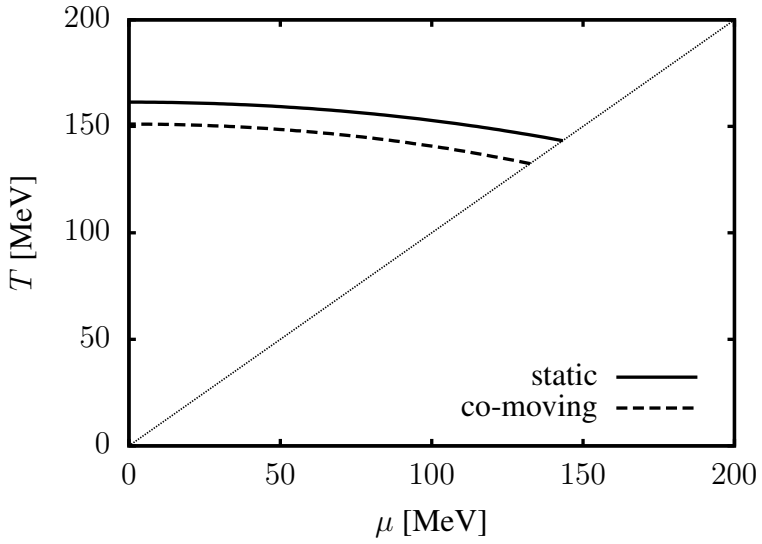

Figure 4.4: Phase diagram for $\mu/T < 1$ (denoted by the dotted diagonal) for the static and co-moving approximations. Both lines show a crossover transition.

elaborate calculation based on the FRG framework. Nevertheless, we follow from the difference of the two curvature values and critical temperatures that at the level of the LPA' truncation, even at small densities a more in-depth study of the field dependence of couplings is necessary to achieve sufficient understanding of the quantitative size of approximation errors.

4.5 Dynamical Hadronization

In the beginning of this chapter, we outlined how the quark-meson model follows from a bosonized four-quark interaction. Full meson dynamics are switched on at a fixed compositeness scale k_ϕ which can be understood as the UV scale of the model [38]. Instead of this well-motivated but crude procedure the dynamical emergence of those effective degrees of freedom from the QCD flow can be incorporated within the FRG. For that purpose, the inclusion of a running wavefunction renormalization $Z_{\phi,k}$ for the mesons as introduced in the previous section is necessary. We retain $N_f = 2$ and only consider the four lightest mesons encoded by the vector ϕ defined in Eq. (4.18).

Since the flow equations—when formulated for renormalized fields—do not depend on the actual value of $Z_{\phi,k}$ but only on the anomalous dimension, we are free to normalize it at an arbitrary scale. Commonly, the wavefunction renormalization is taken to be unity at the UV cutoff scale such that the bare fields of the microscopic theory have the standard kinetic terms, but of course a field redefinition modifying all couplings and thus also $Z_{\phi,k}$ is always possible. In Ref. [133], $Z_{\phi,k}$ is normalized to unity at low scales where the mesons dynamics are relevant.

Based on an ansatz including ghosts and gluons and their respective couplings, it was shown that with the onset of the quark-gluon regime of QCD, i.e. for scales above approximately 800 MeV [133], the hadronic wavefunction renormalization falls off and continuously decreases towards the ultraviolet. Hence, at large scales in the quark-gluon

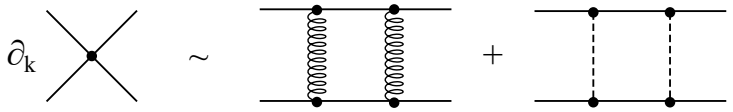

Figure 4.5: Schematic depiction of gluon and meson box diagrams contributing to the regeneration of the four-quark interaction. Figure adapted from Ref. [133].

regime the scalar fields lose their dynamics and become pure auxiliary fields in a bosonized formulation of the local four-quark interaction, while in the hadronic regime where the gluon is gapped they become dynamical and take over as the new effective degrees of freedom. Necessarily, this approach requires the scalar fields to be included already at the UV scale of the QCD calculation which is much larger than k_ϕ; however, as just explained they do not contribute to the dynamics.

The bosonization procedure laid out in Sec. 4.1 only cancels the four-quark interaction at a fixed scale and it will be continuously re-generated during the flow by the quark-meson and quark-gluon box diagrams shown in Fig. 4.5 [133, 141]. Therefore, a dynamical hadronization (or re-bosonization) procedure requires the continuous redefinition of the meson fields at each point in k to shift all contributions to the flow of the four-fermion coupling into the Yukawa interaction. The field in terms of which we formulate the effective action becomes a scale-dependent functional of the bare fields. Following Ref. [166], we choose for its scale derivative

$$\partial_t \phi_{k,a} = \dot{A}_k \, \bar{q} \tilde{\Gamma}_a q + \dot{B}_k \, \phi_{k,a} \tag{4.60}$$

where $\tilde{\Gamma}_a$ is a placeholder for the respective matrix structure of the (pseudo)scalar channel, i.e. $\tilde{\Gamma}_0 := 1/2$ and $\tilde{\Gamma}_i := \mathrm{i}\gamma_5\tau_i/2$ for $i \in \{1,2,3\}$. The coefficient $\dot{A}_k$ encodes the flow of the field shift that cancels the four-fermion interaction while $\dot{B}_k$ is just a rescaling of the field itself. Note that due to chiral symmetry, the four-fermion coupling λ is the same for all (pseudo)scalar subchannels; therefore we can choose $\dot{A}_k$ (and, in any case, $\dot{B}_k$) to be independent of the field index a.

Next, as we want the effective action to be a functional of the scale-dependent scalar fields,

$$\Gamma_k = \Gamma_k[\phi_k, q, \bar{q}, A, c, \bar{c}] \tag{4.61}$$

where A is the gluon and c, $\bar{c}$ are the ghost fields, a modification of the FRG framework is required. It is possible to formulate a modified Wetterich equation for general scale dependent (composite) field vectors Φ_k which are functionals of the non-scale dependent versions Φ. Note that for clarity, we reintroduce a distinction between fluctuating microscopic fields and macroscopic expectation values. As in Ref. [166], the former are expressed as $\tilde{\Phi}$:

$$\mathcal{Z}_k[J] = \int \mathcal{D}\tilde{\Phi} \, \mathrm{e}^{-S[\tilde{\Phi}] - \Delta S_k[\tilde{\Phi}_k] + \int J\tilde{\Phi}_k} \, . \tag{4.62}$$

The source term in the generating functional as well as the FRG modification ΔS_k now couple to the scale-dependent fields. The scale dependence of the fluctuating fields is related to the one of the expectation values via the assumption

$$\left\langle \partial_t \tilde{\Phi}_k \right\rangle = \partial_t \left\langle \tilde{\Phi}_k \right\rangle = \partial_t \Phi_k \, . \tag{4.63}$$

Deriving the flow along the lines of Sec. 3.2, the modified Wetterich equation reads [20]

$$\partial_t|_{\Phi_k}\Gamma_k = \frac{1}{2}\mathrm{STr}(G_k\,\partial_t R_k) + \frac{1}{2}\mathrm{STr}\left(G_{k,ab}\frac{\delta(\partial_t\Phi_{k,c})}{\delta\Phi_{k,b}}R_{k,ca}\right) - \int(\partial_t\Phi_{k,a})\frac{\delta\Gamma_k}{\delta\Phi_{k,a}}\ . \tag{4.64}$$

The remaining indices explicitly denote the individual components of Φ_k and corresponding momentum integrations in the supertraces are implicit. To obtain the second term, the relation [166]

$$\left\langle\tilde{\Phi}_{k,b}\,\partial_t\tilde{\Phi}_{k,c}\right\rangle = \left(\frac{\delta}{\delta J_b}+\Phi_{k,b}\right)\left\langle\partial_t\tilde{\Phi}_{k,c}\right\rangle = \left(\int G_{k,ab}\frac{\delta}{\delta\Phi_{k,b}}+\Phi_{k,b}\right)\left\langle\partial_t\tilde{\Phi}_{k,c}\right\rangle \tag{4.65}$$

was used. With the ansatz (4.60) for the scale dependence of the scalar fields, the only nonvanishing contribution to the second term in Eq. (4.64) stems from the rescaling of the field itself. The Wetterich equation simplifies to

$$\partial_t|_{\Phi_k}\Gamma_k = \frac{1}{2}\mathrm{STr}(G_k\,\partial_t R_k) + \frac{1}{2}\mathrm{Tr}\left(G_{k,a}\dot{B}_k R_{k,a}\right) - \int\left(\dot{A}_k\,\bar{q}\tilde{\Gamma}_a q + \dot{B}_k\phi_{k,a}\right)\frac{\delta\Gamma_k}{\delta\phi_{k,a}} \tag{4.66}$$

The index a now only sums over the mesons contained in ϕ_k. Noteworthy, a nonvanishing $\dot{B}$ leads to the exact same structural contributions as the anomalous dimension. This makes sense since it is just a generalization of such a field rescaling. Hence, the modifications it brings to the previously determined flow equations can be incorporated by the simple shift

$$\eta_{\phi,k} \to \eta_{\phi,k} - 2\dot{B}_k\ . \tag{4.67}$$

To make matters even more simple, we choose $\dot{B}\equiv 0$ as we do not wish any rescalings besides the one due to the wavefunction renormalization. Further, as the expectation values of the macroscopic quark fields vanish, the flow of the effective potential does not receive any modifications due to the $\dot{A}_k$ term in Eq. (4.66). However, we still need to keep this term as the projections for the flow of higher-order couplings are obtained by functional derivatives acting on it.

This leads to a nonvanishing contribution to the flow of the renormalized four-fermi and Yukawa couplings:

$$\partial_t|_{\Phi_k}\bar{\lambda}_k = \partial_t\bar{\lambda}_k + \bar{g}_k\dot{\bar{A}}_k \tag{4.68}$$

and

$$\partial_t|_{\Phi_k}\bar{g}_k = \partial_t\bar{g}_k - \left(p^2+\bar{U}_k'\right)\dot{\bar{A}}_k\ . \tag{4.69}$$

The renormalized coefficient $\dot{\bar{A}}_k$ can be inferred from Eq. (4.60) as

$$\dot{\bar{A}}_k = \frac{Z_{\phi,k}^{1/2}}{Z_{q,k}}\dot{A}_k \tag{4.70}$$

and $\partial_t\bar{\lambda}_k$ as well as $\partial_t\bar{g}_k$ are the flows without dynamical hadronization. For the pure quark-meson truncation, the latter is given in Eq. (4.57). The former can not be extracted unambiguously since the box diagrams generate not only scalar, but also vector channel interactions and we are not working in a Fierz complete basis. Different ansätze can be found in Refs. [20, 133, 141]. Furthermore, terms proportional to $\bar{g}_k'$ which are

taken into account in Ref. [133] are dropped in accordance with our approximation of a field-independent Yukawa coupling. With the starting value $\bar{\lambda}_\Lambda = 0$, implying that all interactions are bosonized already at the UV scale, and for the choice

$$\dot{\bar{A}}_k = -\frac{\partial_t \bar{\lambda}_k}{\bar{g}_k} \tag{4.71}$$

we find $\bar{\lambda}_k \equiv 0$. All contributions to the running of the four-fermi interaction are continuously shifted into the running of the Yukawa coupling. A re-bosonization procedure is also possible in a pure low-energy effective theory without gauge degrees of freedom. The re-generation of the four-quark interaction is then limited to the quark-meson box diagram in Fig. 4.5. However, it has been shown that in vacuum these contributions have negligible impact [133]. It can be argued that at large densities, effects from dynamical hadronization might possibly be larger, but studies in NJL-type models with Fierz complete interactions indicate that in the low-temperature and large-density regime, other interaction channels than the (pseudo)scalar one become more relevant altogether [138, 139]. Thus, in the following quark-meson model study of the equation of state we do not employ dynamical hadronization techniques and postpone further investigations in this direction to future works.

Chapter 5

Nonperturbative Quark-Matter Equation of State

In this chapter we aim to derive a quark-matter equation of state within the quark-meson model and analyze the consequences of such an EoS for the structure of a nonrotating star. In contrast to many previous works using the mean-field approximation, we employ the FRG and thus inherently include additional nonperturbative effects due to quark and meson fluctuations. As shown in Sec. 4.3 those quantum and density fluctuations have significant impact in the vicinity of the phase transition and should not be neglected. In recent years, the application of the FRG method to neutron star matter has therefore experienced increasing interest [27, 167–170]. Moreover, we model a phase transition from hadronic to quark matter in order to investigate the possibility of hybrid stars. The separate consideration of two- and three-flavor versions of the model, see Sec. 4.2, allows to additionally study the impact of strangeness in compact objects. In the quark-matter core of a hybrid star, strange quarks might be suppressed due to their relatively large effective mass [171–174]. In addition, large effective strange-quark masses often destabilize hybrid stars with a strange-quark-matter core, leading to gravitational collapse [172, 173]. Calculating the EoS with the FRG, it becomes feasible to investigate the influence of quantum as well as density fluctuations on macroscopic observables for neutron stars such as the mass-radius relation in a systematic manner.

5.1 Beta Equilibrium and Charge Neutrality

In a neutron star, the assumption of isospin-symmetric matter, be it nuclear or quark matter, does not hold up anymore. To see this, let us consider quark matter and only two flavors at first. The assumption of local electric charge neutrality—such that the global charge of the star is ensured to vanish—demands a sufficient electron density to counter the net positive charge of matter with roughly the same number of up and down quarks. However, the weak interaction allows for β-processes trading electrons and up quarks for down quarks and vice versa. In all of these decays, (anti)neutrinos are produced, but their mean free path in cold neutron-star matter is large enough for them to leave the star [24]. Hence, in a stable star with densities reaching well above nuclear-matter density, we can assume beta equilibrium and neglect neutrinos. Including strangeness as well, the

equilibrium conditions lead to the flavor-dependent chemical potentials

$$\mu_u = \mu - \frac{2}{3}\mu_e \ , \quad \mu_d = \mu_s = \mu + \frac{1}{3}\mu_e \tag{5.1}$$

with the quark chemical potential $\mu = \mu_B/3$ which is related to the conserved baryon number, and the electron chemical potential μ_e which should rather be understood as coupling to (the negative of) the electric charge. The condition of charge neutrality,

$$\frac{2}{3}n_u - \frac{1}{3}n_d - \frac{1}{3}n_s - n_e = 0 \tag{5.2}$$

with the particle densities n_i, eliminates the freedom of choice for μ_e so that one ends up with one independent chemical potential. It is common in the literature to describe the electrons as a free fermi gas which we will do here as well. The contribution of a free fermi gas to the total pressure is given in Eq. (3.68) and the density follows as

$$n_e = \frac{(\mu_e^2 - m_e^2)^{3/2}}{3\pi^2}\,\Theta(\mu_e - m_e) \ . \tag{5.3}$$

Note that symmetric strange matter, i.e., matter with the same number of up, down, and strange quarks, is already electrically neutral. According to the *strange matter hypothesis*, such so-called *strangelets* could exist and be more stable than actual two-flavor nuclear matter if its density becomes large enough [175, 176]. However, the hypothesis is based on a simple bag model calculation for a free gas and thus the picture in the fully interacting theory is not clear [78]. Furthermore, as strange quarks are significantly heavier than up and down quarks, producing sufficient amounts of such matter against their constant weak decay presents a challenge. Casting aside this scenario, in conservative calculations for nuclear or quark matter there are less strange quarks than light quarks or even none of them, depending on the density range of the star. The beta equilibrium condition however favors a decrease of up-quark and electron density in favor of down (and possibly strange) quarks; as expected, nuclear matter in the star becomes more neutron rich.

We generally use the setup outlined in Sec. 4.3 and employ the two- and three-flavor quark-meson model in local potential approximation. The incorporation of different chemical potentials for each quark flavor has already been realized in the flow equations (4.24) and (4.26). Although isospin symmetry is broken in beta-equilibrated matter where $\mu_u \neq \mu_d$, we retain the approximation of only one light chiral condensate σ_l, i.e., we plug in $\sigma_3 \equiv 0$ for the expectation value of the splitting field. As both the $\langle \bar{u}u \rangle$ and $\langle \bar{d}d \rangle$ condensates are equal in the vacuum and become small upon chiral symmetry restoration, the error of this approximation is expected to be only noticeable close to the chiral phase transition. Note the pair of chemical potentials $\{\mu, \mu_e\}$ can be rewritten in terms of an isospin chemical potential μ_I that couples antisymmetrically to up- and down-quarks, i.e.

$$\mu_u = \mu' + \mu_I \ , \quad \mu_d = \mu_s = \mu' - \mu_I \ , \tag{5.4}$$

with $\mu' = \mu - \mu_e/6$ and $\mu_I = -\mu_e/2$. Furthermore, the conserved electric charge should also couple to the charged mesons, e.g., for $N_f = 2$ these are the two off-diagonal pions in flavor space. This would play a role in the case of pion condensation. Due to the Silver-Blaze property, however, for vanishing temperature pion condensation only appears for $\mu_I > m_\pi/2$ [177]. With the electron chemical potentials we found in our calculations, we

do not expect any significant amount of pion condensation and postpone a more in-depth analysis to future works. In the following, we present results for both symmetric and β-stable quark matter. Note that with this model, we consider nonmagnetized matter, but magnetic effects on the EoS are expected to play only a minor role for pulsars [178].

5.2 EoS for Quark and Hybrid Stars

In order to determine the equation of state $p(\varepsilon)$, or rather its inverse $\varepsilon(p)$, we again solve the flow equations for the $N_f = 2$ and $N_f = 2+1$ quark-meson model, Eq. (4.24) and (4.26). The EoS then follows thermodynamically as outlined in Eq. (4.39). A similar computation is made in the standard and renormalized mean-field approximations introduced in Ch. 4. The equations of state (EoS) for symmetric quark matter, i.e., for equal chemical potentials, obtained in MFAs and with the FRG, are compared to each other in Fig. 5.1a. Solid lines are the two-quark flavor findings and the dashed lines the corresponding three-flavor calculations. The numerical results are almost insensitive to the strange quark before the onset of the strange chiral phase transition around energy densities $\varepsilon \approx 550$ MeV/fm^3 but start to deviate thereafter, see Fig. 5.1a. In MFAs the transition is more gradually realized and the deviation is less pronounced than within the FRG. This can already be seen in Fig. 4.2b where the strange condensate in MFA decreases moderately for chemical potentials smaller than the strange-quark mass $m_s \approx 430\,\text{MeV}$. In the FRG curve there is a more rapid onset with a steeper slope around the strange-quark mass. Note that this behavior could also be related to a second phase transition in the light-quark sector that has been found in [33]. Furthermore, it is obvious that vacuum fluctuations reduce the slope of the EoS, i.e. the sound speed, and over most of the shown density range the EoS obtained in FRG has still a smaller slope, see Sec. 5.3.

With the inclusion of a free relativistic electron gas and the conditions for weak equilibrium and charge neutrality, cf. Eqs. (5.1) and (5.2), we obtain slightly modified EoS. The results for β-stable and neutral matter are presented in Fig. 5.1b. Differences to the result for symmetric quark matter are visible almost exclusively for $N_f = 2+1$ where the weak-equilibrium and charge-neutrality conditions render the population of strange quarks more favorable. Hence, the onset of strangeness is pushed to smaller energy densities, leading to a pressure reduction for a given energy density beyond the onset.

Note that our approximation with only one chiral light condensate σ_l for both up- and down-quark flavors yields in all cases degenerated up- and down-quark masses. As discussed in the previous section, for large μ the restoration of chiral symmetry in the light-quark sector suppresses both quark masses such that only small mass differences are expected there in contrast to the behavior in the vicinity of the chiral transition. The impact on the EoS might be more pronounced, and the small difference between symmetric and charge neutral matter in the two-flavor case might be an artifact of this approximation. A more detailed analysis of isospin breaking including a third chiral condensate is beyond the scope of this work and subject to future investigation.

In order to allow for a description of hybrid stars with a phase transition from hadronic to quark matter in the interior of the star, we combine the quark matter EoS with a nuclear one. The transition is achieved with a standard Maxwell construction[1] that maximizes the

[1] This assumes a high surface tension at the hadron-quark interface, see e.g. Ref. [179] for a discussion of this point in the context of a potential hadron-quark transition within hybrid stars.

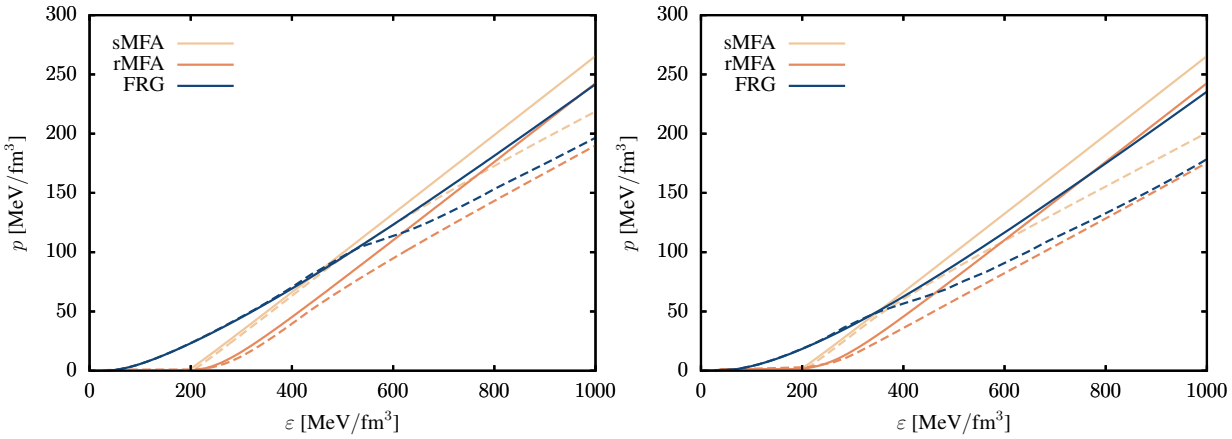

(a) Symmetric quark matter

(b) β-stable and neutral matter

Figure 5.1: Three different EoS of the $N_f = 2$ (solid) and $N_f = 2 + 1$ (dashed) quark-meson model at $T = 0$ for $m_l \approx 300$ MeV, $m_s \approx 430$ MeV and $m_\sigma = 560$ MeV.

pressure for a given chemical potential. For the nuclear EoS we consider some representative models compatible with several nuclear physics constraints as well as the maximum neutron-star mass and the GW170817 tidal deformability. Three of them are energy-density functional models, one is based on a nonrelativistic Skyrme parameterization, RG(SLy4) [180–182], and two are relativistic mean-field models, HS(DD2) [183, 184] and SFHo [185]. The BL EoS [186] is formulated in the framework of the Brueckner-Bethe-Goldstone many-body theory with chiral nuclear forces. In Fig. 5.2 a comparison of different nuclear EoS (dash-dotted lines) with the $N_f = 2$ (solid) and $N_f = 2+1$ (dashed) EoSs evaluated with the FRG respecting β-equilibrium and charge neutrality is given. We do not consider the FRG results as very realistic at low densities below $\mu_B/m_n \lesssim 1.2$, where a hadronic phase is expected. In addition, the attractive meson interactions in the QM model lead to a very high pressure for a given chemical potential in this range. We only present it for completeness. Disregarding the unphysical part of the QM EoS obviously all nuclear EoS except the HS(DD2) EoS produce higher pressure than the QM one at a given baryon chemical potential μ_B for the entire range of interest for compact stars. Hence, no hybrid stars could exist with these model combinations. The pressure of the HS(DD2) EoS intersects the two-flavor FRG pressure curve around $\mu_B/m_n \approx 1.38$ corresponding to the appropriate physical transition from nuclear to quark matter. By construction, the combination of the two-flavor QM EoS from the FRG with the HS(DD2) EoS leads to a first-order phase transition between the confined nuclear matter and the deconfined quark matter which is characterized by a discontinuity in the energy density.

This is observed in Fig. 5.3 which depicts the constructed hybrid $N_f = 2$ (DD2+QM2) and $N_f = 2 + 1$ (DD2+QM2+1) EoSs in comparison to the hybrid EoS QHC19 [187] and a parameterized EoS [82].[2] The QHC19 EoS features a smooth crossover quark-hadron transition. For the parameterized EoS the HS(DD2) EoS is used for the hadronic regime

[2]Note that all employed nuclear EoSs, the QHC19 EoS as well as our hybrid star EoSs with the FRG are available online in the CompStar Online Supernovae Equations of State (CompOSE) database [188], see `https://compose.obspm.fr/`.

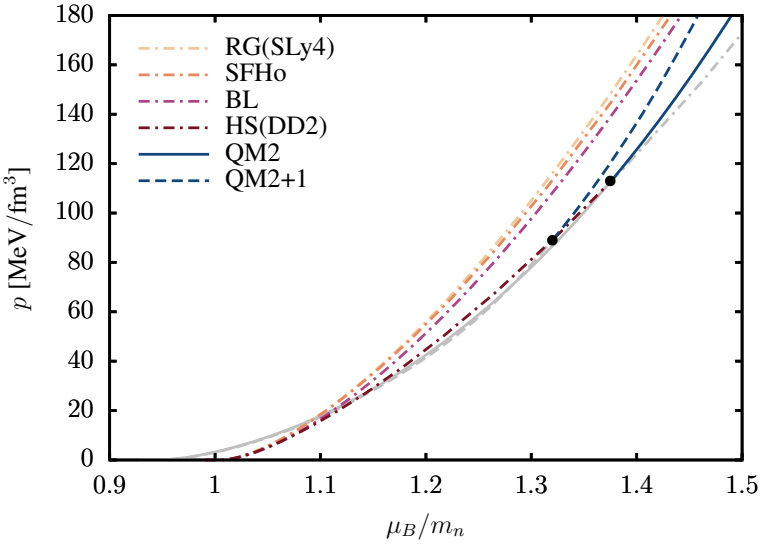

Figure 5.2: Pressure as a function of the baryon chemical potential in units of the neutron mass for various hadronic RMF models (dash-dotted) compared to the $N_f = 2$ (solid) and $N_f = 2+1$ (dashed) QM EoS in FRG (β-equilibrated and neutral quark matter). Intersections (black dots) of the quark-matter pressure with the HS(DD2) model at higher pressure are found while (unphysical) intersections at lower pressure are ignored, see text for details.

and the quark matter side is parameterized as

$$p(\varepsilon) = \begin{cases} p_c, & \varepsilon_c < \varepsilon < \varepsilon_c + \Delta\varepsilon \\ p_c + s\,[\varepsilon - (\varepsilon_c + \Delta\varepsilon)], & \varepsilon > \varepsilon_c + \Delta\varepsilon\ , \end{cases} \tag{5.5}$$

which describes a first-order transition at $\{\varepsilon_c, p_c\}$ with energy gap $\Delta\varepsilon$ and a constant slope $s = \partial p/\partial\varepsilon$, i.e., a constant quark matter sound speed squared, thereafter. Following the idea of Ref. [82], we choose $p_c = 1.89 \times 10^{35}$ dyn cm^{-2} and $\varepsilon_c = 9.02 \times 10^{14}$ g cm^{-3} which corresponds to $n_c \approx 3n_0$ and $\Delta\varepsilon/\varepsilon_c = 0.6$. For the slope, we consider two extreme parameterizations, one with $s = 1/3$ corresponding to the asymptotical QCD value, and one with $s = 1$ corresponding to the maximally allowed sound speed by causality. This ensures the onset of the phase transition at similar densities to those found in our hybrid construction with the two-flavor QM model. The size of the discontinuity of the energy density $\Delta\varepsilon$ determines the stability of the hybrid star against gravitational collapse: a large discontinuity destabilizes the star immediately at the transition point $p = p_c$ whereas for a small discontinuity a small quark core forms and the star remains stable. This scenario can be summarized in terms of the Seidov limit [189]

$$\frac{\Delta\varepsilon_{\text{thresh}}}{\varepsilon_c} = \frac{1}{2} + \frac{3}{2}\frac{p_c}{\varepsilon_c}\ . \tag{5.6}$$

$\Delta\varepsilon_{\text{thresh}}$ denotes here the threshold value below which a stable hybrid star branch is connected to a hadronic star branch. Thus, above the Seidov limit the sequence of stars become unstable immediately.

Even if $\Delta\varepsilon > \Delta\varepsilon_{\text{thresh}}$ and no continuous nuclear-hybrid branch exists, a so-called "third family" [190] stable sequence of hybrid stars, i.e., an additional branch of hybrid

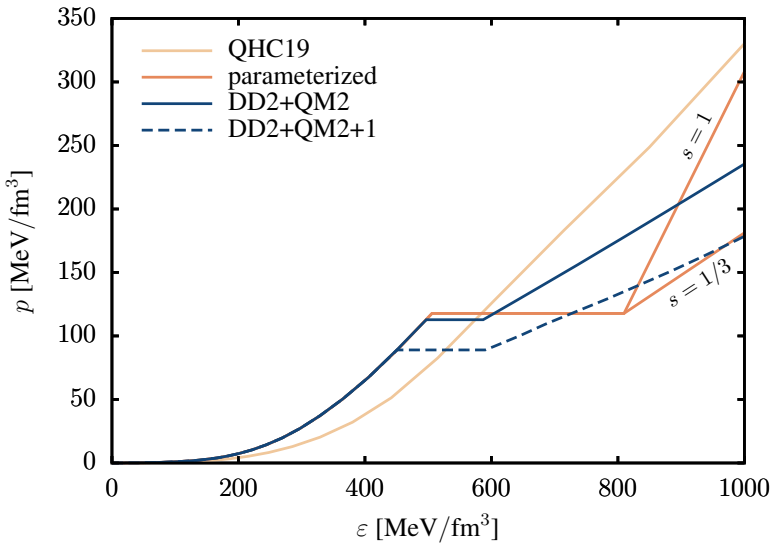

Figure 5.3: Composite EoS for the QM and DD2 nuclear model, cf. Fig. 5.2, compared with the hadron quark EoS QHC19 [187] and a combination of the HS(DD2) EoS with a parameterized quark matter EoS [82] for $c_s^2 \equiv s = 1$ or $1/3$, respectively. While the QHC19 model features a continuous quark-hadron transition, the others employ a Maxwell-constructed first-order transition and a discontinuity in the energy density ε.

stars with the same mass but different radius than their nuclear counterpart [191], may exist at higher central densities for certain conditions. Such twin-star configurations are found, for example, in studies with NJL quark matter including additional repulsive eight-quark interactions [192]. The conditions for the existence of such twin (or even triplet) configurations has been discussed in detail in Ref. [82], characterising the transition by the two parameters ε_c and $\Delta\varepsilon$ together with a constant-speed-of-sound parameterisation of the quark phase. Note that the large energy gap $\Delta\varepsilon/\varepsilon_c = 0.6$ is close to the Seidov limit and has been chosen to allow for a disconnected hybrid branch if the quark-matter EoS is stiff enough. A comparison of that parameterization to the FRG calculation in Fig. 5.3 reveals that the energy gaps in our construction are much too small to produce a disconnected second branch but favor a single connected hybrid-nuclear branch. In fact, our two-flavor hybrid model is well reproduced by values of $\Delta\varepsilon/\varepsilon_c = 0.18$ and $p_c/\varepsilon_c = 0.23$ and a constant $c_s^2 = 1/3$ on the quark-matter side. These values lie well within the region identified in [191] as that giving rise to a connected branch and are also well below the Seidov limit. Similar arguments show that the hybrid model with 2+1 flavors on the quark side again leads to a connected branch.

5.3 Speed of Sound

More information on dense matter can be gained through a detailed investigation of the speed of sound [193]. It measures the stiffness of the EoS for a one-fluid flow by the thermodynamic derivative of the pressure with respect to the energy density at constant entropy and particle numbers

$$c_s^2 \equiv \left.\frac{\partial p(\varepsilon)}{\partial \varepsilon}\right|_{S,N_i} \tag{5.7}$$

and can be identified as the speed of propagation of sound waves. Causality implies an upper bound $c_s^2 \leq 1$ and thermodynamic stability a lower bound $c_s^2 > 0$. For an ideal gas composed of point-like ultrarelativistic (massless) components the squared speed of sound is equal to one third, $c_s^2 = 1/3$. This is common to all systems with conformal symmetry of which an ideal massless gas is just an example. Even for any strongly interacting system the vanishing of the trace of the energy-momentum tensor, a feature of conformal theories, implies that the energy density is connected to the pressure by $\varepsilon = 3p$, hence yielding $c_s^2 = 1/3$ independently of density, temperature, or interactions. The speed of sound is decreased such that $c_s^2 < 1/3$ when a mass for the components is included or when (perturbative) interactions among the components take place. In the case of QCD at asymptotically high densities or temperatures, far exceeding the densities in the core of compact stars, a weak-coupling expansion is valid (pQCD) such that c_s^2 is expected to reach the conformal limit with increasing density from below [194]. This behavior is confirmed in QCD lattice calculations at finite temperature as well as at zero and small baryon chemical potentials [195].

The speed of sound has also been investigated in alternative theories for which, e.g., the AdS/CFT correspondence holds and where calculations in the strong-coupling limit are feasible, see Ref. [196]. It has been conjectured that c_s^2 is always bounded from above in such classes of strongly coupled field theories by the conformal value of $1/3$ [197] although recently counterexamples have been presented [198]. For more details of this conjecture see Ref. [194].

The speed of sound of the QM model in both mean-field approximations and the FRG calculation is found generally to be always smaller than $c_s^2 = 1/3$. An alternative scenario could be the presence of a bump in c_s^2 at intermediate densities before approaching the upper bound from below asymptotically and thus implying the existence of a maximum and a local minimum of c_s^2 as a function of the chemical potential. This scenario is supported by another recent FRG analysis including diquark condensation [27] where a maximum in c_s^2 above $1/3$ is found. The additional inclusion of vector interactions in the quark-meson model [199] is also expected to stiffen the EoS; this is further investigated in the next chapter.

Our result for the speed of sound of quark matter with a flavor-symmetric chemical potential is shown in Fig. 5.4a. In the $N_f = 2$ mean-field approximation (solid lines) the speed of sound converges to the limit $c_s^2 = 1/3$ while the addition of strange quarks (dashed lines) leads to a reduction of c_s^2 around scales of the strange chiral phase transition. This behavior has already been observed in Fig. 5.1a and is expected due to the additionally populated strange-quark states softening the EoS. In the FRG solution, the speed of sound is generally smaller than the asymptotic mean-field values beyond the transition which can be attributed to the quantum fluctuations captured within the FRG approach.

Furthermore, the strength of the first-order chiral phase transition (i.e., the gap in the order parameter) is found to correlate with the size of the jump in the speed of sound. Hence, the strong first-order transition in sMFA leads to a jump of c_s^2 close to its asymptotic Stefan-Boltzmann value $c_s^2 = 1/3$ which leads to the almost linear behavior of the EoS even at low pressure, see Fig. 5.1a. The more washed-out transition in rMFA induces an initially smaller slope of the EoS. This becomes more significant in the FRG calculation: due to an even smoother transition a comparably small gap $\Delta\varepsilon$ is found in Fig. 5.1a. In agreement with Fig. 5.4a the slope is consistently smaller than that of the mean-field calculations. For $N_f = 2 + 1$, c_s^2 is found to be sensitive to the numerical error caused by

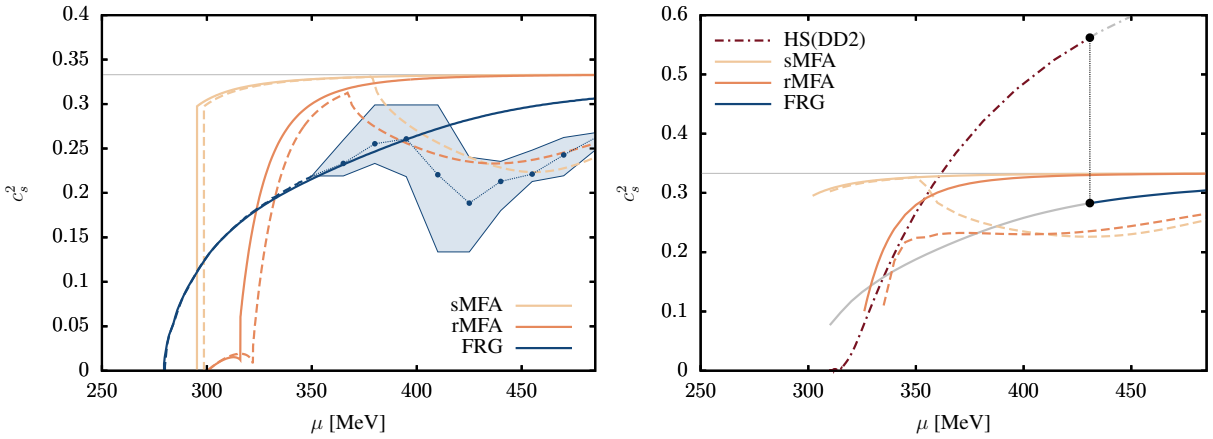

(a) Symmetric quark matter

(b) β-stable and neutral matter

Figure 5.4: Sound speed squared c_s^2 at zero temperature as a function of μ for three different quark matter EoS and the hadronic DD2 EoS (solid $N_f = 2$, dashed $N_f = 2 + 1$; left panel: flavor symmetric matter, right panel: β-equilibrated neutral matter). The thin horizontal lines indicate the Stefan-Boltzmann limit $c_s^2 = 1/3$. The vertical black-dotted line in the right panel illustrates the first-order transition from the hadronic HS(DD2) to the QM2 EoS, cf. Fig. 5.3. The metastable phases are extrapolated in gray color. For the blue error in the left panel band see App. H.

the employed solution method of the flow equation which leads to visible fluctuations at high μ. Therefore, Fig. 5.4a depicts for $\mu > 350\,\mathrm{MeV}$ averaged values in conjunction with error intervals displayed as blue band. For more technical details see App. H.

The speed of sound for β-stable and charge-neutral quark matter is displayed in Fig. 5.4b. Note that due to the usage of only one light condensate, the first-order transition cannot be resolved exactly in this approximation and hence the drop of the speed of sound to zero at low chemical potential is not shown. Due to the numerical uncertainties mentioned above, we postpone a careful $N_f = 2{+}1$ analysis to a future work. Qualitatively, we observe the same behavior as for a flavor-symmetric chemical potential. However, in mean-field approximation we find that the reduction of the speed of sound due to the onset of strangeness takes place at lower chemical potentials and more gradually than in symmetric quark matter. This is in agreement with the onset of strangeness already at small energy density, see Fig. 5.1b and the discussion in the previous section. In Fig. 5.4b we also show the speed of sound for the HS(DD2) nuclear EoS and indicate the transition point to quark matter in the DD2+QM2 EoS by a vertical line. As suggested in Ref. [200], this discontinuity in the speed of sound can be related to a δ-function singularity in the fundamental derivative, leading to possibly nonconvex thermodynamics.

5.4 Quark- and Hybrid-Star Solutions

In order to determine the influence of fluctuations on the mass-radius relation of a neutron star, we employ hydrostatic equilibrium solutions for a relativistic, spherically symmetric compact star composed of a perfect fluid, which have been derived from Einstein's equations by Tolman, Oppenheimer and Volkoff (TOV) [75, 76]. For a given EoS in terms of $p(\varepsilon)$, they yield a one-parameter curve of mass-radius relations, with the free parameter

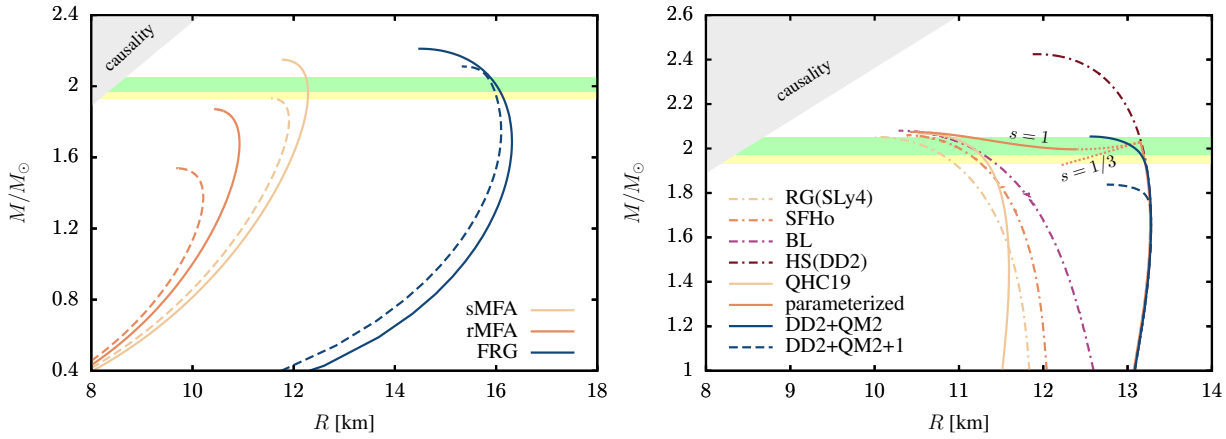

(a) Pure quark stars

(b) Hadronic (dash-dotted) and hybrid (solid, dashed) stars

Figure 5.5: Neutron star mass-radius relations for β-equilibrated and neutral matter. Left: pure quark stars for $N_f = 2$ (solid) and $N_f = 2+1$ (dashed). Right: purely hadronic stars (dash-dotted) obtained from various nuclear model EoS, cf. Figs. 5.2 and 5.3. Hybrid stars from the combined HS(DD2) model with the FRG solutions for QM (solid, dashed). Horizontal bands: PSR J1614-2230 (yellow) and PSR J0348+0432 (green) mass measurements [72, 73]. See text for details.

given by the central pressure p_0. For more details and a derivation of the TOV equation see App. B.

The mass-radius relations for the pure β-stable and charge-neutral quark matter EoS are shown in Fig. 5.5a for three different approximations. Please keep in mind that quark matter is not absolutely stable within our setup and that thus such pure quark stars could not exist. Nevertheless, we show the mass-radius relations since they are instructive to understand the impact of the fluctuations. Solid lines are the solutions for a two-flavor EoS and dashed lines the three-flavor results. In general, all three-flavor calculations yield a smaller maximum mass than the corresponding two-flavor results, which can be understood by the softening of the EoS due to the additional strange degrees of freedom. Only the two-flavor sMFA and both the two- and three-flavor FRG results yield a maximum mass above $2M_\odot$. Furthermore, the inclusion of the renormalized vacuum fluctuations in the rMFA in contrast to the sMFA leads to smaller masses and radii. The additional consideration of mesonic fluctuations via the full FRG computation increases the maximum mass even slightly beyond the sMFA result but also leads to significantly larger radii. The reason is that within the present FRG setup, the density jump at the surface is much smaller than in the MFA calculations, see Fig. 5.1b, such that the star becomes much less compact and can accumulate more mass. For the sake of completeness the causality constraint $R \leq 2.87M$ [24] is also displayed in the figure.

The mass-radius relations from the combined EoSs for a hybrid star with the $N_f = 2$ or $N_f = 2+1$ quark-meson matter side employing the FRG, respectively, and a hadronic phase parameterized by the HS(DD2) EoS are presented in Fig. 5.5b, labeled again as DD2+QM2 and DD2+QM2+1. For $N_f = 2$, the onset of quark matter leads to the visible separation of the DD2 and DD2+QM2 curves slightly below $M = 2M_\odot$ corresponding to a central baryon number density of approximately $0.47\,\mathrm{fm}^{-3}$. Below this value, the

hybrid star mass-radius relation coincides with the nuclear HS(DD2) one as it should. For $N_f = 2 + 1$, the DD2+QM2+1 curve exhibits a similar behavior, but the onset of quark matter occurs at a smaller baryon number density of approximately $0.43\,\mathrm{fm}^{-3}$. Thus, since the transition occurs well above nuclear saturation density, both hybrid EoSs satisfy constraints from nuclear physics as implemented in the HS(DD2) EoS. The maximum hybrid star mass of about $2.1M_\odot$ for $N_f = 2$ complies well with current observations, whereas the $N_f = 2 + 1$ curve does not satisfy the $2M_\odot$ limit. Since the quark-matter onset occurs only for masses slightly below $1.8M_\odot$ and higher, the value of the GW170817 tidal deformability obtained from both hybrid EoS does not change significantly with respect to the HS(DD2) value $\tilde{\Lambda} \approx 795$ for a mass ratio of 0.8 of the two coalescing stars.[3] It is in slight tension with recent LIGO/Virgo data [85, 201] but in agreement with the observation that the HS(DD2) EoS leads to a relatively large radius for intermediate mass stars. The QHC19 model leads to a radius smaller by almost 2 km. For comparison, the M-R relations for four different pure phenomenological nuclear models (dash-dotted lines) are also shown in Fig. 5.5b. As mentioned above, due to the small stiffness of the FRG quark matter EoS at high densities, a hybrid star construction with these nuclear EoS is not possible within the present setup.

As expected from Fig. 5.3, the parameterized EoS leads to a kink in the mass-radius relation at a mass slightly above the DD2+QM2 curve. Contrary to the connected hadronic and hybrid branches in the latter, the large energy gap of the $s = 1$ parameterized EoS leads to a disconnected hybrid branch and therefore twin stars at masses of about $2M_\odot$. For $s = 1/3$, the pressure in the quark-matter phase is not sufficient to counteract the strong gravitational pull due to the large energy density of the quark core [82] and thus does not support a stable hybrid star branch. Hence, we can rule out the occurrence of twin stars in our model due to the small energy gap at the phase transition from nuclear matter to quark-matter and due to the small stiffness of the quark matter EoS. In case of a Maxwell construction with parameters that feature a larger energy gap, there might not even be any stable hybrid stars with a QM model quark-matter description.

5.5 Conclusions

In this part of the work we have studied a nonperturbative quark-matter EoS based on the two- and three-flavor quark-meson model. Calculations have been done in two different versions of mean-field approximation and with the FRG. The aim of this setup was especially to estimate the impact of quantum and density fluctuations on the EoS for vanishing temperature. Since the different approximations of the grand potential were fixed to the same input parameters, our numerical findings are solely attributed to the impact of these fluctuations, with the exception of possible unphysical truncation effects in the FRG, see Ch. 7. As anticipated from studies of the phase diagram and confirmed by our investigations (see Ref. [155] and Ch. 4), fluctuations tend to smoothen the chiral phase transition. Within the EoS, the softening due to the appearance of strange quarks is therefore pushed to higher densities. Quark stars obtained from the FRG, including fluctuations in the quark matter EoS, have higher maximum masses and radii compared to their mean-field counterparts. Furthermore, we found that it is feasible to construct a hybrid nuclear-quark EoS, combining our FRG quark-matter EoS with a nuclear one via

[3] See Ch. 6 for a computation of the dimensionless tidal deformability and App. B for its derivation.

a Maxwell construction. The results for hybrid stars with a two-flavor quark matter core are in reasonable agreement with existing constraints. In contrast to many studies within the mean-field NJL model, see, for example, Ref. [173], our FRG EoS allows for gravitationally stable hybrid stars with a three-flavor core, which however leads to a maximum mass below the highest observed pulsar masses. Along with Refs. [27, 169, 170], this work constitutes one of the first constructions of a nonperturbative EoS for high densities within the FRG. However, several assumptions and approximations have been made, in particular:

(I) We have employed the quark-meson model, taking into account the (pseudo)scalar interaction channels. As discussed in Ch. 4, they are the dominant channels for chiral symmetry breaking at low densities, but they are expected to be insufficient at high densities [138, 139] and the addition of further four-quark generated channels might be necessary. The inclusion of a repulsive vector interaction is expected to additionally stiffen the quark-matter EoS and allow for the construction of hybrid stars with nuclear EoS leading to smaller radii and tidal deformabilities. Moreover, the wealth of possible different color-superconducting phases [70, 202] suggests the consideration of diquark-quark channels.

(II) We have modelled a first-order phase transition from baryonic matter to quark matter. In the latter, dynamical three-quark correlations are not included anymore. Especially at small temperatures, such correlations probably remain important. While the FRG has the general capability to include such interactions, it should be stressed that much work is still necessary to technically cope with this issue.

(III) Furthermore, the effect and origin of the back-bending of the chiral transition line should be settled. The resolution of this phenomenon might have a strong influence on the thermodynamics and thus the EoS at high densities.

Chapter 6

Vector-Meson Effects in Hybrid Stars

In the last chapter, we have studied the impact of fluctuations in the (pseudo)scalar interaction channel on the compact star EoS within the FRG framework. It was found that the fluctuations decrease the sound speed of the quark matter even below the mean-field value of $c_s^2 = 1/3$, leading to a rather soft EoS at high densities. This rather soft EoS does not allow for the construction of hybrid stars with a three-flavor quark core in agreement with present neutron-star mass measurements [72–74]. Therefore, here we will extend this work and investigate the impact of additional vector-meson interactions. While the (pseudo)scalar fields are integrated out within the functional renormalization group framework, the vector mesons are treated on a constant background level. This idea has already been employed to studies of the phase diagram at finite temperature, see e.g. Refs. [169, 203–205]. Vector interactions are expected to add repulsion [206]. This can be seen from classical models of the nucleon-nucleon interaction, from phenomenological models allowing for hyperons in the neutron-star core [207, 208], or from many phenomenological quark-matter studies [199, 209, 210]. The inclusion of a repulsive vector interaction in the quark-meson model should thus stiffen the quark-matter EoS, leading to a higher speed of sound and giving rise to hybrid stars compatible with observations. We continue to neglect the possibility of diquark pairing and do not enter the discussion of the extremely rich phase structure of color-superconducting matter in the density range of neutron stars.

6.1 Vector Mesons in Mean-Field Approximation

On top of the scalar and pseudoscalar fields in our chirally symmetric effective theory, we consider another N_f^2 vector and axial vector mesons each. With the usual $U(N_f)$ flavor transformation generators T_f^a with $a = 0, \ldots, N_f^2 - 1$ the (pseudo)scalar meson matrix is augmented by the (axial) vector one,

$$\begin{aligned} \Sigma &:= T_f^a(\sigma_a + \mathrm{i}\pi_a) && \text{for the (pseudo)scalar mesons and} \\ V_\mu &:= T_f^a(\rho_{a,\mu} + \mathrm{i}a_{1a,\mu}) && \text{for the (axial) vector mesons.} \end{aligned} \tag{6.1}$$

Accordingly, the field strength tensor field is given by $F_{\mu\nu} = \frac{\mathrm{i}}{g_v}[D_\mu, D_\nu] = \partial_\mu V_\nu - \partial_\nu V_\mu - \mathrm{i}g_v[V_\mu, V_\nu]$ with the canonical covariant derivative $D_\mu = \partial_\mu - \mathrm{i}g_v V_\mu$. For two quark flavors

we have the identifications $\rho_{a,\mu} = (\omega_\mu, \boldsymbol{\rho}_\mu)$ and $a_{1a,\mu} = (f_{1,\mu}, \boldsymbol{a}_{1,\mu})$ and for three flavors $\rho_{a,\mu} = (\omega_\mu, \boldsymbol{\rho}_\mu, \boldsymbol{K}_\mu, \phi_\mu)$ and $a_{1a,\mu} = (f_{1,\mu}, \boldsymbol{a}_{1,\mu}, \boldsymbol{K}_{1A,\mu}, f_{1,\mu})$.[1] The mesons interact via a scalar Yukawa coupling g_s and a vector coupling g_v with the quarks which is encoded in the quark-meson Lagrangian in Euclidean space

$$\begin{aligned}\mathcal{L} = \bar{q}\left[\partial\!\!\!/ + g_s T_f^a(\sigma_a + \mathrm{i}\gamma_5\pi_a) - \mathrm{i}g_v T_f^a \gamma_\mu(\rho_{a,\mu} + \gamma_5 a_{1a,\mu})\right] q \\ + \mathrm{Tr}(\partial_\mu\Sigma^\dagger\partial_\mu\Sigma) + \frac{1}{2}\mathrm{Tr}(F_{\mu\nu}F_{\mu\nu}) + U_\Lambda(\rho_1, \ldots, \rho_{N_f}) \\ - c_A\xi - \mathrm{Tr}\left[H(\Sigma^\dagger + \Sigma)\right] \ .\end{aligned} \tag{6.2}$$

Again, U_Λ denotes the chiral potential at the UV scale, ρ_i are the chiral invariants, and ξ is the $U(1)_A$ breaking term, cf. Sec. 4.2. Here, the explicit symmetry breaking has been encoded in the matrix H, i.e. $H = c_a T_f^a$ with c_0 the only nonzero entry for $N_f = 2$, and nonvanishing choices for c_0 and c_8 for $N_f = 2 + 1$ which lead to terms proportional to σ_l and σ_s in the rotated basis (4.14). Recent NJL-model studies treating the flavor-singlet and octet channels with individual couplings see a general stiffening of the equation of state by the former, but a softening at high densities due to the latter in a three-flavor setup [211, 212]; we will not be able to resolve this effect as we do not distinguish between the channels.

As a simplification, the vector mesons are now treated on a mean-field level in the Lagrangian (6.2), i.e., as static background fields such that their kinetic terms are not relevant anymore. Due to rotational symmetry all components of the vector-meson condensates except the temporal ones are assumed to vanish [25]. For three quark flavors the only nonvanishing vector fields are in principle the diagonal scalar fields, the isoscalar-vector fields ω and ϕ and the third isovector-vector field ρ_0^3. As in the previous chapter, we choose to neglect the isospin-breaking condensate σ_3 as an approximation. Hence, to be consistent within our approximation scheme we also omit the isovector-vector condensate ρ_0^3. For three quark flavors this yields finally a diagonal matrix in flavor space for the ω and ϕ vacuum expectation values

$$\langle V_\mu \rangle = \delta_{\mu 0}\frac{\mathrm{i}}{2}\mathrm{diag}_f(\omega, \omega, \sqrt{2}\phi) \ . \tag{6.3}$$

This also assumes an ideal quark mixing such that the quark content of the ω meson consists purely of up and down quarks while the ϕ meson is purely strange. Note that the additional factor of i stems from the Wick rotation, i.e., a real zero component of the vector field in Minkowski space becomes an imaginary one in Euclidean space. This in turn simplifies the Yukawa term in the quark sector of the Lagrangian

$$\mathcal{L}_{\mathrm{vec}} = \frac{g_v}{2}\bar{q}\gamma_0\mathrm{diag}_f(\omega, \omega, \sqrt{2}\phi)q \ , \tag{6.4}$$

which can now be interpreted as a shift in the corresponding chemical potentials, giving rise to modified effective chemical potentials

$$\begin{aligned}\tilde{\mu}_u &= \mu_u - \frac{g_v}{2}\omega \\ \tilde{\mu}_d &= \mu_d - \frac{g_v}{2}\omega \\ \tilde{\mu}_s &= \mu_s - \frac{g_\phi}{2}\phi\end{aligned} \tag{6.5}$$

[1] The two possible isoscalar-axial-vector states are $f_{1,\mu}(1285)$ and $f_{1,\mu}(1420)$.

with $g_\phi := \sqrt{2} g_v$. The constant vector-meson vacuum expectation values also contribute to the mean-field potential we choose as

$$U_{\text{vec}}^{(2+1)}(\omega, \phi) = -\frac{1}{2}\left(m_\omega^2 \omega^2 + m_\phi^2 \phi^2\right) \ , \tag{6.6}$$

wherein the negative sign expresses the repulsive nature of the vector interactions. The mass-like parameters m_ω^2 and m_ϕ^2 are basically unconstrained and not necessarily equal the physical ω- and ϕ-meson pole masses. They can be interpreted as the main contributions to the curvature masses, with the negative sign in the potential again originating from the imaginary condensate in Euclidean metric.[2] Nevertheless, we fix the parameters to the measured vector-meson masses $m_\omega = 782$ MeV and $m_\phi = 1020$ MeV such that the vector-meson coupling g_v is the only remaining free parameter of the system and of the order of one. For two quark flavors, only the ω meson is considered. For simplicity, in the following we will establish the $N_f = 2 + 1$ equations and suppress the flavor index. The two-flavor results arise in an obvious way.

The mean-field approximation can now be augmented with the FRG by adding the vector-meson potential U_{vec} to the scale-dependent chiral effective potential. For an arbitrary renormalization scale k, the total effective potential $\tilde{U}_k$ reads

$$\tilde{U}_k = U_k(\rho_1, \tilde{\rho}_2, \omega, \phi) + U_{\text{vec}}(\omega, \phi) - c_A \xi - c_l \sigma_l - c_s \sigma_s \ . \tag{6.7}$$

The respective condensates are determined in the infrared by solving the gap equations

$$\frac{\partial \tilde{U}_{\text{IR}}}{\partial \omega} = 0 = \frac{\partial \tilde{U}_{\text{IR}}}{\partial \phi} \tag{6.8}$$

where $\tilde{U}_{\text{IR}}$ denotes the fully-evolved effective IR potential including all dynamic quark and (pseudo)scalar-meson fluctuations. The condensates (i.e., the fields at the minimum of the potential) depend on the temperature and chemical potentials. The gap equations for the ω and ϕ condensates (6.8) can be rewritten

$$\omega + \frac{g_v}{2m_\omega^2}\left(\frac{\partial U_{\text{IR}}}{\partial \mu_u} + \frac{\partial U_{\text{IR}}}{\partial \mu_d}\right)\bigg|_{\text{gap}} = 0 = \phi + \frac{g_\phi}{2m_\phi^2}\left.\frac{\partial U_{\text{IR}}}{\partial \mu_s}\right|_{\text{gap}} \ . \tag{6.9}$$

The subscript "gap" in Eq. (6.9) labels the gap equation solution meaning that the potential is evaluated at the field configurations solving the corresponding gap equations. Thus, both gap equations for the vector condensates (6.9) are self-consistent and can be solved numerically by root finding. The thermodynamics are extracted from the infrared potential $\tilde{U}_{\text{IR}}$ in accordance with Eqs. (4.35)-(4.39). A specific role is played by the quark-number densities

$$n_f \equiv -\frac{\partial \Omega(T, \{\mu_f\})}{\partial \mu_f} = -\left.\frac{\mathrm{d}\tilde{U}_{\text{IR}}}{\mathrm{d}\mu_f}\right|_{\text{gap}} \qquad \text{for } f = \{u, d, s\} \ . \tag{6.10}$$

Since the implicit dependence of the infrared potential $\tilde{U}_{\text{IR}}$ on the chemical potentials through the condensates vanishes by virtue of the gap equation, i.e.

$$\left.\frac{\mathrm{d}\tilde{U}_{\text{IR}}}{\mathrm{d}\mu_f}\right|_{\text{gap}} = \left(\frac{\partial \tilde{U}_{\text{IR}}}{\partial \mu_f} + \frac{\partial \tilde{U}_{\text{IR}}}{\partial \omega}\frac{\mathrm{d}\omega}{\mathrm{d}\mu_f} + \dots\right)\bigg|_{\text{gap}} = \left.\frac{\partial \tilde{U}_{\text{IR}}}{\partial \mu_f}\right|_{\text{gap}} = \left.\frac{\partial U_{\text{IR}}}{\partial \mu_f}\right|_{\text{gap}} \tag{6.11}$$

[2] The actual curvature masses receive additional contributions from the scalar chiral potential as it depends on the vector condensates through the fermion loops in the FRG flow.

where the ellipses represent similar derivative terms for all other condensates, we can identify the derivative terms in Eq. (6.9) with the quark-number densities:

$$\omega - \frac{g_v}{2m_\omega^2}(n_u + n_d) = 0 = \phi - \frac{g_\phi}{2m_\phi^2} n_s \ . \tag{6.12}$$

Note that the gap equation (6.12) is solved including the full underlying nonperturbative contributions from the FRG in the (pseudo)scalar channel. This is in contrast to a similar two-flavor FRG study [204] where the gap parameter for the ω condensate is evaluated from a mean-field flow which ignores the back-coupling of the FRG flow. Furthermore, the inclusion of the vector mesons into the (pseudo)scalar sector appears solely by the replacement of the chemical potentials in the flow equation with the effective chemical potentials given in Eq. (6.5).

6.2 Quark Matter with Repulsive Vector Interactions

In the following we will present our findings obtained with the FRG quark-meson truncation including isoscalar-vector mesons for two and three quark flavors. All results are obtained for β-equilibrated and electrically charge-neutral matter. Since we are primarily interested in the physics of older neutron stars for which temperature effects can be neglected, all flow equations are strictly solved for vanishing temperature. We have employed two different and complementary numerical solution strategies for the flow equations as explained in App. H. The two-quark-flavor results are obtained with an upwind finite difference scheme while for the three-flavor calculations a two-dimensional grid of the two scalar field variables has been used. In principle, this enables us to estimate possible numerical artifacts. We found excellent agreement in particular at low chemical potentials with no strange quarks populated, showing the robustness of the numerical scheme.

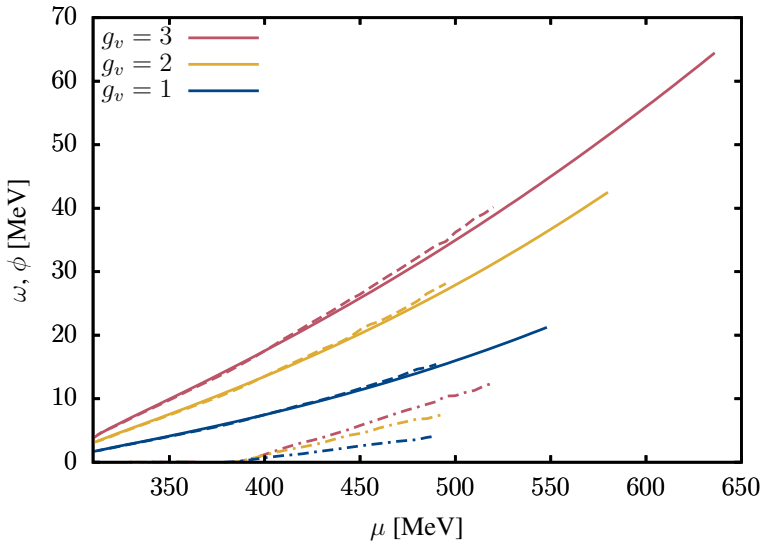

Figure 6.1: Vacuum condensates of the isoscalar ω meson (solid line: $N_f = 2$, dashed: $N_f = 2{+}1$) and ϕ meson (dash-dotted) as a function of the quark chemical potential. The condensates are evaluated for neutral matter in weak equilibrium with vector coupling g_v.

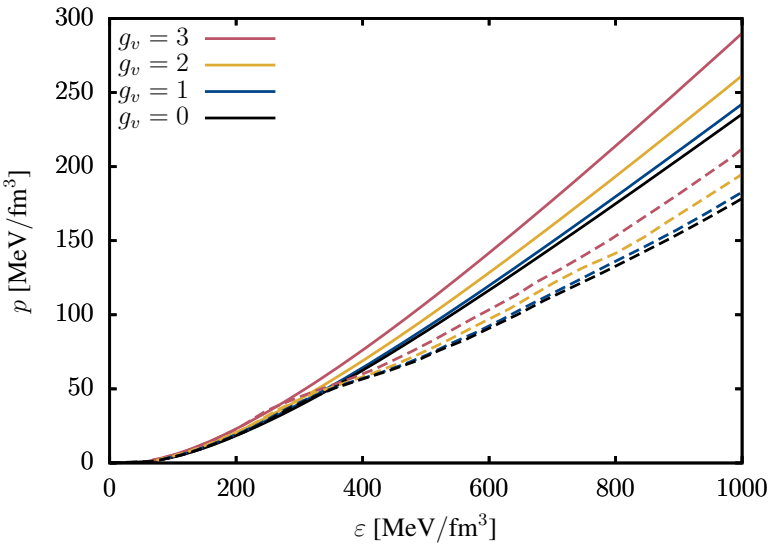

Figure 6.2: Equation of state of the FRG quark-meson model with vector mesons and coupling g_v. Weak-equilibrium and charge-neutrality conditions have been imposed. Solid lines correspond to $N_f = 2$ quark matter and dashed lines to $N_f = 2 + 1$.

This can be seen in Fig. 6.1 where the isoscalar ω- (dashed and solid lines) and ϕ-meson (dash-dotted lines) condensates for three different vector couplings as a function of the quark chemical potential are shown. The difference in the ω condensate with and without strangeness is negligible. From the gap equations (6.9) it is clear that the vector condensates are proportional to the (respective) number densities. Hence, for $T = 0$ the ω condensate vanishes in the chirally broken phase where all occupation numbers are zero, and the ϕ condensate (dash-dotted lines) is zero until $\mu \approx 400$ MeV when the strange-quark states get populated. Since an increase in a vector condensate means a decrease in the respective effective chemical potential(s), cf. Eq. (6.5), which in turn decreases the number density from its initial value, there is always a unique solution to the vector meson gap equations (6.9). Note that since the assumption of one light chiral condensate for both the up and down flavors breaks down close to the chiral phase transition under the assumptions of β-equilibrium and charge neutrality, see Ch. 5 and App. H, only data points above the chiral phase transition in the light scalar sector with $\mu > 310$ MeV are considered.

The effect of the background isoscalar-vector mesons on the equation of state is displayed in Fig. 6.2. In this figure the (normalized) pressure obtained with the FRG quark-meson truncation including the vector-meson condensates is displayed for different vector couplings g_v as a function of the corresponding energy density. As already mentioned, β equilibrium and charge neutrality have been implemented. The two-flavor EoS (solid lines) is stiffer than the corresponding EoS with strangeness (dashed lines) for energy densities beyond the onset of strangeness. This is not astonishing since an additional degree of freedom generally reduces pressure and thus softens the EoS.

Vector mesons contribute to the EoS with two effects. Firstly, since the vector-meson potential (6.6) gives a negative contribution to the grand potential, it follows from Eq. (4.36) that an increasing vector meson condensate leads to an increasing overall pressure. Secondly, at the same time the effective chemical potentials are lowered which reduces the

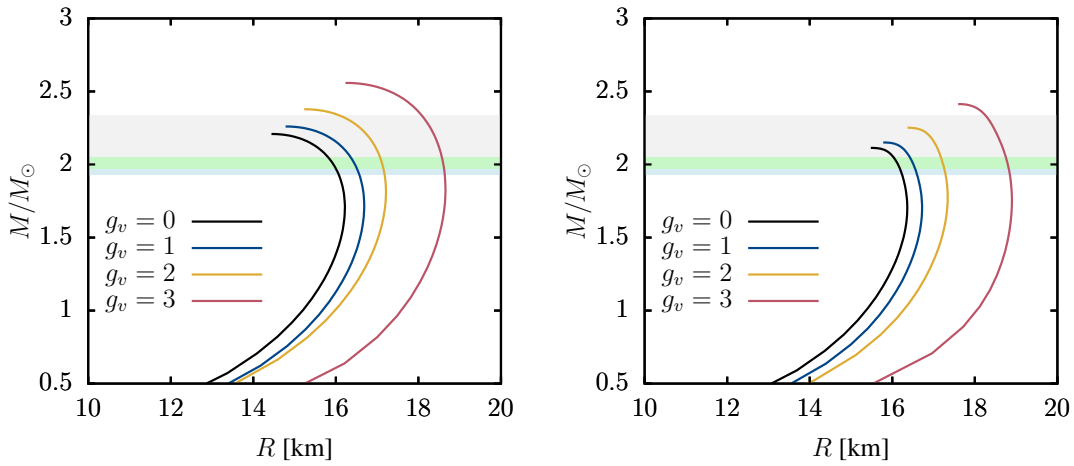

(a) $N_f = 2$ **(b)** $N_f = 2 + 1$

Figure 6.3: Mass-radius relations for pure quark-matter stars with various vector couplings g_v based on the EoS in Fig. 6.2. Horizontal bands: PSR J1614-2230 (blue), PSR J0348+0432 (green), and MSP J0740+6620 (gray) mass measurements [72–74].

contributions to the pressure and also the energy density via the particle densities from the (pseudo)scalar and quark sectors. Altogether, a larger vector coupling leads to an increase of the EoS's stiffness both for $N_f = 2$ and $N_f = 2 + 1$ quark flavors as expected.

As in Ch. 5, quark matter is not absolutely stable within our setup, but it is nevertheless instructive to investigate the mass-radius relation of quark stars with different strengths of the vector coupling. The results are summarized in Fig. 6.3, in the left panel for two-flavor quark matter and in the right panel for the three-flavor analogue. The colored horizontal bands indicate the measured two-solar-mass pulsars [72–74]. Increasing the vector coupling shifts the masses to larger values and increases the radii. Maximum masses are all compatible with observed pulsar masses, and radii are generally larger than current neutron star observations suggest [83, 84, 201, 213], even more so for nonvanishing vector couplings.

6.3 Quark- and Hybrid-Star Solutions

For a more realistic description, we will now turn to the construction of a hybrid-matter EoS. Note that while generally an increasing vector coupling increases the EoS's stiffness, the pressure decreases with increasing vector coupling for a given quark chemical potential. This can be explained by the aforementioned reduction of the effective chemical potential in the quark loop, leading to an overall pressure reduction for a given chemical potential. This has significant consequences for the possible occurrence of hybrid stars. We adapt the hybrid EoS construction method outlined in Ch. 5, also employing the HS(DD2) hadronic equation of state [183, 184] for the nucleonic phase and describing the quark-matter phase by the present FRG quark-meson EoS with additional vector-meson interactions.

The results are shown in Fig. 6.4 where the pressure as a function of the energy density is displayed (left panel for $N_f = 2$ and right panel for $N_f = 2 + 1$). Both phases are separated by a clear boundary and individually fulfill the weak-equilibrium and charge-

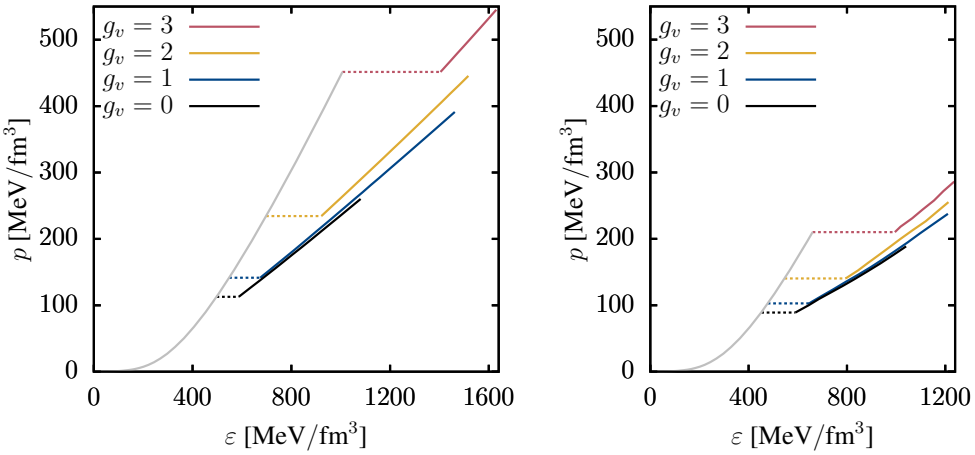

(a) $N_f = 2$

(b) $N_f = 2 + 1$

Figure 6.4: Equation of state for hybrid matter. The nucleonic phase is described by the HS(DD2) EoS (gray color) and the quark-matter phase by the FRG quark-meson EoS with vector mesons (see Fig. 6.2). Both phases separately meet weak-equilibrium and charge-neutrality conditions and are connected via a Maxwell construction. For $N_f = 2 + 1$, energy densities larger than $\varepsilon \sim 1200\,\mathrm{MeV/fm^3}$ corresponding to $\mu > 500\,\mathrm{MeV}$ are dropped.

neutrality conditions. A first-order transition is obtained via a Maxwell construction (horizontal dotted lines in the figure). It can be characterized by an onset energy density $\varepsilon_{\mathrm{trans}}$ in the hadronic phase and a gap $\Delta\varepsilon$ given by the difference between the energy density in the quark phase at the end of the transition and the onset $\varepsilon_{\mathrm{trans}}$. The onset energy density also defines the transition pressure $p_{\mathrm{HS(DD2),trans}} \equiv p_{\mathrm{HS(DD2)}}(\varepsilon_{\mathrm{trans}})$.

Due to the decreasing quark-matter pressure at increasing vector-interaction strength, the phase transition gradually moves to higher quark chemical potentials, i.e., to a higher intersection pressure and a higher $\varepsilon_{\mathrm{trans}}$. A glance back at Fig. 5.2 reveals that, against our previous speculation, the inclusion of vector interactions thus complicates the construction of a hybrid EoS with other nucleonic EoS besides the DD2 one. $\Delta\varepsilon$ also increases for increasing g_v. For $N_f = 2 + 1$, the transition generally occurs at lower pressures and with larger $\Delta\varepsilon$ than for $N_f = 2$ due to the additional strange degree of freedom in the quark-matter EoS. Note that all EoS displayed in Fig. 6.4 remain well below the Seidov limit (5.6). Since even with the inclusion of vector interactions $\Delta\varepsilon$ does not exceed the this limit and the sound speed is only insufficiently increased in the quark phase, the findings discussed for the case $g_v = 0$ remain valid for nonzero vector coupling. We thus confirm the conclusion made in the previous chapter that the occurrence of twin stars in our model is ruled out due to the small energy gap at the phase transition from nuclear matter to quark matter and due to the small stiffness of the quark-matter EoS.

The shift of the phase transition in a hybrid star to higher densities with increasing vector coupling can also be seen in the mass-radius relations, shown in Fig. 6.5 from the combined HS(DD2) and the present FRG quark-matter EoSs. An increase of the vector coupling leads to a continuously smaller quark-matter core in the hybrid star, but an increasing maximum mass. Especially for $N_f = 2 + 1$ (right panel), where without vector interactions the two-solar-mass limit cannot be satisfied, the maximum mass is in agreement with current observations for $g_v \gtrsim 1$. However, a quark-matter core is only

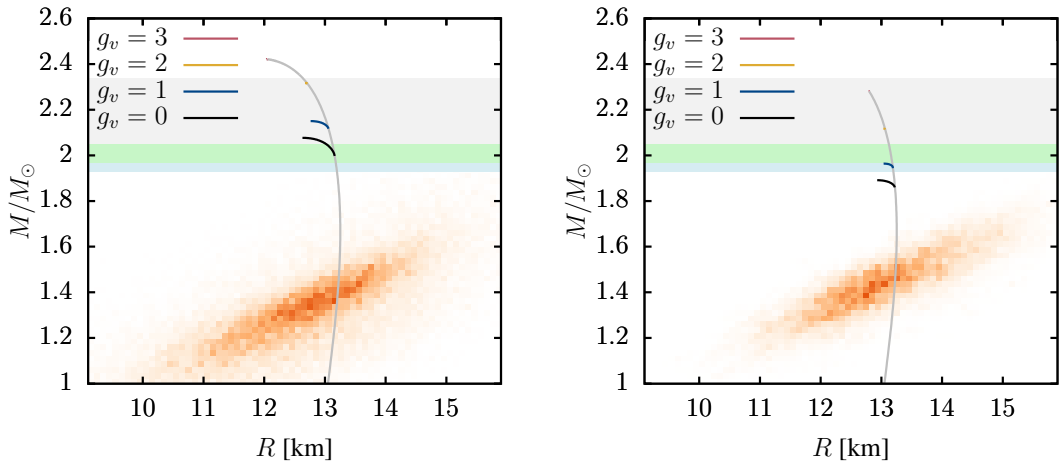

(a) $N_f = 2$ **(b)** $N_f = 2 + 1$

Figure 6.5: Mass-radius relations for hybrid stars from the combined HS(DD2) and quark-matter EoSs (see Fig. 6.4) for various vector couplings g_v. Purely nucleonic stars governed only by the HS(DD2) EoS are depicted in gray color. The horizontal bands are similar to Fig. 6.3. Additionally, the posterior probability distributions for the mass-radius correlations from the two independent recent NICER analyses are depicted (left panel: Riley et al. [83], right panel: Miller et al. [84]).

found as a small, continuous branch. For example, for $g_v = 1$ the $N_f = 2 + 1$ hybrid-star model yields for the heaviest stable star a quark-matter core with a radius of about 3.2 km, constituting approximately 4% of the star's total gravitational mass. For $g_v = 2$, the heaviest star's quark-core radius is 1.6 km and makes up only 0.6% of its total mass.

Below the onset of quark matter, the mass-radius relation coincides with the nuclear HS(DD2) one as it should. This means that the properties of stars with masses below 1.8 $M_\odot$ are given entirely by the HS(DD2) EoS. Among others, the HS(DD2) EoS leads to a relatively large radius for intermediate-mass stars which seems, although being in agreement with recent NICER results, to be disfavored by some radius determinations, see e.g. Ref. [213]. A hybrid construction with other nucleonic EoS leading to smaller radii could thus be appropriate. However, in Ch. 5 we found no intersection of the quark matter EoS with other such nucleonic EoS (see Fig. 5.2) since the nucleonic pressure over the entire relevant range exceeded the quark matter one for given chemical potentials. Since with increasing vector coupling, the pressure is reduced for given chemical potential, we confirm that we do not find hybrid stars that meet these criteria within the present FRG approach to the quark matter EoS.

6.4 Tidal Deformability

Another interesting quantity that is experimentally accessible is the tidal deformability of neutron stars. In the previous chapter we argued that the tidal deformability of hybrid stars will not differ much from the HS(DD2) one in the relevant mass region. Here, we will confirm this by an explicit calculation and additionally extract the tidal deformabilities of pure quark stars.

For a static, spherically symmetric star placed in a static external quadrupolar tidal

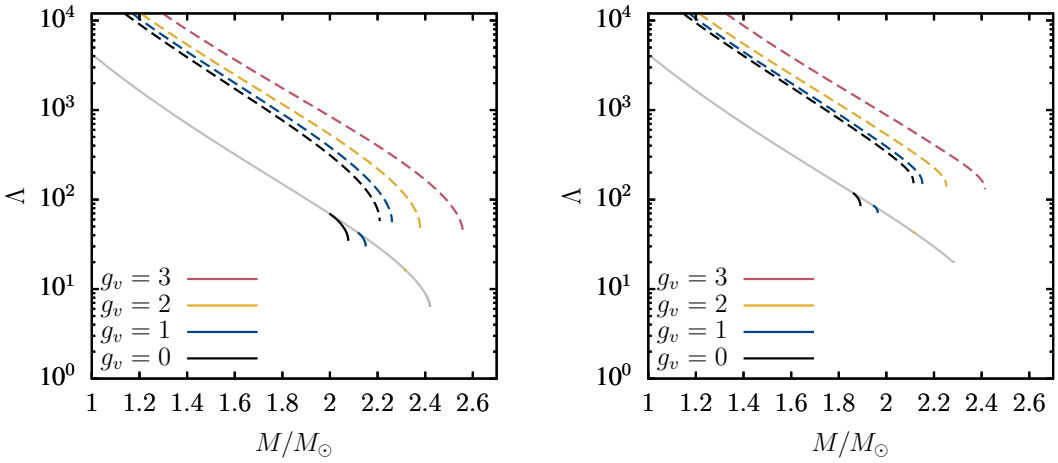

(a) $N_f = 2$ **(b)** $N_f = 2 + 1$

Figure 6.6: Dimensionless tidal deformabilities of pure quark (dashed lines) and hybrid stars (solid lines) with different vector couplings g_v as a function of gravitational mass. Similar to Fig. 6.5, the deformabilities of purely nucleonic stars are shown in gray.

field $\mathcal{E}_{ij}$, the tidal deformability λ can be defined to linear order as

$$Q_{ij} = -\lambda \mathcal{E}_{ij} \ , \tag{6.13}$$

where Q_{ij} represents the star's induced quadrupole moment. The tidal parameter λ can then be computed from a perturbation of the spherical TOV solution. An explicit derivation of the necessary modifications is given in App. B. The results for the dimensionless tidal deformability $\Lambda = \lambda/M^5$ as a function of the star's gravitational mass are shown in Fig. 6.6 for hybrid and quark stars with two and three quark flavors, respectively, and different values of the vector coupling. Note that first-order phase transitions lead to an additional term in the derivative of the metric perturbation right at the critical pressure as they feature a discontinuity in energy density [214], see App. B. This has an impact on the tidal deformabilities, but not the mass-radius relations. For quark stars such a hard surface exists right at the star's boundary $r = R$ whereas hybrid stars exhibit a first-order transition at the quark-hadron interface. In contrast to the published figure [2], these modifications are now included in Fig. 6.6. The additional term is found to increase the tidal deformability for pure quark stars, but has only negligible impact for hybrid stars.

Pure quark stars generally exhibit tidal deformabilities which are significantly too large compared with the GW170817 observations [85, 201].[3] This is also in line with findings from parameterized EoS's in Ref. [215]. As discussed before, we do not expect pure quark stars to exist within our setup. The hybrid-star tidal deformabilities only differ from the HS(DD2) ones close to their respective maximum masses, i.e., the quark cores are too small to have an impact on the tidal deformabilities for all stars of masses below about $1.8\,M_\odot$ or even higher, depending on g_v. As discussed before, the HS(DD2) tidal deformability is in slight tension with the GW170817 observations. A smaller tidal deformability thus requires a hybrid construction based on a different nucleonic EoS. However, such EoS typically also

[3]This holds even without the modification described just prior.

feature smaller radii and as we have already determined, this inhibits quark-matter cores altogether in the present setup.

6.5 Conclusions

We extended the previous study of the quark-matter equation of state based on the two- and three-flavor quark-meson model to include vector mesons. Quantum and density fluctuations of the quarks and the (pseudo)scalar meson channels are treated with the FRG and are dynamically coupled to the mean-field description of the (isoscalar) vector mesons. The impact of different vector-meson coupling strengths on pure quark stars as well as hybrid stars in β-equilibrated and neutral matter is analyzed. As before, the hybrid-star EoS is obtained from a combination of the FRG quark-matter EoS with a nuclear EoS via a Maxwell construction.

In general, an increase of the vector interaction increases the EoS's stiffness while the pressure decreases for a given chemical potential due to a reduction of the effective chemical potential in the quark loop. As a consequence, we observe higher maximum masses for both pure quark-matter as well as hybrid stars. For sufficiently large vector interactions, even three-flavor matter supports maximum masses consistent with experimental pulsar mass determinations. However, for increasing vector couplings quark-matter cores become smaller because the phase transition to quark matter is shifted to higher quark chemical potentials. The possibility of a second twin-star branch can be excluded even for the stiffest considered vector couplings with negligible quark core sizes in the continuous nuclear–hybrid branch. Furthermore, the tidal deformability is mainly determined by the nucleonic EoS and differs from it only in the vicinity of its maximum mass where a quark matter core forms. A hybrid construction with a different nucleonic EoS leading to smaller tidal deformabilities than the one of the HS(DD2) EoS is not possible within the present setup.

In total, regarding repulsive vector interactions the occurrence of hybrid stars with extensive quark cores seems to be disfavored, in particular in view of experimental restrictions on the masses, radii, and tidal deformabilities. Furthermore, many open issues still remain, one of which concerns the robustness of the FRG truncation.

Chapter 7

Regulator Effects at Nonzero Chemical Potential

In Ch. 4 we studied the phase diagram of the quark-meson model as a low-energy effective theory for QCD, with applications to neutron star physics in Chs. 5 and 6. While advances with the FRG towards astrophysics are relatively recent [25, 27, 167, 169], the spontaneous breaking of chiral symmetry and its restoration at finite density has been studied extensively within the quark-meson model in the past [33, 150, 155, 216]. A still open question, however, is posed by the strange back-bending behavior of the chiral transition line [33], see also Fig. 4.1, and the occurrence of negative entropy densities beyond the chiral transition first discussed in Ref. [34]. It is speculated that besides a truncation- or scheme-dependent artifact, this phenomenon could also be a hint of the FRG method towards an incorrect vacuum state, i.e., the existence of inhomogeneous phases or the formation of diquark condensates. In the following, we will attempt to solve this riddle by analyzing the regulator-scheme dependence of the high-density chiral phase transition.

7.1 Fermion Decoupling

First of all, we make some considerations concerning the decoupling behavior of fermions in LPA flows at nonzero chemical potential. In the typical picture of many-body physics, at vanishing temperature fermion states are fully occupied up to the fermi level defined by the chemical potential μ. Since quantum fluctuations can only occur at energies above the fermi level, a chemical potential acts as an effective infrared cutoff to the spatial-momentum integration in loop diagrams. In the context of FRG flows, this implies that at $k > \mu$ where the infrared regularization from the regulator is dominant and leads to fermion energies $E_k(\boldsymbol{p}) > \mu$ for all momenta, the vacuum flow is attained in accordance with the Silver-Blaze property. In contrast, at small scales $k < \mu$—given that the chemical potential is larger than the pole mass—the fermions eventually decouple from the flow as an increasingly large portion of momentum space is occupied by the fermi sphere. This can be seen explicitly in the simple flow structure obtained from a 3d regulator in LPA for a single (massive) fermion field, cf. Eq. (3.84). The step function $\Theta(E_k(\boldsymbol{p}) - \mu)$ cuts off all energies below the fermi level. However, the definition of the energy (3.85), and hence the decoupling behavior of the flow, is strongly dependent on the choice of the regulator shape function.

One simple case to be considered is the mass-like regulator $R_k^{\mathrm{CS,3d}}(\boldsymbol{p}^2) = k^2$ (or rather, its fermionic analogon, cf. Eq. 3.61). It leads to a divergent Callan-Symanzik type flow since the regulator does not vanish for large momenta and thus does not provide proper UV regularization. We will ignore this issue for now and deal with it later. Due the regulator's momentum independence, the dispersion relation is that of a free particle with additional squared mass k^2:

$$E_k^{\mathrm{CS}}(\boldsymbol{p}) = \sqrt{\boldsymbol{p}^2 + k^2 + m^2}\ . \tag{7.1}$$

With the following definition of the fermi momentum,

$$p_F := \begin{cases} \sqrt{\mu^2 - k^2 - m^2} & \text{if } \mu^2 > k^2 + m^2\ , \\ 0 & \text{else}\ , \end{cases} \tag{7.2}$$

the loop integral in Eq. (3.84) can be written

$$\int_{\boldsymbol{p}} \Theta\left(E_k^{\mathrm{CS}}(\boldsymbol{p}) - \mu\right) \frac{\boldsymbol{p}^2\ \left[1 + r_{\mathrm{CS}}^F(x)\right]\ \partial_t r_{\mathrm{CS}}^F(x)}{2E_k^{\mathrm{CS}}(\boldsymbol{p})} = \frac{k^2}{4\pi^2} \int_{p_F}^{\infty} \mathrm{d}|\boldsymbol{p}|\, \frac{\boldsymbol{p}^2}{E_k^{\mathrm{CS}}(\boldsymbol{p})} \tag{7.3}$$

where the infrared-cutoff property of the chemical potential becomes clearly apparent. The decoupling happens gradually as k is integrated downwards and p_F increases. Compared to the vacuum flow, the fermionic flow is therefore suppressed at scales $k^2 < \mu^2 - m^2$ (given $\mu > m$). A completely different result is obtained for the flat regulator (3.62). We find

$$E_k^{\mathrm{flat}} = \sqrt{k^2 + m^2} \tag{7.4}$$

for all relevant momenta smaller than the integral's UV cutoff at $\boldsymbol{p}^2 = k^2$. The energy becomes effectively momentum independent and momenta are always fully integrated out in an empty sphere of radius k:

$$\begin{aligned} \int_{\boldsymbol{p}} \Theta\left(E_k^{\mathrm{flat}} - \mu\right) \frac{\boldsymbol{p}^2\ \left[1 + r_{\mathrm{flat}}^F(x)\right]\ \partial_t r_{\mathrm{flat}}^F(x)}{2E_k^{\mathrm{flat}}} &= \frac{k^2}{4\pi^2 E_k^{\mathrm{flat}}} \Theta\left(E_k^{\mathrm{flat}} - \mu\right) \int_0^k \mathrm{d}|\boldsymbol{p}|\, \boldsymbol{p}^2 \\ &= \frac{k^5}{12\pi^2 E_k^{\mathrm{flat}}} \Theta\left(E_k^{\mathrm{flat}} - \mu\right)\ . \end{aligned} \tag{7.5}$$

As soon as E_k^{flat} falls below μ, the flow discontinuously jumps to zero. Given $\mu > m$, the corresponding scale is $k^{(\mathrm{disc})} = \sqrt{\mu^2 - m^2}$ and the flow, again, remains unaltered for $k > k^{(\mathrm{disc})}$. Since in LPA the momentum dependence of the propagator is always fixed by the canonical p^2 term plus the regulator function, in this truncation the flow has no way of compensating for the individual choice of regulator shape function. This almost arbitrary choice of decoupling behavior feeding into a complex back-coupled flow (which is the case when adding, e.g., bosons in the quark-meson model) can then lead to spurious, unphysical results that should be understood as regulator dependent truncation artifacts.

7.2 Setup and Regulator Choices

As outlined in the last section, possible regulator artifacts might be expected at small temperatures and nonvanishing chemical potentials. Therefore, we will test different regulator functions in the context of the two-flavor quark-meson model in LPA with the focus put especially on the back-bending property in the low-temperature phase diagram.

Regulator Choices

The three regulator functions considered cover both 3d and 4d versions of mass-like regulators that yield regularized Callan-Symanzik flows as well as the previously applied 3d flat regulator:

$$\text{(I)} \qquad R_k^{\text{mass,4d}}(p) = k^2\,\Theta(k_\phi^2 - p^2) \tag{7.6}$$

$$\text{(II)} \qquad R_k^{\text{mass,3d}}(\boldsymbol{p}) = k^2\,\Theta(k_\phi^2 - \boldsymbol{p}^2) \tag{7.7}$$

$$\text{(III)} \qquad R_k^{\text{flat,3d}}(\boldsymbol{p}) = (k^2 - \boldsymbol{p}^2)\,\Theta(k^2 - \boldsymbol{p}^2) \tag{7.8}$$

The same regulator is always employed for both the bosons and the fermions, using the respective fermionic analogon, cf. Eq. (3.61), in the latter case.

(I) The first regulator is of Callan-Symanzik type and does not exhibit any momentum structure besides the regularizing Θ-function. We therefore refer to it as a *mass-term* regulator. The constant mass-like term k^2 added to all momentum modes implies that high momenta are never fully integrated out and don't decouple at small scales in Callan-Symanzik type flows. This has been shown to lead to a comparably bad performance in the computation of critical exponents in vacuum [118]. However, since the momentum dependence of the effective loop propagator $(\Gamma_k^{(2)} + R_k)^{-1}$ is not modified by such a term, this regulator presents a good testing ground for our study and makes it a convenient choice for a 4d regulator as many issues of 4d regulators discussed in Sec. 3.6 can be circumvented. The problem of missing UV regularization is solved by introducing a step function that suppresses the regulator for four-momenta larger than the compositeness scale k_ϕ which serves as a UV scale for the theory; see Ref. [217] for an early application of this regulator function. It is comparable to a simple cutoff regularization in perturbation theory. At finite chemical potential, this momentum argument in the step function becomes a problem as an analytic continuation to complex frequencies is not possible. This continuation, however, is necessary for the Silver-Blaze property to hold, cf. the discussion in Sec. 3.6. We follow the arguments outlined in Ref. [217] and temporarily replace the Θ-function by a smeared-out version Θ_ϵ, assuming such a continuation now exists. The Matsubara sums can then be solved analytically and vacuum and thermodynamic contributions split up:

$$\partial_t U_k(\sigma^2, T, \mu) = \partial_t U_k^{\text{vac}}(\sigma^2) + \partial_t U_k^{\text{th}}(\sigma^2, T, \mu)\ . \tag{7.9}$$

The arguments are omitted when not explicitly needed and, as usual, derivatives with respect to σ^2 are denoted by a prime: $U_k' \equiv dU_k/d\sigma^2$ etc. The vacuum contribution is given by

$$\begin{aligned}\partial_t U_k^{\text{vac}} = k^2 \int_p \Theta(k_\phi^2 - p^2) \Bigg(&\frac{1}{p^2 + k^2 + m_\sigma^2} \\ &+ \frac{3}{p^2 + k^2 + m_\pi^2} - \frac{\nu}{p^2 + k^2 + m_q^2} \Bigg)\end{aligned} \tag{7.10}$$

with $m_\sigma^2 = 2U_k' + 4\sigma^2 U_k''$, $m_\pi^2 = 2U_k'$, $m_q^2 = (g\sigma/2)^2$, and $\nu = 4N_c N_f$. An analytical integration of the expression is possible and straightforward and not explicitly shown

here. The thermal part reads

$$\begin{aligned}\partial_t U_k^{\mathrm{th}} = k^2 \int_{\boldsymbol{p}} \Bigg(& \frac{n_B(E_\sigma, T)}{E_\sigma} + \frac{3 n_B(E_\pi, T)}{E_\pi} \\ & + \frac{\nu \left[n_F(E_q, T, \mu) + n_F(E_q, T, -\mu) \right]}{2 E_\psi} \Bigg)\end{aligned} \tag{7.11}$$

where the momentum arguments of the energies $E_i(\boldsymbol{p}) = \sqrt{\boldsymbol{p}^2 + k^2 + m_i^2}$, $i \in \{\sigma, \pi, q\}$, are omitted for convenience. n_B and n_F denote the standard Bose and Fermi distributions

$$\begin{aligned} n_B(E, T) &= \frac{1}{\mathrm{e}^{E/T} - 1} \ , \\ n_F(E, T, \mu) &= \frac{1}{\mathrm{e}^{(E-\mu)/T} + 1} \ . \end{aligned} \tag{7.12}$$

As an approximation, $k_\phi \to \infty$ in the thermodynamic contributions, formally sending the discontinuity of the step function to infinity. This works since thermodynamic fluctuations are naturally suppressed at high momentum modes and only the divergent vacuum flow must be regularized. Thus, any contributions from additional poles introduced by the smeared-out step function Θ_ϵ can be conveniently ignored.

(II) We next consider the three-dimensional version (7.7) of the mass-term regulator. As only the three-momentum is regularized, the vacuum part of the flow does not exhibit an $SO(4)$ symmetry anymore,

$$\partial_t U_k^{\mathrm{vac}} = \frac{k^2}{2} \int_{\boldsymbol{p}} \Theta(k_\phi^2 - \boldsymbol{p}^2) \left(\frac{1}{E_\sigma} + \frac{3}{E_\pi} - \frac{\nu}{E_\psi} \right) \ . \tag{7.13}$$

The thermal contribution is equal to the 4d version, Eq. (7.11), with the exception of the Θ-function cutoff which can now be included in an exact fashion as it only depends on spatial momenta.

(III) The flat regulator has already been examined in detail in Ch. 3 and all previous computations relied on it. It removes the spatial momentum dependence from the loop propagator, i.e., the energies become $E_i^2 = k^2 + m_i^2$. The step function $\Theta(k^2 - \boldsymbol{p}^2)$ cuts off all momenta above the scale k. Hence, in contrast to the Callan-Symanzik type flow, at any scale k fluctuations with (spatial) momenta larger than k have been completely integrated out. The momentum integrals can now be solved trivially:

$$\partial_t U_k^{\mathrm{vac}} = \frac{k^5}{12\pi^2} \left(\frac{1}{E_\sigma} + \frac{3}{E_\pi} - \frac{\nu}{E_q} \right) \ , \tag{7.14}$$

$$\begin{aligned}\partial_t U_k^{\mathrm{th}} = \frac{k^5}{6\pi^2} \Bigg(& \frac{n_B(E_\sigma, T)}{E_\sigma} + \frac{3 n_B(E_\pi, T)}{E_\pi} \\ & + \frac{\nu \left(n_F(E_q, T, \mu) + n_F(E_q, T, -\mu) \right)}{2 E_q} \Bigg) \ .\end{aligned} \tag{7.15}$$

Note that the combination of these two equations obviously recovers the flow used for the two-flavor quark-meson model throughout the thesis. The splitting is simply obtained from Eq. (4.26) by employing the relations $\coth(E/2T) = 1 + 2 n_B(E, T)$ and $\tanh((E - \mu)/2T) = 1 - 2 n_F(E, T, \mu)$.

Parameter Fixing

We have seen in Ch. 3 that only the flat (Litim) regulator is optimal in LPA according to the Pawlowski criterion (3.56). However, the first two (Callan-Symanzik type) regulators are not even optimized according to the less restrictive Litim criterion (3.50). Their flow equations in vacuum are numerically significantly harder to solve than the flow obtained from the flat regulator due to the close proximity of the pion energies to a pole. This issue is laid out in detail in App. G. It has therefore not been possible to find a quartic starting potential $U_\Lambda(\phi^2) = a\phi^2 + b\phi^4$ that leads to a numerically converging flow with sufficiently strong chiral symmetry breaking. Fortunately, a procedure has been outlined in Ref. [158] and [217] that allows the approximate calculation of coeffiecients in a power expansion of the effective potential in the chirally symmetric regime. The expansion can be used as a starting potential for the LPA flow at the chiral symmetry breaking scale k_χ. We briefly outline the procedure here and refer to App. F for the technical details.

Initially starting at some high UV compositeness scale k_ϕ, we consider flow equations in LPA', i.e., with a running meson wavefunction renormalization $Z_{\phi,k}$ and a running Yukawa coupling $\bar{g}_k$ evaluated at the minimum $\phi = 0$ of the UV potential. In the chirally symmetric regime, the mesons are heavy compared to the quarks. Thus, as an approximation we only consider the purely fermionic contributions to the flows. The Yukawa coupling becomes essentially self-driven and feeds into the flow of the meson wavefunction renormalization, cf. App. F. The corresponding solution for the dimensionless effective potential

$$u_k(\tilde{\rho}) := \frac{U_k(\phi^2)}{k^4} \tag{7.16}$$

exhibits a partial infrared fixed point. To avoid confusion with the notation and numerical fixed point values in Refs. [158, 217], we have formulated the dimensionless potential as a function of the dimensionless renormalized chiral invariant

$$\tilde{\rho} := Z_{\phi,k}\frac{\phi^2}{2k^2} \ . \tag{7.17}$$

Assuming the potential admits a power expansion around the origin,

$$u_k(\tilde{\rho}) = \sum_{n=0}^{\infty} \frac{1}{n!} u_k^{(n)}(0)\, \tilde{\rho}^n \ , \tag{7.18}$$

infrared-attractive solutions can be found for the combinations [158]

$$\frac{u_k^{(2)}(0)}{\bar{g}_k^2} \quad \text{and} \quad \frac{u_k^{(n)}(0)}{\bar{g}_k^{2n}} \quad \text{for } n > 2 \ . \tag{7.19}$$

The approximate flow solution holds for large RG scales k down to the vicinity of k_χ where $u_k^{(1)}(0)$ vanishes [158]. The coefficients $u^{(2)}_{k=k_\chi}(0)$, $u^{(3)}_{k=k_\chi}(0)$, $u^{(4)}_{k=k_\chi}(0)$ are set to their infrared fixed-point values and orders $n > 4$ are neglected. The order-zero coefficient is just a constant and can be ignored.

From k_χ downwards, the Yukawa coupling starts to freeze out. Hence, from there on the full flow is solved in LPA, i.e., for a fixed Yukawa coupling $g = \bar{g}_{k=k_\chi} = 6.5$ and no further field renormalization. For convenience, the bars indicating the renormalized terms can now be omitted. In principle, the only free parameter left is the symmetry breaking

	k_χ [MeV]	k_ϕ [MeV]	$(u_k^{(2)}/\bar{g}_k^2)_*$	$(u_k^{(3)}/\bar{g}_k^6)_*$	$(u_k^{(4)}/\bar{g}_k^8)_*$
mass, 4d	480	690	1	-0.00950	0.00475
mass, 3d	390	610	1	-0.00950	0.00475
flat, 3d	580	–	1	-0.02375	0.02078

Table 7.1: Chiral symmetry breaking and compositeness scales as well as the approximate infrared-attractive values in the chirally symmetric regime (marked by a star) for the three different regulators. Evaluation of the $u_k^{(n)}$ at $\tilde{\rho} = 0$ is implied. Note that the infrared solutions for the three- and four-dimensional mass-term regulators degenerate and the $n = 2$ fixed point is regulator independent; for details see App. F.

scale k_χ. It can be fixed to yield the correct amount of spontaneous symmetry breaking in the infrared by means of the pion decay constant, $\sigma_{\min} \approx f_\pi = 92.4\,\text{MeV}$. For the mass-term regulator, k_ϕ is an additional free parameter because the regulator explicitly depends on it via the step-function regularization. The correct combination of the two parameters is not so clear since, for example, the sigma mass seems to only weakly depend on it. We have chosen parameter sets that seem to lie in a physically acceptable region. All parameters are tabulated in Tab. 7.1. Note that the direct computation of the flow in vacuum was not possible for the mass-like regulators due to the previously mentioned issue with pion pole proximity (see App. G). Numerical treatment, however, was possible at small temperatures and chemical potentials shortly below the (pseudo)critical value μ_c and above. Thus, we were able to infer approximate vacuum solutions by extrapolating into the Silver-Blaze region. We could not determine the precise vacuum sigma mass for the mass-term regulators in this manner because it still strongly depends on μ close to μ_c, but in both cases we expect it to lie roughly at the value found for the flat regulator, $m_\sigma = 510$ MeV, within an error of about 40 MeV.

Furthermore, the starting potential at the scale k_χ is only independent of T and μ for sufficiently low temperatures; hence, this setup is only suited for applications at $T \ll k_\chi$ and intermediate chemical potentials $\mu < k_\chi$. As a final remark, we would like to emphasize that the assumption of sufficient memory loss of the initial values (i.e., close proximity to the fixed point) is not necessarily yet satisfied at the scale k_χ. Rather, the solutions given in Ref. [158] and the generalizations for mass-like regulators found in App. F indicate that the $t \to -\infty$ fixed point value is not nearly established for a ratio $k_\chi/k_\phi \approx 1/2$ which corresponds to an RG time of just $t \approx -\ln 2$. This is in clear opposition to the statements made in Ref. [158]. Nevertheless, we regard this procedure as a good choice for a testing ground, allowing for the comparison of different regulator schemes within a common setup and with only few free parameters.

7.3 Thermodynamics at Low Temperatures

With the setup described in the previous section, we focus the attention of this work on the phase boundary of the chiral phase transition at high densities. The requirement of low temperatures for the UV potential to stay largely invariant under changes in T or μ is thus fulfilled.

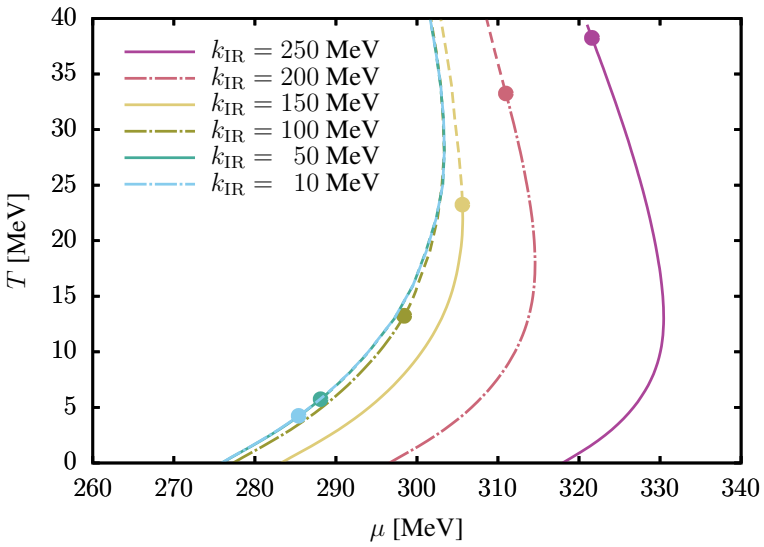

Figure 7.1: Infrared cutoff dependence of the chiral phase transition with the 3d flat regulator. Critical endpoints are marked by dots, solid and dash-dotted lines denote first-order and dashed lines crossover transitions.

Infrared Scale Dependence

One of the first questions concerns the impact of the finite infrared cutoff $k_{\mathrm{IR}} > 0$ introduced for technical reasons. In Fig. 7.1 the phase diagram for the 3d flat regulator is shown for a series of cutoff scales. Towards smaller cutoffs, i.e., the inclusion of more and more infrared fluctuations, the phase boundary moves to lower chemical potentials. This is easily explained by the fact that the infrared flow is dominated by the pions which tend to restore chiral symmetry. For $k_{\mathrm{IR}} \lesssim 100\,\mathrm{MeV}$, below the pion mass, the phase boundary becomes fixed. The critical endpoint, however, still moves towards lower temperatures. This is also not surprising, as it is already known that the location of the critical endpoint is sensitive to the mass of the sigma meson [65] which does not completely freeze out at low RG scales due to the running of the second derivative U_k''. Importantly, the familiar back-bending behaviour can be observed in this setup. Hence, as our setup differs significantly from previous works concerning the UV potential and starting point for the flow, the back-bending seems to be a general feature of the theory, truncation, and/or regulator in use. Furthermore, it occurs already at RG scales as large as 250 MeV and does not seem to be sensitive to the location of the critical endpoint: The back-bending extends even into the crossover region at small k_{IR}. Thus, it is also not a feature of missing IR physics. In the following, we will work with the fixed IR cutoff $k_{\mathrm{IR}} = 50\,\mathrm{MeV}$.

Regulator Effects

A comparison of the phase boundary of the 3d flat regulator to the ones obtained from the 3d and 4d mass-term regulators in Fig. 7.2 reveals that in the latter case, the phase boundary hits the μ-axis in a perpendicular angle. This is clear evidence that the back-bending behavior in LPA is related to the momentum structure of the employed regulator function. We furthermore find that in both the 3d and 4d versions of the mass-term regulator the

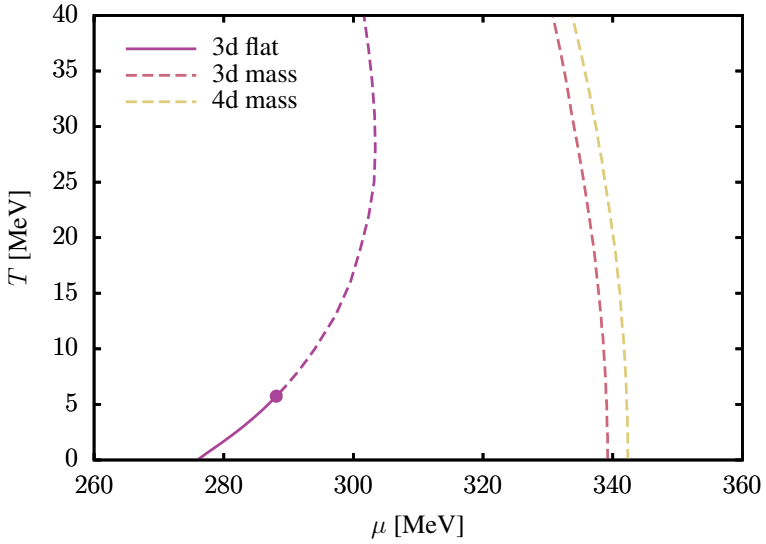

Figure 7.2: Regulator scheme dependence of the chiral transition for a fixed infrared cutoff $k_{\mathrm{IR}} = 50\,\mathrm{MeV}$. Critical endpoints are marked by dots, solid lines denote first-order and dashed lines crossover transitions.

transition is purely crossover even at $T = 0$ where it is located at the pseudocritial chemical potentials $\mu^{(\mathrm{cross,3d})} \approx 339\,\mathrm{MeV}$ and $\mu^{(\mathrm{cross,4d})} \approx 342\,\mathrm{MeV}$, respectively. In the chiral limit, a first-order transition at a much lower chemical potential only slightly above the vacuum quark mass was reported [217]; however, a different (exponential) regulator was employed in the bosonic sector in that work. We would like to stress that FRG studies using more elaborate truncations aided by QCD input [20] suggest the existence of a critical endpoint at a much lower chemical potential and higher temperature. The nonexistence of a critical endpoint here should therefore not be attached with too much physical interpretation. The crossover lines between the 3d and 4d versions of the regulator are separated by about 3 MeV. This difference is of purely quantitative nature and since no particular care was taken in exactly matching the chiral condensates from the starting parameters to better than ~ 1 MeV accuracy, some differences are to be expected and the use of 3d regulators seems to be an appropriate choice for the study of thermodynamics at finite μ. Therefore, we drop the 4d mass-term regulator in the following analysis and concentrate on the difference between the 3d mass-term and flat regulators.

The next question concerns the occurrence of a negative entropy density at small temperatures and chemical potentials beyond the phase transition. As evident from Fig. 7.3, this is confirmed in the back-bending case where an extensive region with negative entropy density is found. Negative entropy densities in this region are in agreement with the Clausius-Clapeyron relation

$$\frac{\mathrm{d}T_c}{\mathrm{d}\mu_c} = -\frac{\Delta n}{\Delta s} \tag{7.20}$$

which predicts that either Δn or Δs must be negative if the slope of a first-order transition is positive, see also Ref. [34]. As expected, the mass-term regulator does not lead to any negative entropy density in that region since there is no back-bending curvature of the transition line.

Naturally, it is desirable to understand the reason behind this phenomenon. It is clear

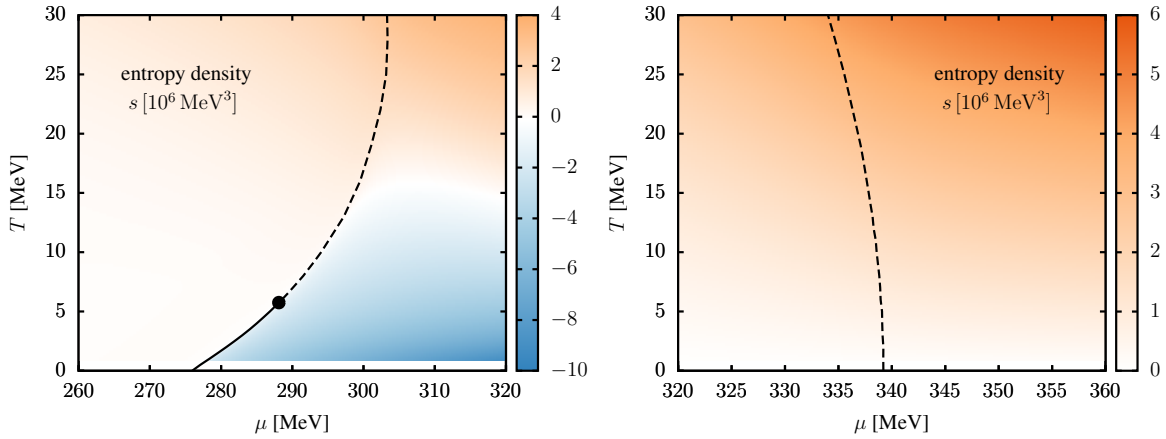

(a) 3d flat regulator. **(b)** 3d mass-term regulator.

Figure 7.3: Entropy density for the 3d flat (left panel) and 3d mass-term (right panel) regulators close to the chiral phase boundary. Blue colors denote negative values.

that when back-bending occurs, the transition line is highly sensitive to small changes in temperature. Therefore, in Fig. 7.4 we compare the effective infrared potentials $\tilde{U}_{\mathrm{IR}} := U_{\mathrm{IR}} - c\sigma$ for both 3d regulators at the infrared scale $k_{\mathrm{IR}} = 50\,\mathrm{MeV}$ for $T = 0$ and $T = 10\,\mathrm{MeV}$. We have chosen the respective (pseudo)critical chemical potentials for $T = 0$, cf. the figure caption. For the mass-term regulator, one recovers the expected behavior: with increasing temperature, the potential at small field values is slightly pushed to lower values, favoring the restoration of chiral symmetry, i.e., the transition line slightly shifts to smaller μ. For the flat regulator, the opposite behavior is observed. Increasing the temperature pushes the potential to larger values and supports the spontaneous breaking of chiral symmetry. Hence, the transition moves to larger μ, leading to the back-bending behavior.

These different effects on the potential, in turn, can be traced back to the momentum dependence of the fermion decoupling outlined in Sec. 7.1. Therefore, we again consider the fermionic part of the flow which is the only explicitly μ-dependent term. At vanishing temperature, the thermodynamic contribution partly (or completely) cancels out the vacuum flow. Let us recall the result for the Callan-Symanzik flow, Eq. (7.3), which is reproduced by the mass-term regulator up to the additional UV cutoff k_ϕ and multiplicity factors due color and flavor subspaces. It reads

$$\partial_t U_k^{F,\mathrm{mass}} = -\frac{\nu k^2}{4\pi^2} \int_{p_F}^{k_\phi} \mathrm{d}|\boldsymbol{p}|\, \frac{\boldsymbol{p}^2}{E_q} \tag{7.21}$$

with $E_q^2 = \boldsymbol{p}^2 + k^2 + m_q^2$ and the fermi momentum p_F defined in Eq. (7.2). As already discussed, the chemical potential serves as an effective infrared cutoff and the gradual occupation of quark states below the fermi surface drives the fermion decoupling. At finite temperatures, the sharp cutoff at p_F induced by the fermi distributions is smeared out, but since the UV cutoff of the integral k_ϕ is sufficiently large, the fermi distributions are completely integrated out in each loop. For the flat regulator, this decoupling is not

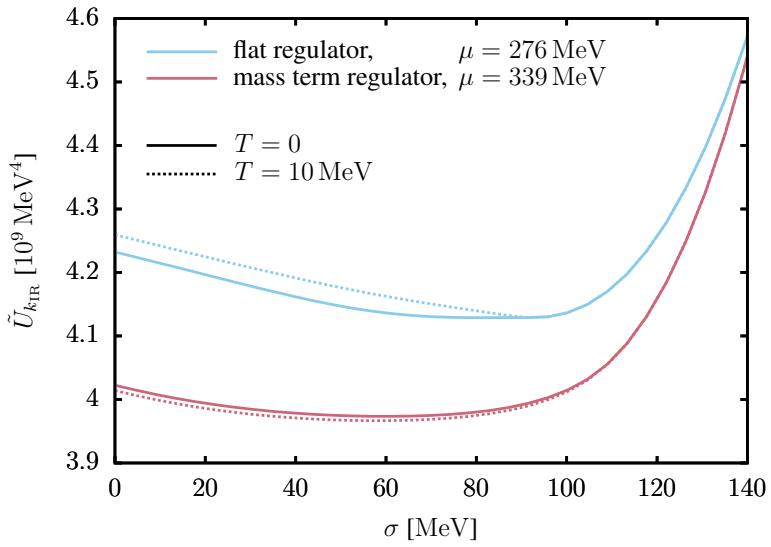

Figure 7.4: Evolved effective potential $\tilde{U}_\mathrm{IR}$ at $k_\mathrm{IR} = 50\,\mathrm{MeV}$ for $T = 0$ (solid) and $T = 10\,\mathrm{MeV}$ (dotted) as a function of the radial field mode σ for the 3d flat and 3d mass-term regulators. The chemical potential is fixed to the corresponding (pseudo)critical value at $T = 0$: $\mu^{(\mathrm{1st-order})} = 276\,\mathrm{MeV}$ for the flat regulator and $\mu^{(\mathrm{cross})} = 339\,\mathrm{MeV}$ for the mass-term regulator. For better comparability the potential obtained with the mass-term regulator has been shifted by a constant.

gradual but occurs at an instant in RG time:

$$\partial_t U_k^{F,\mathrm{flat}} = -\frac{\nu\, k^5}{12\pi^2}\,\Theta(E_q - \mu) \tag{7.22}$$

with $E_q^2 = k^2 + m_q^2$. The fermi distribution is not integrated out in the momentum loop anymore, but instead present in the fermionic flow.

A visualization of this is given in Fig. 7.5. The flow $\partial_t U_k$ as well as its bosonic and fermionic components are shown for $\sigma = 0$ and the same temperatures and chemical potentials as in Fig. 7.4. While for the mass-term regulator (right panel) the fermion decoupling happens smoothly and the sensitivity to a temperature variation is small, the step-function discontinuity in the fermionic flow for the flat regulator (left panel) is very prominent. At finite temperature, the step function smears out and leads to strong variations of the fermionic flux. Since the flow equation is a partial differential equation, this variation couples back into the bosonic flow: the stronger the fermionic fluctuations are, i.e., the more negative U_k' becomes, the stronger the bosonic fluctuations become as the propagator pole at $U_k' = -k^2/2$ (cf. App. G) comes closer. However, the bosons cannot completely mimic the fermion behavior and become weaker at $T = 10\,\mathrm{MeV}$ compared to $T = 0$. Hence, with increasing temperature the total net flow becomes more fermionic, i.e., features a tendency for larger chiral symmetry breaking. This only holds at low overall temperatures but leads to the unphysical back-bending in that region.

A similar reasoning can also be applied to the occurrence of negative entropy densities, effectively connecting those two phenomena. Explicitly writing down the flow equation for the partial derivative of the potential with respect to the temperature which, evaluated at

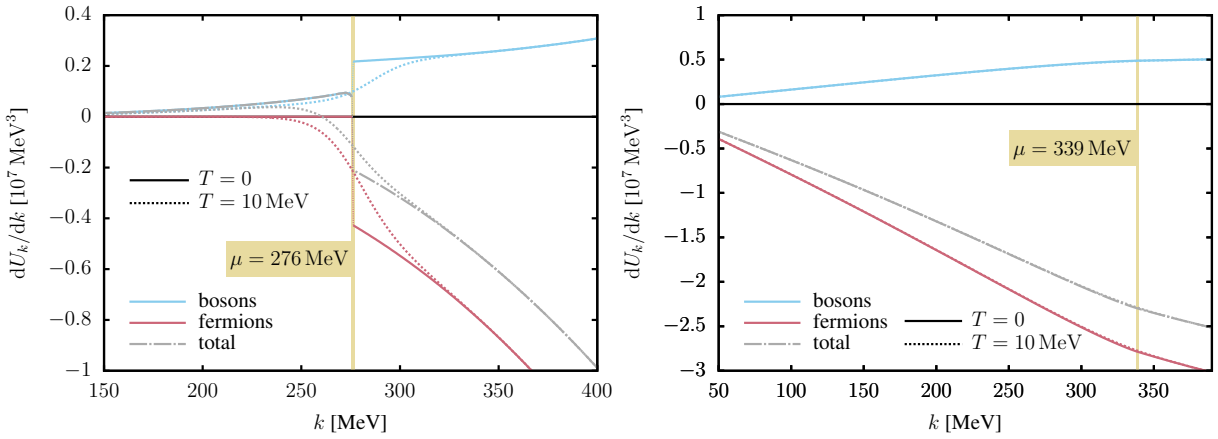

(a) 3d flat regulator.

(b) 3d mass term regulator.

Figure 7.5: Total FRG flow and its bosonic and fermionic components for $T = 0$ (solid and dash-dotted) and $T = 10\,\mathrm{MeV}$ (dotted) at $\sigma = 0$ as a function of the RG scale k. Chemical potentials are chosen as in Fig. 7.4. Note the different scalings on the figure axes.

the minimum, yields the entropy density, we find[1]

$$\partial_t \frac{\partial U_k^{\mathrm{flat}}}{\partial T} = \frac{k^5}{12\pi^2}\left\{ \frac{\nu}{4E_q T^2}\left[\frac{E_q-\mu}{\cosh^2\left(\frac{E_q-\mu}{2T}\right)} + \frac{E_q+\mu}{\cosh^2\left(\frac{E_q+\mu}{2T}\right)}\right] + \sum_b \left[\frac{1}{2T^2}\frac{1}{\sinh^2\left(\frac{E_b}{2T}\right)} - \left(\frac{1}{2T}\frac{1}{\sinh^2\left(\frac{E_b}{2T}\right)} + \frac{1}{E_b}\coth\left(\frac{E_b}{2T}\right)\right)\frac{1}{2E_b^2}\frac{\partial m_b^2}{\partial T}\right]\right\}. \tag{7.23}$$

The sum takes into account all bosons, i.e., one sigma meson and three pions. In the limit of small temperatures all terms smoothly vanish, with two exceptions: Firstly, the back-coupling term $\partial m_b^2/\partial T$ which incorporates derivatives of $\partial U_k^{\mathrm{flat}}/\partial T$ with respect to the fields survives as $\coth(E_b/2T) \to 1$ for $T \to 0$. Secondly, close to the fermi surface where $E_q \approx \mu$ the first term will give nonvanishing contributions because for any positive temperature there is a small region of energies where the argument $(E_q - \mu)/(2T)$ of the cosh-function is suppressed. The latter can be seen as a source term to the back-coupled flow, i.e., the negative entropy density is also created around a sharp fermi surface in the flow. In the case of a mass-term regulator, such contributions close to the fermi surface are washed out by the momentum integration when positive contributions from $E_q \gtrsim \mu$ cancel with negative contributions from $E_q \lesssim \mu$.

These are clear indications that the arbitrary choice of momentum structure in the regulator leads to issues in local potential approximation at low temperatures and finite chemical potential. Since the decoupling behavior of the fermions at increasing chemical potential, and thus the fermionic flow, strongly depends on the regulator choice, such regulator dependencies are expected to be present in the result of truncated flows. In an exact flow such issues cannot occur as the Wetterich equation guarantees the freedom of choice of

[1]Note that in this work, the entropy density was determined in practice by numerical differentiation of the grand potential, not solving the associated flow equation.

regulator functions that fulfill the criteria listed in Ch. 3. As an example, in renormalized mean-field approximation (see Ch. 4) where only the fermion loop is solved and bosonic back-couplings are neglected, the results become (up to cutoff effects) regulator independent. This might be counter-intuitive at first since the fermion loop is the one inducing the back-bending behavior in the truncated case. However, the important observation is that the differences between the integrated fermionic flows at different temperatures, i.e., the total areas between the fermionic $T = 0$ and $T = 10\,\mathrm{MeV}$ curves in Fig. 7.5, are actually regulator independent. Those are the results obtained in mean-field approximation where—due to the missing back-coupling—the differential equation degenerates to an integral. As soon as potential derivatives are introduced and the truncated flow is described by a partial differential equation, this argument fails. The back-bending therefore originates in the bosonic response to the strongly temperature-dependent fermionic flux. Further, because the LPA truncation keeps the momentum structure of the two-point function fixed, generically $\Gamma_k^{(2)}(p) = p^2 + m_k^2$, the Wetterich equation cannot compensate for the particular choice of momentum dependence for $R_k(p^2)$. It might therefore be plausible that such regulator effects do not occur in a truncation allowing—at least to some degree of approximation—for momentum-dependent wavefunction renormalizations $Z_k(p)$. An investigation of this matter is adjourned to future works.

7.4 Conclusions

In this chapter, the regulator scheme dependence of functional renormalization group equations was investigated. The phase diagram of the quark-meson model at high densities was therefore explored with three different regulators. The focus is put on the issue of the back-bending of the chiral transition line at small temperatures and a negative entropy density in the chirally restored region which has been observed in recent years. In light of a large interest in the solution of effective theories at high densities, the understanding of such phenomena in the FRG ansatz is crucial.

We found that the back-bending is most probably not related to cutoff artifacts such as the finite infrared cutoff as it remains a feature throughout large variations of k_{IR} for the popular optimized flat (Litim) regulator. Furthermore, the choice of a 3d regulator also does not seem to be an issue beyond small quantitative errors, which follows from a comparison of the 3d and 4d versions of simple mass-term regulators. It should be stressed that the back-bending issue has also been observed for the flat regulator in related theories such as a parity doublet model [218], i.e., it is not limited to the particular choice of quark-meson model. However, the simple mass-term regulators which lead to Callan-Symanzik type flows do not exhibit any negative entropy density or back-bending behavior in the phase diagram.

This is clear evidence that those two connected phenomena are scheme-dependent truncation artifacts at the level of LPA, induced by a sharp fermi-sea cutoff in the fermionic flow. The decoupling of the fermions at small temperatures depends strongly on the momentum structure of the loop integrals. In LPA, this structure is fully determined by the choice of regulator shape function. Therefore, different shape functions lead to vastly different decoupling behaviors that feed back into the truncated bosonic flow. For the flat regulator, a strong temperature dependence of the fermion flow due to the smearing of the fermi surface is found at low temperatures which is in agreement with the large curvature

of the back-bending transition line. In contrast, the fermi distributions are fully integrated out with the mass-term regulators, leaving only minor changes of the threshold functions with temperature in alignment with thermodynamic expectations.

Another possible scenario is that the back-bending could be an actual effect due to missing vacuum states such as inhomogeneous phases, but the mass-term regulator—which is not optimized and expected to lead to poorer overall convergence of couplings compared to the flat regulator—just cannot capture this phenomenon. However, since our analysis clearly connects it with the bosonic response to scheme-dependent changes in the fermion flows at the fermi surface, we consider this scenario to be extremely unlikely.

Chapter 8

Summary and Outlook

The theory of the strong interaction still poses many open questions concerning the state of matter especially at intermediate to high densities. Due to its inaccessibility by first-principle methods so far, for the description of physics in the cold and dense region of the QCD phase diagram effective theories and models have to be relied upon. Among others, such model studies suggest the possible existence of a wealth of different spatially inhomogeneous and color-superconducting phases [67]. The only observable objects in our universe that contain stable matter of comparable density are compact stars, reaching up to several times nuclear-matter density. Observations of macroscopic neutron-star properties such as high-mass determinations [72, 73, 219] or the GW170817 tidal deformability [85, 201] can help us put constraints on the underlying equation of state. However, many approaches in the literature use simple approximations neglecting quantum and density fluctuations which could have a significant impact on the EoS and the corresponding neutron-star properties.

Therefore, the main goal of this thesis was the examination of fluctuation effects at high densities in a nonperturbative setup. Based on an effective quark-meson truncation in two and three quark flavors, the equation of state for β-equilibrated and neutral quark matter was determined in three different approximations, namely two mean-field approaches—one of which includes vacuum fluctuations—and a functional renormalization group study in local potential approximation. With the FRG method, important fluctuations in the (pseudo)scalar meson channel are added in a systematic manner. The impact of the different approximations on the macroscopic properties of quark-matter stars was found to quite large in general. Vacuum fluctuations induced by the quark loop already at the level of mean-field approximation decrease both the masses and radii of quark stars such that the two-solar-mass limit cannot be reached anymore, even if only the two lightest quark flavors are considered. The additional inclusion of fluctuations in the attractive (pseudo)scalar meson channel via the FRG increases the maximum mass again but leads to significantly larger radii excluded by recent NICER measurements [83, 84] . As expected, the consideration of strange quarks always leads to a softer equation of state and smaller maximum masses. We find that the combination of our quark-matter EoS with the HS(DD2) nuclear EoS [184] via a Maxwell construction, simulating a sharp first-order boundary between the nucleonic and quark phase, allows for the existence of hybrid stars with a continuous nuclear–quark-matter branch in the mass-radius diagram. However, with the inclusion of strangeness the maximum hybrid-star mass drops below $2M_{\odot}$.

Consequently, the model was extended to incorporate repulsive vector-meson inter-

actions. While the effective vector-meson potential is treated on a mean-field level, the vector mesons still dynamically couple to the full flow of the (pseudo)scalar interactions via an effective chemical potential in the quark threshold function. A large vector coupling is found to increase the stiffness of the EoS and allow for the existence of hybrid stars with masses above $2M_\odot$ even for $N_f = 2 + 1$, albeit with very small quark-matter cores. An analysis of the dimensionless tidal deformability reveals that it is too large for quark stars to comply with the GW170817 measurement, which is also in accordance with their large calculated radii. Furthermore, the measured value tends to favor a nucleonic EoS that leads to smaller radii than the HS(DD2) one, but a hybrid construction with a different nucleonic EoS that lead to smaller tidal deformabilities was not possible since the quark-matter equation of state generally is not stiff enough. Against expectations, this could not be remedied by the inclusion of vector mesons. Thus, based on our analysis the existence of extensive quark-matter cores in compact stars is unlikely.

It should be stressed, however, that one needs to be careful about drawing conclusions based on such quantitative statements as there are still many issues to be resolved: The role of many-body quark correlations relevant for a more realistic description of dense matter—such as residual six-quark correlations in the quark phase—is still basically unknown. In terms of bosonized four-quark interactions, the picture looks somewhat more promising: First FRG studies that take diquark channels expected to be relevant at high densities [138, 139] into consideration have come up recently [27, 167, 220] and can be built upon. Nevertheless, without clear experimental input finding an appropriate effective theory able to make quantitative predictions remains a daunting task. Importantly, the robustness of the employed FRG truncation must also be verified, especially in light of the observed unphysical thermodynamic effects, namely the back-bending of the chiral transition line [33] and the occurrence of negative entropy densities [34].

To this end, a second part of this thesis concerns truncation effects at and beyond the level of LPA. Current state-of-the-art approaches taking into consideration field-independent wavefunction renormalizations and a running Yukawa coupling were presented and some of their issues like the occurrence of complex threshold functions at nonzero temperature and chemical potential discussed. Generally, a better understanding of the field dependence of higher-order couplings seems necessary to allow for serious estimates on the quality of the truncation. Finally, the back-bending phenomenon in LPA was related to the employed regulator scheme. While the back-bending is present for the widespread flat (or Litim) regulator, it vanishes along with the negative entropy densities for the choice of simple Callan-Symanzik type regulators. Oddly, the critical endpoint also vanishes in a setup with explicitly broken chiral symmetry and the transition becomes purely crossover. Further analyses revealed that the unphysical behavior is induced by a regulator-dependent decoupling behavior of the fermions at finite chemical potential. While all modifications cancel out in the integrated fermion flow and thus do not lead to issues in mean-field approximation, the back-coupling into the truncated bosonic flow in the partial differential equation leads to spurious contributions to the result. Thus, the most likely explanation for the back-bending phenomenon seems to be that of a scheme-dependent truncation artifact at the level of LPA.

Of course, one of the pressing questions is in which way these artifacts influence the properties of the quark-matter equation of state and other results obtained at low temperatures and finite density. A large impact can be expected, especially since the chiral transition is now crossover. Unfortunately, the simple application of Callan-Symanzik type

regulators towards the determination of the equation of state faces technical difficulties, with flows running too closely to the pion pole in the chirally broken regime. Moreover, the parameter fixing procedure employed in this work uses a very low effective UV scale which inhibits calculations at large chemical potential. There are two possible roads to remedy these issues in the future: First, an improvement of the truncation to allow for a better resolution of momentum structure in the propagator, e.g., via momentum-dependent wavefunction renormalizations, could possibly reduce such truncation errors and allow for the continued use of the flat regulator. Second, the possibility of other regulator options that also do not lead to back-bending artifacts must be explored. Specifically, even hybrid regulator setups using, for example, the flat regulator for the bosonic fields and Callan-Symanzik type regulators for the fermions are thinkable. With these issues resolved, the functional renormalization group can become an important tool leading to powerful predictions even for cold and dense matter.

Appendix A

Basics, Notation, and Conventions

Necessary basic definitions, conventions, and particularities in the notation are summarized in this appendix.

Units

In all parts of this work related to quantum field theory we use the natural units

$$c = \hbar = k_B = 1 \tag{A.1}$$

where c denotes the speed of light, $\hbar$ the reduced Planck constant, and k_B the Boltzmann constant. In this framework, all relevant quantities can be expressed in terms of (positive, zero or negative) dimensions of energy. Typically, results are given in (powers of) mega-electronvolts (MeV). In the general relativity parts, specifically Sec. 2.2 and App. B, we employ geometric units

$$c = G = 1 \tag{A.2}$$

where G is Newton's gravitational constant. Here, all quantities can be expressed in dimensions of length. In Chs. 5 and 6, neutron star radii are given in kilometers. As a notable exception, numerical results for pressure and energy density are expressed in $\mathrm{MeV/fm^3}$.

Metric and Dirac Fields

Throughout the quantum field theory parts of the thesis, we use Euclidean metric $g_{\mu\nu} = \delta_{\mu\nu}$. Starting with physical quantum fields that are assumed to live in Minkowski space $g_{\mu\nu} = \eta_{\mu\nu}$ and the signature choice $(+,-,-,-)$ prevalent in hadron physics, we formally obtain the Euclidean action S from the Minkowski one S_M via a Wick rotation to *imaginary time* $\tau = \mathrm{i}t$, e.g.

$$\begin{aligned} \mathrm{i}S_M[\varphi] &= \mathrm{i}\int_{-\infty}^{\infty} \mathrm{d}t \int_{\boldsymbol{x}} \frac{1}{2}\left[\left(\frac{\partial\varphi}{\partial t}\right)^2 - (\nabla\varphi)^2 - m^2\varphi^2\right] \\ &= -\int_{-\infty}^{\infty} \mathrm{d}\tau \int_{\boldsymbol{x}} \frac{1}{2}\left[\left(\frac{\partial\varphi}{\partial \tau}\right)^2 + (\nabla\varphi)^2 + m^2\varphi^2\right] =: -S[\varphi] \end{aligned} \tag{A.3}$$

for a real scalar field φ. Spacetime indices always go from 0 to 3 regardless of the choice of metric. The effective metric signature obtained from this rotation is purely negative;

to compensate this, a minus sign was pulled out of the definition of the Euclidean Lagrangian. Dirac fermions are described in Minkowski space by four-component bispinors. Mathematically, they consist of two Weyl spinors

$$\psi = \begin{pmatrix} \psi_L \\ \psi_R \end{pmatrix} \tag{A.4}$$

and transform under the $(\frac{1}{2}, 0) \oplus (0, \frac{1}{2})$ representation of the Lorenz group $SO(1,3)$, or rather its double cover $\mathrm{Spin}(1,3) \simeq SL(2,\mathbb{C})$ [221]. The Weyl spinors can be identified with left-handed and right-handed helicity of a particle, respectively. They can be extracted from the bispinor ψ by means of the projection operators

$$P_L := \frac{\mathbb{1} - \gamma_5}{2} \ , \quad P_R := \frac{\mathbb{1} + \gamma_5}{2} \tag{A.5}$$

with $\gamma_5 := \mathrm{i}\gamma_M^0\gamma_M^1\gamma_M^2\gamma_M^3$. The γ_M^μ are 4×4 traceless complex matrices which obey the anticommutation relations

$$\{\gamma_M^\mu, \gamma_M^\nu\} = 2\eta^{\mu\nu}\mathbb{1}_{4\times4} \ . \tag{A.6}$$

From these, a Lorentz-invariant Lagrangian can be constructed, e.g., for a massless Dirac fermion:

$$\mathcal{L}_M = \bar{\psi}(\mathrm{i}\partial_\mu\gamma_M^\mu - m)\psi \tag{A.7}$$

where $\bar{\psi} := \psi^\dagger\gamma_0$ is the Dirac adjoint. We follow the same procedure as above to obtain the Euclidean Lagrangian

$$\mathcal{L} = \bar{\psi}(\partial_\mu\gamma^\mu + m)\psi \tag{A.8}$$

with the zero derivative now defined as $\partial_0 := \partial_\tau$ and the modified gamma matrices given by $\gamma^0 = \gamma_M^0$, $\gamma^i = -\mathrm{i}\gamma_M^i$ for $i = 1 \ldots 3$ such that they obey

$$\{\gamma^\mu, \gamma^\nu\} = 2\delta^{\mu\nu}\mathbb{1}_{4\times4} \ . \tag{A.9}$$

γ_5 remains unaltered, i.e., in the Euclidean setup it reads $\gamma_5 = \gamma^0\gamma^1\gamma^2\gamma^3$. We do not need to specify any representation for the gamma matrices because all necessary calculations can be performed abstractly by means of trace identities. The fermion fields are Grassmann valued, i.e., they anticommute: $\psi_i(x)\psi_j(y) = -\psi_j(y)\psi_i(x)$, where i and j denote individual field components. In general relativity calculations, cf. App. B, the metric generally describes curved spacetime, and asymptotic flat spacetime is represented by the Minkowski metric $\eta_{\mu\nu}$ with signature $(-,+,+,+)$.

Unitary Groups

The group elements of $SU(N)$ (i.e., the unitary $N \times N$ matrices with determinant 1) are generated by the exponential map

$$U = \mathrm{e}^{-\mathrm{i}\theta^a T_a} \tag{A.10}$$

with the $N^2 - 1$ Hermitian traceless basis elements T_a in the fundamental representation satisfying

$$\mathrm{tr}(T_a T_b) = \frac{1}{2}\delta_{ab} \tag{A.11}$$

and $\theta^a \in \mathbb{R}$. They generate the $\mathfrak{su}(N)$ Lie algebra with the commutation relations

$$[T_a, T_b] = \mathrm{i}f^{abc}T_c \ . \tag{A.12}$$

In the adjoint representation, the matrix elements of the generators are given by the structure constants f^{abc}:

$$(T_a)_{bc} = -\mathrm{i} f^{abc} \ . \tag{A.13}$$

The larger group $U(N) \simeq [U(1) \times SU(N)]/\mathbb{Z}_N$ is obtained by adding an additional basis element T_0 with nonvanishing trace in the fundamental representation. T_0 is fully determined by demanding it to be proportional to the unity matrix and to integrate into Eq. (A.11). For $U(2)$, the generators are given by $T_a = \tau_a/2$ with $\tau_0 = \mathbb{1}_{2\times 2}$ and the Pauli matrices

$$\tau_1 = \begin{pmatrix} 0 & 1 \\ 1 & 0 \end{pmatrix} \ , \quad \tau_2 = \begin{pmatrix} 0 & -\mathrm{i} \\ \mathrm{i} & 0 \end{pmatrix} \ , \quad \tau_3 = \begin{pmatrix} 1 & 0 \\ 0 & -1 \end{pmatrix} \ . \tag{A.14}$$

For $U(3)$, the generators are $\lambda_a/2$ with the normalized zero element and the Gell-Mann matrices

$$\begin{aligned}
&\lambda_0 = \sqrt{\frac{2}{3}} \begin{pmatrix} 1 & 0 & 0 \\ 0 & 1 & 0 \\ 0 & 0 & 1 \end{pmatrix} \ , \quad \lambda_1 = \begin{pmatrix} 0 & 1 & 0 \\ 1 & 0 & 0 \\ 0 & 0 & 0 \end{pmatrix} \ , \quad \lambda_2 = \begin{pmatrix} 0 & -\mathrm{i} & 0 \\ \mathrm{i} & 0 & 0 \\ 0 & 0 & 0 \end{pmatrix} \ , \\
&\lambda_3 = \begin{pmatrix} 1 & 0 & 0 \\ 0 & -1 & 0 \\ 0 & 0 & 0 \end{pmatrix} \ , \quad \lambda_4 = \begin{pmatrix} 0 & 0 & 1 \\ 0 & 0 & 0 \\ 1 & 0 & 0 \end{pmatrix} \ , \quad \lambda_5 = \begin{pmatrix} 0 & 0 & -\mathrm{i} \\ 0 & 0 & 0 \\ \mathrm{i} & 0 & 0 \end{pmatrix} \ , \\
&\lambda_6 = \begin{pmatrix} 0 & 0 & 0 \\ 0 & 0 & 1 \\ 0 & 1 & 0 \end{pmatrix} \ , \quad \lambda_7 = \begin{pmatrix} 0 & 0 & 0 \\ 0 & 0 & -\mathrm{i} \\ 0 & \mathrm{i} & 0 \end{pmatrix} \ , \quad \lambda_8 = \frac{1}{\sqrt{3}} \begin{pmatrix} 1 & 0 & 0 \\ 0 & 1 & 0 \\ 0 & 0 & -2 \end{pmatrix} \ .
\end{aligned} \tag{A.15}$$

The respective structure constants can be found, for example, in Ref. [222].

Fourier Transforms

Any bosonic field $\varphi(x)$ is a function of a vector in (Euclidean) position space and can also be expressed by means of its momentum-space modes via

$$\varphi(x) = \int \frac{\mathrm{d}^4 p}{(2\pi)^4} \, \mathrm{e}^{\mathrm{i} p \cdot x} \, \varphi(p) \ . \tag{A.16}$$

For notational simplicity, we use the same symbol for the momentum-space modes that we use for the position-space field. It should be clear from the context which version the symbol refers to, provided that a distinction is necessary at all. The continuous Fourier transform also works backwards,

$$\varphi(p) = \int \mathrm{d}^4 x \, \mathrm{e}^{-\mathrm{i} p \cdot x} \, \varphi(x) \ . \tag{A.17}$$

Fermionic Dirac fields transform similarly,

$$\psi(x) = \int \frac{\mathrm{d}^4 p}{(2\pi)^4} \, \mathrm{e}^{\mathrm{i} p \cdot x} \, \psi(p) \ , \tag{A.18}$$

but the adjoint field $\bar{\psi}(x)$ transforms with a different sign in the momentum as it is obtained by conjugate transposing Eq. (A.18):

$$\bar{\psi}(x) = \int \frac{\mathrm{d}^4 p}{(2\pi)^4} \, \mathrm{e}^{-\mathrm{i} p \cdot x} \, \bar{\psi}(p) = \int \frac{\mathrm{d}^4 p}{(2\pi)^4} \, \mathrm{e}^{\mathrm{i} p \cdot x} \, \bar{\psi}(-p) \ . \tag{A.19}$$

While field contractions take the same argument in position space, one of the arguments changes sign in momentum space, e.g:

$$\int \mathrm{d}^4x\, J(x)\varphi(x) = \int \frac{\mathrm{d}^4p}{(2\pi)^4}\, J(-p)\varphi(p)\ . \tag{A.20}$$

This follows directly from inserting the momentum-space expressions for $J(x)$ and $\varphi(x)$.

Matsubara Formalism

At finite temperature we employ the Matsubara formalism: The path integral for an ensemble in thermodynamic equilibrium varies fields on a compact imaginary time dimension and the three noncompact spatial dimensions,

$$\int \mathrm{d}^4x \ \to \int_0^\beta \mathrm{d}\tau \int \mathrm{d}^3x \tag{A.21}$$

with $\beta = 1/T$. Bosonic and fermionic fields become periodic and antiperiodic, respectively, in the imaginary-time direction, and hence frequency modes become discrete:

$$\int \frac{\mathrm{d}^4p}{(2\pi)^4} \to T \sum_{n=-\infty}^{\infty} \int \frac{\mathrm{d}^3p}{(2\pi)^3} \tag{A.22}$$

with the Matsubara frequencies $p_0 \to \omega_n := 2n\pi T$ for bosons and $p_0 \to \nu_n := (2n+1)\pi T$ for fermions.

Short-hand Notation

We use Feynman slash notation

$$\not{p} := p^\mu \gamma_\mu = p_\mu \gamma^\mu\ . \tag{A.23}$$

Momentum- or position-space integrals are oftentimes abbreviated:

$$\int_x := \int \mathrm{d}^4x\ , \quad \int_{\boldsymbol{x}} := \int \mathrm{d}^3x\ , \quad \int_p := \int \frac{\mathrm{d}^4p}{(2\pi)^4}\ , \quad \int_{\boldsymbol{p}} := \int \frac{\mathrm{d}^3p}{(2\pi)^3}\ . \tag{A.24}$$

When different functions or functionals (or their derivatives) are contracted, we will sometimes indicate this by a simple integral sign and not further specify any arguments. This allows for a formulation in both position or momentum space:

$$\int J\varphi := \int_x J(x)\varphi(x) = \int_p J(-p)\varphi(p)\ . \tag{A.25}$$

Composite Fields and Functional Derivatives

We collect all bosonic and fermionic quantum fields in the composite field vector

$$\Phi(x) = \begin{pmatrix} \phi(x) \\ q(x) \\ \bar{q}^T(x) \end{pmatrix}\ . \tag{A.26}$$

$\phi(x)$ is a vector of all (mesonic) scalar fields. $q(x)$ is a four-component Dirac spinor quark field with additional flavor and color subspaces and $\bar{q}^T(x)$ is the column vector transpose of the Dirac adjoint. In momentum space, the latter receives an additional minus sign in the argument as shown in Eq. (A.18):

$$\Phi(p) = \begin{pmatrix} \phi(p) \\ q(p) \\ \bar{q}^T(-p) \end{pmatrix} . \tag{A.27}$$

In direct QCD applications, (anti)ghost and gauge fields (gluons) are oftentimes collected in Φ, too. These, however, are not present in our truncations. In our convention, functional derivatives in position and momentum space have the following properties:

$$\frac{\delta\Phi_i(x)}{\delta\Phi_j(y)} = \delta_{ij}\,\delta(x-y) , \quad \frac{\delta\Phi_i(p)}{\delta\Phi_j(q)} = \delta_{ij}\,(2\pi)^4\delta(p-q) , \quad \frac{\delta\Phi_i(x)}{\delta\Phi_j(p)} = \delta_{ij}\,\mathrm{e}^{ip\cdot x} , \tag{A.28}$$

where the indices refer to the individual field components of Φ and the last equation follows from the definition of the Fourier transform. Furthermore, the number of derivatives of a functional (e.g., the effective action) is denoted in parenthesis is the upper index, with the left and right numbers indicating the number of derivatives acting from the left and right, respectively:

$$\begin{aligned} \Gamma^{(1,1)}_{ij}(x,y) &:= \frac{\overrightarrow{\delta}}{\delta\Phi_i(x)}\Gamma[\Phi]\frac{\overleftarrow{\delta}}{\delta\Phi_j(y)} \\ \Gamma^{(1,1)}_{ij}(p,p') &:= \frac{\overrightarrow{\delta}}{\delta\Phi_i(-p)}\Gamma[\Phi]\frac{\overleftarrow{\delta}}{\delta\Phi_j(-p')} . \end{aligned} \tag{A.29}$$

The sign change in the momentum-space derivatives is conventional and reflects the sign change in one of the contracted fields:

$$\frac{\delta}{\delta J(-p)}\int_{p'} J(-p')\varphi(p') = \varphi(p) . \tag{A.30}$$

If we are dealing with only non-Grassmann fields and thus the direction from which the derivative acts is irrelevant, only the total number of derivatives is given in the upper index, i.e. $\Gamma^{(1,1)}(p,p') \to \Gamma^{(2)}(p,p')$. Moreover, using locality we can define related functionals with one less argument. In momentum space and for two-point functionals, examples relevant for FRG flows include (cf. Sec. 3.2)

$$\begin{gathered} R_k(p,p') := R_k(p)\,(2\pi)^4\delta(p+p') , \quad G_k(p,p') := G_k(p)\,(2\pi)^4\delta(p+p') , \\ \Gamma^{(1,1)}_k(p,p') := \Gamma^{(1,1)}_k(p)\,(2\pi)^4\delta(p+p') , \end{gathered} \tag{A.31}$$

with obvious generalizations for, e.g., higher-order vertex functions. This convention corresponds to all momenta at vertices being treated as incoming momenta.

Composite Regulator and Wetterich Equation

The FRG regulator function generalizes to the composite field space defined above as

$$R_k(p) = \begin{pmatrix} R^B_k(p^2) & 0 & 0 \\ 0 & 0 & -(R^F_k)^T(-p) \\ 0 & R^F_k(p) & 0 \end{pmatrix} \tag{A.32}$$

with the bosonic and fermionic regulators introduced in Ch. 3. In case of multiple bosonic fields, these encompass a diagonal subspace in the $(0,0)$ component. Similarly, defining

$$\langle \Phi \rangle = \begin{pmatrix} \langle \phi \rangle \\ 0 \\ 0 \end{pmatrix} , \tag{A.33}$$

the FRG modified two-point function evaluated at the expectation value reads

$$\Gamma_k^{(1,1)}(p)\Big|_{\langle\Phi\rangle} = \begin{pmatrix} \Gamma_k^{\phi\phi}(p) & 0 & 0 \\ 0 & 0 & -(\Gamma_k^{\bar{q}q})^T(-p) \\ 0 & \Gamma_k^{\bar{q}q}(p) & 0 \end{pmatrix}\Bigg|_{\langle\Phi\rangle} \tag{A.34}$$

with the respective derivatives indicated in the upper indices. All mixed bosonic–fermionic off-diagonal entries vanish at the expectation value because they still include single q or $\bar{q}$ fields and the diagonal fermionic ones vanish as the quark field and its adjoint appear at most once in each term of our truncation. If there are multiple bosonic fields with more than one nonvanishing expectation value, the situation in the bosonic sector is not so clear. This occurs, for example, in three-flavor calculations where a diagonalization of the two-point function at each scale k is necessary in order to trivially invert it (cf. Ref. [155]). In this general formulation the Wetterich equation reads

$$\partial_t \Gamma_k[\Phi] = \frac{1}{2}\mathrm{STr}\left[\frac{\partial_t R_k}{\Gamma_k^{(1,1)} + R_k}\right] . \tag{A.35}$$

The supertrace gives an additional minus sign in the fermi sector and includes momentum integrals contracting the two terms; the inversion of the denominator term needs to be performed in field space as well.

Appendix B

Compact Stars from General Relativity

In the following, we give a brief overview of the derivation of the Tolman-Oppenheimer-Volkoff equation for a nonrotating star and discuss some general restrictions for equations of state. Afterwards, the tidal deformability is inferred from a perturbation due to an external tidal field. For a broad introduction into general relativity, we refer to textbooks such as Ref. [36]. We mostly follow standard notation from Ref. [36] and use the metric signature $(-,+,+,+)$ for flat Minkowski space. First, let us introduce the most important quantities in general relativity. The covariant derivative of a vector is denoted in the following manner:

$$\nabla_\mu V^\nu = \partial_\mu V^\nu + \Gamma^\nu_{\mu\lambda} V^\lambda \tag{B.1}$$

with the Christoffel symbols (i.e., the torsion-free, metric-compatible connection)

$$\Gamma^\sigma_{\mu\nu} := \frac{1}{2} g^{\sigma\rho}(\partial_\mu g_{\nu\rho} + \partial_\nu g_{\rho\mu} - \partial_\rho g_{\mu\nu}) \ . \tag{B.2}$$

The Riemann curvature tensor

$$R^\rho{}_{\sigma\mu\nu} := \partial_\mu \Gamma^\rho_{\nu\sigma} - \partial_\nu \Gamma^\rho_{\mu\sigma} + \Gamma^\rho_{\mu\lambda}\Gamma^\lambda_{\nu\sigma} - \Gamma^\rho_{\nu\lambda}\Gamma^\lambda_{\mu\sigma} \tag{B.3}$$

gives rise to the Ricci tensor

$$R_{\mu\nu} := R^\lambda{}_{\mu\lambda\nu} \tag{B.4}$$

and the Ricci scalar

$$R := g^{\mu\nu} R_{\mu\nu} \ , \tag{B.5}$$

which in turn combine to the Einstein tensor

$$G_{\mu\nu} := R_{\mu\nu} - \frac{1}{2} R g_{\mu\nu} \ . \tag{B.6}$$

The starting point of the following discussion is then the Einstein equation (without cosmological constant) [23]

$$G_{\mu\nu} = 8\pi T_{\mu\nu} \ . \tag{B.7}$$

It relates the curvature of spacetime on the left-hand side to the presence of matter via the energy-momentum tensor on the right-hand side. Under the assumption of spherical

symmetry, the metric in vacuum (here defined as the local absence of matter, $T_{\mu\nu} = 0$) must be static and asymptotically flat [223, 224]. Its nontrivial solution is the Schwarzschild metric [225, 226]

$$\mathrm{d}s^2 = -\left(1 - \frac{2M}{r}\right)\mathrm{d}t^2 + \left(1 - \frac{2M}{r}\right)^{-1}\mathrm{d}r^2 + r^2\mathrm{d}\Omega^2 \tag{B.8}$$

with the angular part

$$\mathrm{d}\Omega^2 = \mathrm{d}\theta^2 + \sin^2\theta\,\mathrm{d}\phi^2 \ . \tag{B.9}$$

Tolman-Oppenheimer-Volkoff Equation

For the metric inside the star (i.e., in the presence of matter) we make the more general spherically symmetric ansatz

$$\mathrm{d}s^2 = -\mathrm{e}^{\nu(r)}\mathrm{d}t^2 + \mathrm{e}^{\lambda(r)}\mathrm{d}r^2 + r^2\mathrm{d}\Omega^2 \ . \tag{B.10}$$

Matter inside such a compact object in hydrostatic equilibrium is described as a perfect fluid, i.e., shear stresses and viscosity are neglected. The energy-momentum tensor is then fully defined only by the energy density ε and the isotropic pressure p and takes on the simple form

$$T^{\mu\nu} = (\varepsilon + p)\,U^\mu U^\nu + p\,g^{\mu\nu} \tag{B.11}$$

with the four-velocity

$$U^\mu := \frac{\mathrm{d}x^\mu}{\mathrm{d}\tau} \tag{B.12}$$

and the proper time τ. In the rest frame of the fluid, only the time component of the four-velocities is nonzero and the normalization

$$g_{\mu\nu}U^\mu U^\nu = -1 \tag{B.13}$$

yields $(U^t)^2 = \mathrm{e}^{-\nu(r)}$. Using the inverse metric $g^{\mu\nu}$ determined from Eq. (B.10), we obtain the energy-momentum tensor

$$T^{\mu\nu} = \mathrm{diag}\left(\mathrm{e}^{-\nu}\varepsilon, \mathrm{e}^{-\lambda}p, \frac{1}{r^2}p, \frac{1}{r^2\sin^2\theta}p\right) \ , \tag{B.14}$$

and placing the indices downstairs yields

$$T_{\mu\nu} = \mathrm{diag}\left(\mathrm{e}^{\nu}\varepsilon, \mathrm{e}^{\lambda}p, r^2p, r^2\sin^2\theta\,p\right) \ . \tag{B.15}$$

On the left-hand side of the Einstein equation (B.7), only the diagonal entries

$$\begin{aligned}
G_{tt} &= \frac{1}{r^2}\mathrm{e}^{\nu-\lambda}\left(r\partial_r\lambda - 1 + \mathrm{e}^{\lambda}\right)\\
G_{rr} &= \frac{1}{r^2}\left(r\partial_r\nu + 1 - \mathrm{e}^{\lambda}\right)\\
G_{\theta\theta} &= r^2\mathrm{e}^{-\lambda}\left[\frac{1}{2}\partial_r^2\nu + \frac{1}{4}(\partial_r\nu)^2 - \frac{1}{4}\partial_r\nu\partial_r\lambda + \frac{1}{2r}(\partial_r\nu - \partial_r\lambda)\right]\\
G_{\phi\phi} &= \sin^2\theta\,G_{\theta\theta}
\end{aligned} \tag{B.16}$$

survive. The third and fourth conditions degenerate; hence, we are left with three equations for the four parameters p, ε, ν, and λ. A fourth piece of information must be acquired from the underlying state of matter, by means of the equation of state $p(\varepsilon)$. From here, it is reasonable to redefine

$$\mathrm{e}^{\lambda(r)} := \left(1 - \frac{2m(r)}{r}\right)^{-1} \tag{B.17}$$

to bring it in a form similar to the Schwarzschild metric. The tt sector of the Einstein equation becomes

$$\partial_r m(r) = 4\pi r^2 \varepsilon(r) \ . \tag{B.18}$$

$m(r)$ incorporates the total mass inside the (flat space) sphere of radius r. The rr sector can now be formulated as

$$\partial_r \nu(r) = 2\frac{4\pi r^3 p(r) + m(r)}{r(r - 2m(r))} \ . \tag{B.19}$$

The last condition is easiest obtained from energy-momentum conservation $\nabla_\mu T^{\mu\nu} = 0$ which naturally provides a pressure derivative

$$\partial_r p(r) = -\frac{1}{2}[\varepsilon(r) + p(r)]\, \partial_r \nu(r) \ . \tag{B.20}$$

In combination, we obtain the Tolman-Oppenheimer-Volkoff equations

$$\begin{aligned} \frac{\mathrm{d}p}{\mathrm{d}r} &= -\frac{(\varepsilon + p)(m + 4\pi r^3 p)}{r(r - 2m)} \ , \\ \frac{\mathrm{d}m}{\mathrm{d}r} &= 4\pi r^2 \varepsilon \ . \end{aligned} \tag{B.21}$$

They form a system of two coupled first order ordinary differential equations. The inverted equation of state $\varepsilon(p)$ serves as external input and—starting at $r = 0$—one of the initial values $m(0) = 0$ is trivially fixed. The other starting parameter, the central pressure $p_0 := p(0)$, is unknown and leads to a one-parameter curve of possible stars with radius R and mass M. The radius is defined as the point where the pressure goes to zero, $p(R) = 0$. In practice, many equations of state do not lead to a sharp surface and a small pressure value $p(R) = p_{\min}$ is chosen instead. The star's mass is then given by $M = m(R)$ which is equal to the mass parameter for the Schwarzschild metric outside the star. For increasing central pressure p_0, M will usually increase up a maximum mass $M_{\max}$, after which it decreases again. Only the increasing branch signified by

$$\frac{\mathrm{d}M}{\mathrm{d}p_0} > 0 \tag{B.22}$$

is considered to lead to stable stars [227]. Furthermore, the restrictions

$$\frac{\partial n_B}{\partial \mu_B} = \frac{\partial^2 p}{\partial \mu_B^2} > 0 \quad \text{and} \quad c_s^2 = \frac{\partial p}{\partial \varepsilon} \leq 1 \tag{B.23}$$

are commonly placed on the equation of state [40]. The first one is dictated by thermodynamics and prevents an inflection point in the pressure as a function of the chemical potential and the second restriction is motivated by causality. There are, however, also works arguing that $c_s^2 > 1$ might not violate causality after all, see e.g. Ref. [228]. Assuming the causality constraint to be valid and using a maximally stiff equation of state that still fulfills the properties of nuclear matter in the low density regime, the region $R < 2.87M$ in the M-R-plane has been excluded as unphysical [24].

Tidal Deformability

Let us consider the response of a star's perturbed metric to an external gravitational source. In a multipole expansion, the lowest contributing order (suitable for, e.g., the description of the early inspiral phase of two stars) is the quadrupole term. At large distances from the star in asymptotically Cartesian coordinates, this leads to the following approximation to the gravitational potential [229, 230]:

$$-\frac{1+g_{tt}}{2} = -\frac{M}{r} - \frac{3}{2r^3}Q_{ij}n^i n^j + \cdots + \frac{r^2}{2}\mathcal{E}_{ij}n^i n^j + \cdots \tag{B.24}$$

with $n^i := x^i/r$. The metric perturbation Q_{ij} is related to the external tidal field $\mathcal{E}_{ij}$ to linear order by the (dimensionful) tidal deformability λ:

$$Q_{ij} = -\lambda \mathcal{E}_{ij} \ . \tag{B.25}$$

Alternatively, we can do the expansion in spherical harmonics, which relates the quadrupolar tensor elements to the $l = 2$ functions via

$$Q_{ij}n^i n^j = \sum_{m=-2}^{2} Q_m Y_2^m(\theta,\phi) \ , \quad \mathcal{E}_{ij}n^i n^j = \sum_{m=-2}^{2} \mathcal{E}_m Y_2^m(\theta,\phi) \ . \tag{B.26}$$

We can safely specialize to the case of an axisymmetric perturbation and choose coordinates such that only the $m = 0$ terms $Q \equiv Q_0 = -\lambda\mathcal{E}_0 \equiv -\lambda\mathcal{E}$ are nonzero [229]. Next, the metric perturbation inside and outside the star must be calculated from the Einstein equations. To this end, we add a perturbation $h_{\mu\nu}$ to the spherically symmetric background metric $\bar{g}_{\mu\nu}$ given by Eq. (B.10):

$$g_{\mu\nu} = \bar{g}_{\mu\nu} + h_{\mu\nu} \ . \tag{B.27}$$

To linear order in the perturbation, the inverse metric reads

$$g^{\mu\nu} = \bar{g}^{\mu\nu} - h^{\mu\nu} \ . \tag{B.28}$$

We also consider linear corrections in the Ricci tensor $R_{\mu\nu} = \bar{R}_{\mu\nu} + \delta R_{\mu\nu}$ and the Ricci scalar $R = \bar{R} + \delta R$. It can be easily verified that

$$\delta R_{\mu\nu} = \bar{\nabla}_\sigma \delta\Gamma^\sigma{}_{\mu\nu} - \bar{\nabla}_\nu \delta\Gamma^\sigma{}_{\mu\sigma} \tag{B.29}$$

with the tensor

$$\delta\Gamma^\sigma{}_{\mu\nu} := \frac{1}{2}\bar{g}^{\sigma\rho}\left(\bar{\nabla}_\mu h_{\nu\rho} + \bar{\nabla}_\nu h_{\rho\mu} - \bar{\nabla}_\rho h_{\mu\nu}\right) \ , \tag{B.30}$$

as well as

$$\delta R = -\bar{R}_{\mu\nu}h^{\mu\nu} + \bar{\nabla}_\mu\bar{\nabla}_\nu h^{\mu\nu} - \bar{\nabla}_\mu\bar{\nabla}^\mu h^\nu_\nu \tag{B.31}$$

where the bars on the covariant derivatives indicate that the background Christoffel symbols are to be used and indices of the perturbation tensor $h_{\mu\nu}$ are raised and lowered by means of the background metric. We can now write down the linearized Einstein equation:

$$\delta G^\mu_\nu := \bar{g}^{\mu\lambda}\delta R_{\lambda\nu} - h^{\mu\lambda}\bar{R}_{\lambda\nu} - \frac{1}{2}\delta R\delta^\mu_\nu = 8\pi T^\mu_\nu \ . \tag{B.32}$$

From

$$T^\mu_\nu = (\varepsilon + p)U^\mu U_\nu + p\delta^\mu_\nu \tag{B.33}$$

we follow that, in the local rest frame, $\delta T^\mu_\nu = \mathrm{diag}(-\delta\varepsilon, \delta p, \delta p, \delta p)$ and $\delta\varepsilon = (\partial\varepsilon/\partial p)\delta p$.

To solve this complex set of equations, one proceeds with a product ansatz, separating the radial part and expanding the time dependence in terms of frequency modes $\mathrm{e}^{-\mathrm{i}\omega t}$ and the angular parts in spherical harmonics. This was pioneered by Regge and Wheeler in 1957 [231]. They argued that, under spatial rotations, the elements of the perturbation matrix transform as either scalars (h_{00}, h_{01}, h_{11}), vectors [(h_{02}, h_{03}), (h_{12}, h_{13})], or as a tensor h_{ij} with $i, j \in \{2, 3\}$ which leads to specific functional forms for the different terms. Further, vectors and tensors can have even and odd parity contributions, while the scalars always have even parity. Since the background metric is spherically symmetric and the perturbation only appears to linear order in the equation of motion, terms of different angular momentum, parity, or frequency do not mix and can be considered separately [231]. It has been shown that odd-parity perturbations do not contribute to changes in the (perfect fluid) energy-momentum tensor [232]. Therefore, we only need to consider the $l = 2$, $m = 0$, even-parity, and static ($\omega = 0$) solution. Moreover, the linearized equations are ambiguous under an infinitesimal coordinate transformation, i.e., they admit a gauge choice. Regge and Wheeler used this to simplify the expressions they obtained, cf. Ref. [231]. For our choice of perturbation, this leads to

$$h_{\mu\nu} = \mathrm{diag}\left(\left(1 - \frac{2m}{r}\right)H_0, \left(1 - \frac{2m}{r}\right)^{-1} H_2, r^2 K, r^2 K \sin^2\theta\right) Y_2^0(\theta, \phi)\ . \tag{B.34}$$

Another nondiagonal element H_1 arises for nonstatic solutions [231].

The tedious solution of the linearized Einstein equations in the presence of matter has been acquired and checked multiple times in the past [214, 233, 234] and is not done here. It leads to $H_2 = H_0 \equiv H$ and the differential equation

$$\begin{aligned} H'' + H'\left[\frac{2}{r} + \mathrm{e}^\lambda\left(\frac{2m}{r^2} + 4\pi r(p - \varepsilon)\right)\right] \\ + H\left[-\frac{6\mathrm{e}^\lambda}{r^2} + 4\pi\mathrm{e}^\lambda\left(5\varepsilon + 9p + (\varepsilon + p)\frac{\mathrm{d}\varepsilon}{\mathrm{d}p}\right) - \nu'^2\right] = 0 \end{aligned} \tag{B.35}$$

where the primes denote differentiation w.r.t. the radial coordinate. Since we are interested in the perturbation of the time component of the metric to connect with the previously imposed boundary conditions (i.e., the external tidal field), we can neglect the second function K. We follow Ref. [234] and consider the simplified version of Eq. (B.35) outside the star (with the coordinate-independent Schwarzschild mass term M):

$$H'' + H'\left[\frac{2}{r} + \frac{2M}{r^2}\frac{1}{1 - \frac{2M}{r}}\right] + H\left[-\frac{6}{r^2}\frac{1}{1 - \frac{2M}{r}} - \left(\frac{2M}{r^2}\right)^2 \frac{1}{\left(1 - \frac{2M}{r}\right)^2}\right] = 0\ . \tag{B.36}$$

This differential equation can be solved analytically. Under a change of variables $x := r/M - 1$, it turns into the Legendre equation for $l = 2$, $m = 2$:

$$(1 - x^2)H'' - 2xH' + \left(6 - \frac{4}{1 - x^2}\right)H = 0 \tag{B.37}$$

where the primes indicate derivatives w.r.t. x. Its solution is a linear combination of Legendre functions of the first and second kind:

$$H = a\, P_2^2(x) + b\, Q_2^2(x) \tag{B.38}$$

with [235]

$$\begin{aligned} P_2^2(x) &= 3(1-x^2)\ , \\ Q_2^2(x) &= 6x + \frac{x(3x^2-1)}{1-x^2} + \frac{3}{2}(1-x^2)\ln\frac{x+1}{x-1} \quad \text{for } |x|>1\ . \end{aligned} \tag{B.39}$$

At large distances from the star $r/M \gg 1$, the metric perturbation has the dominant contributions

$$H \approx -3a\left(\frac{r}{M}\right)^2 - \frac{8}{5}b\left(\frac{M}{r}\right)^3\ . \tag{B.40}$$

Note that all higher-order terms in Q_2^2 cancel exactly with the first few expansion coefficients of the logarithm. This asymptotic behavior is now inserted into the full expression for the metric perturbation (B.34) and matched with the corresponding orders of the asymptotic expansion of the gravitation potential (B.24), yielding

$$a = \frac{\mathcal{E}M^2}{3}\ , \quad b = \frac{15}{8}\frac{\lambda\mathcal{E}}{M^3}\ . \tag{B.41}$$

Now that the connection with the external tidal field is made, we only need to extract λ. As this value should be independent from $\mathcal{E}$, we consider the dimensionless quantity

$$y := \frac{RH'(R)}{H(R)} \tag{B.42}$$

in which $\mathcal{E}$ trivially cancels. It is evaluated at the surface of the star where a connection between the inside and outside solutions can be made. Based on the solution outside the star (B.38), Eq. (B.42) can be resolved for λ [234]:

$$\begin{aligned} \lambda = \frac{16M^5}{15}(1-2C)^2\,(2+2C(y-1)-y)\Big\{&2C(6-3y+3C(5y-8)) \\ &+4C^3\left[13-11y+C(3y-2)+2C^2(1+y)\right] \\ &+3(1-2C)^2\left[2-y+2C(y-1)\right]\ln(1-2C)\Big\}^{-1}\ . \end{aligned} \tag{B.43}$$

The dimensionless value $C := M/R$ denotes the compactness of the star. It is obtained from the solution of the TOV equations.

To find y, the TOV equations are amended by the full differential equation for H in the presence of matter, Eq. (B.35), i.e., y is now evaluated from the inside out. To this end, the second order differential equation is split into a set of two coupled first-order

equations [230]:

$$\begin{aligned}
\frac{\mathrm{d}H}{\mathrm{d}r} &= \beta \\
\frac{\mathrm{d}\beta}{\mathrm{d}r} &= -\beta\left[\frac{2}{r}+\left(1-\frac{2m}{r}\right)^{-1}\left(\frac{2m}{r^2}+4\pi r(p-\varepsilon)\right)\right] \\
&\quad - H\left(1-\frac{2m}{r}\right)^{-1}\left[-\frac{6}{r^2}+4\pi\left(5\varepsilon+9p+(\varepsilon+p)\frac{\mathrm{d}\varepsilon}{\mathrm{d}p}\right)\right. \\
&\qquad\qquad \left. -4\left(1-\frac{2m}{r}\right)^{-1}\left(\frac{m}{r^2}+4\pi r p\right)^2\right] .
\end{aligned} \tag{B.44}$$

The required value for ν' (cf. Eq. (B.35)) has been taken from Eq. (B.19). There is, however, one remaining free parameter related to the initial value for the perturbation at the center of the star. An expansion of Eq. (B.35) in powers of r reveals [234]

$$H(r) = a_0 r^2 + \mathcal{O}(r^4) \tag{B.45}$$

and thus $H(0) = 0$, $\beta(0) \equiv H'(0) = 0$, $\beta'(0) \equiv H''(0) = 2a_0$. The linear dependence of H and β on a_0 near the origin coupled with their linear occurrence in Eq. (B.44) implies that they will remain proportional to a_0 throughout the integration, i.e., the ratio y is independent of the choice of a_0. The calculated value of y at the star's surface can now be inserted into Eq. (B.43), effectively matching it to the outside solution.

There is, however, one last caveat: So far, it was assumed that both $H(r)$ and $H'(r)$ are continuous functions of r. While this has to be true for the metric component $H(r)$, as argued in Ref. [214] its derivative $H'(r)$ will exhibit a discontinuity if matter undergoes a first-order phase transition. Such a transition is always related to a discontinuity in the energy density (cf., for example, Fig. 5.3). This in turn leads to a delta peak in the derivative $\mathrm{d}\varepsilon/\mathrm{d}p = (\mathrm{d}p/\mathrm{d}r)^{-1}\mathrm{d}\varepsilon/\mathrm{d}r$ in above differential equation for β. Inserting $\mathrm{d}p/\mathrm{d}r$ from the TOV equation, the singular part reads

$$\frac{\mathrm{d}\beta^{(\mathrm{sing})}}{\mathrm{d}r} = \frac{4\pi r^2 H}{m+4\pi r^3 p}\,\frac{\mathrm{d}\varepsilon}{\mathrm{d}r} \ . \tag{B.46}$$

Let us make the reasonable assumption that, going radially outwards, the transition occurs at a specific radius r_c and leads into a phase of smaller density, i.e., $\mathrm{d}\varepsilon/\mathrm{d}r = -\Delta\varepsilon\,\delta(r-r_c)$ in the proximity of r_c. Integrating this term in the infinitesimal interval $r_c-\delta r < r < r_c+\delta r$ then gives

$$\beta^+ - \beta^- = -\frac{4\pi r_c^2 H_c \Delta\varepsilon}{m_c + 4\pi r_c^3 p_c} \tag{B.47}$$

where the index c indicates that these quantities are evaluated at $r = r_c$. In a numerical calculation, one would integrate the system of ordinary differential equations until the critical pressure is reached, add this term to β, and then continue the evaluation. A special case is constituted by stars with a nonzero density at the surface. This typically happens for pure quark matter stars (such as the ones presented in this work) as they exhibit a first-order transition to the vacuum phase at $p_c \approx 0$ [230]. The modification

term can then be simply added to y after the calculation to correctly determine the metric just outside the star (which is the one that was needed for the matching procedure):

$$y = \frac{R\beta^+(R)}{H(R)} = \frac{R\beta^-(R)}{H(R)} - \frac{4\pi R^3 \Delta\varepsilon}{M} \ . \tag{B.48}$$

Once λ is determined, it can be made dimensionless by dividing either by M^5 or R^5:

$$\begin{aligned} \Lambda &:= \lambda M^{-5} \\ k_2 &:= \frac{3}{2}\lambda R^{-5} = \frac{3}{2}\Lambda C^5 \end{aligned} \tag{B.49}$$

Λ is called the dimensionless tidal deformability and k_2 is the tidal Love number.

Appendix C

Derivation of the Polchinski Equation

This appendix continues the discussion on Polchinski's equation started in Sec. 3.2. We derive the Polchinski equation (3.41) within our modern path integral formalism and make a connection of Polchinski's effective action S_k^{eff} to the modified Schwinger functional W_k. For this, we need to find a setup with two complementary path integrals as in Wilson's original idea, Eq. (3.21), but generalized to arbitrary cutoff functions (as long as they fulfill elementary conditions, such as the three regulator conditions provided in the previous section). Some helpful notes on the derivation were found in Ref. [236]. We start with the full partition function for the bare action $S[\varphi]$ and add a source term for convenience:

$$\mathcal{Z}[J] = \int \mathcal{D}\varphi \, \mathrm{e}^{-S[\varphi]+\int J\varphi} = \mathrm{e}^{-S^{\text{int}}[\frac{\delta}{\delta J}]} \int \mathcal{D}\varphi \, \mathrm{e}^{-\frac{1}{2}\int \varphi\, G_0^{-1}\, \varphi + \int J\varphi} \ . \tag{C.1}$$

For simplicity, we will furthermore stick to abstract notation for the (position or momentum space) integrals. The Gaussian path integral can be performed which gives, up to determinants,

$$\mathcal{Z}[J] = \mathrm{e}^{-S^{\text{int}}[\frac{\delta}{\delta J}]}\, \mathrm{e}^{\frac{1}{2}\int J G_0 J} \ . \tag{C.2}$$

At this point, we can separate the propagator into a low- and a high-momentum part,

$$\int J G_0 J = \int J G_0 K J + \int J G_0 (1-K) J \ , \tag{C.3}$$

and insert a Gaussian path integral for each individual term, both coupling to the same source J:

$$\begin{aligned} \mathcal{Z}[J] &= \mathrm{e}^{-S^{\text{int}}[\frac{\delta}{\delta J}]} \int \mathcal{D}\varphi \, \mathrm{e}^{-\frac{1}{2}\int \varphi\, G_0^{-1}\, K^{-1} \varphi} \int \mathcal{D}\chi \, \mathrm{e}^{-\frac{1}{2}\int \chi\, G_0^{-1} (1-K)^{-1}\, \chi + \int J(\chi+\varphi)} \\ &= \int \mathcal{D}\varphi \, \mathrm{e}^{-\frac{1}{2}\int \varphi\, G_0^{-1}\, K^{-1} \varphi} \int \mathcal{D}\chi \, \mathrm{e}^{-\frac{1}{2}\int \chi\, G_0^{-1} (1-K)^{-1}\, \chi - S^{\text{int}}[\chi+\varphi] + \int J(\chi+\varphi)} \ . \end{aligned} \tag{C.4}$$

We can now set J to zero again and identify the scale-dependent effective interaction (cf. Eq. (3.39)) with the inner path integral

$$\begin{aligned} \mathrm{e}^{-S_k^{\text{int}}[\varphi]} &= \int \mathcal{D}\chi \, \mathrm{e}^{-\frac{1}{2}\int \chi\, G_0^{-1} (1-K)^{-1}\, \chi - S^{\text{int}}[\chi+\varphi]} \\ &= \int \mathcal{D}\chi \, \mathrm{e}^{-\frac{1}{2}\int \chi\, G_0^{-1} (1-K)^{-1}\, \chi - S^{\text{int}}[\chi] + \int \varphi\, G_0^{-1} (1-K)^{-1}\, \chi - \frac{1}{2}\int \varphi\, G_0^{-1} (1-K)^{-1}\, \varphi} \ . \end{aligned} \tag{C.5}$$

In the second line, we have shifted $\chi \to \chi - \varphi$ in order to remove the φ-argument from S^{int}. With the identification $R_k = G_0^{-1}[(1-K)^{-1} - 1] = K/[G_0(1-K)]$ the bare propagator term for χ can be combined with $S^{\mathrm{int}}[\chi]$ to yield the full bare action and a standard regulator term as defined in Eq. (3.23). The mixed term in the fields takes the role of a source $J = G_0^{-1}(1-K)^{-1}\varphi$ for $W_k[J]$. In total, we obtain

$$S_k^{\mathrm{int}}[\varphi] = -W_k[G_0^{-1}(1-K)^{-1}\varphi] + \frac{1}{2}\int \varphi\, G_0^{-1}(1-K)^{-1}\,\varphi \ . \tag{C.6}$$

Since $W_k[J]$ is the generator for connected diagrams, but each functional derivative of $S_k^{\mathrm{int}}[\varphi]$ is effectively a derivative of W_k multiplied with an inverse (RG-modified) bare propagator, S_k^{int} can be understood as the generating functional for n-point vertices with external legs amputated. The free propagator is removed via the second term. The scale derivative, keeping φ fixed, reads

$$\begin{aligned}\partial_t|_\varphi\, S_k^{\mathrm{int}}[\varphi] = -\left(\partial_t|_J + \int G_0^{-1}[\partial_t(1-K)^{-1}]\,\varphi\frac{\delta}{\delta J}\right) W_k[J]\Big|_{J=G_0^{-1}(1-K)^{-1}\varphi} \\ + \frac{1}{2}\int \varphi\, G_0^{-1}[\partial_t(1-K)^{-1}]\,\varphi \ .\end{aligned} \tag{C.7}$$

Inserting Eq. (3.30) and replacing the functional derivatives of W_k with those of S_k^{int} according to Eq. (C.6),

$$\begin{aligned}\frac{\delta W_k[J]}{\delta J}\bigg|_{J=G_0^{-1}(1-K)^{-1}\varphi} &= -(1-K)G_0\frac{\delta S_k^{\mathrm{int}}[\varphi]}{\delta\varphi} + \varphi \ , \\ \frac{\delta^2 W_k[J]}{\delta J\delta J}\bigg|_{J=G_0^{-1}(1-K)^{-1}\varphi} &= -(1-K)^2G_0^2\frac{\delta^2 S_k^{\mathrm{int}}[\varphi]}{\delta\varphi\delta\varphi} + (1-K)G_0 \ ,\end{aligned} \tag{C.8}$$

Polchinski's equation (3.41) is indeed recovered up to field-independent terms. Notably, the field φ here has the role of an external source term and should not be confused with the argument of $\Gamma_k[\phi]$ which is the expectation value of the high-momentum field in the presence of a source J. If we take $k = 0$ and determine the vacuum expectation value of the quantum field such that it satisfies the quantum equation of motion

$$\frac{\delta\Gamma[\phi]}{\delta\phi} - J = 0 \tag{C.9}$$

for vanishing source $J = 0$, we can alternatively extract ϕ from Polchinski's ansatz via

$$\phi = -\,G_0\frac{\delta S_0^{\mathrm{int}}[\varphi]}{\delta\varphi}\bigg|_{\varphi=0} \ . \tag{C.10}$$

Appendix D

Matsubara Sums

The derivation of flow equation requires the solution of Matsubara sums which arise at finite temperature instead of an integral in the (imaginary) frequency component of momentum loops, see App. A. We consider here the case of the two-flavor quark-meson model. Employing 3d regulators (or the 4d mass-term regulator within the approximation made in Ch. 7), the frequency only occurs in the standard quadratic term in the propagator. Hence, we only need to consider Matsubara sums over different powers of propagators. To this end, we define the renormalized propagators

$$\begin{aligned} \bar{G}_k^{\phi}(\omega_n, \boldsymbol{p}^2) &:= \frac{1}{\omega_n^2 + E_\phi^2} \ , \\ \bar{G}_k^{q}(\nu_n, \boldsymbol{p}^2) &:= \frac{1}{(\nu_n + \mathrm{i}\mu)^2 + E_q^2} \ , \end{aligned} \tag{D.1}$$

with ϕ denoting either a σ or π field and the renormalized energies

$$\begin{aligned} E_\sigma^2 &:= \boldsymbol{p}^2(1 + r_k^B) + 2\bar{U}' + 4\bar{\sigma}^2\bar{U}_k'' \ , \\ E_\pi^2 &:= \boldsymbol{p}^2(1 + r_k^B) + 2\bar{U}_k' \ , \\ E_q^2 &:= \boldsymbol{p}^2(1 + r_k^F)^2 + \left(\frac{\bar{g}_k}{2}\right)^2 \bar{\sigma}^2 \ . \end{aligned} \tag{D.2}$$

Any Matsubara sum occurring in this work has at most two different propagator ingredients. Thus, we define

$$\mathcal{M}_a^{(j)} := T \sum_n \left(\bar{G}_k^a\right)^j \ , \quad \mathcal{M}_{ab}^{(i,j)} := T \sum_n \left(\bar{G}_k^a\right)^i \left(\bar{G}_k^b\right)^j \ . \tag{D.3}$$

Note that we have omitted any momentum arguments for brevity. Generally, all propagators depend on the single loop momentum. Additionally, any nonvanishing external fermionic frequency ν_{ext} is routed through the quark propagators. In a precise formulation, the momentum-space propagators are discrete coefficients in the Fourier expansion of the imaginary-time component, i.e., they depend on the discrete frequency index n and not on the frequency value ω_n, ν_n itself. The external frequency $\nu_{\mathrm{ext}} = \pi T$ corresponds to the value $n_{\mathrm{ext}} = 0$, hence we have

$$\bar{G}_k^q(n + n_{\mathrm{ext}}, \boldsymbol{p}^2) = \bar{G}_k^q(n, \boldsymbol{p}^2) \tag{D.4}$$

and do not need to additionally consider the external frequency. Alternatively, we can—in a sloppy notation—keep up the notion of a continuous argument like in Eq. (D.1) where the argument is the frequency value itself. In that case, the bosonic loop frequency ω_n directly enters the quark propagator and the external momentum $\nu_{\text{ext}} = \pi T$ switches it to a fermionic frequency which is already taken into account in Eq. (D.1):

$$\bar{G}_k^q(\omega_n + \nu_{\text{ext}}, \boldsymbol{p}^2) = \bar{G}_k^q(\nu_n, \boldsymbol{p}^2) \ . \tag{D.5}$$

In both cases, we end up with the same result and do not have to further worry about the external frequency. An exception arises when continuing it to complex values, which is discussed at hand of the mixed fermion–boson sum below.

Evaluating the sums. Generally, Matsubara sums can be calculated by taking advantage of the residue theorem. Writing $\omega_n, \nu_n \to -\mathrm{i}z$, the sum can be replaced by an integral over the summand multiplied by a factor of $1/(2\pi\mathrm{i})$ and

$$u_\beta(z) := \begin{cases} \frac{1}{2T} \coth\left(\frac{z}{2T}\right) & \text{(bosons)} \\ \frac{1}{2T} \tanh\left(\frac{z}{2T}\right) & \text{(fermions)} \end{cases} \tag{D.6}$$

on a closed contour around the imaginary axis. The function u_β has poles with residue one at the imaginary Matsubara frequencies $\mathrm{i}\omega_n$ or $\mathrm{i}\nu_n$, respectively. This contour is then deformed to include the propagator poles instead of the ones of u_β. Further details can be found in Refs. [125, 237]. Note that only the respective lowest-order sums of each type need to be calculated this way. All higher orders can be obtained by taking derivatives w.r.t the corresponding squared energy,

$$\begin{aligned} \mathcal{M}_a^{(j)} &= \frac{(-1)^{j-1}}{(j-1)!} \left(\frac{\mathrm{d}}{\mathrm{d}E_a^2}\right)^{j-1} \mathcal{M}_a^{(1)} \ , \\ \mathcal{M}_{ab}^{(i,j)} &= \frac{(-1)^{i+j-2}}{(j-1)!(i-1)!} \left(\frac{\mathrm{d}}{\mathrm{d}E_a^2}\right)^{i-1} \left(\frac{\mathrm{d}}{\mathrm{d}E_b^2}\right)^{j-1} \mathcal{M}_{ab}^{(1,1)} \ , \end{aligned} \tag{D.7}$$

with $a \neq b$ and $i, j > 1$.

Lowest order results. For the single-propagator Matsubara frequencies, we obtain the standard results

$$\mathcal{M}_\phi^{(1)} = \frac{1}{2E_\phi} \coth\left(\frac{E_\phi}{2T}\right) \ , \quad \mathcal{M}_q^{(1)} = \frac{1}{4E_q} \left[\tanh\left(\frac{E_q - \mu}{2T}\right) + \tanh\left(\frac{E_q + \mu}{2T}\right)\right] \ . \tag{D.8}$$

These results enter the flow for the effective potential. The zero-temperature limit for the distribution functions[1] relevant for the computation of the equation of state is

$$\lim_{T\to 0} \coth\left(\frac{E}{2T}\right) = 1 \ , \quad \lim_{T\to 0} \tanh\left(\frac{E-\mu}{2T}\right) = 1 - 2\Theta(\mu - E) \ . \tag{D.9}$$

The mixed bosonic sums evaluate to

$$\mathcal{M}_{\sigma\pi}^{(1,1)} = \frac{1}{E_\pi^2 - E_\sigma^2} \mathcal{M}_\sigma^{(1)} + \frac{1}{E_\sigma^2 - E_\pi^2} \mathcal{M}_\pi^{(1)} \ . \tag{D.10}$$

[1] We will oftentimes refer to the following functions as distribution functions because they are linearly related to the bose and fermi distributions.

At the field origin where the pion and sigma masses degenerate, the pole singularity can be lifted and the sum correspondingly degenerates with the second order sums $\mathcal{M}_\sigma^{(2)}$, $\mathcal{M}_\pi^{(2)}$. The mixed fermionic–bosonic sum reads

$$\begin{aligned}\mathcal{M}_{q\phi}^{(1,1)} = \frac{1}{4E_\phi}\left[\frac{1}{E_q^2-(E_\phi-\mu+\mathrm{i}\nu_{\mathrm{ext}})^2}+\frac{1}{E_q^2-(E_\phi+\mu-\mathrm{i}\nu_{\mathrm{ext}})^2}\right]\coth\left(\frac{E_\phi}{2T}\right)\\ +\frac{1}{4E_q}\left[-\frac{1}{E_\phi^2-(E_q-\mu+\mathrm{i}\nu_{\mathrm{ext}})^2}\coth\left(\frac{E_q-\mu+\mathrm{i}\nu_{\mathrm{ext}}}{2T}\right)\right.\\ \left.+\frac{1}{E_\phi^2-(E_q+\mu-\mathrm{i}\nu_{\mathrm{ext}})^2}\coth\left(\frac{E_q+\mu-\mathrm{i}\nu_{\mathrm{ext}}}{2T}\right)\right].\end{aligned} \tag{D.11}$$

Here, we explicitly keep the external fermionic frequency argument in the expression and stick to the notation in terms of the frequency value instead of the index. As discussed before, the sum is then performed over the bosonic loop frequencies ω_n, leading to number densities described by the coth-function. Note that the choice $\nu_{\mathrm{ext}} = \pi T$ again correctly reproduces the fermi distributions in the second and third line by means of the identity $\coth(x-\mathrm{i}\pi/2) = -\coth(x+\mathrm{i}\pi/2) = \tanh(x)$. Furthermore, we see that the additional imaginary shift $\nu_{\mathrm{ext}} \to \nu_{\mathrm{ext}} - \mathrm{i}\mu$ discussed in Chs. 3.6 and 4.4 is necessary in order to cancel the μ-dependencies in the fraction terms and recover the Silver-Blaze property. However, this would also lead to a cancellation of the chemical potential in the fermi distribution functions. Another way to see this is to make the shift immediately in the fermionic propagator in Eq. (D.1)—it would completely eliminate all μ-dependence. The root of the problem lies in the fact that we continue a function that is defined only on discrete set of integral numbers, the Matsubara frequencies, to continuous complex numbers. As discussed in Ref. [238], such a continuation is not unique, and one needs to take into account additional analytic properties to find the correct continuation. In the example at hand, this becomes obvious when we insert $\nu_{\mathrm{ext}} = (2n_{\mathrm{ext}}+1)\pi T$. The distribution functions become independent of n_{ext} as long as it is integer-valued:

$$\coth\left(\frac{E_q-\mu+\mathrm{i}\nu_{\mathrm{ext}}}{2T}\right) = -\tanh\left(\frac{E_q-\mu}{2T}+\mathrm{i}\pi n_{\mathrm{ext}}\right) = -\tanh\left(\frac{E_q-\mu}{2T}\right). \tag{D.12}$$

Clearly, there are multiple functions which degenerate for n_{ext} integer, but will yield different results when n_{ext} is continued to complex values. Our ansatz to find the correct version is simple [239]: based on Eq. (D.12) we first remove any dependence of the distribution functions on n_{ext} before making the continuation. This yields the expected thermodynamic behavior, in total:

$$\begin{aligned}\mathcal{M}_{q\phi}^{(1,1)} = \frac{1}{4E_\phi}\left[\frac{1}{E_q^2-(E_\phi+\mathrm{i}\pi T)^2}+\frac{1}{E_q^2-(E_\phi-\mathrm{i}\pi T)^2}\right]\coth\left(\frac{E_\phi}{2T}\right)\\ +\frac{1}{4E_q}\left[\frac{1}{E_\phi^2-(E_q+\mathrm{i}\pi T)^2}\tanh\left(\frac{E_q-\mu}{2T}\right)\right.\\ \left.+\frac{1}{E_\phi^2-(E_q-\mathrm{i}\pi T)^2}\tanh\left(\frac{E_q+\mu}{2T}\right)\right].\end{aligned} \tag{D.13}$$

Nevertheless, we still find that for $\mu \neq 0$ the Matsubara sum becomes complex. This might be interpreted as an artifact of the derivative expansion in conjunction with the nonzero external frequency. A discussion of this issue can be found in Sec. 4.4.

Appendix E

Notes on the Derivation of Flow Equations

In this appendix, general comments on the derivation of the flow equations, especially beyond local potential approximation (see Sec. 4.4), as well as explicit, regulator independent expressions are given. Note that we refer to the two-flavor quark-meson model, i.e., the field content consists of a sigma meson with possibly nonvanishing vacuum expectation value, three pions, and $N_c N_f = 6$ Dirac quarks.

Effective Potential

The flow of the effective potential can be derived straightforwardly from the Wetterich equation evaluated at the expectation value as expressed by the projection (4.43). The scale derivative of a general 3d regulator with wavefunction renormalizations included can be expressed as

$$\begin{aligned} \partial_t R_k^B(\boldsymbol{p}^2) &= \boldsymbol{p}^2 \left[Z_{\phi,k} \partial_t r^B(x) + (\partial_t Z_{\phi,k}) r^B(x) \right] \\ &= Z_{\phi,k} \boldsymbol{p}^2 \left[\partial_t r^B(x) - \eta_{\phi,k} r^B(x) \right] =: Z_{\phi,k} \boldsymbol{p}^2 \, \tilde{\partial}_t r^B(x) \end{aligned} \tag{E.1}$$

in the bosonic sector and similarly

$$\partial_t R_k^F(\boldsymbol{p}) = Z_{q,k} \mathrm{i}\not{\boldsymbol{p}} \left[\partial_t r^F(x) - \eta_{q,k} r^F(x) \right] =: Z_{q,k} \mathrm{i}\not{\boldsymbol{p}} \, \tilde{\partial}_t r^F(x) \tag{E.2}$$

for the fermions. The operator $\tilde{\partial}_t$ will be of further use later on. It is defined to act exclusively on the shape functions of the regulators in the general fashion

$$\tilde{\partial}_t r(x) := \frac{1}{Z_k} \partial_t \left(Z_k r(x) \right) = -2x r'(x) - \eta_k r(x) \tag{E.3}$$

and ignores all other scale dependencies. The prime denotes a derivative w.r.t. the argument $x := \boldsymbol{p}^2/k^2$. The bosonic parts of the flow then generally evaluate to

$$\begin{aligned} \frac{1}{2} \int_{\boldsymbol{p}} T \sum_n \left. \frac{\partial_t R_{k,\phi}^B}{\Gamma_k^{\sigma\sigma} + R_{k,\phi}^B} \right|_{\langle \Phi \rangle} &= \frac{1}{4\pi^2} \int_0^\infty \mathrm{d}|\boldsymbol{p}| \, \boldsymbol{p}^4 \, T \sum_n \frac{\partial_t r^B - \eta_{\phi,k} r^B}{\omega_n^2 + \boldsymbol{p}^2 (1 + r^B) + 2\bar{U}_k' + 4\bar{\sigma}^2 \bar{U}_k''} \\ &= \frac{1}{4\pi^2} \int_0^\infty \mathrm{d}|\boldsymbol{p}| \, \boldsymbol{p}^4 \, \left(\partial_t r^B - \eta_{\phi,k} r^B \right) \mathcal{M}_\sigma^{(1)} \end{aligned} \tag{E.4}$$

and

$$\begin{aligned}\frac{3}{2}\int_{\boldsymbol{p}} T\sum_n \frac{\partial_t R^B_{k,\phi}}{\Gamma^{\pi\pi}_k + R^B_{k,\phi}}\bigg|_{\langle\Phi\rangle} &= \frac{3}{4\pi^2}\int_0^\infty \mathrm{d}|\boldsymbol{p}|\,\boldsymbol{p}^4\, T\sum_n \frac{\partial_t r^B - \eta_{\phi,k} r^B}{\omega_n^2 + \boldsymbol{p}^2(1+r^B) + 2\bar{U}'_k} \\ &= \frac{3}{4\pi^2}\int_0^\infty \mathrm{d}|\boldsymbol{p}|\,\boldsymbol{p}^4\,\left(\partial_t r^B - \eta_{\phi,k} r^B\right)\mathcal{M}^{(1)}_\pi\ .\end{aligned} \tag{E.5}$$

The factor of 3 in the pion sector comes from the trace in field space, as there are three identical pions. The two equal contributions in fermion field space, see Eq. (A.34), add up to

$$\begin{aligned}&-\int_{\boldsymbol{p}} T\sum_n \mathrm{tr}\left[\frac{\partial_t R^F_k}{\Gamma^{\bar{q}q}_k + R^F_k}\right]\bigg|_{\langle\Phi\rangle} \\ &\qquad= -\frac{N_c N_f}{2\pi^2}\int_0^\infty \mathrm{d}|\boldsymbol{p}|\,\boldsymbol{p}^4\, T\sum_n \frac{(1+r^F)(\partial_t r^F - \eta_{q,k} r^F)}{(\nu_n + \mathrm{i}\mu)^2 + \boldsymbol{p}^2(1+r^F)^2 + \frac{\bar{g}_k^2}{4}\bar{\sigma}^2} \\ &\qquad= -\frac{N_c N_f}{2\pi^2}\int_0^\infty \mathrm{d}|\boldsymbol{p}|\,\boldsymbol{p}^4\,(1+r^F)\left(\partial_t r^F - \eta_{q,k} r^F\right)\mathcal{M}^{(1)}_q\ .\end{aligned} \tag{E.6}$$

Higher Order Couplings

To extract the flow of couplings beyond the effective potential, we need to project these sub-terms out of the effective action by means of the projections defined in Sec. 4.4. Further, it is wise to reformulate the Wetterich equation to facilitate extracting the non-vanishing diagrams contributing to the flow. This can be achieved by using the operator $\tilde{\partial}_t$ defined above:

$$\mathrm{STr}\left[\frac{\partial_t R_k}{\Gamma^{(1,1)}_k + R_k}\right] = \tilde{\partial}_t\,\mathrm{STr}\left[\ln(\Gamma^{(1,1)}_k + R_k)\right]\ . \tag{E.7}$$

Note that $\tilde{\partial}_t$ ignores the scale dependence of the two-point function by definition. Furthermore, we define the fluctuating part of the two-point function

$$\Delta\Gamma^{(1,1)}_k := \Gamma^{(1,1)}_k - \left\langle\Gamma^{(1,1)}_k\right\rangle \tag{E.8}$$

where the second term on the rhs has the expectation values of the fields inserted. This allows us to write

$$\ln(\Gamma^{(1,1)}_k + R_k) = \ln\left(\left\langle\Gamma^{(1,1)}_k\right\rangle + R_k\right) + \ln\left(\mathbb{1} + \frac{\Delta\Gamma^{(1,1)}_k}{\left\langle\Gamma^{(1,1)}_k\right\rangle + R_k}\right)\ . \tag{E.9}$$

Note that all functional derivatives act on the fluctuating fields. Thus, the first term vanishes in any truncation that includes field derivatives and those only act on $\Delta\Gamma^{(1,1)}_k$. Moreover, $\Delta\Gamma^{(1,1)}_k$ vanishes when evaluated at the expectation value by definition. Consequently, a Taylor expansion of the logarithm in the second term of Eq. (E.9) yields only a small number of terms that survive the projection. Explicit example calculations of this can be found in Ref. [141]. A Taylor expansion is also a viable tool to determine the external momentum derivative needed for the wavefunction renormalization flows. One

generically encounters propagators of the form $G_k(p+p_{\text{ext}})$ where p is a loop momentum. Using an expansion around the loop three-momentum (omitting the frequency argument for clarity),

$$G_k(\boldsymbol{p}+\boldsymbol{p}_{\text{ext}}) = \mathrm{e}^{\boldsymbol{p}_{\text{ext}}\cdot\boldsymbol{\nabla}} G_k(\boldsymbol{p}) \ , \tag{E.10}$$

and the additional information that G_k depends only on the length of the momentum vector squared, i.e. $\partial_{p_j} G_k = 2p_j \partial_{\boldsymbol{p}^2} G_k$, together with the generic identity that for a rotationally invariant integrand $I(\boldsymbol{p}^2)$ one has

$$\int_{\boldsymbol{p}} p_i p_j I(\boldsymbol{p}^2) = \frac{1}{3}\delta_{ij} \int_{\boldsymbol{p}} \boldsymbol{p}^2 I(\boldsymbol{p}^2) \ , \tag{E.11}$$

allows for the extraction of the few nonvanishing terms in the projection. More details can be found in Ref. [240]. Using the tools laid out here we obtain the following flows for a general 3d regulator:

Meson anomalous dimension. The meson anomalous dimension is calculated from the projection (4.52) and reads

$$\begin{aligned}
\eta_{\phi,k} = &-\frac{2}{3}\bar{V}_{\pi\sigma\pi}^2 \int_{\boldsymbol{p}} \boldsymbol{p}^2 (1+r^B+xr^{B\prime}) \Big\{ \mathcal{M}_{\sigma\pi}^{(2,2)} 2(\tilde{\partial}_t r^B + \tilde{\partial}_t x r^{B\prime}) \\
&\qquad - \Big[\mathcal{M}_{\sigma\pi}^{(3,2)} + \mathcal{M}_{\sigma\pi}^{(2,3)}\Big] \boldsymbol{p}^2 (1+r^B+xr^{B\prime}) \tilde{\partial}_t r^B \Big\} \\
&- \frac{2}{3} 4 N_c N_f \frac{\bar{g}_k^2}{4} \int_{\boldsymbol{p}} \Big\{ \mathcal{M}_q^{(2)} 2 x r^{F\prime} \tilde{\partial}_t x r^{F\prime} \\
&\qquad + \mathcal{M}_q^{(3)} \boldsymbol{p}^2 \Big[2(1+r^F)^3 \tilde{\partial}_t x r^{F\prime} \\
&\qquad\quad + \Big(4(1+r^F)^3 + 6(1+r^F)^2 x r^{F\prime} - 4(1+r^F) x^2 (r^{F\prime})^2 \Big) \tilde{\partial}_t r^F \Big] \\
&\qquad - \mathcal{M}_q^{(4)} 6 \boldsymbol{p}^4 \Big((1+r^F)^5 + 2(1+r^F)^4 x r^{F\prime} \Big) \tilde{\partial}_t r^F \Big\}
\end{aligned} \tag{E.12}$$

with the renormalized meson three-vertex $\bar{V}_{\pi\sigma\pi} := 4\bar{\sigma}\bar{U}_k''$. Similar to Eq. (E.3), the modified RG time derivatives here also act on the terms xr', for example:

$$\tilde{\partial}_t x r^{B\prime} = (-2x\partial_x - \eta_{\phi,k}) x r^{B\prime} = -2x^2 r^{B\prime\prime} - (2+\eta_{\phi,k}) x r^{B\prime} \ . \tag{E.13}$$

Quark anomalous dimension. In the same fashion, the anomalous dimension of the quarks follows from the projection (4.54):

$$\begin{aligned}
\eta_{q,k} = -\frac{2}{3}\frac{\bar{g}_k^2}{4} \sum_j \int_{\boldsymbol{p}} \boldsymbol{p}^2 \Big\{ &\mathcal{M}_{qj}^{(1,2)} \Big[(1+r^B+xr^{B\prime}) \tilde{\partial}_t r^F + (1+r^F)(\tilde{\partial}_t r^B + \tilde{\partial}_t x r^{B\prime}) \Big] \\
&- \mathcal{M}_{qj}^{(2,2)} 2\boldsymbol{p}^2 (1+r^F)^2 (1+r^B+xr^{B\prime}) \tilde{\partial}_t r^F \\
&- \mathcal{M}_{qj}^{(1,3)} 2\boldsymbol{p}^2 (1+r^F)(1+r^B+xr^{B\prime}) \tilde{\partial}_t r^B \Big\} \ .
\end{aligned} \tag{E.14}$$

The sum goes over the meson fields, i.e. $j \in \{\sigma, \pi, \pi, \pi\}$.

Yukawa coupling. The Yukawa coupling is obtained from projection (4.56). A discussion of different projections is given in the main text. The flow of the bare coupling is given by

$$\partial_t g_k = g_k \frac{\bar{g}_k^2}{4} \int_{\boldsymbol{p}} \boldsymbol{p}^2 \left\{ \left[\mathcal{M}_{q\sigma}^{(1,2)} - \mathcal{M}_{q\pi}^{(1,2)} \right] \tilde{\partial}_t r^B + \left[\mathcal{M}_{q\sigma}^{(2,1)} + \mathcal{M}_{q\pi}^{(2,1)} \right] 2(1+r^F) \tilde{\partial}_t r^F \right\} . \quad \text{(E.15)}$$

Flat regulator flows. A further general note concerns the insertion of the flat regulator. Due to the use of a Heaviside step function in the shape function and the appearance of higher orders and powers of its derivative in above flows, there are nonvanishing contributions due to integrals over terms such as $\Theta(x)\delta(x)$. These expressions can be resolved by reverting to smeared-out versions of the distributions, leading to the formula [241]

$$\lim_{\epsilon \to 0} f(x, \Theta_\epsilon(x))\, \delta_\epsilon(x) = \delta(x) \int_0^1 \mathrm{d}u\, f(0,u) \; . \quad \text{(E.16)}$$

In general, many of above terms vanish with the flat regulator and the remaining expressions are given in Sec. 4.4.

Appendix F

Approximate Flows in the Chirally Symmetric Regime

In Ch. 7 it was argued that approximate flows in the two-flavor quark-meson model exhibit a partial IR fixed point behavior in the chirally symmetric regime. This has been taken advantage of to constrain the effective potential at the chiral symmetry breaking scale k_χ. We detail here the technical derivation of the fixed-point values in a general, regulator-independent way. This follows closely the arguments made in Ref. [158] but generalizes them to regulators that incorporate an additional scale, such as the mass-term regulators (7.6) and (7.7) which depend on k_ϕ. The chain of argument relies on the consideration of vacuum flows in LPA'. At large RG scales $k > k_\chi$, they are dominated by the purely fermionic contributions. Picking up the definitions for $\tilde{\rho}$ and $u_k(\tilde{\rho})$, Eqs. (7.17) and (7.16), the approximate flow of the dimensionless potential at fixed $\tilde{\rho}$ becomes

$$\partial_t u_t(\tilde{\rho}) = -4u_t + (2+\eta_{\phi,t})\,\tilde{\rho}\,u_t'(\tilde{\rho}) - \frac{N_c N_f}{4\pi^2} l_{0,t}^F(\tilde{m}_{q,t}^2)\ . \tag{F.1}$$

To simplify the notation in the upcoming discussion, an explicit scale dependence is now expressed by the RG time $t = \ln(k/k_\phi)$ instead of the corresponding dimensionful scale k in the lower index. The first term in Eq. (F.1) is just the dimensional running, the second term subtracts the flow of $\tilde{\rho}$ and the last term is just the dimensionless fermion loop, now written in terms of the threshold function which reads for 4d regulators

$$l_{0,t}^{F,4\mathrm{d}}(\tilde{m}_{q,t}^2) = \int_0^\infty \mathrm{d}y\, y^2\, \frac{1+r_t^F(y)}{y\left[1+r_t^F(y)\right]^2 + \tilde{m}_{q,t}^2}\,\partial_t r_t^F(y) \tag{F.2}$$

and for 3d regulators

$$l_{0,t}^{F,3\mathrm{d}}(\tilde{m}_{q,t}^2) = 2\int_0^\infty \mathrm{d}x\, x^{3/2}\, \frac{1+r_t^F(x)}{\sqrt{x\left[1+r_t^F(x)\right]^2 + \tilde{m}_{q,t}^2}}\,\partial_t r_t^F(x)\ . \tag{F.3}$$

The dimensionless quark mass is given by

$$\tilde{m}_{q,t}^2 = \frac{\bar{g}_t^2}{2}\tilde{\rho}\ . \tag{F.4}$$

Note the factors in the definitions of the threshold functions have been chosen in agreement with Ref. [158] for better comparability. We allow for an explicit scale dependence

of r_t^F beyond that of its argument $y = p^2/k^2$ or $x = \boldsymbol{p}^2/k^2$, as denoted by the index t. Such a dependence exists, for example, for the mass-term regulators via the dimensionless UV scale $\tilde{k}_\phi := k_\phi/k = \mathrm{e}^{-t}$. If the shape function does not possess an explicit scale dependence, the RG-time derivative can be written $\partial_t r^F(y) = -2y\, r^{F\prime}(y)$ and the corresponding threshold functions $l_n^F(\tilde{m}_{q,t}^2)$ also only depend on t implicitly via the quark-mass argument. By definition, the threshold functions with a larger number of propagators $l_{n,t}^F$ are related to $l_{0,t}^F$ via [158]

$$l_{n,t}^F(\tilde{m}_{q,t}^2) := \frac{(-1)^n}{(n-1)!}\left(\frac{\mathrm{d}}{\mathrm{d}\tilde{m}_{q,t}^2}\right)^n l_{0,t}^F(\tilde{m}_{q,t}^2)\ . \tag{F.5}$$

From Eq. (E.14) we follow that the quark anomalous dimension vanishes in our approximation and from Eq. (E.12) we infer the meson anomalous dimension[1]

$$\eta_{\phi,t} = \frac{N_c N_f}{16\pi^2}\,\bar{g}_k^2\,\kappa_t^F\ . \tag{F.6}$$

κ_t^F denotes the corresponding purely fermionic threshold function evaluated at $\tilde{\rho} = 0$. The flow of the Yukawa coupling is solely fed by its renormalization,

$$\partial_t \bar{g}_t^2 = \eta_{\phi,t}\,\bar{g}_t^2\ . \tag{F.7}$$

This can be seen in Eqs. (E.15) and (4.57). It is an ordinary differential equation with the solution

$$\bar{g}_t^2 = \frac{\bar{g}_0^2}{1 - \frac{N_c N_f}{16\pi^2}\bar{g}_0^2\int_0^t \mathrm{d}s\,\kappa_s^F} \tag{F.8}$$

where g_0 is the initial value at $t = 0$. Instead of finding a full solution[2] for $u_t(\tilde{\rho})$ we immediately assume that a power expansion of the potential around the origin, see Eq. (7.18), is possible. Flow equations for the coefficients $u_t^{(n)}(0)$ can be inferred from Eq. (F.1) and admit simple exact solutions. For $n = 2$, one finds

$$\frac{u_t^{(2)}(0)}{\bar{g}_t^2} = \frac{\frac{u_0^{(2)}(0)}{\bar{g}_0^2} - \frac{N_c N_f}{16\pi^2}\bar{g}_0^2\int_0^t \mathrm{d}s\, l_{2,s}^F(0)}{1 - \frac{N_c N_f}{16\pi^2}\bar{g}_0^2\int_0^t \mathrm{d}s\,\kappa_s^F}\ . \tag{F.9}$$

Note that $\kappa^F = l_2^F(0) \equiv 1$ is attained for any regulator shape function r^F that does not explicitly depend on t. In this case, the solution simplifies to [158]

$$\frac{u_t^{(2)}(0)}{\bar{g}_t^2} = 1 - \frac{1 - \frac{u_0^{(2)}(0)}{\bar{g}_0^2}}{1 - \frac{N_c N_f}{16\pi^2}\bar{g}_0^2\, t} \tag{F.10}$$

and for $t \to -\infty$ approaches the infrared fixed point

$$\left.\frac{u_t^{(2)}(0)}{\bar{g}_t^2}\right|_* = 1\ . \tag{F.11}$$

[1] Eqs. (E.12) and (E.14) specifically assume 3d regulators, but the statements made here hold in general.
[2] Such a solution is given in Ref. [158] for the case of regulators without explicit scale dependence.

For the two mass-term regulators, the same infrared value is approached even though they require the more complex solution (F.9): At large negative RG times t, the UV cutoff parameter $\tilde{k}_\phi = \mathrm{e}^{-t}$ diverges quickly and both κ_t^F and $l_{2,t}^F(0)$ become effectively scale-independent, tending to unity. Thus, the leading contributions to the integrals in Eq. (F.9) behave like t and all subleading terms vanish for $t \to -\infty$. A similar analysis works at all orders $n \geq 3$ where the solution for the expansion coefficients reads

$$\frac{u_t^{(n)}(0)}{\bar{g}_t^{2n}} = \mathrm{e}^{2(n-2)t}\,\frac{u_0^{(n)}(0)}{\bar{g}_0^{2n}} - \frac{N_c N_f}{4\pi^2}\,\frac{(-1)^n(n-1)!}{2^n}\,\mathrm{e}^{2(n-2)t}\int_0^t \mathrm{d}s\, l_{n,s}^F(0)\,\mathrm{e}^{-2(n-2)s}\ . \tag{F.12}$$

In the case of scale-independent threshold functions $l_n^F(0)$, the integral can be solved trivially and the infrared fixed point is given by

$$\left.\frac{u_t^{(n)}(0)}{\bar{g}_t^{2n}}\right|_* = \frac{N_c N_f}{8\pi^2}\,\frac{(-1)^n(n-1)!}{2^n(n-2)}\,l_n^F(0)\ . \tag{F.13}$$

At these orders of the expansion, the threshold functions depend on the explicit choice of shape function, i.e., they yield different fixed points for different regulators. From similar arguments as above, it follows that the infrared-attractive points for the mass-term regulators are determined by inserting the asymptotic threshold functions $l_{n,t\to-\infty}^F(0)$ for $l_n^F(0)$ in Eq. (F.13).

Appendix G

Pole Proximity of Vacuum Flows

In general, nonperturbative flow equations are composed of threshold functions that accommodate prospective singularities governed by the sign of the potential derivatives. A typical phenomenon occurs for vacuum flows in LPA of quark-meson model truncations or related theories on a discretized grid in the σ-field: for small σ-values the pion threshold function is the dominant one towards the IR evolution and the pion mass term $m_\pi^2 = 2U_k'(\sigma^2)$ becomes increasingly negative until it almost enters the pole in the (Euclidean) propagator. For the remaining flow it then runs closely along this regulator-dependent pole [33]. This poses a significant challenge to the numerical implementation as small numerical errors can easily hit this pole. In the following we argue that the proximity of the pion pole can be estimated by analytical means. We rely on the regulator choices introduced in Ch. 7. With the effective inverse pion propagator in LPA given for a general (4-dimensional) regulator function by

$$\Gamma_k^{(\pi\pi)}(p^2) + R_k(p^2) = k^2 P^2(p^2/k^2) + m_\pi^2 \ , \tag{G.1}$$

see Eq. (3.48) for the definition of P^2, and using positivity of the first term, we conclude that a pole is encountered in the momentum loop as soon as m_π^2 falls below a threshold given by the negative of the massless propagator gap,

$$m_{\pi,\text{thresh}}^2 = -k^2 \min_{y\geq 0} P^2(y) \ . \tag{G.2}$$

This argument can easily be generalized to dimensionally reduced regulators, i.e., to a 3d regulator where the modified two-point function is given by

$$\Gamma_k^{(\pi\pi)}(p_0, \boldsymbol{p}^2) + R_k(\boldsymbol{p}^2) = p_0^2 + k^2 P^2(\boldsymbol{p}^2/k^2) + m_\pi^2 \ . \tag{G.3}$$

It is easy to see that the condition (G.2) still holds. Furthermore, in the following discussion we always assume the potential and its derivatives to be evaluated at vanishing field, i.e., $U_k := U_k(\sigma = 0)$ etc., in which case the sigma field degenerates with the three pions.

3d Flat Regulator

Due to the simple structure of its flow equation, we first regard the 3d flat regulator. Since $P_{\text{flat}}^2(y) = 1$ for $0 \leq y \leq 1$, the pole is located at $U_k' = -k^2/2$, which can also easily be read off from Eq. (7.14). Utilizing the modified dimensionless potential derivative,

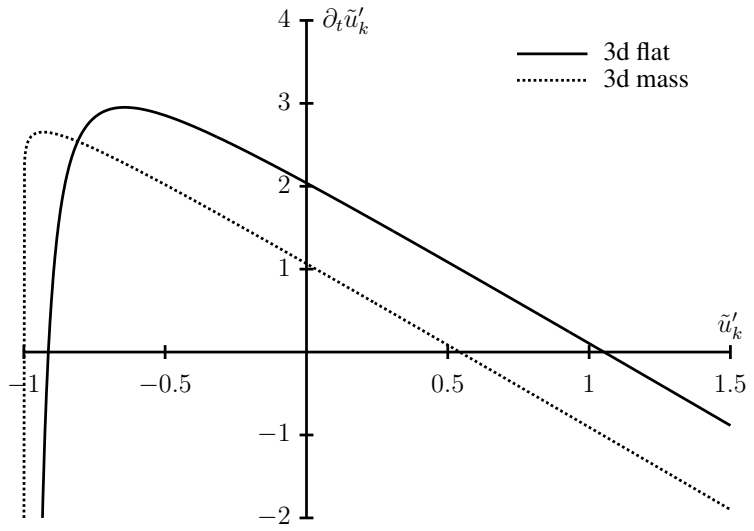

Figure G.1: Flow of the modified dimensionless first derivative of the effective potential at $\sigma = 0$, $\tilde{u}'_k$, for the two 3d regulators, cf. Eqs. (G.4) and (G.6). U''_k and—in case of the mass term regulator—$\tilde{k}_\phi$ are set to unity.

$\tilde{u}'_k := 2U'_k/k^2$, the pion propagator pole is located at $\tilde{u}'_k = -1$ and the corresponding flow equation is given by

$$\begin{aligned} \partial_t \tilde{u}'_k &= 2(\partial_t U'_k)/k^2 - 2\tilde{u}'_k \\ &= \frac{1}{\pi^2}\left[-\frac{U''_k}{(1+\tilde{u}'_k)^{3/2}} + \frac{\nu}{12}\left(\frac{g}{2}\right)^2\right] - 2\tilde{u}'_k \ . \end{aligned} \tag{G.4}$$

Setting $\partial_t \tilde{u}'_k = 0$ yields an equation for the stationary points of the flow. Clearly, several cases need to be distinguished:

$\boldsymbol{U''_k \leq 0}$**.**[1] There is always exactly one solution $\tilde{u}'^{(1)}_k$ to this equation which is located at $\tilde{u}'_k > 0$, with the flow becoming negative for $\tilde{u}'_k > \tilde{u}'^{(1)}_k$ and positive for $\tilde{u}'_k < \tilde{u}'^{(1)}_k$. Since the flow is integrated in negative t-direction, $\tilde{u}'^{(1)}_k$ takes the role of a repulsive point. Hence, in the former case $\tilde{u}'_k$ becomes increasingly positive (no chiral symmetry breaking), while in the latter case it runs into the pole. Note that these stationary points are not actually fixed points in the sense that they still depend on k via U''_k. Thus, the position of $\tilde{u}'_k$ in relation to those points can change in the course of the flow.

$\boldsymbol{U''_k > 0}$ **and sufficiently large.** $\partial_t \tilde{u}'_k$ becomes negative for all values of $\tilde{u}'_k$, which pushes $\tilde{u}'_k$ to positive values and again inhibits chiral symmetry breaking.

$\boldsymbol{U''_k > 0}$ **but small enough to allow for two stationary points.** This is the physically most interesting case, see the solid line in Fig. G.1 where $\partial_t \tilde{u}'_k$ is plotted for $U''_k = 1$ and the parameters $\nu = 24$ and $g = 6.5$ used in this work. Let us denote the two stationary points as $\tilde{u}'^{(0)}_k$ and $\tilde{u}'^{(1)}_k$. While $\tilde{u}'^{(1)}_k$ still has the same features of a repulsive point as for

[1] Since U''_k itself is dimensionless, we have kept the notation in terms of the dimensionful potential U_k.

$U_k'' \leq 0$, $\tilde{u}_k'^{(0)}$ is an attractive point for the flow. As long as $\tilde{u}_k' < \tilde{u}_k'^{(1)}$, it is always pushed towards $\tilde{u}_k'^{(0)}$ and thus never runs into the pole. However, $\tilde{u}_k'^{(0)}$ is usually located close to the pole at value -1: for $U_k'' = 1$ the stationary points have been numerically determined to be $\tilde{u}_k'^{(0)} \approx -0.9133$ and $\tilde{u}_k'^{(1)} \approx 1.053$. This explains the numerical observation of the flow running in the vicinity of the pole.

With the potential becoming convex in the infrared [33], the second derivative U_k'' tends to zero. From Eq. (G.4) it is clear that this moves the stationary point even closer to the pole. A good estimate can be obtained by defining $\tilde{u}_k' = -1 + \delta_u$ and multiplying both sides in Eq. (G.4) with $\delta_u^{3/2}$. Again setting $\partial_t \tilde{u}_k' = 0$ and expanding to lowest order in δ_u, we find

$$\delta_u \approx \left[\frac{U_k''}{2\pi^2 + \frac{\nu}{12}\left(\frac{g}{2}\right)^2} \right]^{2/3} . \tag{G.5}$$

For $U_k'' = 1$ this yields $\delta_u \approx 0.0843$ which is in agreement with the previous numerical determination of $\tilde{u}_k'^{(0)}$ to an error of less than 1%.

3d and 4d Mass-term Regulators

This analysis becomes much more relevant in case of the mass-term regulator. Since the pole is also reached for $U_k' = -k^2/2$, we can essentially reuse all definitions from above. The vacuum flow of $\tilde{u}_k'$ in the 3d version then reads

$$\begin{aligned} \partial_t \tilde{u}_k' = &- \frac{3U_k''}{\pi^2} \left[-\frac{\tilde{k}_\phi}{\sqrt{\tilde{k}_\phi^2 + 1 + \tilde{u}_k'}} + \operatorname{arcsinh}\left(\frac{\tilde{k}_\phi}{\sqrt{1 + \tilde{u}_k'}} \right) \right] \\ &+ \frac{\nu}{4\pi^2} \left(\frac{g}{2}\right)^2 \left[-\frac{\tilde{k}_\phi}{\sqrt{\tilde{k}_\phi^2 + 1}} + \operatorname{arcsinh}(\tilde{k}_\phi) \right] - 2\tilde{u}_k' \end{aligned} \tag{G.6}$$

with the dimensionless UV regularization parameter $\tilde{k}_\phi := k_\phi / k \geq 1$ which increases towards the infrared. Despite its more complex analytic structure, the flow exhibits the same qualitative features as the dotted line in Fig. G.1 shows. However, for $U_k'' = 1$ and $\tilde{k}_\phi = 1$, $\tilde{u}_k'^{(0)}$ already moves significantly closer to the pole than for the flat regulator. Setting $\partial_t \tilde{u}_k' = 0$, an expansion in δ_u to lowest order is possible after exponentiating both sides in Eq. (G.6) which yields

$$\delta_u \approx \tilde{k}_\phi^2 \exp\left\{ -2[1 - \ln(2)] - \frac{4\pi^2}{3U_k''} - \frac{\nu}{6U_k''}\left(\frac{g}{2}\right)^2 \left[\operatorname{arcsinh}(\tilde{k}_\phi) - \frac{\tilde{k}_\phi}{\sqrt{\tilde{k}_\phi^2 + 1}} \right] \right\} . \tag{G.7}$$

Already for $U_k'' = 1$ (and $\tilde{k}_\phi = 1$) one finds $\delta_u \approx 6.619 \times 10^{-10}$, with a further exponential suppression with decreasing U_k'' as compared to the power law behavior of the

flat regulator. This does not improve much in the 4d case either, where

$$\begin{aligned}\partial_t \tilde{u}'_k = &-\frac{3U''_k}{2\pi^2}\left[-\frac{1}{1+\frac{1+\tilde{u}'_k}{\tilde{k}^2_\phi}}+\ln\left(1+\frac{\tilde{k}^2_\phi}{1+\tilde{u}'_k}\right)\right] \\ &+\frac{\nu}{8\pi^2}\left(\frac{g}{2}\right)^2\left[-\frac{1}{1+\tilde{k}^{-2}_\phi}+\ln(1+\tilde{k}^2_\phi)\right]-2\tilde{u}'_k\end{aligned} \tag{G.8}$$

and

$$\delta_u \approx \frac{\tilde{k}^2_\phi}{\exp\left\{\frac{1}{3U''_k}\left[4\pi^2+\frac{\nu}{4}\left(\frac{g}{2}\right)^2\left(-\frac{1}{1+\tilde{k}^{-2}_\phi}+\ln(1+\tilde{k}^2_\phi)\right)\right]+1\right\}-1} \tag{G.9}$$

yields $\delta_u \approx 1.198 \times 10^{-8}$ for the same parameters.

Already in Ref. [117] it was shown that an optimized regulator according to criterion (3.50) pushes the propagator poles as far down on the negative U'_k axis as possible and speculated that such regulators, in particular the flat regulator, thus lead to the smoothest and numerically most stable flow. For the mass-term regulator, the issue of a very close pion pole proximity seems to be particularly grave. As shown above, for $k \to 0$ the first derivative moves arbitrarily close to the pole. In the future, the analytic estimates for $\tilde{u}'^{(0)}_k$ obtained here could also be used to stabilize the numerical setup.

Appendix H

Numerical Solution Techniques

Numerical calculations for this thesis have generally been implemented in C++, making use of costum implementations of, e.g., vector and matrix classes as well as adaptions of widespread numerical algorithms found in publications such as Ref. [242]. The numerical methods employed for the solution of the FRG flow equations and for the TOV equations are outlined in this appendix. FRG flow equations are partial differential equations (PDEs) including a partial derivative w.r.t. the RG scale k and field derivatives encoded in the mass terms. For $N_f = 2$, these field derivatives are confined to one dimension, the light sigma field. Most research in the field so far has also been done for flows in one field dimension. Hence, we start discussing this case and follow up with additional points and extensions:

One-dimensional grid. Traditionally, these flows have been solved on equidistant grids in the field variable σ or σ^2, with field derivatives obtained from finite differences, coupled Taylor approximations [243, 244], or cubic splines [155, 245]. Global approaches with pseudo-spectral methods have also been employed [246]. Recently, it has been shown that such PDEs which result from Wetterich flows in LPA can be recast into another shape: by a reformulation in terms of a flow for the first potential derivative $\partial_t U_k'$ a conservative form with distinct convective and diffusive fluxes can be obtained [247]. This admits a modern treatment within a hydrodynamic framework, utilizing finite volume methods [248–251] or more advanced setups like discontinuous Galerkin methods [32, 247]. Especially, shocks that occur in the flow with a flat regulator due to the discontinuity at the Fermi surface can be resolved in great detail within such a novel framework. However, in a first detailed study of the phase diagram of the quark-meson model based on discontinuous Galerkin methods [32] a similar phase structure to traditional approaches is found and the back-bending behavior of the chiral transition line at finite densities is confirmed. We therefore retain a more well-tried, computationally less expensive setup with a simpler implementation based on a cubic spline over a grid of points equidistantly distributed in σ-field space. The two missing boundary conditions for the spline are obtained by fixing the first derivative at the left- and rightmost points of the interval via a three-point finite difference stencil. The chosen interval is $\sigma \in [0, 170\,\mathrm{MeV}]$, and $n = 40$ grid points are used in most cases, with up to 80 points for the computation of the crossover lines. Furthermore, the $N_f = 2$ results in Ch. 6 have been obtained with an upwind finite difference scheme [247]. All results in Ch. 7 have been cross-checked with the Taylor–grid method as outlined in Ref. [243]. In all cases, reasonable agreement within the methods has been observed. The

solution of the remaining coupled set of ordinary differential equations (ODEs) resulting from these procedures is then performed with an explicit higher-order Runge-Kutta type ODE stepper with adaptive stepsize [252].

Two-dimensional grid. For $N_f = 2 + 1$, a two-dimensional setup is required. We employ a grid for the chiral potential in the variables

$$x = \sigma_l^2 \quad \text{and} \quad y = 2\sigma_s^2 - \sigma_l^2 \ , \tag{H.1}$$

and again interpolate the derivatives with (clamped) cubic splines as outlined in Ref. [155]. We also use three- and five-point stencils to fix the first derivative at the edges of the grid and generally obtain the mixed derivative $\partial_x \partial_y$ by an appropriate three-point formula applied on the x-derivatives in y-direction or vice versa.

Treatment of numerical errors at small pressures. In the context of this work, especially the $T = 0$ limit of the flow equations is oftentimes utilized wherein the fermionic threshold functions reduce to Heaviside functions. This also encodes the Silver-Blaze property of the theory because

$$E_l \geq m_l = g\sigma_l/2 \tag{H.2}$$

implies that $\Theta(E_f - \mu) = 1$ for all $\mu < m_f$ and hence the flow at the IR minimum σ_l does not change with respect to the vacuum flow. Here we have assumed for simplicity a flavor-independent chemical potential. Of course, this property only holds for $\mu < \mu_c$ where μ_c signifies the chiral first-order transition. In both the sMFA and FRG solutions, we observe $\mu_c < m_l$, cf. Fig. 4.2b. Unfortunately, due to the utilized grid method the Silver-Blaze property is subject to a numerical error. For any chemical potential, all grid points located at $\sigma_l < 2\mu/g$ display a different running than in vacuum. Since the bosonic energies incorporate field derivatives that are approximated from an interpolation of all grid points, the flow experiences small modifications at the IR minimum even if $\mu < m_l$. This effect aggravates when μ approaches m_l from below, $\mu \lesssim m_l$. It leads to fluctuations of the chiral condensate around the vacuum IR value. Those fluctuations are small and hardly visible in Fig. 4.2b. However, they lead to an unphysical phase of very small but nonzero pressure. Furthermore, for a flavor-dependent chemical potential the first-order transition is additionally distorted by the error of our approximation, see Ch. 5. Thus, in the numerical treatment of the FRG EoS in Chs. 5 and 6, data points close to the phase transition are omitted and the EoS from the physical phase with restored chiral symmetry is polynomially extrapolated down to $p = 0$. This procedure only affects the low-pressure outer region of the calculated pure quark stars. The dependence of the star radius on the extrapolation error has been checked and found to be negligible.

Numerical fluctuations in the speed of sound. For $N_f = 2 + 1$, similar numerical fluctuations as discussed above are also found when μ_s approaches the order of the strange quark mass m_s at the current IR minimum. They are most prevalent in the determination of the speed of sound. A strong dependence of these fluctuations on the exact grid point configuration is observed and gives strong evidence for the claim as a numerical artifact. Therefore, in Fig. 5.4a for $\mu > 350$ MeV only the average derivative $\bar{c}_s^2 := \Delta p/\Delta\varepsilon$ is shown as dots, uniformly spaced at a distance of 15 MeV. For each dot, $\bar{c}_s^2$ has been calculated from the (p, ε) tupels at the dot to its left, itself, and the dot to its right. Furthermore,

the highest deviation of the microscopically calculated, fluctuating speed of sound c_s^2 from $\bar{c}_s^2$ in the respective interval is indicated by the border points of the shaded region such that all c_s^2 data points lie within this region.

Combined mean-field and FRG approach with vector mesons. Adding vector mesons (see Ch. 6) presents the additional challenge of solving for multiple gap equations (6.9) simultaneously, whereas for each trial point a full FRG flow equation in the (pseudo)scalar sector has to be solved. In order to retain reasonable computation times, we solve the vector meson gap equations by computing data points on a discrete set of vector meson condensates and interpolating key quantities like the number densities (6.10). This allows us to use the same basic set of points for all coupling strengths. The same process is used for the electron chemical potential to satisfy charge neutrality, see Eq. (5.2). Instead of keeping the interpolated values for the equation of state, we then calculate new data points with the appropriate shifts in the chemical potentials inserted. This way, we have a method to check to what extent the gap equations and charge neutrality condition are actually fulfilled and to thereby gauge the quality of the interpolation.

Solving the TOV equation. In the neutron star calculations, the TOV equation, just like the discretized flow equation, is solved with an explicit Runge-Kutta algorithm. The evolution is stopped when the radial pressure $p(r)$ reaches a value of 10^{-5} (Ch. 5), 10^{-8} (pure quark matter in Ch. 6), or 10^{-10} (hybrid construction in Ch. 6) relative to the central pressure. The EoS data points are interpolated with cubic splines (quark stars) or linearly (hybrid stars), utilizing two separate interpolations in case of a discontinuity due to a first-order transition.

General minimization and integration. Both the potentials in mean-field approximation and the infrared potentials in the FRG framework must be minimized. Note that the explicit symmetry-breaking terms guarantee that the global minimum will never be at exactly vanishing fields, i.e., the global minimum is also always a local minimum even in a parameterization in terms of the field squared. For numerical precision, we generally determine all extrema by applying standard root-finding algorithms [242] to the derivative of the potential and then determining the global minimum among the candidates. In two dimensions, we additionally apply a minimization algorithm on the potential and start from multiple points in field space to ensure that the global minimum is found. Integrals are mostly solved with a Romberg integration routine [242].

Appendix I

Parameter Fixing

In this appendix the input parameters for the FRG and mean-field evaluations in Chs. 4, 5, and 6 are summarized. For further information see also Ref. [65, 155]. Note that the parameter setup for Ch. 7 is discussed explicitly in Sec. 7.2 of the main text. In the rest of the work, the following setup has been used:

Parameterized chiral potential. The chiral potentials are parameterized as follows: in MFA, for $N_f = 2+1$ the chiral potential reads

$$U_{\mathrm{mes}}^{(2+1)}(\rho_1, \rho_2) = m^2\rho_1 + \lambda_1\rho_1^2 + \lambda_2\rho_2 \tag{I.1}$$

and for $N_f = 2$ it follows analogously as

$$U_{\mathrm{mes}}^{(2)}(\phi^2) = \frac{m^2}{2}\phi^2 + \frac{\lambda}{4}\phi^4 \ . \tag{I.2}$$

In the FRG setup, we use the same definitions but for $N_f = 2+1$ we instead multiply the factor λ_2 with the modified invariant $\tilde{\rho}_2 := \rho_2 - \rho_1^2/3$:

$$U_{\Lambda}^{(2+1)}(\rho_1, \tilde{\rho}_2) = m^2\rho_1 + \lambda_1\rho_1^2 + \lambda_2\tilde{\rho}_2 \ . \tag{I.3}$$

Fixing the chiral parameters. In the following, we only discuss the case $N_f = 2+1$, with $N_f = 2$ following trivially by leaving out quantities and particles with strange content. The three free parameters in the ultraviolet chiral potential are fixed by the (broad) sigma meson resonance mass which is chosen as $m_\sigma = 560$ MeV and the two vacuum condensates $\sigma_l = f_\pi = 92.4$ MeV and $\sigma_s = (2f_K - f_\pi)/\sqrt{2} = 94.5$ MeV. The latter relations include the pion and kaon decay constants f_π and $f_K = 113$ MeV and are derived from partially conserved axial vector current (PCAC) relations. The constituent light and strange quark masses follow from the single Yukawa coupling $g = 6.5$, i.e., $m_l = g\sigma_l/2 \approx 300$ MeV and $m_s = g\sigma_s/\sqrt{2} \approx 434$ MeV. For $N_f = 2$, we proceed in an analogous fashion.

Numerical optimization. The parameter sets for the FRG and rMFA flow equations have been optimized numerically by a global differential evolution algorithm [253] with an initial UV cutoff of $\Lambda = 1$ GeV. In the full FRG case we stop the evolution at $k_{\mathrm{IR}} = 80$ MeV where the condensates are already frozen and in the rMFA case we stop at $k_{\mathrm{IR}} = 1$ MeV. Note that all obtained numerical results are insensitive to IR values when chosen in this

region while a UV cutoff dependence for the rMFA results can still be seen. However, when choosing a UV cutoff larger than $\Lambda > 2$ GeV for the rMFA results any cutoff dependence disappears [31]. The used input parameters for the mean-field potentials can be found in Tab. I.1. The UV coefficients a_{ij} for the chiral potentials in the FRG calculations are listed in Tab. I.2.

N_f	approx.	$m^2\,[\mathrm{MeV}^2]$	λ_1	λ_2
2	sMFA	$-(358.1)^2$	17.25	
2	rMFA	901.09^2	-5.38	
2	LPA	706.31^2	10.58	
2+1	sMFA	384.71^2	-0.36	46.48
2+1	rMFA	1040.94^2	-2.65	11.73
2+1	LPA	515.70^2	18.73	47.68

Table I.1: Input parameters for the chiral potential in the $N_f = 2$ and $N_f = 2 + 1$ quark-meson model for the sMFA and rMFA as well as the FRG solution in LPA. In the latter case, the λ_2 coefficient is multiplied with the modified chiral invariant $\tilde{\rho}_2$ as defined in the main text. For $N_f = 2$, we have $\lambda_1 \equiv \lambda$ and no second invariant.

Fixed explicit symmetry breaking parameters. The finite pseudoscalar masses of the pions, $m_\pi = 138$ MeV, and kaons, $m_K = 496$ MeV, are fixed via the explicit chiral symmetry breaking terms $c_l = (120.73\,\mathrm{MeV})^3$ and $c_s = (336.41\,\mathrm{MeV})^3$. These numerical values arise from the gap equations, i.e., the vanishing derivative of the total effective infrared potential

$$\left.\frac{\partial \tilde{U}_{\mathrm{IR}}}{\partial \sigma_l}\right|_{\langle\Phi\rangle} = 0 = \left.\frac{\partial \tilde{U}_{\mathrm{IR}}}{\partial \sigma_s}\right|_{\langle\Phi\rangle} \tag{I.4}$$

which yields

$$c_l = f_\pi m_\pi^2\ , \quad c_s = \sqrt{2} f_K m_K^2 - \frac{1}{\sqrt{2}} f_\pi m_\pi^2 \tag{I.5}$$

where the expressions for the masses (cf. Ref. [155]) and numerical fixes for the field expectation values from above have been inserted. Without an explicit symmetry breaking all pseudoscalar masses would vanish in a chirally invariant or spontaneously broken theory due to the Goldstone theorem [254]. Note that in our procedure the curvature masses are fixed, and not the pole masses. In LPA, the pole masses are equal to the curvature masses; however, by solving the flow for the two-point function more momentum resolution can be gained and the parameters can be fixed to a differing pole mass [127]. The summed squares of the η and η' masses $m_\eta^2 + m_{\eta'}^2 = (1103.2\,\mathrm{MeV})^2$ are reproduced with the axial $U(1)_A$ symmetry breaking parameter $c_A = 4807.84$ MeV which can be determined analytically in sMFA and has been taken over for the other calculations as well.

Beyond local potential approximation. In LPA', the renormalized running Yukawa coupling needs to be fixed additionally such that it reaches the value $\bar{g}_{\mathrm{IR}} = 6.5$ in the infrared and yields the same vacuum quark masses as the other truncations. Since the

approx.	m^2 [MeV^2]	λ	g	c [MeV^3]
static	665.85^2	50.28	8.01	133.22^3
co-moving	1116.1^2	271.4	11.92	154.26^3

Table I.2: Bare UV parameters for the $N_f = 2$ quark-meson model solution in LPA' in the static and co-moving approximations. The potential is parameterized similarly to its LPA counterpart. The bare Yukawa coupling and explicit symmetry-breaking term c are additionally required.

absolute values of the wavefunction renormalizations do not occur in the flows, they do not have to be fixed, but it is customary to set them to unity in the UV, such that all quantities at this scale can be identified as bare quantities. Note that the bare explicit breaking term now has to be fixed as well such that the correct renormalized one is obtained in the infrared; its running is trivially determined by the anomalous dimension. Further note that the UV scale for the LPA' calculations has been chosen as $\Lambda = 900\,\text{MeV}$ which slightly differs from the choice in the LPA calculations. All relevant starting values are given in Tab I.2.

Bibliography

[1] K. Otto, M. Oertel, and B.-J. Schaefer, *Hybrid and quark star matter based on a non-perturbative equation of state,* Phys. Rev. D **101**, 103021 (2020), arXiv:1910.11929.

[2] K. Otto, M. Oertel, and B.-J. Schaefer, *Nonperturbative quark matter equations of state with vector interactions,* Eur. Phys. J. ST **229**, 3629 (2020), arXiv:2007.07394.

[3] A. Aspect, *From Huygens' waves to Einstein's photons: Weird light,* Comptes Rendus Physique **18**, 498 (2017).

[4] N. Bohr, *I. On the constitution of atoms and molecules,* The London, Edinburgh, and Dublin Philosophical Magazine and Journal of Science **26**, 1 (1913).

[5] A. Einstein, *Zur Elektrodynamik bewegter Körper,* Annalen der Physik **322**, 891 (1905).

[6] S.-I. Tomonaga, *On a relativistically invariant formulation of the quantum theory of wave fields.* Progress of Theoretical Physics **1**, 27 (1946).

[7] J. Schwinger, *Quantum Electrodynamics. I. A Covariant Formulation,* Phys. Rev., **74**, 1439 (1948).

[8] R. P. Feynman, *Space-Time Approach to Quantum Electrodynamics,* Phys. Rev., **76**, 769 (1949).

[9] M. Gell-Mann, *Symmetries of baryons and mesons,* Physical Review **125**, 1067 (1962).

[10] M. Gell-Mann, *A Schematic Model of Baryons and Mesons,* Phys.Lett., **8**, 214 (1964).

[11] P. W. Higgs, *Broken Symmetries and the Masses of Gauge Bosons,* Phys. Rev. Lett., **13**, 508 (1964).

[12] F. Englert and R. Brout, *Broken Symmetry and the Mass of Gauge Vector Mesons,* Phys. Rev. Lett., **13**, 321 (1964).

[13] G. S. Guralnik, C. R. Hagen, and T. W. B. Kibble, *Global Conservation Laws and Massless Particles,* Phys. Rev. Lett., **13**, 585 (1964).

[14] G. Aad et al. [ATLAS], *Observation of a new particle in the search for the Standard Model Higgs boson with the ATLAS detector at the LHC,* Phys. Lett. B, **716**, 1 (2012), arXiv:1207.7214.

[15] S. Chatrchyan et al. [CMS], *Observation of a New Boson at a Mass of 125 GeV with the CMS Experiment at the LHC,* Phys. Lett. B, **716**, 30 (2012), arXiv:1207.7235.

[16] A. Deur, S. J. Brodsky, and G. F. de Teramond, *The QCD Running Coupling,* Nucl. Phys., **90**, 1 (2016), arXiv:1604.08082.

[17] P. de Forcrand, *Simulating QCD at finite density,* PoS, **LAT2009**, 010 (2009), arXiv:1005.0539.

[18] F. Gao and J. M. Pawlowski, *QCD phase structure from functional methods,* Phys. Rev. D **102**, 034027 (2020), arXiv:2002.07500.

[19] P. J. Gunkel and C. S. Fischer, *Locating the critical endpoint of QCD: Mesonic backcoupling effects,* Phys. Rev. D **104**, 054022 (2021), arXiv:2106.08356.

[20] W.-j. Fu, J. M. Pawlowski, and F. Rennecke, *QCD phase structure at finite temperature and density,* Phys. Rev. D **101**, 054032 (2020), arXiv:1909.02991.

[21] K. Fukushima, J. M. Pawlowski, and N. Strodthoff, *Emergent Hadrons and Diquarks,* arXiv:2103.01129.

[22] W. Pauli, *Über den Zusammenhang des Abschlusses der Elektronengruppen im Atom mit der Komplexstruktur der Spektren,* Z. Physik, **31**, 765 (1925).

[23] A. Einstein, *Die Grundlage der allgemeinen Relativitätstheorie,* Annalen der Physik **354**, 769 (1916).

[24] J. M. Lattimer and M. Prakash, *Neutron Star Observations: Prognosis for Equation of State Constraints,* Phys. Rept., **442**, 109 (2007), arXiv:astro-ph/0612440.

[25] M. Drews and W. Weise, *From asymmetric nuclear matter to neutron stars: a functional renormalization group study,* Phys. Rev. C **91**, 035802 (2015), arXiv:1412.7655.

[26] P. Pósfay, G. G. Barnaföldi, and A. Jakovác, *The effect of quantum fluctuations in compact star observables,* Publ. Astron. Soc. Austral., **35**, 19 (2018), arXiv:1710.05410.

[27] M. Leonhardt, M. Pospiech, B. Schallmo, J. Braun, C. Drischler, K. Hebeler, and A. Schwenk, *Symmetric nuclear matter from the strong interaction,* arXiv:1907.05814.

[28] O. Hajizadeh and A. Maas, *A G2-QCD neutron star,* PoS, **LATTICE2016**, 358 (2016), arXiv:1609.06979.

[29] S.-S. Xu, Y. Yan, Z.-F. Cui, and H.-S. Zong, *2+1 flavors QCD equation of state at zero temperature within Dyson–Schwinger equations,* Int. J. Mod. Phys. **A30**, 1550217 (2015), arXiv:1506.06846.

[30] T. Ishii, M. Järvinen, and G. Nijs, *Cool baryon and quark matter in holographic QCD,* JHEP, **07**, 003 (2019), arXiv:1903.06169.

[31] S. Carignano, M. Buballa, and B.-J. Schaefer, *Inhomogeneous phases in the quark-meson model with vacuum fluctuations,* Phys. Rev. D, **90**, 014033 (2014), 1404.0057.

[32] E. Grossi, F. J. Ihssen, J. M. Pawlowski, and N. Wink, *Shocks and quark-meson scatterings at large density,* Phys. Rev. D **104**, 016028 (2021), arXiv:2102.01602.

[33] B.-J. Schaefer and J. Wambach, *The Phase diagram of the quark meson model,* Nucl. Phys., **A757**, 479 (2005), arXiv:nucl-th/0403039.

[34] R.-A. Tripolt, B.-J. Schaefer, L. von Smekal, and J. Wambach, *Low-temperature behavior of the quark-meson model,* Phys. Rev. **D97**, 034022 (2018), arXiv:1709.05991.

[35] M. E. Peskin and D. V. Schroeder, *An introduction to quantum field theory* (Perseus Books, Reading, 1995).

[36] S. M. Carroll, *Spacetime and geometry. An introduction to general relativity* (Pearson, 2004).

[37] J. Schaffner-Bielich, *Compact Star Physics* (Cambridge University Press, 2020).

[38] B. Friman, C. Hohne, J. Knoll, S. Leupold, J. Randrup, R. Rapp, and P. Senger, *The CBM physics book: Compressed baryonic matter in laboratory experiments,* Lect. Notes Phys., **814** (2011).

[39] O. Philipsen, *Lattice Constraints on the QCD Chiral Phase Transition at Finite Temperature and Baryon Density,* Symmetry **13**, 2079 (2021), arXiv:2111.03590.

[40] G. Baym, T. Hatsuda, T. Kojo, P. D. Powell, Y. Song, and T. Takatsuka, *From hadrons to quarks in neutron stars: a review,* Rept. Prog. Phys. **81**, 056902 (2018), arXiv:1707.04966.

[41] L. D. Faddeev and V. N. Popov, *Feynman diagrams for the Yang-Mills field,* Physics Letters B **25**, 29 (1967).

[42] C. Becchi, A. Rouet, and R. Stora, *Renormalization of Gauge Theories,* Annals Phys., **98**, 287 (1976).

[43] I. V. Tyutin, *Gauge Invariance in Field Theory and Statistical Physics in Operator Formalism,* arXiv:0812.0580.

[44] V. N. Gribov, *Quantization of Nonabelian Gauge Theories,* Nucl. Phys. B, **139**, 1 (1978).

[45] D. Zwanziger, *Local and Renormalizable Action From the Gribov Horizon,* Nucl. Phys. B, **323**, 513 (1989).

[46] A. Maas, *Describing gauge bosons at zero and finite temperature,* Phys. Rept., **524**, 203 (2013), arXiv:1106.3942.

[47] J. C. Ward, *An Identity in Quantum Electrodynamics,* Phys. Rev., **78**, 182 (1950).

[48] Y. Takahashi, *On the generalized Ward identity,* Nuovo Cim., **6**, 371 (1957).

[49] A. A. Slavnov, *Ward Identities in Gauge Theories,* Theor. Math. Phys., **10**, 99 (1972).

[50] J. C. Taylor, *Ward Identities and Charge Renormalization of the Yang-Mills Field,* Nucl. Phys. B, **33**, 436 (1971).

[51] J. M. Pawlowski, *Aspects of the functional renormalisation group,* Annals Phys., **322**, 2831 (2007), arXiv:hep-th/0512261.

[52] A. K. Cyrol, M. Mitter, J. M. Pawlowski, and N. Strodthoff, *Nonperturbative quark, gluon, and meson correlators of unquenched QCD,* Phys. Rev. **D97**, 054006 (2018), arXiv:1706.06326.

[53] A. K. Cyrol, L. Fister, M. Mitter, J. M. Pawlowski, and N. Strodthoff, *Landau gauge Yang-Mills correlation functions,* Phys. Rev. **D94**, 054005 (2016), arXiv:1605.01856.

[54] A. K. Cyrol, M. Mitter, J. M. Pawlowski, and N. Strodthoff, *Nonperturbative finite-temperature Yang-Mills theory,* Phys. Rev. D **97**, 054015 (2018), arXiv:1708.03482.

[55] H. D. Trottier and R. M. Woloshyn, *Flux tubes in three-dimensional lattice gauge theories,* Phys. Rev. D, **48**, 2290 (1993), arXiv:hep-lat/9303008.

[56] G. S. Bali, H. Neff, T. Duessel, T. Lippert, and K. Schilling [SESAM], *Observation of string breaking in QCD,* Phys. Rev. D, **71**, 114513 (2005), arXiv:hep-lat/0505012.

[57] C.-N. Yang and R. L. Mills, *Conservation of isotopic spin and isotopic gauge invariance,* Physical review **96**, 191 (1954).

[58] D. Zwanziger, *Fundamental modular region, Boltzmann factor and area law in lattice gauge theory,* Nucl. Phys. B, **412**, 657 (1994).

[59] T. Kugo and I. Ojima, *Local Covariant Operator Formalism of Nonabelian Gauge Theories and Quark Confinement Problem,* Prog. Theor. Phys. Suppl., **66**, 1 (1979).

[60] S. L. Adler, *Axial-vector vertex in spinor electrodynamics,* Physical Review **177**, 2426 (1969).

[61] J. S. Bell and R. Jackiw, *A PCAC puzzle: $\pi^0 \to \gamma\gamma$ in the σ model,* Nuovo Cim. A, **60**, 47 (1969).

[62] R. D. Peccei, *The Strong CP problem and axions,* Lect. Notes Phys., **741**, 3 (2008), arXiv:hep-ph/0607268.

[63] A. Andronic, P. Braun-Munzinger, K. Redlich, and J. Stachel, *Decoding the phase structure of QCD via particle production at high energy,* Nature **561**, 321 (2018), arXiv:1710.09425.

[64] M. Asakawa and K. Yazaki, *Chiral Restoration at Finite Density and Temperature,* Nucl. Phys. A, **504**, 668 (1989).

[65] B.-J. Schaefer and M. Wagner, *The Three-flavor chiral phase structure in hot and dense QCD matter,* Phys. Rev., **D79**, 014018 (2009), arXiv:0808.1491.

[66] E. Syresin et al., *NICA Accelerator Complex at JINR,* in Proc. 10th International Particle Accelerator Conference (IPAC'19) (JACoW Publishing, 2019) pp. 452–454.

[67] M. Buballa, *NJL model analysis of dense quark matter,* Phys. Rept., **407**, 205 (2005), arXiv:hep-ph/0402234.

[68] A. Schmitt, *Introduction to Superfluidity: Field-theoretical approach and applications*, Lecture Notes in Physics, Vol. 888 (2015) arXiv:1404.1284.

[69] M. G. Alford, K. Rajagopal, and F. Wilczek, *Color flavor locking and chiral symmetry breaking in high density QCD,* Nucl. Phys. B, **537**, 443 (1999), arXiv:hep-ph/9804403.

[70] M. G. Alford, A. Schmitt, K. Rajagopal, and T. Schafer, *Color superconductivity in dense quark matter,* Rev.Mod.Phys., **80**, 1455 (2008), arXiv:0709.4635.

[71] J. M. Lattimer and M. Prakash, *The physics of neutron stars,* Science, **304**, 536 (2004), arXiv:astro-ph/0405262.

[72] P. Demorest, T. Pennucci, S. Ransom, M. Roberts, and J. Hessels, *Shapiro Delay Measurement of A Two Solar Mass Neutron Star,* Nature, **467**, 1081 (2010), arXiv:1010.5788.

[73] J. Antoniadis et al., *A Massive Pulsar in a Compact Relativistic Binary,* Science, **340**, 6131 (2013), arXiv:1304.6875.

[74] H. T. Cromartie et al. [NANOGrav], *Relativistic Shapiro delay measurements of an extremely massive millisecond pulsar,* Nature Astron. **4**, 72 (2019), arXiv:1904.06759.

[75] R. C. Tolman, *Static solutions of Einstein's field equations for spheres of fluid,* Physical Review **55**, 364 (1939).

[76] J. R. Oppenheimer and G. M. Volkoff, *On massive neutron cores,* Physical Review **55**, 374 (1939).

[77] J. L. Friedman and J. R. Ipser, *On the Maximum Mass of a Uniformly Rotating Neutron Star,* The Astrophysical Journal, **314**, 594 (1987).

[78] A. Schmitt, *Dense matter in compact stars: A pedagogical introduction*, Lecture Notes in Physics, Vol. 811 (Springer Berlin, 2010) arXiv:1001.3294.

[79] D. G. Yakovlev and C. J. Pethick, *Neutron star cooling,* Ann. Rev. Astron. Astrophys., **42**, 169 (2004), arXiv:astro-ph/0402143.

[80] L. Tolos and L. Fabbietti, *Strangeness in Nuclei and Neutron Stars,* Prog. Part. Nucl. Phys., **112**, 103770 (2020), arXiv:2002.09223.

[81] M. Alford, M. Braby, M. W. Paris, and S. Reddy, *Hybrid stars that masquerade as neutron stars,* Astrophys. J., **629**, 969 (2005), arXiv:nucl-th/0411016.

[82] M. G. Alford and A. Sedrakian, *Compact stars with sequential QCD phase transitions,* Phys. Rev. Lett. **119**, 161104 (2017), arXiv:1706.01592.

[83] T. E. Riley et al., *A NICER View of PSR J0030+0451: Millisecond Pulsar Parameter Estimation,* Astrophys. J. Lett. **887**, L21 (2019), arXiv:1912.05702.

[84] M. Miller et al., *PSR J0030+0451 Mass and Radius from NICER Data and Implications for the Properties of Neutron Star Matter,* Astrophys. J. Lett. **887**, L24 (2019), arXiv:1912.05705.

[85] B. Abbott et al. [Virgo, LIGO Scientific], *GW170817: Observation of Gravitational Waves from a Binary Neutron Star Inspiral,* Phys. Rev. Lett. **119**, 161101 (2017), arXiv:1710.05832.

[86] E. Annala, T. Gorda, A. Kurkela, J. Nättilä, and A. Vuorinen, *Evidence for quark-matter cores in massive neutron stars,* Nature Phys. **16**, 907 (2020), arXiv:1903.09121.

[87] F. J. Dyson, *The S matrix in quantum electrodynamics,* Physical Review **75**, 1736 (1949).

[88] J. Schwinger, *On the Green's functions of quantized fields I+II,* Proc. Nat. Acad. Sci, **37**, 452 (1951).

[89] G. 't Hooft, *Renormalization of Massless Yang-Mills Fields,* Nucl. Phys. B, **33**, 173 (1971).

[90] R. Alkofer and L. von Smekal, *The Infrared Behavior of QCD Green's Functions - Confinement, Dynamical Symmetry Breaking, and Hadrons as Relativistic Bound States,* Phys. Rept., **353**, 281 (2001), hep-ph/0007355v2.

[91] P. Isserstedt, C. S. Fischer, and T. Steinert, *Thermodynamics from the quark condensate,* Phys. Rev. D **103**, 054012 (2021), arXiv:2012.04991.

[92] P. Isserstedt, M. Buballa, C. S. Fischer, and P. J. Gunkel, *Baryon number fluctuations in the QCD phase diagram from Dyson-Schwinger equations,* Phys. Rev. D **100**, 074011 (2019), arXiv:1906.11644.

[93] F. Gao and J. M. Pawlowski, *Chiral phase structure and critical end point in QCD,* Phys. Lett. B, **820**, 136584 (2021), arXiv:2010.13705.

[94] P. C. Wallbott, G. Eichmann, and C. S. Fischer, *Disentangling different structures in heavy-light four-quark states,* Phys. Rev. D **102**, 051501 (2020), arXiv:2003.12407.

[95] N. Santowsky, G. Eichmann, C. S. Fischer, P. C. Wallbott, and R. Williams, *σ-meson: Four-quark versus two-quark components and decay width in a Bethe-Salpeter approach,* Phys. Rev. D **102**, 056014 (2020), arXiv:2007.06495.

[96] N. Santowsky and C. S. Fischer, *Light scalars: Four-quark versus two-quark states in the complex energy plane from Bethe-Salpeter equations,* Phys. Rev. D **105**, 034025 (2022), arXiv:2109.00755.

[97] N. Santowsky and C. S. Fischer, *Four-quark states with charm quarks in a two-body Bethe–Salpeter approach,* Eur. Phys. J. C **82**, 313 (2022), arXiv:2111.15310.

[98] E. E. Salpeter and H. A. Bethe, *A Relativistic Equation for Bound-State Problems,* Phys. Rev., **84**, 1232 (1951).

[99] M. Q. Huber, C. S. Fischer, and H. Sanchis-Alepuz, *Quenched glueballs in the DSE/BSE framework,* in 19th International Conference on Hadron Spectroscopy and Structure (2022) arXiv:2201.05163.

[100] M. Q. Huber, *Correlation functions of Landau gauge Yang-Mills theory,* Phys. Rev. D, **101**, 114009 (2020), arXiv:2003.13703.

[101] J. Berges, *N-particle irreducible effective action techniques for gauge theories,* Phys. Rev., **D70**, 105010 (2004), arXiv:hep-ph/0401172.

[102] C. G. Callan, *Broken scale invariance in scalar field theory,* Physical Review D **2**, 1541 (1970).

[103] K. Symanzik, *Small distance behaviour in field theory and power counting,* Communications in Mathematical Physics **18**, 227 (1970).

[104] L. P. Kadanoff, *Scaling laws for Ising models near Tc,* Physics, **2**, 263 (1966).

[105] K. G. Wilson, *Renormalization group and critical phenomena. I. Renormalization group and the Kadanoff scaling picture,* Physical review B **4**, 3174 (1971).

[106] K. G. Wilson, *Renormalization group and critical phenomena. II. Phase-space cell analysis of critical behavior,* Physical Review B **4**, 3184 (1971).

[107] A. Eichhorn, *Asymptotically safe gravity,* in 57th International School of Subnuclear Physics: In Search for the Unexpected (2020) arXiv:2003.00044.

[108] J. Berges and D. Mesterhazy, *Introduction to the nonequilibrium functional renormalization group,* Nucl. Phys. B Proc. Suppl., **228**, 37 (2012), arXiv:1204.1489.

[109] J. V. Roth, D. Schweitzer, L. J. Sieke, and L. von Smekal, *Real-time methods for spectral functions,* arXiv:2112.12568.

[110] Y.-y. Tan, Y.-r. Chen, and W.-j. Fu, *Real-time dynamics of the $O(4)$ scalar theory within the fRG approach,* SciPost Phys., **12**, 026 (2022), arXiv:2107.06482.

[111] C. Wetterich, *Average action and the renormalization group equations,* Nuclear Physics B **352**, 529 (1991).

[112] C. Wetterich, *Exact evolution equation for the effective potential,* Physics Letters B **301**, 90 (1993).

[113] J. Polchinski, *Renormalization and effective Lagrangians,* Nuclear Physics B **231**, 269 (1984).

[114] P. M. Stevenson, *Optimized Perturbation Theory,* Phys. Rev. D, **23**, 2916 (1981).

[115] R. D. Ball, P. E. Haagensen, J. I. Latorre, and E. Moreno, *Scheme independence and the exact renormalization group,* Phys. Lett. B, **347**, 80 (1995), arXiv:hep-th/9411122.

[116] D. F. Litim, *Mind the gap,* Int. J. Mod. Phys. A, **16**, 2081 (2001), arXiv:hep-th/0104221.

[117] D. F. Litim, *Optimization of the exact renormalization group,* Phys. Lett. B, **486**, 92 (2000), arXiv:hep-th/0005245.

[118] D. F. Litim, *Critical exponents from optimized renormalization group flows,* Nucl. Phys. B, **631**, 128 (2002), arXiv:hep-th/0203006.

[119] D. F. Litim, *Optimized renormalization group flows,* Phys. Rev. D, **64**, 105007 (2001), arXiv:hep-th/0103195.

[120] I. Nandori, *Functional renormalization group with a compactly supported smooth regulator function,* JHEP, **04**, 150 (2013), arXiv:1208.5021.

[121] J. M. Pawlowski, M. M. Scherer, R. Schmidt, and S. J. Wetzel, *Physics and the choice of regulators in functional renormalisation group flows,* Annals Phys., **384**, 165 (2017), arXiv:1512.03598.

[122] T. D. . Cohen, *Functional integrals for QCD at nonzero chemical potential and zero density,* Phys. Rev. Lett., **91**, 222001 (2003), arXiv:hep-ph/0307089.

[123] G. Markó, U. Reinosa, and Z. Szép, *Bose-Einstein condensation and Silver Blaze property from the two-loop Φ-derivable approximation,* Phys. Rev. D **90**, 125021 (2014), arXiv:1410.6998.

[124] N. Khan, J. M. Pawlowski, F. Rennecke, and M. M. Scherer, *The Phase Diagram of QC2D from Functional Methods,* arXiv:1512.03673.

[125] J. I. Kapusta and C. Gale, *Finite-temperature field theory: Principles and applications* (Cambridge University Press, 2006).

[126] J. M. Pawlowski and N. Strodthoff, *Real time correlation functions and the functional renormalization group,* Phys. Rev. D **92**, 094009 (2015), arXiv:1508.01160.

[127] A. J. Helmboldt, J. M. Pawlowski, and N. Strodthoff, *Towards quantitative precision in the chiral crossover: masses and fluctuation scales,* Phys. Rev. **D91**, 054010 (2015), arXiv:1409.8414.

[128] J. Braun, M. Leonhardt, and J. M. Pawlowski, *Renormalization group consistency and low-energy effective theories,* SciPost Phys. **6**, 056 (2019), arXiv:1806.04432.

[129] J. M. Pawlowski, private communication.

[130] J. Braun, T. Dörnfeld, B. Schallmo, and S. Töpfel, *Renormalization group studies of dense relativistic systems,* Phys. Rev. D **104**, 096002 (2021), arXiv:2008.05978.

[131] S. Scherer, *Introduction to chiral perturbation theory,* Adv. Nucl. Phys., **27**, 277 (2003), arXiv:hep-ph/0210398.

[132] H. Leutwyler, *On the foundations of chiral perturbation theory,* Annals Phys., **235**, 165 (1994), arXiv:hep-ph/9311274.

[133] J. Braun, L. Fister, J. M. Pawlowski, and F. Rennecke, *From Quarks and Gluons to Hadrons: Chiral Symmetry Breaking in Dynamical QCD,* Phys. Rev. **D94**, 034016 (2016), arXiv:1412.1045.

[134] R. Alkofer and H. Reinhardt, *Chiral quark dynamics*, Vol. 33 (Springer Science & Business Media, 1995).

[135] Y. Nambu and G. Jona-Lasinio, *Dynamical model of elementary particles based on an analogy with superconductivity. I,* Physical Review **122**, 345 (1961).

[136] Y. Nambu and G. Jona-Lasinio, *Dynamical model of elementary particles based on an analogy with superconductivity. II,* Physical Review **124**, 246 (1961).

[137] S. Klevansky, *The Nambu–Jona-Lasinio Model of Quantum Chromodynamics,* Reviews of Modern Physics, **64**, 649 (1992).

[138] J. Braun, M. Leonhardt, and M. Pospiech, *Fierz-complete NJL model study: Fixed points and phase structure at finite temperature and density,* Phys. Rev. **D96**, 076003 (2017), arXiv:1705.00074.

[139] J. Braun, M. Leonhardt, and M. Pospiech, *Fierz-complete NJL model study. II. Toward the fixed-point and phase structure of hot and dense two-flavor QCD,* Phys. Rev. **D97**, 076010 (2018), arXiv:1801.08338.

[140] M. Mitter, J. M. Pawlowski, and N. Strodthoff, *Chiral symmetry breaking in continuum QCD,* Phys. Rev., **D91**, 054035 (2015), arXiv:1411.7978.

[141] J. Braun, *Fermion Interactions and Universal Behavior in Strongly Interacting Theories,* Journal of Physics G: Nuclear and Particle Physics **39** (2012), 1108.4449v1.

[142] J. Hubbard, *Calculation of partition functions,* Physical Review Letters **3**, 77 (1959).

[143] R. Stratonovich, *On a method of calculating quantum distribution functions,* in Soviet Physics Doklady, Vol. 2 (1957) p. 416.

[144] G. 't Hooft, *Symmetry breaking through Bell-Jackiw anomalies,* Physical Review Letters **37**, 8 (1976).

[145] E. Nakano, B. J. Schaefer, B. Stokic, B. Friman, and K. Redlich, *Fluctuations and isentropes near the chiral critical endpoint,* Phys. Lett., **B682**, 401 (2010), arXiv:0907.1344.

[146] B.-J. Schaefer, J. M. Pawlowski, and J. Wambach, *The Phase Structure of the Polyakov–Quark-Meson Model,* Phys. Rev., **D76**, 074023 (2007), arXiv:0704.3234.

[147] S. Roessner, C. Ratti, and W. Weise, *Polyakov loop, diquarks and the two-flavour phase diagram,* Phys. Rev., **D75**, 034007 (2007), arXiv:hep-ph/0609281.

[148] K. Fukushima, *Phase diagrams in the three-flavor Nambu-Jona-Lasinio model with the Polyakov loop,* Phys. Rev., **D77**, 114028 (2008), arXiv:0803.3318.

[149] T. K. Herbst, J. M. Pawlowski, and B.-J. Schaefer, *The phase structure of the Polyakov–quark–meson model beyond mean field,* Phys. Lett., **B696**, 58 (2011), arXiv:1008.0081.

[150] T. K. Herbst, M. Mitter, J. M. Pawlowski, B.-J. Schaefer, and R. Stiele, *Thermodynamics of QCD at vanishing density,* Phys. Lett. B, **731**, 248 (2014), arXiv:1308.3621.

[151] O. Ivanytskyi, M. A. Pérez-García, V. Sagun, and C. Albertus, *Second look to the Polyakov loop Nambu–Jona-Lasinio model at finite baryonic density,* Phys. Rev. D **100**, 103020 (2019), arXiv:1909.07421.

[152] K. Fukushima and V. Skokov, *Polyakov loop modeling for hot QCD,* Prog. Part. Nucl. Phys., **96**, 154 (2017), arXiv:1705.00718.

[153] W.-j. Fu, J. M. Pawlowski, and F. Rennecke, *Strangeness Neutrality and QCD Thermodynamics,* SciPost Phys. Core, **2**, 002 (2020), arXiv:1808.00410.

[154] F. Rennecke and B.-J. Schaefer, *Fluctuation-induced modifications of the phase structure in (2+1)-flavor QCD,* Phys. Rev. **D96**, 016009 (2017), arXiv:1610.08748.

[155] M. Mitter and B.-J. Schaefer, *Fluctuations and the axial anomaly with three quark flavors,* Phys. Rev. **D89**, 054027 (2014), arXiv:1308.3176.

[156] K. Otto, *High Density Fluctuations in Neutron Stars*, Master's thesis, Justus-Liebig University Giessen (2017).

[157] A. Zacchi and J. Schaffner-Bielich, *Implications of the fermion vacuum term in the extended SU(3) quark meson model on compact star properties,* Phys. Rev. **D100**, 123024 (2019), arXiv:1909.12071.

[158] J. Berges, D. U. Jungnickel, and C. Wetterich, *Two flavor chiral phase transition from nonperturbative flow equations,* Phys. Rev. D, **59**, 034010 (1999), arXiv:hep-ph/9705474.

[159] N. Tetradis and C. Wetterich, *Critical exponents from effective average action,* Nucl. Phys., **B422**, 541 (1994), arXiv:hep-ph/9308214.

[160] J. Braun, *Thermodynamics of QCD low-energy models and the derivative expansion of the effective action,* Phys. Rev. D, **81**, 016008 (2010), arXiv:0908.1543.

[161] J. M. Pawlowski and F. Rennecke, *Higher order quark-mesonic scattering processes and the phase structure of QCD,* Phys. Rev. **D90**, 076002 (2014), arXiv:1403.1179.

[162] W.-j. Fu, J. M. Pawlowski, F. Rennecke, and B.-J. Schaefer, *Baryon number fluctuations at finite temperature and density,* Phys. Rev. **D94**, 116020 (2016), arXiv:1608.04302.

[163] C. Busch, *Chiral Symmetry Breaking and Thermodynamics Beyond Local Potential Approximation*, Master's thesis, Justus-Liebig University Giessen (2019).

[164] A. Bazavov et al. [HotQCD], *Chiral crossover in QCD at zero and non-zero chemical potentials,* Phys. Lett., **B795**, 15 (2019), arXiv:1812.08235.

[165] R. Bellwied, S. Borsanyi, Z. Fodor, J. Günther, S. D. Katz, C. Ratti, and K. K. Szabo, *The QCD phase diagram from analytic continuation,* Phys. Lett., **B751**, 559 (2015), arXiv:1507.07510.

[166] F. Rennecke, *The Chiral Phase Transition of QCD*, Ph.D. thesis, University of Heidelberg (2015).

[167] J. Braun and B. Schallmo, *Zero-temperature thermodynamics of dense asymmetric strong-interaction matter,* arXiv:2204.00358.

[168] B. Friman and W. Weise, *Neutron Star Matter as a Relativistic Fermi Liquid,* Phys. Rev. C, **100**, 065807 (2019), arXiv:1908.09722.

[169] M. Drews and W. Weise, *Functional renormalization group studies of nuclear and neutron matter,* Prog. Part. Nucl. Phys., **93**, 69 (2017), arXiv:1610.07568.

[170] P. Pósfay, G. G. Barnaföldi, and A. Jakovác, *Effect of quantum fluctuations in the high-energy cold nuclear equation of state and in compact star observables,* Phys. Rev. **C97**, 025803 (2018), arXiv:1610.03674.

[171] Z.-G. Dai, Q.-H. Peng, and T. Lu, *The conversion from two - flavor to three - flavor quark matter in a supernova core,* Astrophys. J., **440**, 815 (1995).

[172] M. Baldo, M. Buballa, F. Burgio, F. Neumann, M. Oertel, and H. J. Schulze, *Neutron stars and the transition to color superconducting quark matter,* Phys. Lett., **B562**, 153 (2003), arXiv:nucl-th/0212096.

[173] M. Buballa, F. Neumann, M. Oertel, and I. Shovkovy, *Quark mass effects on the stability of hybrid stars,* Phys. Lett., **B595**, 36 (2004), arXiv:nucl-th/0312078.

[174] A. Drago, A. Lavagno, and I. Parenti, *Burning of an hadronic star into a quark or a hybrid star,* Astrophys. J., **659**, 1519 (2007), arXiv:astro-ph/0512652.

[175] E. Witten, *Cosmic separation of phases,* Phys. Rev. D, **30**, 272 (1984).

[176] E. Farhi and R. Jaffe, *Strange Matter,* Phys. Rev. D, **30**, 2379 (1984).

[177] K. Kamikado, N. Strodthoff, L. von Smekal, and J. Wambach, *Fluctuations in the quark-meson model for QCD with isospin chemical potential,* Phys. Lett., **B718**, 1044 (2013), arXiv:1207.0400.

[178] D. Chatterjee, T. Elghozi, J. Novak, and M. Oertel, *Consistent neutron star models with magnetic field dependent equations of state,* Mon. Not. Roy. Astron. Soc., **447**, 3785 (2015), arXiv:1410.6332.

[179] N. K. Glendenning, *First order phase transitions with more than one conserved charge: Consequences for neutron stars,* Phys. Rev., **D46**, 1274 (1992).

[180] F. Gulminelli and A. R. Raduta, *Unified treatment of subsaturation stellar matter at zero and finite temperature,* Phys. Rev. **C92**, 055803 (2015), arXiv:1504.04493.

[181] P. Danielewicz and J. Lee, *Symmetry Energy I: Semi-Infinite Matter,* Nucl. Phys., **A818**, 36 (2009), arXiv:0807.3743.

[182] E. Chabanat, P. Bonche, P. Haensel, J. Meyer, and R. Schaeffer, *A Skyrme parametrization from subnuclear to neutron star densities. 2. Nuclei far from stablities,* Nucl. Phys., **A635**, 231 (1998).

[183] S. Typel, G. Ropke, T. Klahn, D. Blaschke, and H. H. Wolter, *Composition and thermodynamics of nuclear matter with light clusters,* Phys. Rev., **C81**, 015803 (2010), arXiv:0908.2344.

[184] M. Hempel and J. Schaffner-Bielich, *Statistical Model for a Complete Supernova Equation of State,* Nucl. Phys., **A837**, 210 (2010), arXiv:0911.4073.

[185] A. W. Steiner, M. Hempel, and T. Fischer, *Core-collapse supernova equations of state based on neutron star observations,* Astrophys. J., **774**, 17 (2013), arXiv:1207.2184.

[186] I. Bombaci and D. Logoteta, *Equation of state of dense nuclear matter and neutron star structure from nuclear chiral interactions,* Astron. Astrophys., **609**, A128 (2018), arXiv:1805.11846.

[187] G. Baym, S. Furusawa, T. Hatsuda, T. Kojo, and H. Togashi, *New Neutron Star Equation of State with Quark-Hadron Crossover,* Astrophys. J., **885**, 42 (2019), arXiv:1903.08963.

[188] S. Typel, M. Oertel, and T. Klähn, *CompOSE CompStar online supernova equations of state harmonising the concert of nuclear physics and astrophysics compose.obspm.fr,* Phys. Part. Nucl. **46**, 633 (2015), arXiv:1307.5715.

[189] Z. F. Seidov, *The Stability of a Star with a Phase Change in General Relativity Theory,* Sov. Astron., **15**, 347 (1971).

[190] K. Schertler, C. Greiner, J. Schaffner-Bielich, and M. Thoma, *Quark phases in neutron stars and a 'third family' of compact stars as a signature for phase transitions,* Nucl. Phys. A, **677**, 463 (2000), arXiv:astro-ph/0001467.

[191] M. G. Alford, S. Han, and M. Prakash, *Generic conditions for stable hybrid stars,* Phys. Rev. **D88**, 083013 (2013), arXiv:1302.4732.

[192] S. Benic, D. Blaschke, D. E. Alvarez-Castillo, T. Fischer, and S. Typel, *A new quark-hadron hybrid equation of state for astrophysics - I. High-mass twin compact stars,* Astron. Astrophys., **577**, A40 (2015), arXiv:1411.2856.

[193] I. Tews, J. Carlson, S. Gandolfi, and S. Reddy, *Constraining the speed of sound inside neutron stars with chiral effective field theory interactions and observations,* Astrophys. J. **860**, 149 (2018), arXiv:1801.01923.

[194] P. Bedaque and A. W. Steiner, *Sound velocity bound and neutron stars,* Phys. Rev. Lett. **114**, 031103 (2015), arXiv:1408.5116.

[195] S. Borsanyi, G. Endrodi, Z. Fodor, S. D. Katz, S. Krieg, C. Ratti, and K. K. Szabo, *QCD equation of state at nonzero chemical potential: continuum results with physical quark masses at order mu^2,* JHEP, **08**, 053 (2012), arXiv:1204.6710.

[196] P. Benincasa and A. Buchel, *Hydrodynamics of Sakai-Sugimoto model in the quenched approximation,* Phys. Lett., **B640**, 108 (2006), arXiv:hep-th/0605076.

[197] A. Cherman, T. D. Cohen, and A. Nellore, *A Bound on the speed of sound from holography,* Phys. Rev., **D80**, 066003 (2009), arXiv:0905.0903.

[198] C. Ecker, C. Hoyos, N. Jokela, D. Rodríguez Fernández, and A. Vuorinen, *Stiff phases in strongly coupled gauge theories with holographic duals,* JHEP, **11**, 031 (2017), arXiv:1707.00521.

[199] Z.-Y. Zhu, E.-P. Zhou, and A. Li, *Neutron Star Equation of State from the Quark Level in Light of GW170817,* Astrophys. J. **862**, 98 (2018), arXiv:1802.05510.

[200] M. A. Aloy, J. M. Ibáñez, N. Sanchis-Gual, M. Obergaulinger, J. A. Font, S. Serna, and A. Marquina, *Neutron star collapse and gravitational waves with a non-convex equation of state,* Mon. Not. Roy. Astron. Soc., **484**, 4980 (2019), arXiv:1806.03314.

[201] B. P. Abbott et al. [LIGO Scientific, Virgo], *GW170817: Measurements of neutron star radii and equation of state,* Phys. Rev. Lett. **121**, 161101 (2018), arXiv:1805.11581.

[202] K. Fukushima and T. Hatsuda, *The phase diagram of dense QCD,* Rept. Prog. Phys., **74**, 014001 (2011), arXiv:1005.4814.

[203] J. Eser, M. Grahl, and D. H. Rischke, *Functional Renormalization Group Study of the Chiral Phase Transition Including Vector and Axial-vector Mesons,* Phys. Rev. D **92**, 096008 (2015), arXiv:1508.06928.

[204] H. Zhang, D. Hou, T. Kojo, and B. Qin, *Functional renormalization group study of the quark-meson model with ω meson,* Phys. Rev. **D96**, 114029 (2017), arXiv:1709.05654.

[205] R. Câmara Pereira, R. Stiele, and P. Costa, *Functional renormalization group study of the critical region of the quark-meson model with vector interactions,* Eur. Phys. J. C **80**, 712 (2020), arXiv:2003.12829.

[206] Y. Song, G. Baym, T. Hatsuda, and T. Kojo, *Effective repulsion in dense quark matter from nonperturbative gluon exchange,* Phys. Rev. D **100**, 034018 (2019), arXiv:1905.01005.

[207] S. Weissenborn, D. Chatterjee, and J. Schaffner-Bielich, *Hyperons and massive neutron stars: vector repulsion and SU(3) symmetry,* Phys. Rev. C **85**, 065802 (2012), arXiv:1112.0234.

[208] M. Oertel, C. Providência, F. Gulminelli, and A. R. Raduta, *Hyperons in neutron star matter within relativistic mean-field models,* J. Phys. G **42**, 075202 (2015), arXiv:1412.4545.

[209] D. Alvarez-Castillo, D. Blaschke, A. Grunfeld, and V. Pagura, *Third family of compact stars within a nonlocal chiral quark model equation of state,* Phys. Rev. D **99**, 063010 (2019), arXiv:1805.04105.

[210] M. Buballa, *The Problem of matter stability in the Nambu-Jona-Lasinio model,* Nucl. Phys. A, **611**, 393 (1996), arXiv:nucl-th/9609044.

[211] M. Ferreira, R. Câmara Pereira, and C. Providência, *Neutron stars with large quark cores,* Phys. Rev. D **101**, 123030 (2020), arXiv:2005.10543.

[212] M. Ferreira, R. Câmara Pereira, and C. Providência, *Hybrid stars with large strange quark cores constrained by GW170817,* Phys. Rev. D **103**, 123020 (2021), arXiv:2105.06239.

[213] F. Özel and P. Freire, *Masses, Radii, and the Equation of State of Neutron Stars,* Ann. Rev. Astron. Astrophys., **54**, 401 (2016), arXiv:1603.02698.

[214] T. Damour and A. Nagar, *Relativistic tidal properties of neutron stars,* Phys. Rev. D, **80**, 084035 (2009), arXiv:0906.0096.

[215] T. Zhao and J. M. Lattimer, *Tidal Deformabilities and Neutron Star Mergers,* Phys. Rev. D **98**, 063020 (2018), arXiv:1808.02858.

[216] B.-J. Schaefer and J. Wambach, *Renormalization Group Approach towards the QCD Phase Diagram,* Phys. Part. Nucl., **39**, 1025 (2008), hep-ph/0611191.

[217] J. Berges, D.-U. Jungnickel, and C. Wetterich, *The Chiral phase transition at high baryon density from nonperturbative flow equations,* Eur. Phys. J. C, **13**, 323 (2000), arXiv:hep-ph/9811347.

[218] R.-A. Tripolt, C. Jung, L. von Smekal, and J. Wambach, *Vector and axial-vector mesons in nuclear matter,* Phys. Rev. D **104**, 054005 (2021), arXiv:2105.00861.

[219] Z. Arzoumanian et al. [NANOGrav], *The NANOGrav 11-year Data Set: High-precision timing of 45 Millisecond Pulsars,* Astrophys. J. Suppl. **235**, 37 (2018), arXiv:1801.01837.

[220] J. Braun and B. Schallmo, *From quarks and gluons to color superconductivity at supranuclear densities,* Phys. Rev. D **105**, 036003 (2022), arXiv:2106.04198.

[221] W.-K. Tung, *Group Theory in Physics* (World Scientific, 1985).

[222] T.-P. Cheng and L.-F. Li, *Gauge theory of elementary particle physics* (Clarendon press Oxford, 1984).

[223] J. Jebsen, *Über die allgemeinen kugelsymmetrischen Lösungen der Einsteinschen Gravitationsgleichungen im Vakuum,* Arkiv för Matematik, Astronomi och Fysik **15**, 1 (1921).

[224] G. D. Birkhoff, *Relativity and Modern Physics* (Harvard University Press, 1923).

[225] K. Schwarzschild, *Über das Gravitationsfeld eines Massenpunktes nach der Einsteinschen Theorie,* in Sitzungsberichte der Königlich Preussischen Akademie der Wissenschaften zu Berlin (1916) pp. 189–196.

[226] K. Schwarzschild, *Über das Gravitationsfeld einer Kugel aus inkompressibler Flüssigkeit nach der Einsteinschen Theorie,* in Sitzungsberichte der Königlich Preussischen Akademie der Wissenschaften zu Berlin (1916) pp. 424–434.

[227] N. K. Glendenning, *Compact stars: Nuclear physics, particle physics, and general relativity* (1997).

[228] G. Ellis, R. Maartens, and M. A. H. MacCallum, *Causality and the speed of sound,* Gen. Rel. Grav., **39**, 1651 (2007), arXiv:gr-qc/0703121.

[229] K. S. Thorne, *Tidal stabilization of rigidly rotating, fully relativistic neutron stars,* Phys. Rev. D, **58**, 124031 (1998), arXiv:gr-qc/9706057.

[230] T. Hinderer, B. D. Lackey, R. N. Lang, and J. S. Read, *Tidal deformability of neutron stars with realistic equations of state and their gravitational wave signatures in binary inspiral,* Phys. Rev. D, **81**, 123016 (2010), arXiv:0911.3535.

[231] T. Regge and J. A. Wheeler, *Stability of a Schwarzschild singularity,* Phys. Rev., **108**, 1063 (1957).

[232] K. S. Thorne and A. Campolattaro, *Non-Radial Pulsation of General-Relativistic Stellar Models. I. Analytic Analysis for L >= 2,* Astrophysical Journal, **149**, 591 (1967).

[233] L. Lindblom, G. Mendell, and J. R. Ipser, *Relativistic stellar pulsations with near - zone boundary conditions,* Phys. Rev. D, **56**, 2118 (1997), arXiv:gr-qc/9704046.

[234] T. Hinderer, *Tidal Love numbers of neutron stars,* Astrophys. J., **677**, 1216 (2008), arXiv:0711.2420.

[235] I. N. Bronstein, K. A. Semendjajew, G. Musiol, and H. Mühlig, *Taschenbuch der Mathematik*, 7th ed. (Verlag Harri Deutsch, Frankfurt am Main, 2008).

[236] B. Sathiapalan, An Introduction to Exact RG, (2019), lecture notes.

[237] A. Nieto, *Evaluating Sums over the Matsubara Frequencies,* Comput. Phys. Commun., **92**, 54 (1995), hep-ph/9311210.

[238] G. Baym and N. D. Mermin, *Determination of Thermodynamic Green's Functions,* J. Math. Phys., **2**, 232 (1961).

[239] F. Rennecke, private communication.

[240] S. Rechenberger, *Asymptotic Safety of Yukawa Systems*, Diploma thesis, Friedrich-Schiller University Jena (2010).

[241] W. Metzner, M. Salmhofer, C. Honerkamp, V. Meden, and K. Schönhammer, *Functional renormalization group approach to correlated fermion systems,* Rev. Mod. Phys., **84**, 299 (2012).

[242] W. H. Press, *Numerical recipes 3rd edition: The art of scientific computing* (Cambridge University Press, 2007).

[243] J. A. Adams, J. Berges, S. Bornholdt, F. Freire, N. Tetradis, and C. Wetterich, *Solving nonperturbative flow equations,* Mod. Phys. Lett., **A10**, 2367 (1995), arXiv:hep-th/9507093.

[244] O. Bohr, B. J. Schaefer, and J. Wambach, *Renormalization Group Flow Equations and the Phase Transition in O(N)-models,* Int.J.Mod.Phys. A, **16**, 3823 (2001), hep-ph/0007098.

[245] S. Resch, F. Rennecke, and B.-J. Schaefer, *Mass sensitivity of the three-flavor chiral phase transition,* Phys. Rev. D **99**, 076005 (2019), arXiv:1712.07961.

[246] J. Borchardt and B. Knorr, *Solving functional flow equations with pseudo-spectral methods,* Phys. Rev., **D94**, 025027 (2016), arXiv:1603.06726.

[247] E. Grossi and N. Wink, *Resolving phase transitions with Discontinuous Galerkin methods,* arXiv:1903.09503.

[248] A. Koenigstein, M. J. Steil, N. Wink, E. Grossi, J. Braun, M. Buballa, and D. H. Rischke, *Numerical fluid dynamics for FRG flow equations: Zero-dimensional QFTs as numerical test cases - Part I: The $O(N)$ model,* arXiv:2108.02504.

[249] A. Koenigstein, M. J. Steil, N. Wink, E. Grossi, and J. Braun, *Numerical fluid dynamics for FRG flow equations: Zero-dimensional QFTs as numerical test cases – Part II: Entropy production and irreversibility of RG flows,* arXiv:2108.10085.

[250] M. J. Steil and A. Koenigstein, *Numerical fluid dynamics for FRG flow equations: Zero-dimensional QFTs as numerical test cases - Part III: Shock and rarefaction waves in RG flows reveal limitations of the $N \to \infty$ limit in $O(N)$-type models,* arXiv:2108.04037.

[251] J. Stoll, N. Zorbach, A. Koenigstein, M. J. Steil, and S. Rechenberger, *Bosonic fluctuations in the $(1+1)$-dimensional Gross-Neveu(-Yukawa) model at varying μ and T and finite N,* arXiv:2108.10616.

[252] J. Dormand and P. Prince, *A family of embedded Runge-Kutta formulae,* Journal of Computational and Applied Mathematics **6**, 19 (1980).

[253] R. Storn and K. Price, *Differential evolution–a simple and efficient heuristic for global optimization over continuous spaces,* Journal of global optimization **11**, 341 (1997).

[254] J. Goldstone, *Field theories with «Superconductor» solutions,* Il Nuovo Cimento (1955-1965) **19**, 154 (1961).

Acknowledgments

First of all, I would like to thank Bernd-Jochen Schaefer for presenting me with this interesting and interdisciplinary project, for the large amount of time he invested in me, and for the countless physics and off-topic discussions. I am especially grateful for the many opportunities he gave me to participate in various conferences and present our collaborative work.

I thank Micaela Oertel for very fruitful collaborations and expert advice on neutron star physics. I also wish to thank my working-group colleague Christopher Busch for his helpfulness, teamwork, and friendship.

I am grateful to Christian Fischer for keeping me in touch with the Seattle exchange project and organizing funding when I was in need, and to Lorenz von Smekal for being a referee on my thesis.

Furthermore, I would like to thank Pascal Gunkel, Jonas Wilhelm, and Emil Leeb-Lundberg for spending some extremely memorable times with me at the summer schools in Trento and Mainz.

I am thankful to my office-mate Julian Bernhardt for always having an open ear, and to all other past and present members of the institute for the numerous chats and social interactions.

My deepest gratitude goes to my family and friends who have been keeping me sane for so many years. I am indebted to all of them for their patience and understanding whenever I was preoccupied with my PhD project. I would especially like to mention my parents who convinced me to pursue the study of physics after school. Without their continuous emotional and financial support this would not have been possible.

I gratefully acknowledge funding by the Studienstifung des deutschen Volkes and by HGS-HIRe.

Eigenständigkeitserklärung

Ich erkläre:

Ich habe die vorgelegte Dissertation selbstständig und ohne unerlaubte fremde Hilfe und nur mit den Hilfen angefertigt, die ich in der Dissertation angegeben habe. Alle Textstellen, die wörtlich oder sinngemäß aus veröffentlichten Schriften entnommen sind, und alle Angaben, die auf mündlichen Auskünften beruhen, sind als solche kenntlich gemacht. Ich stimme einer evtl. Überprüfung meiner Dissertation durch eine Antiplagiat-Software zu. Bei den von mir durchgeführten und in der Dissertation erwähnten Untersuchungen habe ich die Grundsätze guter wissenschaftlicher Praxis, wie sie in der „Satzung der Justus-Liebig-Universität Gießen zur Sicherung guter wissenschaftlicher Praxis“ niedergelegt sind, eingehalten.

(Konstantin Otto)